Applied Computational Electromagnetics Society

Journal

May 2013 Vol. 28 No. 5

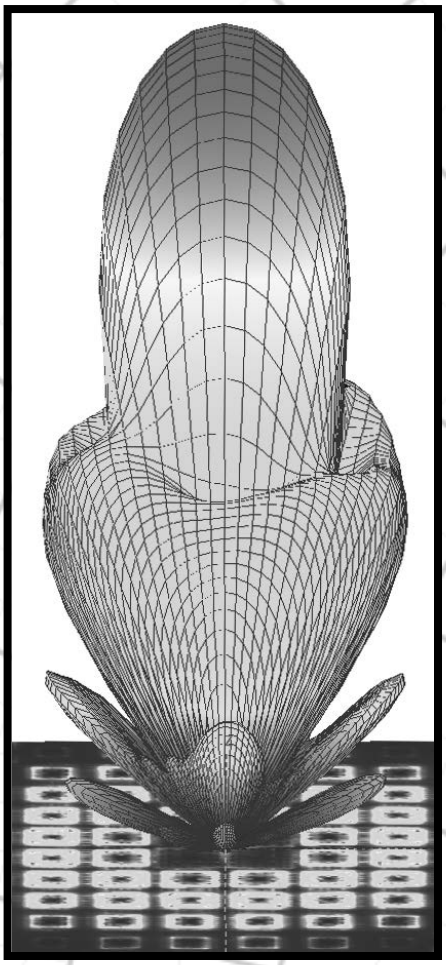

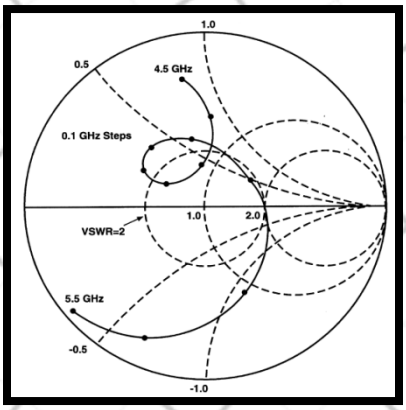

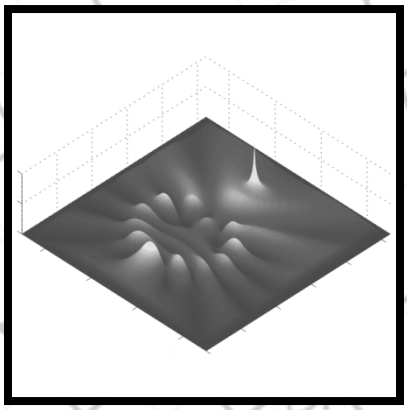

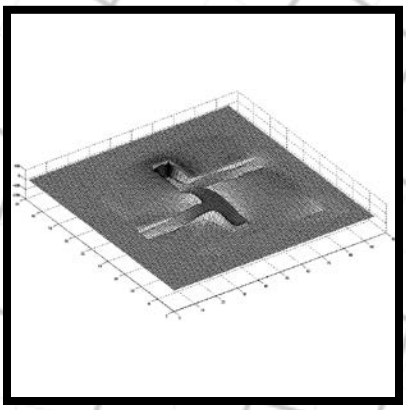

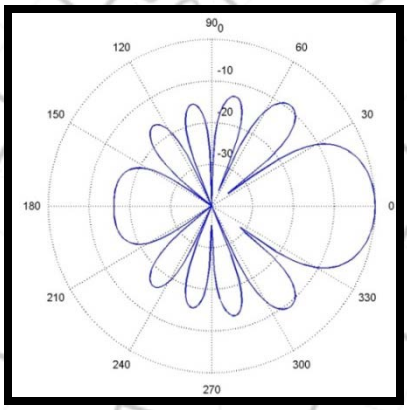

ISSN 1054-4887

GENERAL PURPOSE AND SCOPE: The Applied Computational Electromagnetics Society ***(ACES)*** Journal hereinafter known as the ***ACES Journal*** is devoted to the exchange of information in computational electromagnetics, to the advancement of the state-of-the art, and the promotion of related technical activities. The primary objective of the information exchange is to inform the scientific community on the developments of new computational electromagnetics tools and their use in electrical engineering, physics, or related areas. The technical activities promoted by this publication include code validation, performance analysis, and input/output standardization; code or technique optimization and error minimization; innovations in solution technique or in data input/output; identification of new applications for electromagnetics modeling codes and techniques; integration of computational electromagnetics techniques with new computer architectures; and correlation of computational parameters with physical mechanisms.

SUBMISSIONS: The ***ACES Journal*** welcomes original, previously unpublished papers, relating to applied computational electromagnetics. Typical papers will represent the computational electromagnetics aspects of research in electrical engineering, physics, or related disciplines. However, papers which represent research in applied computational electromagnetics itself are equally acceptable.

Manuscripts are to be submitted through the upload system of ***ACES*** web site http://www.aces-society.org See "Information for Authors" on inside of back cover and at ***ACES*** web site. For additional information contact the Editor-in-Chief:

Dr. Atef Elsherbeni
Department of Electrical Engineering
The University of Mississippi
University, MS 386377 USA
Phone: 662-915-5382
Email: atef@olemiss.edu

SUBSCRIPTIONS: All members of the Applied Computational Electromagnetics Society are entitled to access and download the ***ACES Journal*** any published journal article available at http://aces.ee.olemiss.edu. Printed issues of the ***ACES Journal*** are delivered to institutional members. Each author of published papers receives a printed issue of the ***ACES Journal*** in which the paper is published.

Back issues, when available, are $50 each. Subscription to ***ACES*** is through the web site. Orders for back issues of the ***ACES Journal*** and change of address requests should be sent directly to ***ACES*** office at:

Department of Electrical Engineering
The University of Mississippi
University, MS 386377 USA
Phone: 662-915-7231
Email: aglisson@olemiss.edu

Allow four weeks advance notice for change of address. Claims for missing issues will not be honored because of insufficient notice, or address change, or loss in the mail unless the ***ACES*** office is notified within 60 days for USA and Canadian subscribers, or 90 days for subscribers in other countries, from the last day of the month of publication. For information regarding reprints of individual papers or other materials, see "Information for Authors".

LIABILITY. Neither ***ACES***, nor the ***ACES Journal*** editors, are responsible for any consequence of misinformation or claims, express or implied, in any published material in an ***ACES Journal*** issue. This also applies to advertising, for which only camera-ready copies are accepted. Authors are responsible for information contained in their papers. If any material submitted for publication includes material which has already been published elsewhere, it is the author's responsibility to obtain written permission to reproduce such material.

APPLIED COMPUTATIONAL ELECTROMAGNETICS SOCIETY JOURNAL

May 2013
Vol. 28 No. 5
ISSN 1054-4887

The ACES Journal is abstracted in INSPEC, in Engineering Index, DTIC, Science Citation Index Expanded, the Research Alert, and to Current Contents/Engineering, Computing & Technology.

The illustrations on the front cover have been obtained from the research groups at the Department of Electrical Engineering, The University of Mississippi.

JANUARY 2013 REVIEWERS

Ahmed Abdelrahman
Iftikhar Ahmed
Seyed Armaki
Adem Aydin
Abdul Ali Babar
Mohamed Bakr
Toni Björninen
William Coburn
Veysel Demir
Khaled ElMahgoub
Mark Ingalls
Arkom Kaewrawang
Yasushi Kanai
B. David Moore
Payam Nayeri
Ozlem Ozgun
Ali Ozmetin
Stergios Papantonis
Seyyed Sedighy
Lotfollah Shafai
Sellakkutti Suganthi
Yasuhiro Tsunemitsu
Yuhao Wang
Su Yan
Xiaohua Yi

THE APPLIED COMPUTATIONAL ELECTROMAGNETICS SOCIETY

JOURNAL

Vol. 28 No. 5 May 2013

TABLE OF CONTENTS

Plasmonic Enhancement of Irregular Shape Nano-Patch for Thin Film Silicon Solar Cells

Nathan Burford[1] and Magda El-Shenawee[2]

[1,2]Computational Electromagnetics Group
[1]Microelectronics-Photonics Program
[2]Department of Electrical Engineering
University of Arkansas, Fayetteville, AR, 72701, United States
nburford@uark.edu, magda@uark.edu

Abstract – In this work plasmonic resonance of highly irregular aluminum nanostructures on a silicon photovoltaic substrate is investigated. These structures are inspired by natural surface structuring that occurs during the top-down aluminum induced crystallization of amorphous silicon. The computer simulations are obtained using the Ansys® HFSS allowing studying the enhanced fields transmitted into the silicon layer. The obtained results show significant light trapping and enhancement of the transmitted fields when these nanostructures are composed of high aluminum and low silicon concentration. These effects decrease for lower aluminum and high silicon concentrations cases nanostructures.

Index Terms **–** Aluminum nanostructures, enhanced electromagnetic fields, plasmons, and solar energy.

I. INTRODUCTION

Solar energy is one of the most promising sources of clean, renewable energy. Silicon (Si) thin-film technology holds potential to greatly reduce solar cell production costs, thus decreasing the cost-per-watt of solar energy enough to make it competitive against the non-renewable fossil fuels that dominate the market today [1-3]. However, a major issue of poor light absorption prevents thin-film technology from being competitive with traditional wafer based solar cells [4-8]. Due to the greatly reduced thickness of the absorbing layer, much of the incident light in a Si thin-film photovoltaic will pass through or be reflected from the interface back out before it is absorbed, thus greatly decreasing the efficiency of thin-films compared to thicker wafer based solar cells [9]. As such, novel methods for trapping light within thin-film photovoltaic are needed to make this technology advantageous over existing traditional solar cell technologies [10-12].

Recently, nanoplasmonics offer a promising method for solving some of the issues with thin-film Si technology [13-22]. By taking advantage of the plasmonic properties of the metallic nanostructures, it is possible to improve light trapping and hence photon absorption in Si thin-films. When exposed to an external electromagnetic wave (e.g., light), sub-wavelength scale metallic nanoparticles will undergo strong electrons oscillations if the frequency of the electromagnetic wave matches the plasmon frequency of the nanoparticle. First, this can lead to strong localization and enhancement of the near electric fields at the surface of the photovoltaic (PV) absorbing layer [23-25]. Second, this can cause scattering of transmitted electromagnetic waves into lateral modes, which effectively increases the path length of the transmitted wave traveling in the Si thin-film layer [10-12]. These mechanisms can improve the absorption of the light, thus increasing PV device efficiency.

Extensive work by various groups has been put forth to investigate the various parameters that influence the frequency and strength of particles plasmon resonance [26-33]. Size, shape, material properties, local dielectric environment, and local interactions with nearby particles have all illustrated strong influence on the plasmon resonance of metallic nanoparticles [13-22], and

Submitted On: Oct. 30, 2012
Accepted On: Mar. 17, 2013

[26-33]. Some examples; Cao *et al.* investigated the plasmon resonance of cylindrical, triangular, and square shaped silver nanoparticles through numerical simulation of single nanoparticles and dark-field optical microscopy of fabricated nanoparticle arrays. Their work demonstrated strong shifts in the resonant wavelength between various nanoparticle shapes and inter-particle spacing [26]. Sundar studied the effects of focused beam interactions of single metallic nanoparticles [27]. Langhammer *et al.* investigated the nanodisk geometry made of aluminum (Al) showing a strong shift in plasmon resonance from infrared to ultraviolet using varying disk aspect ratios [28]. El-Shenawee *et al.* studied, through the use of method of moments, the plasmonic interactions of single pairs of closely spaced gold nanotoroidsin [29] and finite gold nanotoroid arrays, both uniform and non-uniform in [30]. Additionally, Large *et al.* illustrated the strong shift in plasmon resonance by alteration of minor details in the nanoparticle geometry, such as rounding of nanoparticle edges that are ideally sharp 90 degree corners [31].

In addition to plasmonic resonance behavior, previous works have investigated the absorption enhancing effects for plasmonic nanoparticles located on PV devices for a wide range of cases [3, 18, 19, 34-37]. Early experimental work by Derkacs *et al.* illustrated this potential application by investigating gold spherical nanoparticles deposited on a Si thin-film, observing 8.3 % enhancement in conversion efficiency [3]. The spectral behavior of the photocurrent enhancement of gold nanospheres deposited on a Si thin-film solar cell was investigated experimentally by Lim *et al.*, with numerical simulations being performed to verify and explain the mechanisms for this enhancement [18]. Nakayama *et al.* experimentally studied this photocurrent enhancement by gold nanospheres, but for GaAs thin-films, instead of Si. In addition, it is noted that these surface localized nanoparticles reduce the surface sheet resistance of the cell, thus improving the device fill factor and providing an additional mechanism for improving the conversion efficiency [34]. Akimov*et al.* compared silver and Al nanospheres located on Sithin-films, demonstrating stronger absorption of electromagnetic energy in the Si layer by the Al nanoparticles, as well as significantly less detrimental effects by the addition of an oxide layer in the Al nanoparticles, as opposed to silver [35]. This work is continued by Akimov*et al.* to investigate the tuning of the nanoparticle geometries from the idealistic perfect sphere to elliptical nanospheroids, with the results showing optimal performance by nanoparticles of non-perfect sphere geometry [19]. Al nanospheres are also investigated and compared to gold and silver by Kocherginet *al.*, only for organic thin-film solar cells. Both experimental and theoretical results of this work show significantly higher improvement in absorption enhancement by the Al nanoparticles over gold and silver [36]. All of these works show that while plasmonic nanoparticles can indeed provide enhanced light absorption in PV devices, the performance is highly dependent on the design of the plasmonic structure. The majority of these works encompass simple, ideal geometries of plasmonic nanostructures, with less work investigating more complex irregular structures.

The current work does not deal with engineered nanostructures but it deals with irregular Al nano-patches produced during the fabrication process of the thin-film photovoltaic technology [37]. Inspiration for the structure geometry comes from an unintentional byproduct of the top-down Al induced crystallization (TAIC) of amorphous silicon (a-Si) as discussed in [37]. In traditional metal induce crystallization an a-Si thin film is deposited over a substrate, followed by the deposition of a thin metallic layer, typically on the order of tens to several hundred nanometers [38]. The bonding energy of the a-Si is much lower at the a-Si/metal interface. As such, the crystallization energy is greatly reduced. Low temperature annealing causes layer exchange between the a-Si and metallic layers and crystallizes the s-Si into polycrystalline Si [38, 39]. TAIC is a variant of metal induced crystallization in which layer exchange is minimized. Layer exchange that does occur can be controlled and result in engineered texturing [37, 39]. Movement of a-Si:H is limited by Al thickness in this case [39].

The paper is organized as follows: the computational model is presented in section II, including key analysis techniques and the full range of parameters to be investigated. In section III, the numerical results along with an interpretation of their significance are presented,

and finally concluding remarks are discussed in section IV.

II. COMPUTATIONAL METHODOLOGY

In this work, we utilize the commercially available electromagnetic simulation software Ansys® HFSSto investigate the plasmonic enhancement properties of the highly shape irregular Al/Si composite nano-patches inspired by thin film photovoltaic (see Fig. 1 in [39]). All results are obtained using the University of Arkansas Razor High Performance Computing cluster. Each node of this computing cluster contains two hex-core Xeon X5670 processors operating at 2.93 GHz and 2x12MB cache. Four nodes of this cluster contain 96 GB of memory and these nodes specifically were the ones used in this work. Each of the single nano-patch simulations consist of approximately 680,000 mesh cells, requiring 51.2 GB of memory and 15.5 hours of computational time per frequency. Using HFSS's multiprocessing licensing this was solved using 10 processing cores, which provided a significantly reduced time of approximately 1.7 hours per frequency point.

A. Validation

The computational study of plasmonic nanostructures offers unique challenges, as different methods can generate vastly different results if care is not taken to validate results [40]. To ensure that HFSS is being utilized correctly, specifically that an appropriate mesh cell density is used, a comparison of a single gold torus shaped nanoparticle is conducted using HFSS and a custom parallelized method of moments code (MoM) [22]. A single gold nanotoroid immersed in air is considered, since the geometry is simple yet shares a resemblance to certain features of the model of interest in this work. The toroid of interest has an outer radius of 42 nm, while the radius of the central air circle is 27 nm. Additionally, previous validation of the MoM code was performed with the Mie solution for gold nanospheres [32].

Figure 1 illustrates the results of this validation. These results are normalized scattering coefficients for each method, which allows for comparison of the resonant peak location. The observed spectral location of the peak using the

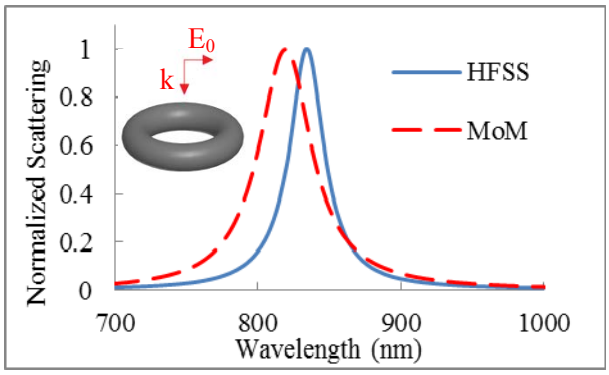

Fig. 1. Normalized scattering coefficient by a single gold toroid in air, calculated using HFSS (solid blue line) and MoM (dashed red line).

HFSS is 833 nm and using the MoM is 820 nm, indicating a 1.6 % difference in the spectral locations of the peaks. The agreement between the HFSS and MoM results confirm that the mesh density utilized here provides accurate results when applied to the other simulations presented in this work. These results are also consistent with previous studies of gold nanotoroids reported in [33].

B. Model development

The parameters for the simulations are as follows. The computational domain extends 2000 nm in the *x* and *y* directions and 1000 nm in the *z* direction. The top portion (z = 0 to 500 nm) is modeled as air and the bottom portion (z = 0 to 500 nm) is modeled as the thin film Si photovoltaic layer. The simulation domain is excited via plane wave incident at *z* = 500, propagating in the –*z* direction and polarized along the *x*-axis. Two boundary cases are considered; (i) a single structure and (ii) an infinite array of structures. For the case of the single structure, all external surfaces of the domain are set to radiating boundary conditions. This allows scattered waves to propagate out of the simulation domain with no back reflections. Often, perfectly matched layer (PML) boundaries are used in place of radiation boundaries, as they generally provide more accurate results. However, PML boundaries require the addition of artificial layers at the external surfaces, which must be solved inside as well, increasing the computational burden of the simulation. In section III, results comparing and justifying the use of radiation boundaries as

opposed to PML boundaries are presented. The excitation for the single structure case is that of an incident plane wave propagating through the finite radiation boundary on the *x*-*y* face at $z = 500$ nm.

In the simulation of the infinite arrays, only the external surfaces at $\pm z = 500$ nm are set to radiating boundary conditions. The opposing *x*-*z* faces at $y = 0$ and 2000 nm and the opposing *y*-*z* faces at $x = 0$ and 2000 nm are both set to master/slave boundary condition pairs, so as to emulate an infinite array of nano-patches in the *x* and *y* directions by matching the fields at the slave boundary to the corresponding master boundary. This effectively mirrors the unit cell depicted in Fig. 2 (c) infinitely in the *x* and *y* directions, generating an infinite 2D square array of the nanostructures and Si substrate. The most basic method for simulating infinite arrays is to utilize perfect electric and perfect magnetic symmetry boundaries. This also effectively mirrors the computational domain infinitely in two dimensions, but requires that the excitation have electric and magnetic field components normal to the electric and magnetic symmetry planes, respectively. Master/slave boundaries allow for excitations where this requirement of normal electric and magnetic field components is not met by introducing an appropriate phase shift in the slave boundary as compared to the reference field of the corresponding master boundary. For normal angles of incidence as described in this work the phase shift between the master and slave boundaries is zero, which is effectively identical to using traditional perfect electric and perfect magnetic symmetry boundaries. However, using the master/slave boundaries allows for possible future studies of non-normal angles of incidence. In this case, the center to center separation between the nano-patch elements is 2000 nm. For the infinite arrays, these boundary conditions enforce that the plane wave excitation will be modeled as infinitely uniform in the *x* and *y* directions. Figure 2 (c), then, illustrates for the infinite 2D square array case a single unit cell of the array, with *x*-*y* size of 2000 nm by 2000 nm.

The HFSS 3D model of these highly irregular nanostructures is based on the Matlab model described by Hassan and El-Shenawee, in which 2D irregular malignancy shapes are randomly generated [41]. This model is utilized to produce a random 2D shape that resembles the SEM images

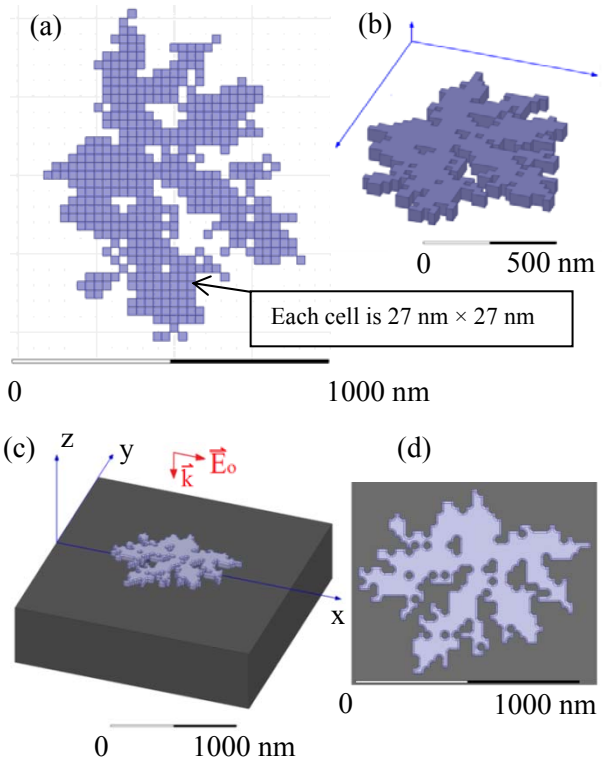

Fig. 2. HFSS model of the nano-patch to be investigated, all units in nm. (a) Top view of 2D nano-patch pattern constructed using 27 nm by 27 nm unit cells, (b) initial 3D model, produced by Boolean addition of unit cells and 50 nm extrusion along the *z*-direction, (c) final computational model, 10 nm radius rounding of all sharp edges and placement a top 500 nm thick silicon layer, (d) top view of finalized 3D model.

of the nanostructures (see Fig. 2 in [37]). The output data of the model is in the form of an array of coordinates for each of the individual square sheets that together form the entire nano-patch structure. The coordinates are then scaled to a typical nanostructure size and from here the coordinate data is used as a guide for placing 27 nm by 27 nm square sheets in the *x*-*y* plane at $z = 0$ nm in the HFSS model. These separate squares collectively form the basis of the entire irregular nano-patch structure, as shown in Fig. 2 (a). This is a time consuming process, as this model is based on approximately 535 of these individual square sheets, each of which must be manually placed in its appropriate location. Once all unit cells are in place, they are combined using the Boolean add feature and extruded 50 nm along the

z-direction, thus producing a 3D object from the 2D sheet, illustrated in Fig. 2 (b). Finally, all edges of the structure are rounded to a 10 nm radius curvature, so as to reduce unrealistic edge effects that can arise from the presence of sharp corners. This final 3D model of the nanostructure is illustrated in Fig. 2 (c), with a top view of the final structure shown in Fig. 2 (d).

As known, purely noble metallic particles exhibit plasmonic resonance. However, the surface structures observed during the TAIC process are not purely Al, but instead some mixture of Al and Si. As such, we consider not only cases of purely Al nano-patches, but also nano-patches of 30 % and 5 % Al, with the remainder being Si. For these mixture cases, the electrical properties for the nano-patch are calculated by taking a weighted average of the Al and Si properties. Both the Si and Al are frequency dependent in this band. We approximated the nanostructure to be a function of Al percentage, comprising the material (%Al); we used effective permittivity calculated using associated weights, of material percentage, of the electrical properties of pure Al and pure Si given by,

$$\varepsilon_{eff}(\%Al) = \varepsilon_{Al}\,\%Al + \varepsilon_{Si}(1 - \%Al). \quad (1)$$

Here, ε_{Al} represents the permittivity of pure Al and ε_{Si} is the permittivity of pure Si. The frequency dependent values for the electrical properties of Si and Al are taken from Palik [42]. Figures 3 and 4 illustrate the frequency dependent real and imaginary parts of the electrical permittivity for pure Si and pure Al, as well as the effective permittivity of the nanostructure at 30 % and 70 % Si and 5 % Al and 95 % Si, respectively.

The results are quantitatively compared by calculating the frequency dependent enhancement factor, EF(λ) for each of the cases. Inside the Si layer the only field that exists is either the fields scattered by the Si surface alone (reference case) or the fields scattered by both the Si surface and the nano-patch (enhanced case). The EF(λ) is calculated as the ratio of the average scattered field intensity absorbed in the Si layer with and without the nanostructure presented in [18],

$$\mathrm{EF}(\lambda) = \frac{\int \left|\boldsymbol{E}_{\mathrm{Si}_{\mathrm{with}}}\right|^2 \mathrm{dV}}{\int \left|\boldsymbol{E}_{\mathrm{Si}_{\mathrm{without}}}\right|^2 \mathrm{dV}}. \quad (2)$$

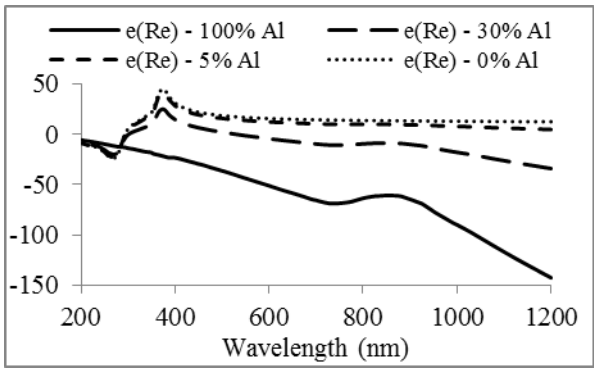

Fig. 3. Real part of the relative permittivity pure Al (solid line), pure a-Si (dotted line) and 30%, 5% Al weighted averages calculated using equation (1).

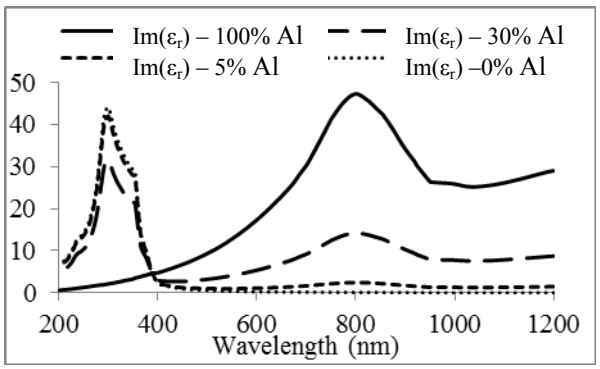

Fig. 4. Imaginary part of the relative permittivity pure Al (solid line), pure a-Si (dotted line) and 30%, 5% Al weighted averages calculated using equation (1).

In addition to the calculation of EF(λ), visual comparisons of wave interaction with the surface structure will be shown in section III.

III. NUMERICAL RESULTS AND DISCUSSION

In this section, the enhancement factor, EF(λ),will be shown for single and infinite arrays of the nano-patch geometry defined in Figs. 2 (c) and 2 (d) where the computational domain is 2000 nm × 2000 nm × 1000 nm. Three cases of Al composite material will be considered for the nano-patch positioned on top of Si as 100 %, 30 % and 5 %.

A. Enhancemnet factor EF(λ)

The results of Fig. 5 show the enhancement factor, EF(λ), for six cases versus the wavelength from 500 nm to 1200 nm. The plot of diamond symbols (red color) represents the 100 % Al nano-patches, the plot in of square symbols represents the 30 % Al and 70 % Si (green color), and the plot of triangular symbols represents (blue color) represent nano-patches made of 5 % Al and 95 % Si. The nano-patch structure, depicted in Fig. 2, has highly irregular shape with several air gaps in the structure that could contribute to the observed multiple resonances. Consider Fig. 2 (d), the top view of the nano-patch, the light blue coloring represents the nano-patch and the dark gray represents the Si substrate. The incident wave is propagating down into the structure with horizontal polarization across the nano-patch. It is observed that there are several different locations on the nano-patch where the electric field is applied across air gap locations. When the nano-patch is considered made of 100 % Al, this will cause capacitive coupling with the incident light at certain frequencies. Due to the variance of sizes and shapes of the air gap locations there is a variance in the capacitive resonances as well, which could explain why multiple peaks are observed in the EF(λ) plots in Fig. 5.

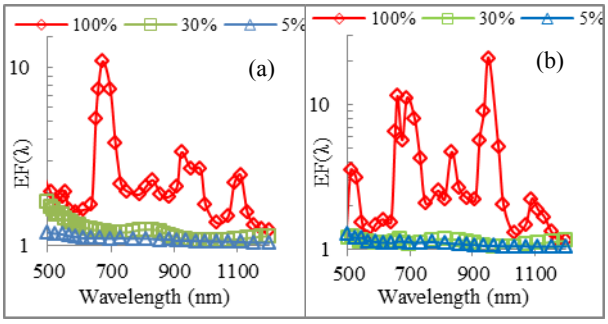

Fig. 5. Enhancement factor EF(λ) for nano-patch surface structures composed of 100 %, 30 %, and 5% aluminum for (a) single nano-patch and (b) infinite array of nano-patches.

The results show a maximum peak at a wavelength of 674 nm for the single nano-patch as shown in Fig. 5 (a) and at a wavelength of 952 nm for the array as shown in Fig. 5 (b). As anticipated, when the material of the nano-patches are assumed made of 30 % and 70 % Si or 5 % Al and 95 % Si, the resonance peak is much smaller and occurs at a wavelength 810 nm for both the single and infinite array cases. As reported in El-Shenawee *et al.* in [30], the resonance of an array of nanotoroids of the far fields occurs at the same wavelength of a single nanotoroid when the separation distance between elements is in the order of a wavelength. Therefore, the results reported in [30] show accumulative behavior in the extinction coefficient in the case of such array. However, the results of Fig. 5 show distinct differences between the resonances and peaks of the single nano-patch and the infinite array cases. Note that the results of Fig. 5 are for fields at 500 nm away from the interface, which is considered near fields. The wave propagation inside the Si layer exhibit a strong likelihood inter-particle coupling that can also explain the observed differences in the plasmons in Figs. 5 (a) and 5 (b), as will be shown in wave propagation graphs of Figs. (8) to (15).

Note that the enhancement factor (EF) of equation (2) is the wave absorption in Si with the presence of the nano-patch compared with that without it. The results of Fig. 5 show slight increase in the EF for both of the 5 % Al cases, with slight improvement in the 30 % Al cases. For these cases, the majority of the electrical properties of the structures come from Si, which has low electrical permittivity in the frequency range considered. As such, plasmonic effects that arise from the presence of the Al are reduced. The enhancement that does take place increases slightly as the wavelength decreases. At shorter wavelengths the many smaller features and holes in the structure of Fig. 2 contribute to slight scattering of the transmitted fields, which yield a small increase of the transmitted energy into the Si layer. At the longer wavelengths these small features become negligible due to the low Al composition. The features produce little effect on the transmitted fields and as such there is little difference between the case with the nano-patch and the reference case making the EF close to 1 as shown in Fig. 5.

B. Comparison of boundary conditions

A particular concern in HFSS is the application of proper boundary conditions, in particular the external absorbing boundaries. HFSS provides several options for absorbing boundaries, of particular interest here are the

radiation boundary condition and the perfectly matched layer (PML) boundaries. In Fig. 6, a comparison of the radiation boundaries and the PML boundaries is shown for the EF(λ). In this case a single 100 % Al nano-patch is investigated; once using the radiation boundaries as external boundaries and again using the PML boundaries. The results show good agreement between the two cases, with some minor deviation. The radiation boundaries are recommended for situations where scattering bodies are more than λ/4 away from the boundary, which is the case for this work. Using the radiation boundary requires approximately 0.68 million mesh cells and 51.2 GB of memory, while using the PML boundaries requires approximately 1.12 million mesh cells and 131 GB of memory. This is due to the addition of the artificial absorbing layer around the simulation domain, which must be accurately meshed as well. Although this absorbing layer does theoretically represent a more accurate solution, the radiation boundaries give nearly as good results at less than half the computational resources. As such, the radiation boundaries are adopted for this work.

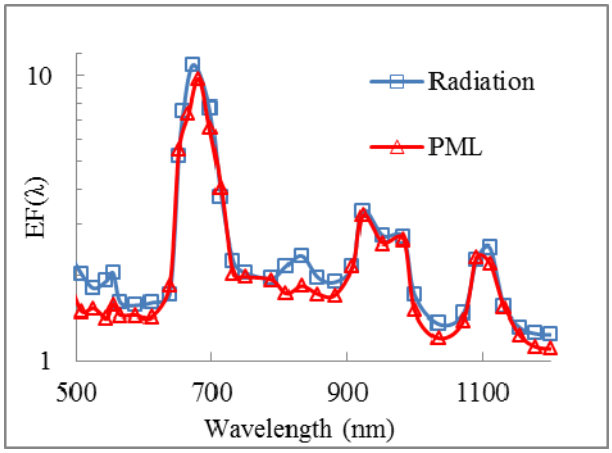

Fig. 6. Enhancement factor for a single 100 % aluminum nano-patch using radiation boundaries and PML boundaries.

C. Two irregular nano-patches

The infinite uniform array approximation is used here to manage the computational requirement, but it would be more practical to investigate the coupling between non-identical nanostructures. Here, two different irregular structures are generated using the same method described in section II. Both structures are approximately 450 nm and 600 nm across, respectively, 50 nm thick in the *z* direction and 900 nm center to center spacing with the incident excitation polarization oriented across the gap (see Fig. 7 (a)). The electrical properties used for the nano-patch structures are 100 % Al, with electrical properties depicted by the solid black line in Figs. 3 and 4. The Si layer is 1800 nm by 2600 nm by 500 nm, the air region above the Si is 500 nm thick in the *z* direction. For consistency in this work, the external boundaries are set to absorbing radiation boundaries. The configuration is illustrated in Fig. 7 (a). The high computational cost of this model restricts the overall size and number of different nano-patches that can be modeled, however, by implementing more efficient solvers it may be possible to increase the complexity of these models [43].

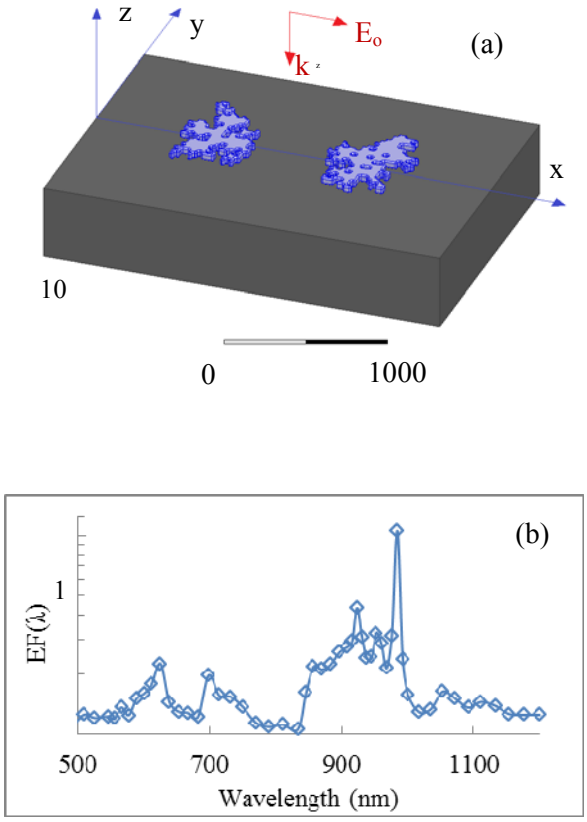

Fig. 7. (a) Computational configuration of a finite dual 100 % Al nano-patch simulation and (b) EF(λ) results of Fig. 7 (a).

In this case, the enhancement factor is calculated using equation (2) and the results are illustrated in Fig. 7 (b). Between λ = 770 nm and λ = 833 nm EF(λ) falls below 1, indicating to deterioration in efficiency, reaching its lowest value of 0.84 at λ = 833 nm. Aside from this range, the EF(λ) is above 1, indicating enhancement of the electromagnetic fields in the Si layer for most of the considered spectrum. On the other hand, between wavelengths of 845 nm and 992 nm a varying level of enhancement is observed. Upon comparison with Fig. 6, the EF(λ) levels of the single 100 % Al nano-patch occurs between 909 nm and 980 nm.

D. Wave propagation in silicon due to a single nano-patch

Figures 8 and 9 illustrate 2D plots of the magnitude of the real part of the electric fields for single nano-patch made of 100 % and 30 % Al, respectively. Due to space limitations, all 2D electric field plots for the 5 % Al cases are excluded, as in these cases the structure minimally affects the transmitted electromagnetic wave. The plots are shown in the *x*-*z* plane at *y* = 0 nm. The results shown in Figs. 8 and 9 are obtained at wavelengths of 682 nm and 810 nm, respectively. A sweep over the phase of the incident plane wave is conducted in steps of 60 degrees in the range from 0 to 120 degrees. This sweep shows the wave propagation in the computational domain. Due to the difference in the values of the electric fields in air and in Si, two different scales are shown in the figures, one for air and one for Si. The fields inside the nano-patch itself is not shown here. Figure 8 shows the 100 % single Al nano-patch case at a wavelength of 682 nm and Fig. 9 shows the 30 % single Al nano-patch at a wavelength of 810 nm. The observed wavelengths are at peaks in the enhancement factor for each of the cases.

Figure 8 illustrates the fields at the plasmonic resonance of the single 100 % Al nano-patch at λ = 682 nm, which is associated with the largest peak in the enhancement factor (EF) in Fig. 5 (a) (red color curve). The graph of Fig. 8 provides insight to the propagation behavior of the electromagnetic waves transmitted into the Si layer. Notice the oblique angle of the wave propagation into the Si when the nano-patch is present (see the arrow in Fig. 8 (a)). This observation can indicate the increase of light path in the Si and hence more absorption of the photon energy and increase in photocurrent generation.

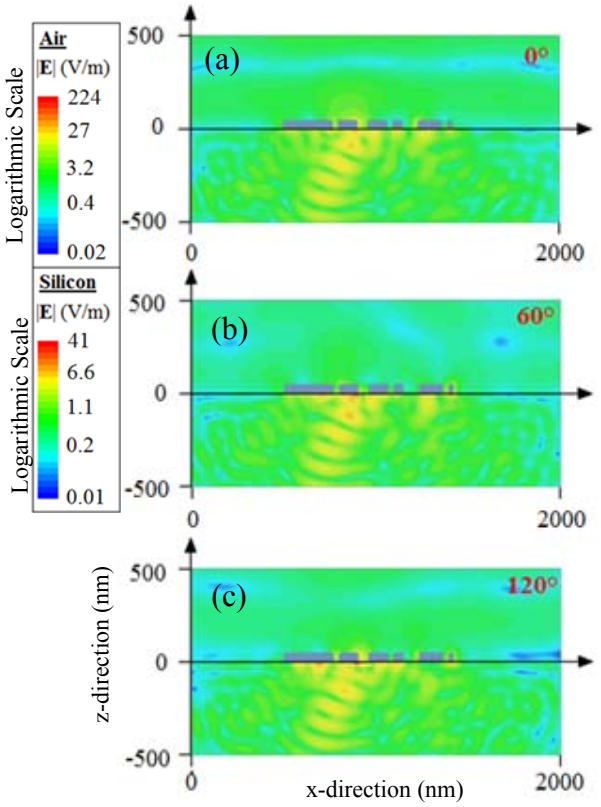

Fig. 8. Real part of the electric field on the *x*-*z* plane at y = 0 nm. Sweep over the phase at λ = 682 nm. Single nano-patch of 100 % aluminum composition.

A significantly reduced scattering in the 30 % Al nano-patch is shown in Fig. 9 (3.1V/m) compared with the 100 % Al shown in Fig. 8 (41V/m). This is supported by the EF(λ) plot of Fig. 5, where no distinct resonant peaks observed for the 30 % Al.

The phase sweep for the 30 % Al single nano-patch cases is shown in Fig. 9. For this 30 % Al case, lateral propagation of the transmitted wave is still observed, although not nearly as prominent as the 100% Al case. Similarly, the 5 % Al case (not shown for space limits) demonstrates even more reduction in the scattering in the *x*-*z* directions (i.e., lateral scattering). Additionally, the minimal scattering and enhancement for both cases that does take place does not extend far away from the structure, returning to plane wave propagation further away from the nanostructure; unlike in the

single 100 % Al nano-patch case. As such, it is expected that scattering for the 30 % and 5 % Al cases will not have drastic differences between the single and infinite array cases.

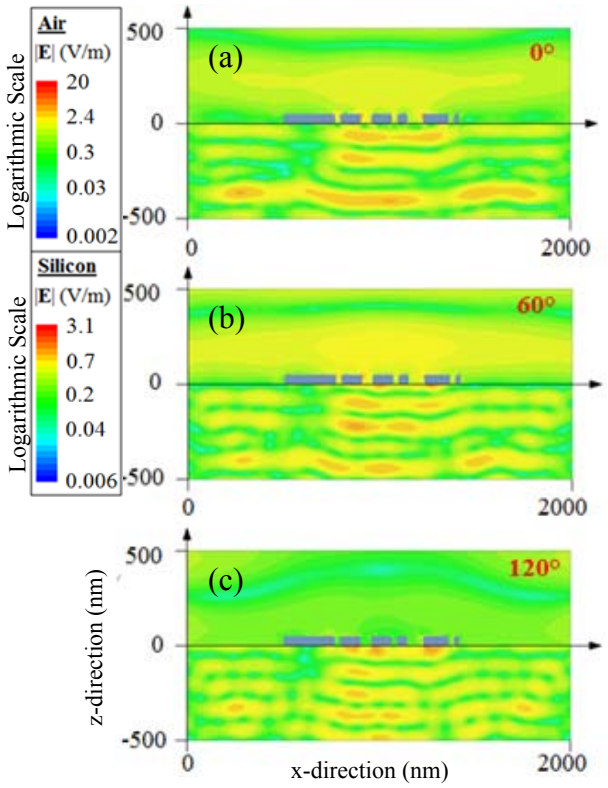

Fig. 9. Real part of the electric field on the *x*-*z* plane at y = 0 nm. Sweep over the phase at λ = 810 nm. Single nano-patch of 30 % aluminum composition.

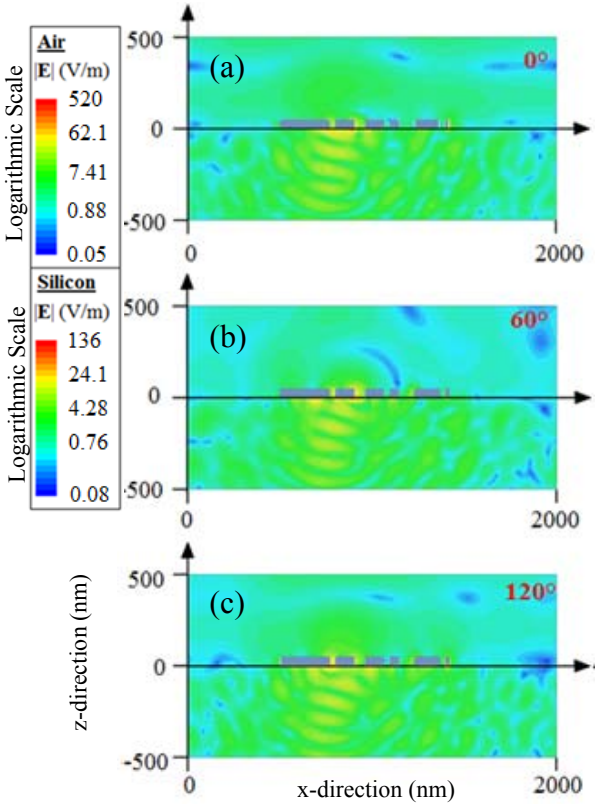

Fig. 10. Real part of the electric field on the *x*-*z* plane at y = 0 nm. Sweep over the phase at λ = 697 nm. Infinite nano-patch array of 100 % aluminum composition.

E. Wave propagation in silicon due to infinitearray of nano-patches

The graphs of wave propagation (phase sweep) in Si of the single nano-patch are repeated here for the infinite array. The results of Figs.10 and 11 illustrate similar 2D plots of the magnitude of the real part of the electric fields, for the same three composite material cases. All graphs are confined under one element of the array for comparison reasons. Figure 10 shows the 100 % Al nano-patch case at a wavelength of 697 nm and Fig. 11 shows the 30 % Al nano-patch at a wavelength of 810 nm. These wavelengths are the observed peaks in the enhancement factor for each of the cases shown in Fig. 5 (b).

Just as with the single nano-patch cases, in the infinite array cases strongest lateral propagation is observed for the 100 % with reduced scattering for the 30 % case and 5 % case (not shown). Consider Fig. 10, which illustrates the 2D fields for the 100 % Al infinite array case at the peak in the EF(λ) plot. This peak is shifted by approximately 15 nm as compared to the single nano-patch case. In addition, note that the pattern of the transmitted fields is somewhat different.The scattering of the transmitted waves in the single 100 % Al nano-patch case appears to be slightly more in the lateral directions as compared to the infinite array case of Fig. 10. Additionally, the peak magnitudes of the electric fields are significantly different; 41 V/m for the single 100 % Al nano-patch case versus 136 V/m for the infinite array case, as expected.

In the 30% Al nano-patch array illustrated in Fig. 11, there again is greatly reduces scattering for the 30 % case as compared to the 100 % case

and even more reduction in the 5 % case. As compared to the single nano-patch counter part of the 30 % Al nano-patch array from Fig. 9, the infinite array field graphs of the 30 % Al nano-patches have some distinct similarities as well as some differences. In both cases the maximum field values are the similar, 4.0 (V/m) and 3.1 (V/m) for the 30 % Al infinite array and single nano-patch cases, respectively and 0.87 (V/m) and 0.83 (V/m) for the 5 % Al infinite array and single nano-patch cases, respectively. Differences do exist in the field patterns for the two cases. In the 30 % Al single nano-patch case (Fig. 9) note that the fields decay at the x = 0 nm and x = 2000 nm faces, as opposed to the infinite array cases (Fig. 11) where the fields continue uniformly at these faces. The same is observed in the 5 % Al nano-patch cases.

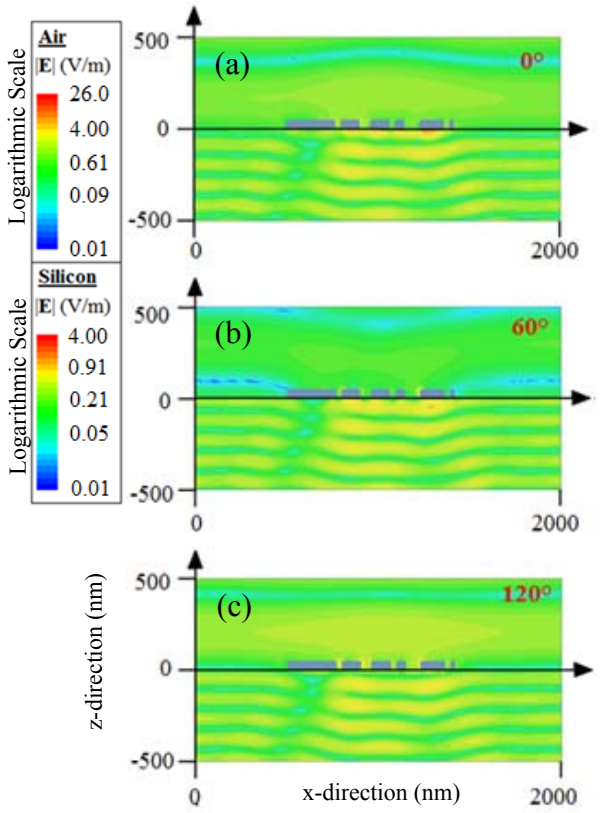

Fig. 11. Real part of the electric field on the x-z plane at y = 0 nm. Sweep over the phase at λ = 810 nm. Infinite nano-patch array of 30 % aluminum composition.

F. Field in silicon due to single nano-patch versus wavelength

In this sub-section, we show the magnitude of the fields versus the wavelength as shown in Figs. 12 and 13 for the single nano-patch cases of 100 % and 30 % Al, respectively. For each of the two cases, three different incident wavelengths are observed. The electric field graphs for these various material composites of the nano-patches provide insights into the various mechanisms of field enhancement in the Si layer.

In Fig. 12, the 100 % single Al nano-patch, the 2D electric field plots are observed for incident wavelength values of 682 nm, 750 nm, and 952 nm. The plots at 682 nm and 952 nm associated with select enhancement peaks in Fig. 5 (a), while the 750 nm plot is a non-resonant value for the sake of comparison. Visually, these field plots match well with what would be expected after considering the enhancement factor in Fig. 5 (a). The strong EF(λ) peak observed at 682 nm in Fig. 5 (a) is visual confirmed in Fig. 12 (a). Here, we observe not only strong enhancements of the near fields at the nano-patch/silicon interface but also significant enhancement of the propagating waves transmitted into the Si layer. The second observed peak is shown in Fig. 12 (c) for 952 nm. This shows significant enhancement of the transmitted propagating waves, though reduced in magnitude from that, which occurs at λ = 682 nm. At λ = 1111 nm there is another slight peak in EF(λ) observed in Fig. 5 (a). In the field plot of this wavelength (not shown) the enhancement seems to be localized more closely to the structures than in the other three observed peaks, which show strong enhancement of the waves transmitted deeper in the Si layer.

Figure 13 shows similar 2D field graphs for the 30 % Al single nano-patch case. In the 100 % Al single nano-patch case the highest values of the electric field is approximately 41 V/m while for the 30 % Al single nano-patch case it is around 9 V/m. From Fig. 5 (a), the main peak in EF(λ) for the 30 % Al case occurs at λ = 833 nm. This is supported by Fig. 13 (b), where we see slightly higher magnitudes in the fields transmitted into the Si layer as opposed to the other observed wavelengths. Compared to the 100 % Al case, there is not nearly as dramatic differences between the observed wavelengths in the 30 % Al single nano-patch case. This can be attributed to the

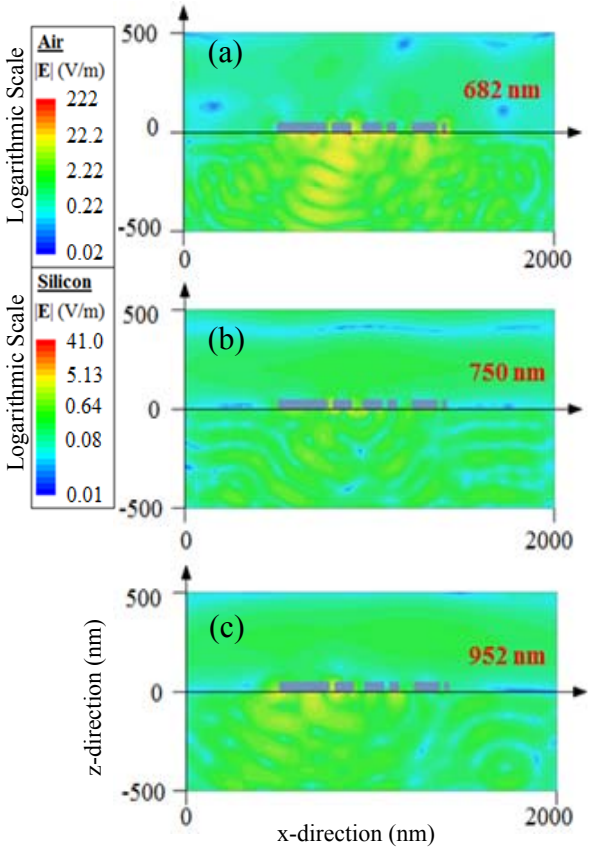

Fig. 12. Real part of the electric field on the *x*-*z* plane at y = 0 nm. Sweep over the wavelength at constant phase. Single nano-patch of 100 % aluminum composition.

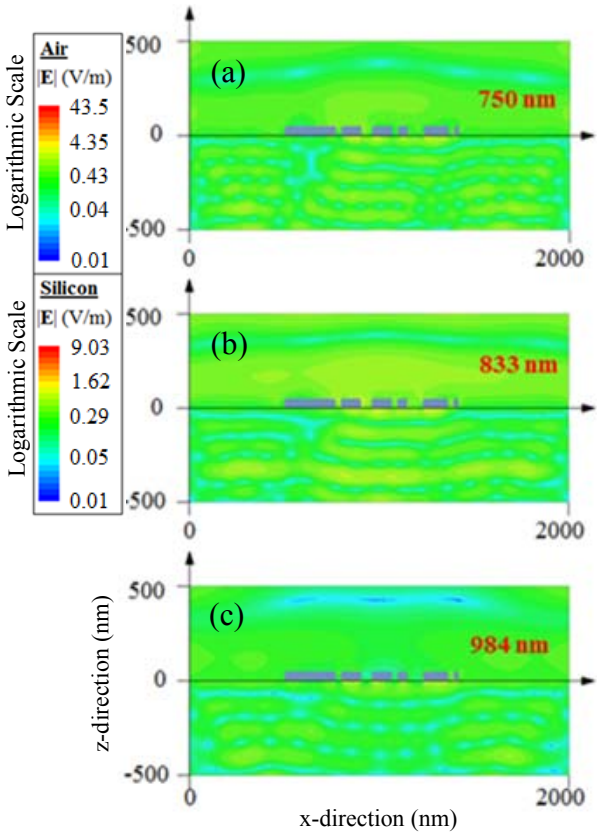

Fig. 13. Real part of the electric field on the *x*-*z* plane at y = 0 nm. Sweep over the wavelength at constant phase. Single nano-patch of 30 % aluminum composition.

greatly reduced magnitude of resonance of the structure as shown in Fig. 5 (a). From the 2D electric field graphs for various wavelengths in the 5 % Al single nano-patch case (not shown), we see a significant decrease in the maximum electric field value in the Si layer for this case, 0.8 V/m, as compared to 9 V/m for the 30 % Al case, 9 V/m. This trend indicates that for Al-Si mixed nanostructures, plasmonic enhancement is strongly dependent on the concentration of Al within the nano-structure.

G. Field in silicon due to infinite array versus wavelength

The magnitude of the electric field is plotted in Figs. 14 and 15 associated with infinite nano-patch array of the 100 % and 30 % Al nano-patch compositions. The fields are obtained at various wavelengths of the incident plane wave. A key difference between the field graphs and the single nano-patch graphs in Figs. 12 and 13 is the possibility of electromagnetic coupling between adjacent nanostructures in the infinite array configuration as discussed earlier. Interactions such as these can have significant effects on the spectral location and magnitude of plasmonic resonances. Consider the EF(λ) plots in Fig. 5 for the two 100 % Al nano-patch for single and array cases. The major peak in the single element of 100 % Al nano-patch occurs at λ = 674, with other peaks at λ = 833, 923, and 1111 nm (see Fig. 5 (a)). By comparison, the infinite array results from Fig. 5 (b) illustrate peaks at locations λ = 697, 833, 952, and 1090 nm, which are close, but not the same, to those of the single nano-patch peaks of Fig. 5 (a). The peaks occurring at λ = 833 nm and λ = 952 nm show considerably increased magnitude as compared to the comparative peaks in the single nano-patch case, as anticipated. The peak in the single nano-patch case occurring at λ =

674 nm is slightly shifted in the infinite array case to λ = 697 nm. Additional peaks are observed in the infinite array case at λ = 659 and 508 nm. The shift in the resonance peaks between the single and array cases are consistent with *El-Shenawee et al* [29].

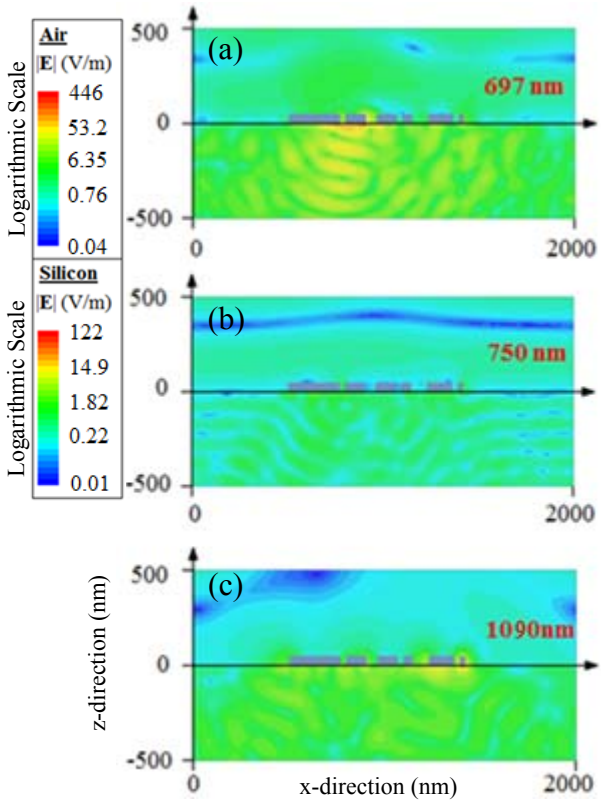

Fig. 14. Real part of the electric field on the *x*-*z* plane at y = 0 nm. Sweep over the wavelength at constant phase. Infinite nano-patch array of 100 % aluminum composition.

Figure 14 (b) illustrates an incident wavelength of 750 nm. This wavelength represents a non-resonant point in the EF(λ) of Fig. 5. Note at these wavelengths that although the structure does cause some scattering of the incident plane wave, this scattering seems to be located close to the nanostructure surface and does not extend to the periodic boundaries at the *x* = 0 and 2000 nm and *y* = 0 and 2000 nm extremities. Figures 14 (a) and 14 (c) are associated with the incident wavelengths of 697 and 1000 nm, respectively, where peaks in the EF(λ) in Fig. 5 (b) plot occur. At these wavelengths, the nano-patch structure exhibits strong scattering of the incident plane wave. This scattering clearly extends to the periodic boundaries, thus indicating that coupling between adjacent particles is possible in the nano-patch array case. Consider this infinite array case compared to the single nano-patch case depicted in Fig. 12. In both cases we see very similar patterns in the scattering of the transmitted field in the Si layer. The major difference between the two lies in the peak values of the electric fields in both cases. In the single nano-patch case, the peak electric field in the Si layer is ~41 V/m, while the peak value in the infinite array case is approximately 122.5 V/m. The observed wavelengths are not exactly the same, 682 nm for the single nano-patch and 697 for the array.

Similar plots are shown in Fig. 15 for the 30 % Al nano-patches infinite array. Upon comparing the maximum transmitted fields in Si between the three infinite nano-patch array cases, the maximum field value occurs in Fig. 14 as 122 V/m, in Fig. 15 as 4 V/m and in the 5 % Al nano-patch array case as 0.888 V/m (not shown). Note

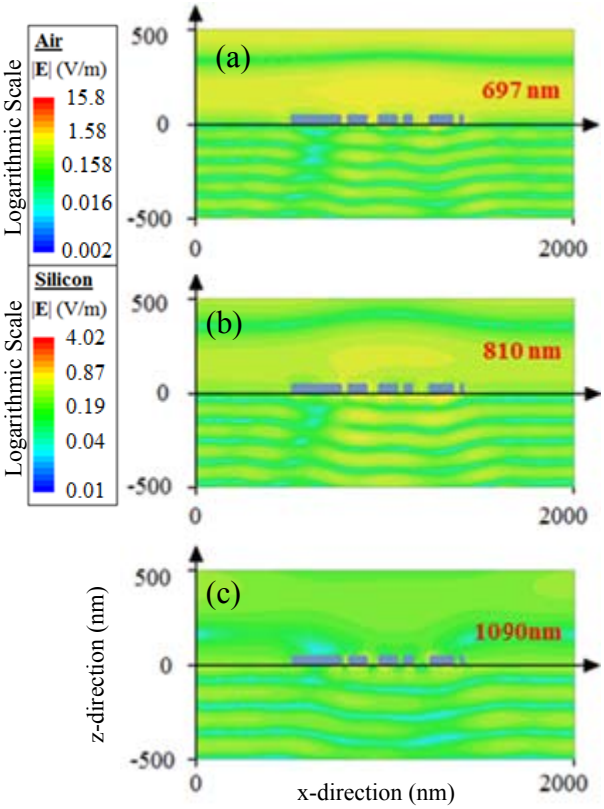

Fig. 15. Real part of the electric field on the *x*-*z* plane at y = 0 nm. Sweep over the wavelength at constant phase. Infinite nano-patch array of 30 % aluminum composition.

that in Fig. 15 the scattering of the transmitted wave caused by the nanostructure does not extend to the periodic boundaries located at the $x = 0$ and 2000 nm and $y = 0$ and 2000 nm extremities for all observed wavelengths, with a similar observation made for the 5 % Al nano-patch array. As such, the coupling between adjacent structures is not present in the 30 % Al case compared with the 100 % Al case. This explains the similarities observed between Figs. 13 and 15 and also the similar plots of EF(λ) for both the single and infinite array of 30 % Al nano-patch cases.

Figure 14 also illustrates the mechanism by which this irregular geometry has multiple resonance peaks. Consider Fig. 14 (a), which shows excitation at λ = 697 nm. Here, the strongest field enhancements are located just left of the center point of the nano-patch at approximately x = 900 nm, y = 0 nm. This indicates that the local nano-patch geometry at this location resonates strongly at 697 nm, much stronger than other locations on the nano-patch. Now consider Fig. 14 (c) associated with incident wavelength of 1000 nm, which is another strong resonant peak in the 100 % Al infinite array case. Here, the strongest resonance occurs are the far right of the nanostructure at approximately x = 1400, y = 0 nm. This change in the physical location of the plasmon resonance indicates that in highly irregular nanostructure geometries, where holes can represent cavity-like structure, can support localized enhanced fields at various locations on the structure.

IV. CONCLUSION

In this work, we have investigated the enhancement of electromagnetic energy transmission into an Si thin-film layer due to highly irregular surface nanostrucutres. These structures, inspired by naturally occurring structuring formed during the thin film fabrication technology process, show localized field enhancement in the Si layer when the nanostructure composite includes more Al than Si. The enhanced field magnitude being the highest observed for nano-patches of 100 % Al composition and is reduced greatly as the Al/Si ratio of the nano-patch is decreased. Since the experimentally observed structures forming from the TAIC process are predicted to have a low Al concentration (< 5 %) the results of this work indicate that the presence of these structures would cause neither significant enhancement nor degradation of energy absorption in a Si thin film [39]. However, pure Al irregular nanostructures hold promising potential for providing absorption enhancement in thin-film Si solar cells, particularly in the development of multi and wide-band resonating nanostructures.

ACKNOWLEDGEMENT

This work is supported mainly through the NSF/ECCS award no. 1006927 and in part through NSF GK12 award no. 0538645, NSF Cyber infrastructure awards EP-0918970 and MRI no. 072265.

REFERENCES

[1] G. Crabtree and N. Lewis, "Solar energy conversion," *Physics Today*, pp. 37-42, Mar., 2007.

[2] D. Kotter, S. Novack, W. Slafer, and P. Pinhero, "Solar nantenna electromagnetic collectors," *Proc. 2nd Int. Conf. Energy and Sustainability*, pp. 1-7, Jacksonville, FL, 2008.

[3] D. Derkacs, S. Lim, P. Matheu, W. Mar, and E. Yu, "Improved performance of amorphous silicon solar cells via scattering from surface plasmon polaritons in nearby metallic nanoparticles," *Appl. Phys. Lett.*, vol. 89, no. 093103, pp. 1-3, Aug. 2006.

[4] W. Warrick, R. Kappera, and M. Tayahi, "Enhanced optical absorption in thin film solar cells by surface plasmons," *in International Conference on Photonics*, Langkawi, pp. 1-5, 2010.

[5] B. Rand, P. Peumans, and S. Forrest, "Long-rang absorption enhancement in organic tandem thin-film solar cells containing silver nanoclusters," *J. Appl. Phys.*, vol. 96, no. 12, pp. 7519-7526, Dec. 2004.

[6] J. Zhu, M. Xue, H. Shen, Z. Wu, S. Kim, J. Ho, A. Hassani-Afshar, B. Zeng, and K. Wang, "Plasmonic effects for light concentration in organic photovoltaic thin films induced by hexagonal periodic metallic nanospheres," *Appl. Phys. Lett.*, vol. 98, no. 151110, pp. 1-3, Apr. 2011.

[7] A. Ostfeld and D. Pacifici, "Plasmonic concentrators for enhanced light absorption in ultrathin film organic photovoltaics," *Appl. Phys. Lett.*, vol. 98, no. 113112, pp. 1-3, Mar. 2011.

[8] M. Dühring, N. Mortensen, and O. Sigmund, "Plasmonic versus dielectric enhancement in thin-film solar cells," *Appl. Phys. Lett.*, vol. 100, no. 211914, pp. 1-4, May 2012.

[9] G. Beaucarne, "Silicon thin-film solar cells," *Advances in Opto. Electronics*, vol. 2007, no. 36970, pp. 1-12, Aug. 2007.

[10] V. Ferry, M. Verschuuren, H. Li, E. Verhagen, R. Walters, R. Schropp, H. Atwater, and A. Polman, "Light trapping in ultrathin plasmonic solar cells," *Optics Express*, vol. 18, no. S2, pp. A237-A245, June 2010.

[11] S. Mokkapati, F. Beck, A. Polman, and K. Catchpole, "Designing periodic arrays of metal nanoparticles for light-trapping applications in solar cells," *Appl. Phys. Lett.*, vol. 95, no. 053115, pp. 1-3, Aug. 2009.

[12] S. Mokkapati, F. Beck, R. Waele, A. Polman, and K. Catchpole, "Resonant nano-antennas for light trapping in plasmonic solar cells," *J. Phys. D: Appl. Phys.*, vol. 44, no. 185101, pp. 1-9, Apr. 2011.

[13] H. Atwater and A. Polman, "Plasmonics for improved photovoltaic devices," *Nature*, vol. 9, pp. 205-213, Mar. 2010.

[14] S. Pallai and M. Green, "Plasmonics for photovoltaic applications," *Solar Energy Materials and Solar Cells,* vol. 94, pp. 1481-1486, Mar. 2010.

[15] F. Tsai, J. Wang, J. Huang, Y. Kiang, and C. Yang, "Absorption enhancement of an amorphous Si solar cell through surface plasmon-induced scattering with metal nanoparticles," *Optics Express*, vol. 18, no. S2, pp. A207-A220, 2010.

[16] F. Beck, E. Verhagen, S. Mokkapati, A. Polman, and K. Catchpole, "Resonant SPP modes supported by discrete metal nanoparticles on high-index substrates," *Optics Express*, vol. 19, no. S2, pp. A146-A156, Feb. 2011.

[17] H. Fischer and O. Martin, "Engineering the optical response of plasmonic nanoantennas," *Optics Express*, vol. 16, no. 12, pp. 9144-9154, June 2008.

[18] S. Lim, W. Mar, P. Matheu, D. Derkacs, and E. Yu, "Photocurrent spectroscopy of optical absorption enhancement in silicon photodiodes via scattering from surface plasmon polaritons in gold nanoparticles," *J. Appl. Phys.*, vol. 101, no. 104309, pp. 1-7, May 2007.

[19] Y. Akimov and W. Koh, "Design of plasmonic nanoparticles for efficient subwavelength light trapping in thin-film solar cells," *Plasmonics*, vol. 6, pp. 155-161, Oct. 2010.

[20] M. Yang, Z. Fu, F. Lin, and X. Zhu, "Incident angle dependence of absorption enhancement in plasmonic solar cells," *Optics Express*, vol. 19, no. S4, pp. A763-A771, July 2011.

[21] J. Khurgin and G. Sun, "Impact of disorder on surface plasmons in two-dimensional arrays of metal nanoparticles," *Appl. Phys. Lett.*, vol. 94, no. 221111, pp. 1-3, June 2009.

[22] N. Burford and M. El-Shenawee, "Parallel MoM computation of localized field in silicon due to finite array of nanotoroids," *Proc. 29th Annual Review of Progress in Applied Computational Electromagnetics*, March 24-28, 2013.

[23] J. Wang, F. Tsai, J. Huang, C. Chen, N. Li, Y. Kiang, and C. Yang, "Enhancing InGaN-based solar cell efficiency through localized surface plasmon interaction by embedding Ag nanoparticles in the absorbing layer," *Optics Express*, vol. 18, no. 3, pp. 2682-2694, Feb. 2010.

[24] N. Lal, B. Soares, J. Sinha, F. Huang, S. Mahajan, P. Bartlett, N. Greenham, and J. Baumberg, "Enhancing solar cells with localized plasmons in nanovoids," *Optics Express*, vol. 19, no. 12, pp. 11256-11263, June 2011.

[25] Z. Ouyang, S. Pillai, F. Beck, O. Kunz, S. Varlamov, K. Catchpole, P. Campbell, and M. Green, "Effective light trapping in polycrystalline silicon thin-film solar cells by means of rear localized surface plasmons," *Appl. Phys. Lett.*, vol. 96, no. 261109, July 2010.

[26] W. Cao, T. Huang, X. Xu, and H. Elsayed-Ali, "Localized surface plasmon resonance of single silver nanoparticles studies by dark-field optical microscopy and spectroscopy, " *J. Appl. Phys*., vol. 109, no. 034310, pp. 1-6, Feb. 2011.

[27] K. Sendur, "Optical aspects of the interaction of focused beams with plasmonic nanoparticles," *Appl. Comp. Electro. Society (ACES) Journal*, vol. 27, no. 2, pp. 181-188, Feb. 2012.

[28] L. Hammer, M. Schwind, B. Kasemo, and I. Zorić, "Localized surface plasmon resonances in aluminum nanodisks," *Nano Lett.*, vol. 8, no. 5, pp. 1461-1471, Feb. 2008.

[29] M. El-Shenawee, "Polarization dependence of plasmonic nanotoroid dimer antenna," *IEEE Antennas Propagat. Lett.*, vol. 9, pp. 463-466, 2010.

[30] M. El-Shenawee, P. Blake, A. M. Hassan, and D. K. Roper, "Surface plasmons of finite nanoring arrays," *Proc. of the IEEE International Symposium on Antennas and Propagation and USNC/URSI National Radio Science Meeting*, pp. 1609-1612, 2011

[31] N. Large, J. Aizpurua, V. Lin, S. Teo, R. Marty, S. Tripathy, and A. Mlayah, "Plasmonic properties of gold ring-disk nano-resonators: fine shape details matter," *Optics Express*, vol. 19, no. 6, pp. 5587-5595, Mar. 2011.

[32] M. El-Shenawee, D. Macias, A. Baudrion, and R. Bachelot, "Torus nano-antenna: enhanced field and radiation pattern," *Proc. of the IEEE Int. Symp. on Antennas and Prop., and USNC/URSI National Radio Science Meeting*, Charleston SC, USA, June 1-5, 2009.

[33] A. Mary, D. Koller, A. Hohenau, J. Krenn, A. Bouhelier, and A. Dereux, "Optical absorption of torus-shaped metal nanoparticles in the visible range," *Phys. Rev. B*, vol. 76, no. 245422, pp. 1-5, 2007.

[34] K. Nakayama, K. Tanabe, and H. Atwater, "Plasmonic nanoparticle enhanced light absorption in GaAs solar cells," *Appl. Phys. Lett.*, vol. 93, no. 121904, pp. 1-3, Sept. 2008.

[35] Y. Akimov and W. Koh, "Resonant and nonresonant plasmonic nanoparticle enhancement for thin-film silicon solar cells," *Nanotechnology*, vol. 21, no. 235201, pp. 1-6, May 2010.

[36] V. Kochergin, L. Neely, C. Jao, and H. Robinson, "Aluminum plasmonic nanostructures for improved absorption in organic photovoltaic devices," *Appl. Phys. Lett.*, vol. 98, no. 133305, pp. 1-3, Mar. 2011.

[37] N. Burford, M. El-Shenawee, S. Shumate, D. Hutchings, and H. Naseem, "Field enhancement due to surface structuring during aluminum induced crystallization of amorphous silicon," *Proc. of the IEEE Int. Symp. on Antennas and Prop. and USNC/URSI National Radio Science Meeting*, Chicago, USA, July 8-13, 2012.

[38] Z. Wang, L. Jeurgens, J. Wang, and E. Mittemeijer, "Fundamentals of metal-induced crystallization of amorphous semiconductors," *Advanced Eng. Materials*, vol. 11, no. 3, 2009.

[39] S. D. Shumate, M. K. Hafeezuddin, H. A. Naseem, and D. A. Hutchings, "Microstructural influence of hydrogenated amorphous silicon on polycrystalline emitter solar cells prepared by top-down aluminum induced crystallization," P*roc. of the 2011 IEEE PVSC*, Seattle, Washington, June 19-24, 2011.

[40] J. Hoffmann, C. Hafner, P. Leidenberger, J. Hasselbarth, and S. Burger, "Comparison of electromagnetic field solvers for the 3D analysis of plasmonic nano antennas," *Proc. SPIE*, vol. 7390, pp. 73900J-73900J-11, 2009.

[41] A. M. Hassan and M. El-Shenawee, "Mathematical modeling of breast lesion growth" *Proceedings of the Annual Review of Progress in Applied Computational Electromagnetics*, pp. 86-91, Niagara Falls, Canada, March 30 -April 4, 2008.

[42] E. Palik, *Handbook of Optical Constants of Solids*, New York: Academic, 1985.

[43] J. M. Taboada, M. G. Araújo, J. Rivero, L. Landesa, and F. Obelleiro, "Surface integral equation solvers for large-scale conductors, metamaterials and plasmonic nanostructures," *Applied Computational Electromagnetics Society (ACES) Journal*, vol. 27, no. 2, pp. 189-197, Feb. 2012.

Nathan M. Burford received his B.Sc. in Physics from Southeast Missouri State University in 2011. He is currently finishing his M.Sc. in Microelectronics-Photonics at the University of Arkansas and will be pursuing a Ph.D. in the same field starting in the summer of 2013. His research interest includes computational design of plasmonic nano-antennas and solar cells, electromagnetic metamaterials and THz imaging and spectroscopy. Mr. Burford is a member of Sigma Pi Sigma honor society and is an NSF GK-12 Fellow.

Magda El-Shenawee (M'91–SM'02) received the Ph.D. degree in Electrical Engineering from the University of Nebraska, Lincoln, in 1991. After obtaining her Ph.D., she joined the Center for Electro-Optics as a Research Associate from 1992 to 1994, focusing on the enhanced backscatter phenomenon from random rough ground surfaces. She furthered her research at the National Research Center, Cairo, Egypt, from 1994 to 1996, then at the University of Illinois at Urbana-Champaign, Urbana, from 1997 to 1999. Directly before joining the University of Arkansas faculty, she served as a member of the Multidisciplinary University Research Initiative team working on the antipersonnel landmine detection at Northeastern University, Boston, MA, from 1999 to 2001. Currently, she is a Professor of Electrical Engineering with the University of Arkansas in Fayetteville where she joined as an Assistant Professor in 2001. Her current research interests involve terahertz imaging and spectroscopy, computational inverse scattering algorithms, MEMS antennas, nano-antennas for energy enhancement of photovoltaic solar cells, and biomedical engineering applications to breast cancer using biopotentials and biological tumor growth modeling. Dr. El-Shenawee is a member of Eta Kappa Nu Electrical Engineering honor society.

High Accuracy Time Domain Modeling of Microstrip Discontinuities by Using Modified TDR Based on Barker Codes with Flat Spectrum and Integrated Side-Lobes

Mohammad Ojaroudi and Esfandiar Mehrshahi

Faculty of Electrical and Computer Engineering,
Shahid Beheshti University, Tehran, Iran
m_ojaroudi@sbu.ac.ir and mehr@sbu.ac.ir

Abstract ─ In this paper, a novel time domain method by using a modified time domain reflectometry is presented for high accuracy modeling of microstrip discontinuities. The ordinary stimulus signals used in the TDR technique are voltage step or voltage impulse. In this paper, we propose an alternative technique, whereby a modified excitation pulse based on Barker-Code orthogonal pulses is employed as the stimulus signal in TDR. The advantage conferred by "Barker codes TDR" is that more energy is available at higher frequencies in contrast with conventional step or impulse TDR, and so a higher bandwidth and higher accuracy of the line impedance is achieved. It can also be advantageous when the user is looking for precision in spatial localization, say in a connector or similar in-line structure, as the increased energy at higher frequencies can help. Simulated results are presented to validate the usefulness of the proposed method for calculating the precise amount of time-dependent equivalent circuit of microstrip discontinuity.

Index Terms ─ Finite difference time domain (FDTD), microstrip discontinuity, time domain reflectometry (TDR), and time domain modeling.

I. INTRODUCTION

Time domain reflectometry (TDR) is a well known technique that is typically used to measure the impedance of discontinuities as a function of time (or distance) in electronic systems [1-3]. A TDR instrument consists primarily of an oscilloscope and a test signal generator, where the test signal is traditionally a voltage step. As a consequence of the Fourier transform, the energy in the spectrum of a step falls as the frequency increases. On the other hand, an ideal impulse (Dirac delta) test signal has a theoretically flat bandwidth. Recent studies have demonstrated that step TDR can successfully be used to characterize the reflection scattering parameter S_{11} of antennas [4-6].

Several factors affect a TDR system's ability to resolve closely-spaced discontinuities. If a TDR system has insufficient resolution, small or closely-spaced discontinuities may be smoothed together into a single aberration in the waveform. This effect may not only obscure some discontinuities, but it also may lead to inaccurate impedance readings. Rise time, settling time, and pulse aberrations of the stimulus signal can also significantly affect a TDR system's resolution. Two neighboring discontinuities may be indistinguishable to the measurement instrument if the distance between them amounts to less than half the system rise time [2, 3]. Also, many factors contribute to the accuracy of a TDR results. These include the TDR system's step response, probe and interconnect reflections and DUT losses, step amplitude accuracy, baseline correction, and the accuracy of the reference impedance (ZO) used in the measurements. All TDR measurements are relative; they are made by comparing reflected amplitudes to incident amplitude.

In this paper, we explore the advantages of making modified impulse TDR results, similar to a traditional step TDR but employing a modified signal by using orthogonal codes instead of a step like or impulse like (Gaussian) signal. This allows us to compare theory with simulation. The

Submitted On: Sept. 11, 2012
Accepted On: Mar. 17, 2013

motivation behind this work is driven by the fact that a TDR is less expensive than a vector network analyzer (VNA), but more importantly the time localization of the energy in the transient test signal means that the user can dispense with the anechoic chamber that is required for antenna measurements with a sine wave exciting signal. The advantage conferred by "Barker codes TDR" is that more energy is available at higher frequencies than with conventional step or impulse TDR, and so a higher bandwidth and higher accuracy of the line impedance is achieved. Simulated results are presented to validate the usefulness of the proposed method for calculating precise amount of time-dependent equivalent circuit of microstrip discontinuity.

II. FREQUENCY DOMAIN COMPARISON OF THE STIMULUS SIGNALS SPECTRUM

The unit impulse (Dirac delta) function is defined as having zero amplitude for all time except at $t = 0$, where it has infinite amplitude,

$$\delta(t) = \begin{cases} 0 & t \neq 0 \\ \infty & t = 0 \end{cases} . \quad (1)$$

The Fourier transform for the unit impulse is,

$$F[\delta(t)] = 1 . \quad (2)$$

In general the unit impulse is a theoretical construct and cannot physically exist [7], it is used as a limiting case for when the width of a pulse approaches zero. Derived from the convolution of two rectangular ("rect") functions, the trapezoid function provides an approximation of a realistic impulse with finite rise and fall times [7],

$$h(t) = \frac{1}{\tau} rect\left(\frac{t}{\tau}\right) \otimes A.rect\left(\frac{t}{T}\right) \quad (3)$$

in which A is the trapezoid amplitude, T is the full width at half maximum (FWHM), and τ is the rise/fall time from 0 % to 100 % of the amplitude. The Fourier transform of $h(t)$ is given by,

$$F[h(t)] = AT \sin c(f\tau) \sin c(fT) . \quad (4)$$

The second order of the Barker-code functions is defined as,

$$B_2(t) = h(t+1) - h(t-1) . \quad (5)$$

The Fourier transform of $B_2(t)$ is given by,

$$F[B_2(t)] = (e^{-j2\pi f} - e^{j2\pi f}).AT \sin c(f\tau) \sin c(fT) . \quad (6)$$

Generally, we can write the i^{th} order of the Barker-code stimulus signal as [8],

$$B_i(t) = \sum_{i=1}^{N} \beta_i h(t + \alpha_i \tau) \quad (7)$$

where, β and α are the amplitude and the order of shifting in the Barker-codes sequence, respectively. Generally, Barker-codes are subsets of pseudo-noise (PN) sequences [8]. The origin of the name pseudo-noise is that the digital signal has an autocorrelation function, which is very similar to that of a white noise signal: Impulse like. PN sequence may also be periodic. Such sequences are known as Barker sequences. Barker-codes are commonly used for frame synchronization in digital communication systems. Barker-codes have a length of at most 13 and have low correlation side lobes. Barker sequences are too short to be of practical use for spectrum spreading. A correlation side lobe is the correlation of a code word with a time-shifted version of itself. The correlation side lobe, C_k for a k-symbol shift of an N-bit code sequence, $\{X_j\}$ is given by,

$$C_k = \sum_{j=1}^{N-k} X_j X_{j+k} \quad (8)$$

where, X_j is an individual code symbol taking values +1 and -1, for $0 < j < N$, and the adjacent symbols are assumed to be zero. The Barker-code generator block provides the codes with various order listed in Table 1.

Table 1: Barker-codes for various orders.

Order (i)	Barker-Code (β_i)
1	[-1]
2	[-1 1]
3	[-1 -1 1]
4	[-1 -1 1 -1]
5	[-1 -1 -1 1 -1]
7	[-1 -1 -1 1 1 -1 1]
11	[-1 -1 -1 1 1 1 -1 1 1 -1 1]
13	[-1 -1 -1 -1 -1 1 1 -1 -1 1 -1 1 -1]

Figure 1 presents a number of stimulus signals with their spectra that will be compared with the spectrum of Barker-codes. It can be seen that even the realistic, limited Barker signal contains more energy than an ideal rectangular pulse. When the step waveform is not ideal, but similar to what is

practically available today, the comparison becomes even more favorable, as can be seen in the same figure in [9]. Finally, as shown in Fig. 1, the Barker-codes with higher orders have a flat frequency response with integrated side-lobes [10].

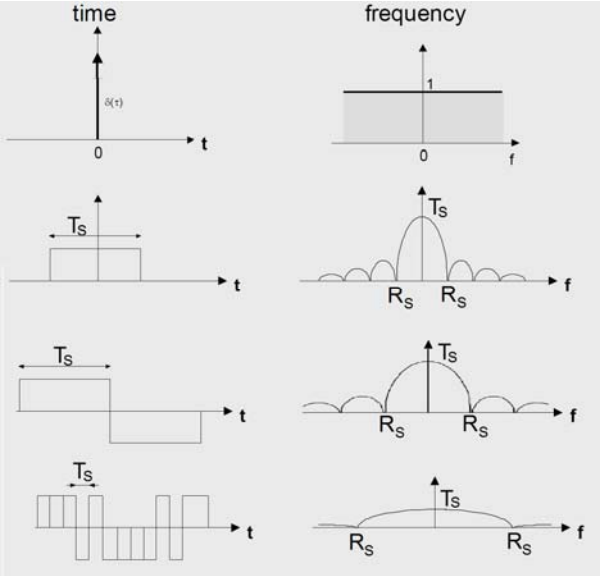

Fig. 1. An ideal unit impulse, rectangular pulse, and some practical Barker-codes of unit amplitude and its Fourier transform.

III. RESULTS AND SISCUSSIONS

This section describes the simulated line impedance of the microstrip discontinuity using the proposed Barker-codes TDR and compares it with the simulated line impedance obtained using the conventional step TDR and the equivalent circuit methods. In order to illustrate the proposed method performance, a step-like microstrip discontinuity with mentioned design parameters were simulated, and the TDR results of the input impedance for them in equivalent circuit and full-wave analysis cases are presented and discussed. The simulated full-wave TDR results are obtained using the Ansoft simulation software high-frequency structure simulator (HFSS) [11].

The proposed microstrip transmission line with step like discontinuity is shown in Fig. 2 (a), which is printed on an FR4 substrate of thickness 0.8 mm, permittivity 4.4, and loss tangent 0.018. This defected structure on the 50-Ω microstrip line will perturb the incident and return currents and induce a voltage difference on the microstrip line. These two effects can be modelled as a T-shaped LC circuit, as shown in Fig. 2 (b) [12]. The equivalent circuit parameters are defined as,

$$C = 0.00137h\frac{\sqrt{\varepsilon_{reff}}}{Z_{C1}}\left(1-\frac{W_2}{W_1}\right)\left(\frac{\varepsilon_{reff}+0.3}{\varepsilon_{reff}-0.258}\right)\left(\frac{W_1/h+0.264}{W_1/h+0.8}\right) \quad (9)$$

$$L_1 = \frac{L_{W1}}{L_{W1}+L_{W2}}L \text{ , and } L_2 = \frac{L_{W2}}{L_{W1}+L_{W2}}L$$

where,

$$L_{Wi} = Z_{Ci}\sqrt{\varepsilon_{reff}}/c \text{ , and } L = 0.000987h\left(1-\frac{Z_{C1}}{Z_{C2}}\right)^2,$$

where L_{Wi} for i =1, 2 are the inductances per unit length of the appropriate microstrips, having widths W_1 and, W_2, respectively. Z_c and ε_{reff} denote the characteristic impedance and effective dielectric constant corresponding to width, and h is the substrate thickness in micrometres [12]. The optimal dimensions of the equivalent circuit model parameters for the proposed microstrip transmission line with step-like discontinuity are specified in Table 2.

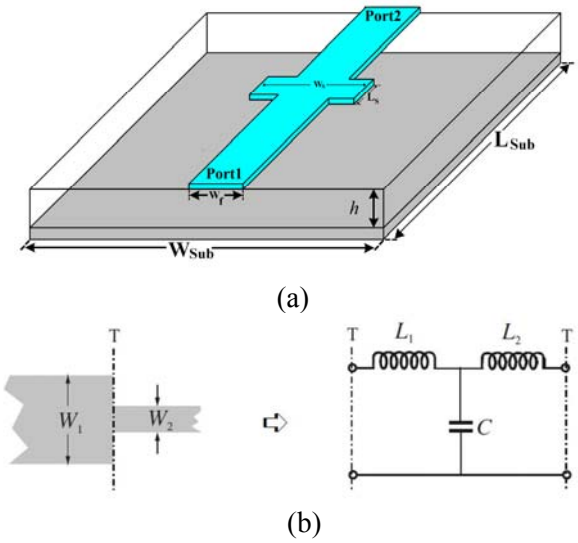

Fig. 2. (a) Geometry of the proposed microstrip transmission line with step-like discontinuity and (b) step-like microstrip discontinuity and its equivalent circuit model [12].

Table 2: The dimensions of proposed microstrip transmission line with step-like discontinuity.

Param.	mm	Param.	mm	Param.	mm
W_{Sub}	12	L_{Sub}	18	W_f	1.5
h	0.8	W_S	4	L_S	2

The equivalent circuit model parameters are listed in Table 3.

Table 3: Equivalent circuit model parameters.

Element	DGS
L_1	1.131 (nH)
C	1.181 (pF)
L_2	0.858 (nH)

The simulated TDR curves with different values of rise time and discontinuity distance from reference port (*d*) are plotted in Fig. 3. As shown in Fig. 3, when the distance between the reference port and the discontinuity location increases from 10 mm to 50 mm, the amount of the line impedance is varied from 33 Ω to 37.5 Ω. Also, as the rise time of the excitation signal increases from 20 psec to 30 psec, the port reflection over shoot is varied from 4 % to 7 %. From these results, we can conclude that the accuracy of discontinuity is varied by changing *d* and rise time [13]. Therefore, due to variation of the results in various conditions of distance and T_{rise}, to have an accurate judgment for the proposed method performance we need to plot TDR curves in a stable and constant condition for all of scenarios, as shown in Figs. 4 and 5.

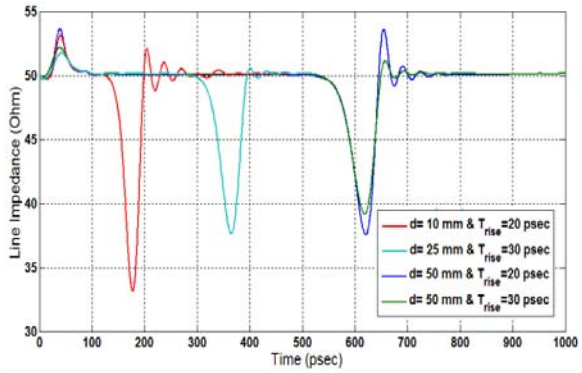

Fig. 3. Simulated TDR characteristic with different values of rise time (T_{rise}) and discontinuity distance from reference port (*d*).

Figure 4 shows the effects of T_{rise} with different values on the line impedance (TDR) in comparison with the ideal step for the proposed microstrip transmission line with step-like discontinuity. As shown in Fig. 4, these reports start, for t = 0.5 nsec, with an impedance just under 50 Ω. This is indeed the characteristic impedance of the microstrip line. At impedance discontinuities, part of the input signal is reflected. These reflections, after traveling back, reach terminal port 1 and are observed there [9]. From these observations, the characteristic impedances along the transmission line can be computed. As shown in Fig. 4, when the T_{rise} increases from zero in ideal step case to 30 psec, the line impedance in the center location of the step discontinuity is varied from 35 GHz to 38 GHz. From these results, we can conclude that the line impedance in the discontinuity location is controllable by changing the T_{rise}. In order to decrease the discrepancy between the simulated TDR data and the ideal step result and also to achieve the accurate impedance characteristics for the designed discontinuity, we need a stimulus signal with lower T_{rise}.

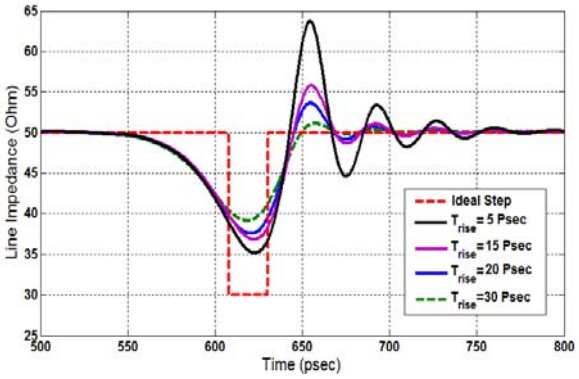

Fig. 4. Time dependent impedance with incident pulse having different rise time when a 1 mm step is inserted.

To improve the accuracy of the TDR results, without decreasing T_{rise}, Fig. 5 shows the simulated reflection waveform observed at port 1 of the defected structures, with a 50 Ω termination at port 2. The excitation source is a step wave with amplitude of 1 V and rise time of 20 psec. The TDR results for the equivalent circuit with C = 1.181 pF, L_1 = 1.131 nH, and L_2 = 0.858 nH based on the method described in [4] and specified in Table 1 are also shown for comparison. The corresponding results generated by Barker-codes TDR are also shown in this figure. Two cases are studied for Barker-codes TDR, with different code length. It is clearly shown that our TDR results with modified excitation signal by Barker-codes

gives a very good accuracy, and the error is less than 1 % in this case in our simulation. It is apparent from this figure that the energy in the modified TDR reflection exceeds the energy in the step TDR reflection. Therefore, the modified Barker-codes TDR results follows the transmission line reference more closely than does the ordinary step TDR results.

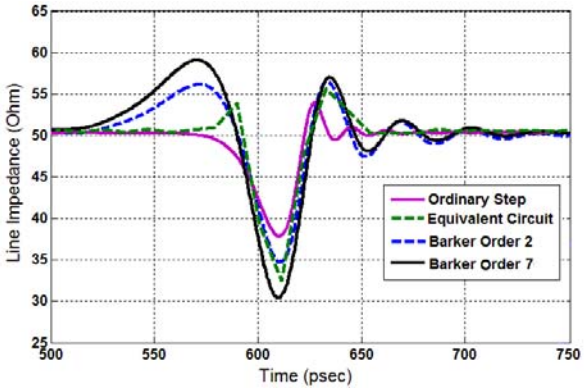

Fig. 5. The reflected waveforms comparison for simulated results by HFSS, equivalent circuit model, and two cases of Barker-codes for the proposed defected microstrip structure shown in Fig. 2 (a).

IV. CONCLUSION

Time domain reflectometry (TDR) with finite difference time domain (FDTD) method analysis is a novel technique that is typically used to calculate the time modeling of a microstrip structure. To improve the accuracy of the TDR results, without decreasing T_{rise}, we proposed an alternative technique, whereby a modified excitation pulse based on Barker-code orthogonal pulses is employed instead of the stimulus signal in TDR. It can also be advantageous when the user is looking for precision in spatial localization, say in a connector or similar in-line structure, as the increased energy at higher frequencies can help. The simulated results showed good agreement with the numerical prediction.

REFERENCES

[1] R. Tamas, G. Caruntu, and D. Popa, "A time-domain measuring technique for ultra-wide band antennas," *Microwave and Optical Technology Letters*, vol. 53, no. 2, pp. 281-286, Feb. 2011.

[2] *Time Domain Reflectometry Theory*, Agilent Technologies, USA, Application Note 1304-2, 2006.

[3] A. Cataldo, G. Monti, E. De Benedetto, G. Cannazza, L. Tarricone, and L. Catarinucci, "Assessment of a TD-based method for characterization of antennas," *IEEE Trans. Instrum. Meas.*, vol. 58, no. 5, pp. 1412-1419, May 2009.

[4] M. Ojaroudi and E. Mehrshahi, "Novel band-stop small square monopole antenna by using interdigital strip protruded inside the recangular slot as a band-stop filter with its equivalen circuit based in TDR analysis for UWB applications," *International Symposium on Antennas and Propagation* , ISAP 2012, NAGOYA – JAPAN, 2012.

[5] C. Chiu, W. Chen, K. Liao, B. Chen, Y. Teng, G. Huang, and L.Wu, "Pad characterization for CMOS technology using time domain reflectometry," *in Proc. IEEE Int. RF and Microwave Conf.*, in Kuala Lumpur, pp. 215-217, Dec. 2008.

[6] M. Harper, N. Ridler, and M. Salter, "Comparison between root-impulse-energy and vector network analyzer methods for measuring loss on printed circuit boards," *in ARFTG Microwave Measurement Symp.*, in Portland, OR, pp. 20-25, 2008.

[7] M. Kowalski, "A simple and efficient computational approach to chafed cable time-domain reflectometry signature prediction," *25th Annual Review of Progress in Applied Computational Electromagnetics (ACES)*, Monterey, California, March, 2009.

[8] S. Golomb and R. Scholtz, "Generalized Barker sequences (transformations with correlation function unaltered, changing generalized Barker sequences)," *IEEE Trans. Inf. Theory*, vol. 11, pp. 533-537, Oct. 1965.

[9] C. Lo and C. Furse, "Modeling and simulation of branched wiring networks," *Applied Computational Electromagnetics Society (ACES) Journal*, vol. 23, no. 2, pp. 143-146, June 2008.

[10] R. N. Bracewell, *The Fourier Transform and its Applications*, 3rd Edition, McGraw-Hill International Editions, pp. 61, 2000.

[11] Ansoft High Frequency Structure Simulation (HFSS), Ver. 13, Ansoft Corporation, 2010.

[12] T. C. Edwards, *Foundations for Microstrip Circuit Design*, Wiley, Great Britian, 1981.

[13] C. H. Cheng, C. H. Tsai, and T. L. Wu, "A novel time domain method to extract equivalent circuit model of patterned ground structures," *IEEE Microw. Wireless Compon. Lett.*, vol. 17, no. 11, Nov. 2010.

Mohammad Ojaroudi was born on 1984 in Germi, Iran. He received his B.Sc. degree in Electrical Engineering from Azad University, Ardabil Branch and M.Sc. degree in Telecommunication Engineering from Urmia University. From 2010, he is working toward the Ph.D. degree at Shahid Beheshti University. From 2007 until now, he is a Teaching Assistant with the Department of Electrical Engineering, Islamic Azad University, Ardabil Branch, Iran. Since March 2009, he has been a Research Fellow (Chief Executive Officer) in the Microwave Technology Company (MWT), Tehran, Iran. From 2012, Mr. Ojaroudi is a member of the IEEE Transaction on Antennas and Propagation (APS) reviewer group and the Applied Computational Electromagnetic Society (ACES). From 2013 he is a student member of the IEEE. His research interests include analysis and design of microstrip antennas, design and modeling of microwave structures, radar systems, and electromagnetic theory. He is author and coauthor of more than 100 journal and international conferences papers. His papers have more than 300 citations with 10 h-index.

Esfandiar Mehrshahi was born in Tehran, Iran, in 1964. He received the B.Sc. degree from the Iran University of Science and Technology, Tehran, Iran, in 1987, and the M.Sc. and Ph.D. degrees from the Sharif University of Technology, Tehran, Iran, in 1991 and 1998, respectively. Since 1990, he has been involved in several research and engineering projects at the Iran Telecommunications Research Center (ITRC). He is currently an Associate Professor at Shahid Beheshti University, Tehran, Iran. His main areas of interest are the nonlinear simulation of microwave circuits and microwave oscillator's spectrum.

Studying and Analysis of the Characteristic of the High-Order and MRTD and RK-MRTD Schemes

Min Zhu, Qunsheng Cao, and Siping Gao

College of Electronic and Information Engineering
Nanjing University of Aeronautics and Astronautics, Nanjing 210016, China
minzhu215@gmail.com and qunsheng@nuaa.edu.cn

Abstract ─ In this paper, the stability, dispersion, and convergence of the high-order FDTD (HO-FDTD), the multi-resolution time-domain (MRTD), and the Runge-Kutta multi-resolution time-domain (RK-MRTD) schemes are derived, analyzed, and compared. The computational cost and memory requirements of the three methods are also investigated. It is found that the RK-MRTD method is of considerable potential due to its dispersion properties and computational abilities.

Index Terms ─ Convergence, dispersion, HO-FDTD, MRTD, RK-MRTD, and stability.

I. INTRODUCTION

The classical Yee FDTD [1] method has become the most important numerical technique in the computational electromagnetics time domain over the past few decades, and has been applied widely to simulate electromagnetic wave propagation, scattering, radiation, and various microwave geometries, owing to its simple implementation and versatility. However, the technique suffers from serious limitations due to the substantial computer resources required when it involves modeling a complex problem, which has large stencil size at least 10 cells or more per wavelength. It is well known that the FDTD method has a second order accuracy in spatial-temporal and brought significant computational errors. In order to improve the limitations of the FDTD method, a mass of methods are proposed, including the HO-FDTD [2-4], the MRTD [5], the RK-MRTD method [6] have been raised. The HO-FDTD approach, firstly presented by Fang [2], using the Taylor series instead of the spatial and temporal derivatives to reducing the dispersion error. It is noted that the HO-FDTD method adopted a second-order approximation in time, fourth-order accurate in space-domain called HO-FDTD (2, 4) scheme, and the HO-FDTD (2, 6) with sixth-order in space and second-order in time was developed to deal with the electric large size problem [3]. Zhang and Chen [7] put forward to the general updated equations and dispersion relations for the arbitrary HO-FDTD (2N, 2M). The fourth-order accurate FDFD scheme is proposed and applied in the waveguide structures. The results demonstrate that the proposed method can save more time and memory than MRFD and the traditional FDFD methods [8]. The MRTD method, introduced by Krumpholz and Katehi, are based mainly on the filed expansions of different basis scaling and wavelet function, such as the Battle-Lemarie [9-10] basis, the Daubechies basis [11], Cohen - Daubechies - Feauveau (CDF) bi-orthogonal functions [12, 13] basis, and Coifman function basis [14, 15]. In [16], Cao and Tamma discussed the MRTD method based on different scaling function expansions, and computed the reflected and transmission coefficients for stratified slab media, and the results show that the cubic spline Battle-Lemarie, Daubechies D4 and Coiflet bases are in excellent agreement with the analytic solutions. Cao and Tamma also applied the MRTD methods based on different basis functions to study the scattering of planar stratified medium and rectangular dielectric cylinder [17]. In [18] the MRTD method has been discussed in detail, especially a non-uniform Cartesian grid and a uniaxial perfectly matched layer implementation for arbitrary levels of wavelet resolution. A procedure to implement the PML absorbing

Submitted On: Sept. 20, 2012
Accepted On: Mar. 16, 2013

boundary conditions into the MRTD method based on the discrete wavelet transform has been developed in [19]. The strong stability Runge-Kutta (SSP-RK) method was first introduced and extended in [20] and [21]. Compactly supported n^{th}-order wavelets and m^{th}-order, m^{th}-stage Runge-Kutta are applied in spatial discretization and time integration, respectively. Numerical experiments have shown that much better numerical dispersion properties are obtained by employing the RK-MRTD scheme.

In summary, the HO-FDTD, the MRTD, and the RK-MRTD methods are the high order accuracy time domain methods and have extremely low numerical dispersion errors. In section II, the update equations of the HO-FDTD, the MRTD, and the RK-MRTD schemes are discussed. The numerical properties of the HO-FDTD, the MRTD, and the RK-MRTD methods are derived including stability conditions, dispersion relation, and convergence in section III. The computational cost and memory requirements of the three schemes are investigated in section IV. In section V, a numerical example will be simulated for different methods. Conclusions are summarized in section VI.

II. THEORY AND ALGORITHM

A. HO-FDTD method

For simplicity (σ = 0) and without loss of generality, in three-dimensional (3D), one update equation of the arbitrary HO-FDTD (2N, 2M) [7] can be written as,

$$E_{x,i+1/2,j,k}^{n+N} = E_{x,i+1/2,j,k}^{n+1-N} - \frac{1}{a(N)}\sum_{v=1}^{N-1} a(v)\left(E_{x,i+1/2,j,k}^{n+v} - E_{x,i+1/2,j,k}^{n+1-v}\right) + \frac{\Delta t}{a(N)\varepsilon\Delta y}\sum_{v=1}^{M} a(v)\left(H_{z,i+1/2,j-1/2+v,k}^{n+1/2} - H_{z,i+1/2,j+1/2-v,k}^{n+1/2}\right) - \frac{1}{a(N)}\frac{\Delta t}{\varepsilon\Delta z}\sum_{v=1}^{M} a(v)\left(H_{y,i+1/2,j,k-1/2+v}^{n+1/2} - H_{y,i+1/2,j,k+1/2-v}^{n+1/2}\right) \tag{1}$$

where Δt, Δy, and Δz are the time step size and the spatial step size in the y- and z-directions, 2N means the $(2N)^{\text{th}}$-order central difference approximation in time domain, 2M is the $(2M)^{\text{th}}$-order in space time, ε is the permittivity, and the coefficients $a(v)$ [7] are listed in Table 1.We note that the HO-FDTD (2, 2M) equations are similar to the MRTD method. Here in this paper, we mainly discuss the HO-FDTD (2, 2M) scheme.

B. MRTD method

Similarly, considering the same electromagnetic condition as the HO-FDTD method, one update equation of the MRTD scheme based on Daubechies scaling functions [6] can be written as follows,

$$E_{i+1/2,j,k}^{\phi x,n+1} = E_{i+1/2,j,k}^{\phi x,n} + \frac{1}{\varepsilon}\sum_{v} a(v) \times \left(H_{i+1/2,j+v+1/2,k}^{\phi z,n+1/2}\frac{\Delta t}{\Delta y} - H_{i+1/2,j,k+v+1/2}^{\phi y,n+1/2}\frac{\Delta t}{\Delta z}\right) \tag{2}$$

where Δx, Δy ,Δz, and Δt represent the space and time discretization intervals in x-, y-, z- and t-directions, respectively, and ϕ refers to the Daubechies or Coifman scaling functions, ε is the permittivity, and the coefficients $a(v)$ are listed in Table 2 for Daubecies (D2), (D3), and (D4) schemes [6] and Coifman scheme [14], and the coefficients $a(v)$ have the symmetric relations, namely, $a(-v) = -a(v-1)$.

C. RK-MRTD method

For the same conditions above, one update equation of the RK-MRTD scheme [6], which is based on the same convergence rate for the time and space, can be written as,

$$\frac{\partial_{\phi x} E_{i+1/2,j,k}(t)}{\partial t} = \frac{1}{\varepsilon}\sum_{v} a(v) \times \left({}_{\phi z}H_{i+1/2,j+v+1/2,k}(t)\frac{1}{\Delta y} - {}_{\phi y}H_{i+1/2,j,k+v+1/2}(t)\frac{1}{\Delta z}\right) \tag{3}$$

where the coefficients $a(v)$ is the same as the MRTD method listed in Table 2.

The general form for equation (3) as in [6], can be written as

$$\frac{\partial F}{\partial t} = uF + S(t), \tag{4}$$

where $F = \{E, H\}^T$, E and H are expressed as $E = \{E_x, E_y, E_z\}^T$, $H = \{H_x, H_y, H_z\}^T$, where T is the transpose of the vector, u is a operator and defined as $u = \begin{bmatrix} 0 & u_H \\ u_E & 0 \end{bmatrix}$, $S(t)$ is a source, the form of the m'^{th}-order m' stage strong stability preserving Rung-Kutta (SSP-RK) [6] schemes are shown as,

$$F^{(0)} = F_n$$
$$F^{(i)} = F^{(i-1)} + \Delta t u F^{(i-1)} + \Delta t S^{(i)}, \quad i = 1,2,...,m \tag{5}$$
$$F_{n+1} = \sum_{l=0}^{m} \alpha_{m,l} F^{(l)}$$

where $S^{(i)} = (I + \Delta t \frac{\partial}{\partial t})^{i-1} S(t_n)$, i=1,2,…m , I is identity matrix, the coefficients $\alpha_{m,l}$ [6] are,

$$\alpha_{m,m} = \frac{1}{m!}, \quad l = m$$
$$\alpha_{m,l} = \frac{1}{l}\alpha_{m-1,l-1}, \quad l = 1,2,...m-1, m \geq 2, \tag{6}$$
$$\alpha_{m,0} = 1 - \sum_{l=1}^{m} \alpha_{m,l}, \quad l = 0 .$$

Now, we use the Fourier method [22] to analyze the stability of the RK-MRTD, following the [23], we solve the update equations of RK-MRTD and obtain,

$$\frac{\partial}{\partial t}\begin{bmatrix} E(t) \\ H(t) \end{bmatrix} = \begin{bmatrix} \mathbf{0} & u_H \\ u_E & \mathbf{0} \end{bmatrix}\begin{bmatrix} E(t) \\ H(t) \end{bmatrix} \tag{7}$$

where

$$E(t) = \begin{Bmatrix} E_x(t) \\ E_y(t) \\ E_z(t) \end{Bmatrix}, \qquad H(t) = \begin{Bmatrix} H_x(t) \\ H_y(t) \\ H_z(t) \end{Bmatrix},$$

Table 1: Coefficients $a(v)$ for the HO-FDTD (2N, 2M) method.

	(2, 6)	(2, 10)	(2, 14)	(2, 16)
a (1)	1.171875	1.211242676	1.228606224	1.23409107
a (2)	-0.0651041667	-0.0897216797	-0.102383852	-0.106649846
a (3)	0.0046875000	0.0138427734	0.0204767704	0.0230363667
a (4)		-0.00176565988	-0.00417893273	-0.0053423856
a (5)		0.000118679470	0.000689453549	0.00107727117
a (6)			-0.0000769225034	-0.000166418878
a (7)			0.00000423651475	0.0000170217111
a (8)				-0.000000852346421

Table 2: Coefficients $a(v)$ for the MRTD method.

	D2	D3	D4	Coifman
a (1)	1.2291666667	1.2918129281	1.3110340773	1.31103179882954
a (2)	-0.0937500000	-0.1371343465	-0.1560100710	-0.15600971692384
a (3)	0.0104166667	0.0287617723	0.0419957460	0.04199608161407
a (4)		-0.0034701413	-0.0086543236	-0.00865439622799
a (5)		0.0000080265	0.0008308695	8.30874303205e-04
a (6)			0.0000108999	1.09002750582e-05
a (7)			-0.0000000041	-4.10840975298e-09
a (8)				-7.977050410221e-13

$$u_E = \begin{bmatrix} 0 & u_{E1} & u_{E2} \\ u_{E3} & 0 & u_{E4} \\ u_{E5} & u_{E6} & 0 \end{bmatrix}, u_H = \begin{bmatrix} 0 & u_{H1} & u_{H2} \\ u_{H3} & 0 & u_{H4} \\ u_{H5} & u_{H6} & 0 \end{bmatrix},$$

the component 0 is a 3 by 3 zero matrix, and u_{E1}, u_{E2}, u_{E3}, u_{E4}, u_{E5}, u_{E6}, u_{H1}, u_{H2}, u_{H3}, u_{H4}, u_{H5}, u_{H6} are

$$u_{E1} = -\frac{2\mathrm{i}\sum_{v=0}^{Nv-1} a(v)\sin(k_z(1/2+v)\Delta z)}{\varepsilon \Delta z},$$

$$u_{E2}=\frac{2\mathrm{i}\sum_{v=0}^{Nv-1}a(v)\sin(k_y(1/2+v)\Delta y)}{\varepsilon\Delta y},$$
$$u_{E3}=\frac{2\mathrm{i}\sum_{v=0}^{Nv-1}a(v)\sin(k_z(1/2+v)\Delta z)}{\varepsilon\Delta z},$$
$$u_{E4}=-\frac{2\mathrm{i}\sum_{v=0}^{Nv-1}a(v)\sin(k_x(1/2+v)\Delta x)}{\varepsilon\Delta x},$$
$$u_{E5}=-\frac{2\mathrm{i}\sum_{v=0}^{Nv-1}a(v)\sin(k_y(1/2+v)\Delta y)}{\varepsilon\Delta y},$$
$$u_{E6}=\frac{2\mathrm{i}\sum_{v=0}^{Nv-1}a(v)\sin(k_x(1/2+v)\Delta x)}{\varepsilon\Delta x},$$
$$u_{H1}=\frac{2\mathrm{i}\sum_{v=0}^{Nv-1}a(v)\sin(k_z(1/2+v)\Delta z)}{\mu\Delta z},$$
$$u_{H2}=-\frac{2\mathrm{i}\sum_{v=0}^{Nv-1}a(v)\sin(k_y(1/2+v)\Delta y)}{\mu\Delta y},$$
$$u_{H3}=-\frac{2\mathrm{i}\sum_{v=0}^{Nv-1}a(v)\sin(k_z(1/2+v)\Delta z)}{\mu\Delta z},$$
$$u_{H4}=\frac{2\mathrm{i}\sum_{v=0}^{Nv-1}a(v)\sin(k_x(1/2+v)\Delta x)}{\mu\Delta x},$$
$$u_{H5}=\frac{2\mathrm{i}\sum_{v=0}^{Nv-1}a(v)\sin(k_y(1/2+v)\Delta y)}{\mu\Delta y},$$
$$u_{H6}=-\frac{2\mathrm{i}\sum_{v=0}^{Nv-1}a(v)\sin(k_x(1/2+v)\Delta x)}{\mu\Delta x}. \quad (8)$$

We use the characteristic equation to solve u for equation (7) and be obtained as follows,

$$\begin{aligned}\left|\lambda I-u\right|&=\lambda^6+8c^2\lambda^4\left[(\xi_x)^2+(\xi_y)^2+(\xi_z)^2\right]\\&+16c^4\lambda^2\left[2(\xi_x\xi_y)^2+2(\xi_x\xi_z)^2+2(\xi_y\xi_z)^2\right.\\&\left.+(\xi_x)^4+(\xi_y)^4+(\xi_z)^4\right]=0\end{aligned} \quad (9)$$

$$\xi_\tau=\frac{\sum_{v=0}^{Nv-1}a(v)\sin(k_\tau(1/2+v)\Delta\tau)}{\Delta\tau}, \quad (10)$$

where $\mathrm{i}=\sqrt{-1}$, $\tau = x, y, z$, the positive part of the Eigen value for u can be derived as,

$$\lambda=\mathrm{i}2c\sqrt{(\xi_x)^2+(\xi_y)^2+(\xi_z)^2}=\mathrm{i}\lambda' \quad (11)$$

where c is the speed of light in vacuum in this paper, λ' is the imaginary part of λ.

III. NUMERICAL PROPERTIES

A. Stability

Based on the stability condition of the Yee's FDTD with the uniform discretization size $\Delta x = \Delta y = \Delta z = \Delta l$, the HO-FDTD ($2N$, $2M$) stability condition can be derived as,

$$\Delta t\le\frac{\Delta l(\sum_{v=1}^{N}|a(v)|)}{c(\sum_{v=1}^{M}|a(v)|)\sqrt{d}}. \quad (12)$$

We only discuss the HO-FDTD (2, $2M$) case, so the stability condition relation above can be modified as,

$$\Delta t\le\frac{\Delta l}{c(\sum_{v=1}^{N}|a(v)|)\sqrt{d}}. \quad (13)$$

The stability condition for MRTD scheme is derived, as in [11],

$$\Delta t\le\frac{\Delta l}{c(\sum_{v}|a(v)|)\sqrt{d}} \quad (14)$$

where $a(v)$ are listed in Table 2, and d is the number of dimensions (1, 2, or 3).

The RK-MRTD method is based on the SSP-RK algorithm and the MRTD scheme, so the stability condition of the scheme should be considered as the combination of the two algorithms. In reference [20], equation (5) can take the general forms as,

$$F(t_{n+1})=\sum_{l=0}^{m'}\frac{1}{l!}(\Delta tL)F(t_n)=GF(t_n) \quad (15)$$

where m' is the order of the SSP-RK, L is the spatial amplification matrix of the Eigen value λ, and G is the general growth factor, so the absolute value of G is lower or equal to 1, from equation (15) we can define the growth factor σ [23] as,

$$\sigma = \sum_{l=0}^{m'} \frac{1}{l!}(\lambda \Delta t)^l . \tag{16}$$

If $m' = 4$, then the stability condition of the RK_4-MRTD-D_4 method, which $RK_{m'}$-MRTD-$D_{m'}$ refers to the m'^{th}-order m' stage SSP-RK method based on Daubechies m' scaling function [24], is obtained as,

$$\left|\sum_{l=0}^{4} \frac{1}{l!}(\lambda \Delta t)^l\right| = \left|\sum_{l=0}^{4} \frac{1}{l!}(\mathrm{i}\lambda' \Delta t)^l\right| \le 1$$

$$\left|1 + \mathrm{i}\lambda' \Delta t - \frac{1}{2}(\lambda' \Delta t)^2 - \frac{1}{6}(\lambda' \Delta t)^3 + \frac{1}{24}(\lambda' \Delta t)^4\right| \le 1$$

$$\lambda' \Delta t \le 2\sqrt{2}\,, \tag{17}$$

substituting equations (11) into (17), then the RK_4-MRTD-D_4 stability condition can be derived as,

$$\Delta t \le \frac{\Delta 2\sqrt{2}}{c(\sum_v |a(v)|)\sqrt{d}} . \tag{18}$$

The stability conditions of the other order $RK_{m'}$-MRTD-$D_{m'}$ algorithm are derived as the same procedure of the RK_4-MRTD-D_4, which was not described here for simplicity.

The maximum Courant-Friedrichs-Lewy (CFL) number of the HO-FDTD (2, 2*M*), MRTD, and RK-MRTD methods are listed in Table 3, and the Dubechies $D_{m'}$ ($m' = 2, 3, 4$) and Coifman basis are used in the MRTD and RK-MRTD methods. It is found that the higher order in the spatial and temporal discretizations, the more strict stability condition required, but the RK_4-MRTD-D_4 is less restrictive than any other method, and the RK_2-MRTD-D_2 is unconditionally unstable.

Table 3: The maximum CFL number for the HO-FDTD, MRTD, and RK-MRTD method.

	HO-FDTD	MRTD	RK-MRTD
(2,6) / D2	0.4650	0.4330	-
(2,10) / D3	0.4385	0.3951	0.3422
(2,14)/ D4	0.4256	0.3802	0.5377
(2,16)/ coif	0.4213	0.3802	0.53770

B. Dispersion

The dispersion characteristics are typically derived by assuming a time harmonic plane wave solution in an isotropic, linear, and lossless medium. The dispersion relation for the arbitrary HO-FDTD (2*N*, 2*M*) [7] method can be written as,

$$\begin{aligned}
[\sum_{v=1}^{N} a(v)\sin(\frac{(2v-1)\omega\Delta t}{2})]^2 = \\
= [\frac{c\Delta t}{\Delta x}\sum_{v=1}^{M} a(v)\sin(\frac{(2v-1)k_x\Delta x}{2})]^2 \\
+ [\frac{c\Delta t}{\Delta y}\sum_{v=1}^{M} a(v)\sin(\frac{(2v-1)k_y\Delta y}{2})]^2 \\
+ [\frac{c\Delta t}{\Delta z}\sum_{v=1}^{M} a(v)\sin(\frac{(2v-1)k_z\Delta z}{2})]^2
\end{aligned} \tag{19}$$

where k is the numerical wave number vector, λn is the numerical wavelength, its components are $k_x = k\sin\theta\cos\phi$, $k_y = k\sin\theta\sin\phi$, $k_z = k\cos\theta$. (θ, ϕ) is the wave propagation angle in the spherical coordinate, the uniform spatial step size is assumed as $\Delta x = \Delta y = \Delta z = \Delta$. Defining the CFL number $q = (c\Delta t)/\Delta$ and the number of cells per wavelength $p = \lambda c/\Delta$. The ratio of the theoretic wavelength value λc to the numerical wavelength λn is defined as $u = \lambda c/\lambda n$. Therefore, the dispersion relationship can be written as,

$$\begin{aligned}
(\frac{1}{q}\sum_{v=1}^{N} a(v)\sin(\frac{\pi q}{p}\sin(2v-1)))^2 = \\
= (\sum_{v=1}^{M} a(v)\sin(\frac{\pi u}{p}(2v\text{-}1)\sin\theta\cos\phi))^2 \\
+ (\sum_{v=1}^{M} a(v)\sin(\frac{\pi u}{p}(2v\text{-}1)\sin\theta\sin\phi))^2 \\
+ (\sum_{v=1}^{M} a(v)\sin(\frac{\pi u}{p}(2v\text{-}1)\cos\theta))^2 .
\end{aligned} \tag{20}$$

With the same procedure above, the dispersion relation for the MRTD [11] method can be obtained as follows,

$$\begin{aligned}
(\frac{1}{q}\sin(\frac{\pi q}{p}))^2 = (\sum_{i=1}^{Nv\text{-}1} a(i)\sin(\frac{\pi u}{p}(2\mathrm{i}\text{-}1)\sin\theta\cos\phi))^2 \\
+ (\sum_{i=1}^{Nv\text{-}1} a(i)\sin(\frac{\pi u}{p}(2\mathrm{i}\text{-}1)\sin\theta\sin\phi))^2 \\
+ (\sum_{i=1}^{Nv\text{-}1} a(i)\sin(\frac{\pi u}{p}(2\mathrm{i}\text{-}1)\cos\theta))^2 .
\end{aligned} \tag{21}$$

The dispersion of the RK-MRTD needs to use the theory of the SSP-RK [24], take RK_3-MRTD-D_3 for example, and according to [25], by substituting equations (11) and (16) in to equation

(22), then the dispersion relation can be derived in equation (23) as,

$$\omega t = Arg(\sigma) \tag{22}$$

$$(\frac{2\pi q}{up})^2 = (\arctan(\frac{6\lambda_i\Delta t - (\lambda_i\Delta t)^3}{6-3(\lambda_i\Delta t)^2}))^2 . \tag{23}$$

With the wave propagation angle θ=90° and ϕ=0°, CFL number q = 0.25. Figures (1) to (3) show the dispersion error Vn/c versus the number of cells per wavelength p for different methods in 3D. A summarized performance of the three methods is presented in Fig. 4.

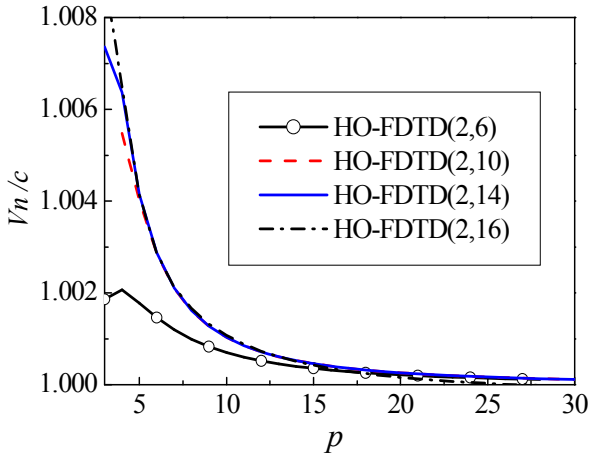

Fig. 1. Dispersion error of the HO-FDTD method.

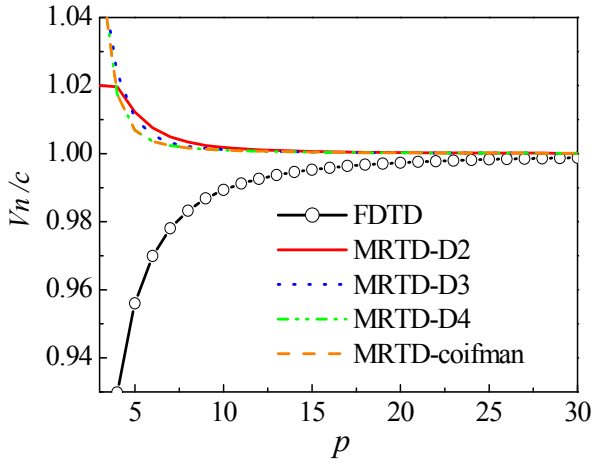

Fig. 2. Dispersion error of the MRTD methods.

Figure 1 shows the dispersion error Vn/c, where Vn refers to the numerical phase velocity, for the HO-FDTD (2, 6), (2, 10), (2, 14), (2, 16). With increasing p, the HO-FDTD (2, 16) is obviously superior to the other three low order schemes (2, 6), (2, 10), and (2, 14), especially when p is larger than 17.

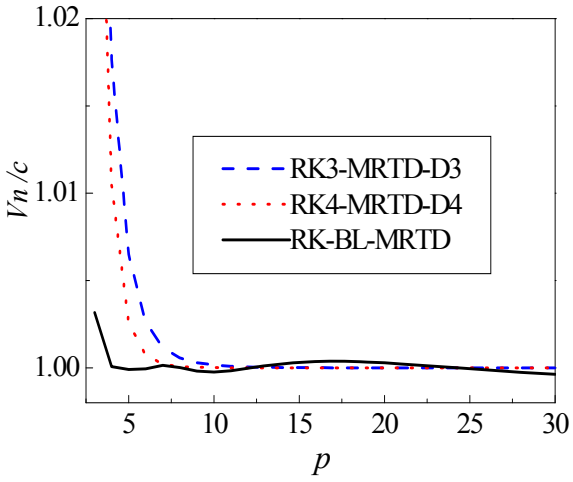

Fig. 3. Dispersion error of the RK-MRTD method.

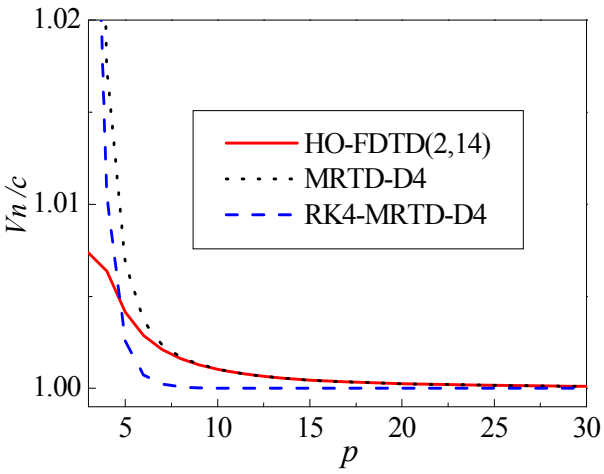

Fig. 4. Dispersion error of the different methods.

Figures 5 to 9 show the dispersion error versus the wave propagation angle ϕ for θ = 90° and Δx = Δy = Δz = Δ=λ /5. From the figures, we can see that: (*i*) the larger the stencil spatial size the minimum is the dispersion error for the same method; (*ii*) for different methods and with the same spatial stencil size, the HO-FDTD and RK-MRTD method both provide the better dispersion characteristics than their corresponding MRTD counterparts.

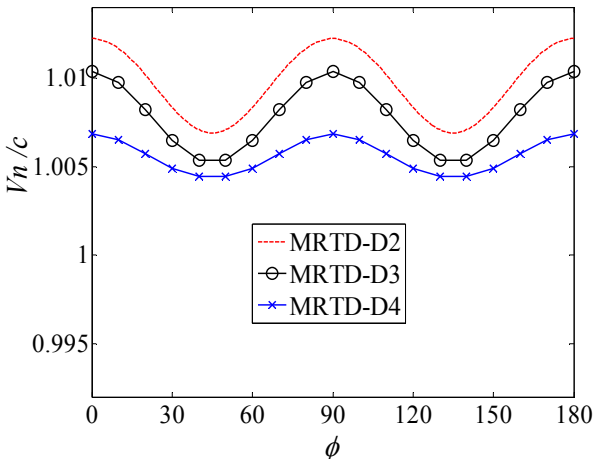

Fig. 5. Dispersion error versus ϕ for the MRTD methods.

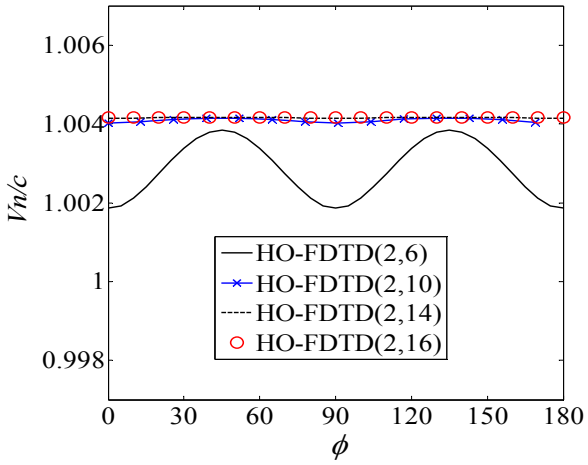

Fig. 6. Dispersion error versus ϕ of the HO-FDTD method.

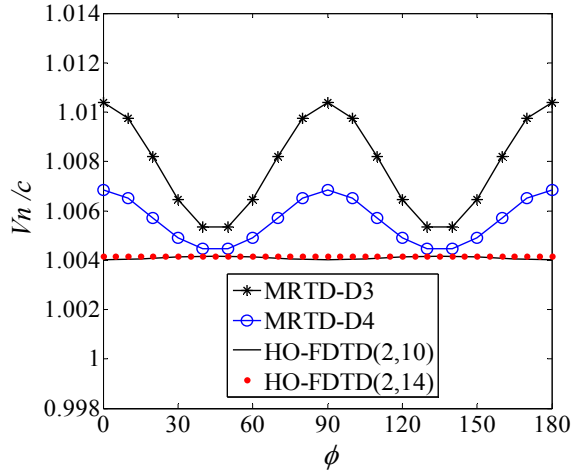

Fig. 7. Dispersion error versus ϕ of the MRTD and HO-FDTD methods.

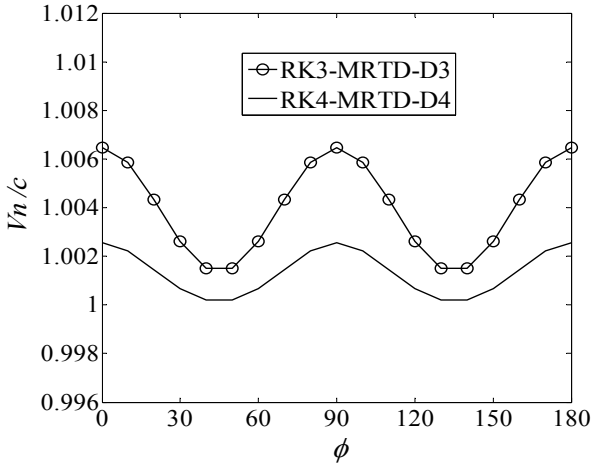

Fig. 8. Dispersion error versus ϕ of the RK-MRTD methods.

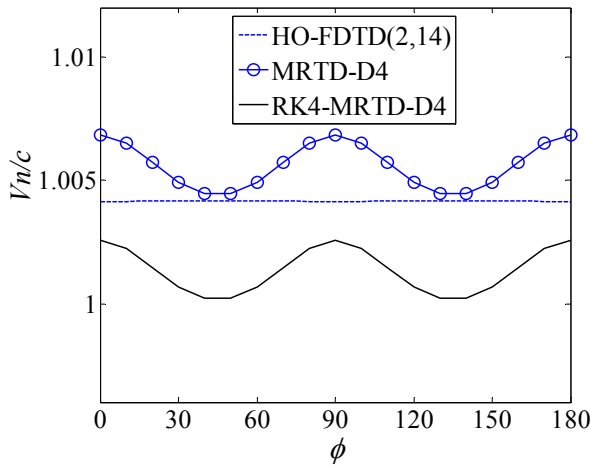

Fig. 9. Dispersion error versus ϕ of the different methods.

C. Convergence

Because the HO-FDTD method uses Taylor series to expand the Maxwell's equations, the arbitrary HO-FDTD ($2N$, $2M$) schemes employ the $2N^{\text{th}}$-order Taylor series expansion in time and the $2M^{\text{th}}$-order Taylor series expansion in space, therefore,

$$\left\| f - \sum \frac{f^{N}(t)}{N!}(\Delta t)^{N} \right\| \le C_{\tilde{n}} (\Delta t)^{\tilde{n}} \left\| f^{\tilde{n}} \right\| \tag{24}$$

$$\left\| f - \sum \frac{f^{M}(x)}{M!}(\Delta x)^{M} \right\| \le C_{\tilde{m}} (\Delta x)^{\tilde{m}} \left\| f^{\tilde{m}} \right\|, \tag{25}$$

$$R_{r'}(\zeta) = \frac{f^{r'}(\zeta)}{r'!}(\Delta\zeta)^{r'} = C_{r'}(\Delta\zeta)^{r'} \left\| f^{r'} \right\|,$$

$$\lim_{r' \to \infty} R_{r'}(\zeta) = 0, \tag{26}$$

where equation (26) is the Taylor series remainder, $C_{\tilde{n}}$, $C_{\tilde{m}}$ and C_r, are the coefficients, so the error is a convergence relation that can be written as the RK-MRTD in [6],

$$\text{HO-FDTD } (2N, 2M)\text{-error} \le A'\Delta t^{\tilde{n}} + B'\Delta x^{\tilde{m}}. \quad (27)$$

Thus, the convergence relation of HO-FDTD (2, 2*M*) scheme can be derived as,

$$\text{HO-FDTD } (2, 2M) \text{ -error} \le C'\Delta t^2 + B'\Delta x^{m'} \quad (28)$$

where A', B', and C' are the constant coefficients. Take the Daubechies N' scaling functions, for example, and the CFL stability condition $\Delta t = q\Delta x/c$ ($q \le 1$), then the convergence relation of the MRTD schemes [6] can be derived as,

$$\text{MRTD-error} \le A\Delta x^{N'} + B\Delta t^2 \le A\Delta x^{N'} + B(\alpha\frac{\Delta x}{c})^2 \le C\Delta x^2. \quad (29)$$

The RK-MRTD method based on the MRTD uses the m^{th}-order m' stage SSP-RK method in temporal discretization. It is known in [6] that

$$\text{RK-MRTD error} \le C_t\Delta t^{m'} + C_x\Delta x^{N'}, \quad (30)$$

simplified and summarized as,

$$\text{RK-MRTD -error} \le C_{N'}\Delta x^{N'}. \quad (31)$$

From Fig. 10, it is easily to find the RK-MRTD scheme based on Daubechies basis functions that have the higher temporal and spatial convergence than other cases.

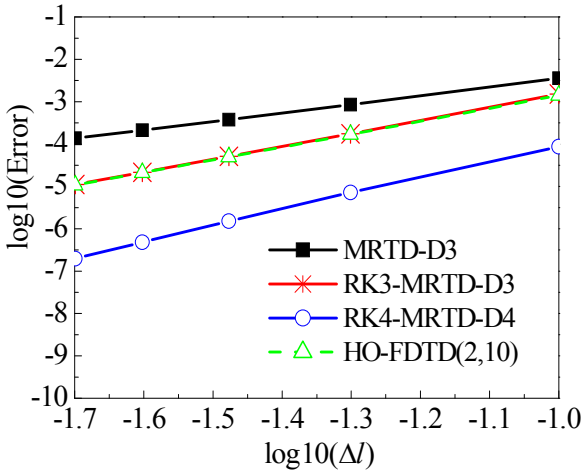

Fig. 10. Convergence of the MRTD, HO-FDTD, and RK-MRTD methods.

IV. COMPUTATIONAL COST AND MEMORY REQUIREMENTS

Here, we analyze and discuss the computational cost and memory requirements of the HO-FDTD (2, 2*M*), MRTD and RK-MRTD method. As in [6], for 3D case, the fields at a final time for the HO-FDTD (2, 2*M*) and MRTD methods only E^n and $H^{n-1/2}$ need to be stored at each time step, while the RK-MRTD method demand to store the values of $F^{(i)}$ and F_{n+1}, so the memory requirements of the RK-MRTD method are twice that of the other two methods.

The computational cost of the MRTD method [6] for a single time step is,

$$\text{Cost}_{\text{MRTD}} = 2(n_1)^3 \times (4N' - 2) \quad (32)$$

where N' is the order of the scaling function $D_{N'}$, n_1 is the number of cells in a single direction. If the domain is the unit size, then $n_1 = 1/\Delta x_1$, and Δx_1 is the grid spacing. Similarly, the computational cost of the HO-FDTD (2, 2*M*) method is,

$$\text{Cost}_{\text{HO-FDTD}} = 2(n_2)^3 \times 2M \quad (33)$$

where n_2 is the number of the cells in a single direction, $n_2 = 1/\Delta x_2$ for unit size and Δx_2 is the grid spacing for the HO-FDTD (2, 2*M*) method. We know that the RK-MRTD method base on the m' stage m'^{th}-order SSP-RK algorithm (cf. (5)), for a single time step, the computational cost [6] is,

$$\text{Cost}_{\text{RK-MRTD}} = 2(n_{m'})^3 \times m' \times (4N' - 1) \quad (34)$$

where $n_{m'}$ is the number of the cells in a single direction, $n_{m'} = 1/\Delta x_{m'}$ for unit size and $\Delta x_{m'}$ is the grid spacing for the RK-MRTD method.

From equations (32) and (33), we found that the MRTD and HO-FDTD (2, 2*M*) methods have the same computational cost if they have the same number of the cells in a single direction and the spatial stencil size. If the computational domain is unit size, and Δt_1 is the maximal stable time step for the MRTD method and $m' = N'$, the time step $\Delta t_{N'}$ for the RK-MRTD must be chosen as $\Delta t_{N'} = 2\Delta t_1 / N'$, the same as the HO-FDTD method, Δt_2 is the maximal stable time step for the HO-FDTD (2, 2*M*) method and the time step must be chosen as $\Delta t_{N'} = 2\Delta t_2 / N'$. If the total computational time is 1, then the cost of the three methods are,

$$\textbf{Cost}_{\textbf{MRTD}} = 2(n_1)^3 \times (4N'-2) \times \frac{1}{\Delta t_1} \quad (35)$$

$$\mathbf{Cost}_{\text{HO-FDTD}} = 2(n_2)^3 \times 2M \times \frac{1}{\Delta t_2} \tag{36}$$

$$\begin{aligned}\mathbf{Cost}_{\text{RK-MRTD}} &= 2(n_{m'})^3 \times m' \times (4N'\text{-}1) \times \frac{1}{\Delta t_{N'}} \\ &= 2(n_{m'})^3 \times N' \times (4N'\text{-}1) \times \frac{1}{\Delta t_{N'}} \\ &= (n_{m'})^3 \times (N')^2 \times (4N'\text{-}1) \times \frac{1}{\Delta t_1} \\ &= (n_{m'})^3 \times (N')^2 \times (4N'\text{-}1) \times \frac{1}{\Delta t_2}. \end{aligned} \tag{37}$$

For a given accuracy, and using the above equations, the computational cost relations among the MRTD, HO-FDTD, and RK-MRTD methods can be derived as,

$$\begin{aligned}\mathbf{Cost}_{\text{RK-MRTD}} &= 2(n_{m'})^3 \times N' \times (4N'\text{-}1) \times \frac{1}{\Delta t_{N'}} \\ &= (n_{m'})^3 \times (N')^2 \times (4N'\text{-}1) \times \frac{1}{\Delta t_1} \\ &= \left(\frac{n_{m'}}{n_1}\right)^3 \frac{(N')^2 \times (4N'\text{-}1)}{2(4N'\text{-}2)} \times \left(2(n_1)^3 \times (4N'\text{-}2) \times \frac{1}{\Delta t_1}\right) \\ &= \eta_1 \times \left(\mathbf{Cost}_{\text{MRTD}}\right) \end{aligned} \tag{38}$$

$$\begin{aligned}\mathbf{Cost}_{\text{RK-MRTD}} &= 2(n_{m'})^3 \times N' \times (4N'\text{-}1) \times \frac{1}{\Delta t_{N'}} \\ &= (n_{m'})^3 \times (N')^2 \times (4N'\text{-}1) \times \frac{1}{\Delta t_2} \\ &= \left(\frac{n_{m'}}{n_2}\right)^3 \frac{(N')^2 \times (4N'\text{-}1)}{4M} \times \left(2(n_2)^3 \times 2M \times \frac{1}{\Delta t_2}\right) \\ &= \eta_2 \times \left(\mathbf{Cost}_{\text{HO-FDTD}}\right), \end{aligned} \tag{39}$$

where

$$\eta_1 = \left(\frac{n_{m'}}{n_1}\right)^3 \frac{(N')^2 \times (4N'\text{-}1)}{2(4N'\text{-}2)} \tag{40}$$

$$\eta_2 = \left(\frac{n_{m'}}{n_2}\right)^3 \frac{(N')^2 \times (4N'\text{-}1)}{4M}, \tag{41}$$

where η_1 and η_2 are constants dependent on $n_{m'}$, n_1, N', n_2, and M. From equations (38) and (39), we know that the computational time of the RK-MRTD method is η_1 times of the MRTD and η_2 times of the HO-FDTD method, and η_1, η_2 can be controllable.

V. NUMERICAL EXAMPLE

In this section, the three above methods will be validated via a simple classical metal sphere scattering example. The radius of the sphere is 1 m, and illuminated by a Gaussian pulse at a Gaussian pulse at $\theta = 0°$, $\varphi = 90°$, and the polarization of the electric field along x-direction with increasing centre frequencies from 1 MHz to 300 MHz. The CFL number is 0.3, the cell size Δ = 0.05 m, the time step size Δt = 0.3 Δ / c, and the total computational time is 2000 steps. Backward scattering RCS for different methods of the metal sphere are shown in Fig. 11, including the Mie series solution, HO-FDTD (2, 14), MRTD-D_4 and RK_4-MRTD-D_4. From the Fig. 11, we can see that errors are increased with increasing the centre frequency because the number of per wavelength decreases with increasing the centre frequency for fixed cell size. But in the lower frequency part, the RK_4-MRTD-D_4 method is better in comparison with the Mie series solution than other methods. The results also agree with those shown in Figs. 4 and 9.

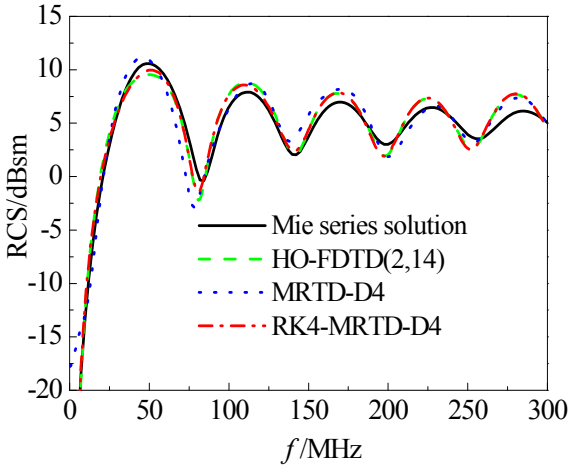

Fig. 11. Backward scattering RCS of the metal sphere.

Figure 12 shows the convergence of the metal sphere scattering in a 3D case. From the figure, we can see that the convergence rate of the RK_4-MRTD-D_4, MRTD-D_4, and HO-FDTD (2, 14) are 4, 2, 2, respectively, and the RK_4-MRTD-D_4 is faster than the other two methods, which are in accordance with the conclusion in Fig. 10.

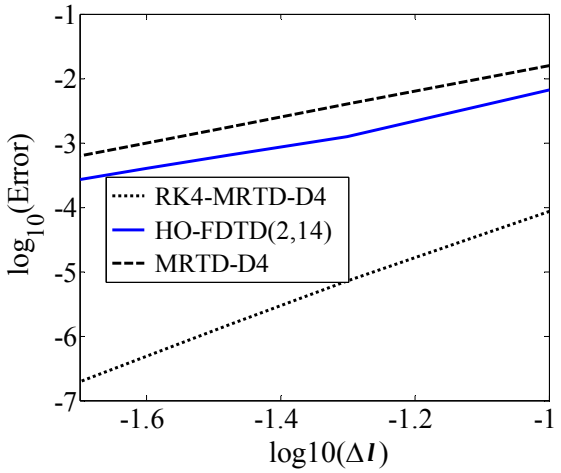

Fig. 12. Convergence of different methods for the scattering of a metal sphere in a 3D case.

VI. CONCLUSION

In this paper, the stability, numerical dispersion, and convergence of the HO-FDTD, MRTD, and RK-MRTD schemes have been investigated, respectively. Analytical stability condition expression for the arbitrary HO-FDTD (2*N*, 2*M*) method has been derived. It is proved that the HO-FDTD schemes have less restrictive conditions of the stability than those of the MRTD method. The dispersion relation for the RK-MRTD schemes also has been derived. It is found, that for the same scheme, for example the HO-FDTD schemes, finer discretizations in time and space domains can decrease the numerical dispersion; among different methods the RK-MRTD schemes demonstrate better dispersion than the HO-FDTD and MRTD methods. The computational cost and memory requirements are discussed in this paper. In section V, a simple and classical example has been used to prove that these methods have certain research value, especially the RK-MRTD method, which has both the better numerical properties and controllable computational time. The conclusions demonstrate that the RK-MRTD method has the potential ability and research significance in computational electromagnetics.

ACKNOWLEDGMENT

This work was supported by the National Nature Science Foundation of China under Contract 61172024. It was also supported by the Funding of Jiangsu Innovation Program for Graduate Education and the Fundamental Research Funds for the Central Universities under Contract cxzz12-0156.

REFERENCES

[1] K. S. Yee, "Numerical solution of initial boundary value problems involving Maxwell's equation in isotropic media," *IEEE Trans. Antennas Propagat.*, vol. 14, no.3, pp. 302-307, May1966.

[2] J. Fang, *Time Domain Finite Difference Computation for Maxwell's Equation*, Ph.D. Dissertation, University of California at Berkeley, Berkeley, CA, 1989.

[3] C. W. Manry, S. L. Broschat, and J. B. Schneider, "High-order FDTD methods for large problems," *Appl. Comp. Electro. Soc. Journal*, vol. 10, no. 2, pp. 17-29, 1995.

[4] D. W. Zingg, "Comparison of the high-accuracy finite difference methods for linear wave propagation," *SIAM Journal Sci. Comput.*, vol. 22, no. 2, pp. 476-502, 2000.

[5] M. Krumpholz and L. P. B. Katehi, "MRTD: New time-domain schemes based on multiresolution analysis," *IEEE Trans. Microw. Theory Tech.*, vol. 44, pp. 555-571, Apr. 1996.

[6] Q. Cao, R. Kanapady, and F. Reitich, "High-order Runge-Kutta multiresolution time-domain methods for computational electromagnetics," *IEEE Trans. Microw. Theory Tech.*, vol. 54, no. 8, pp. 3316-3326, Aug. 2006.

[7] J. Zhang and Z. Chen, "Low-dispersive super high-order FDTD schemes," *IEEE Antennas and Propagation Society International Symposium*, vol. 3, pp. 1510-1513, 2000.

[8] L. Kuzu, M. Gokten, A. Yagli, V. Yanikgonul, and E. Demircioglu, "Fourth-order accurate FDFD method for general waveguide structures," *28th Annual Review of Progress in Applied Computational Electromagnetics Society*, pp. 405-410, Columbus, Ohio, April 2012.

[9] M. Aidam and P. Russer, "Application of biorthogonal B-spline wavelets to Telegrapher's equations," *Proc. of the 14th Annual Review of Progress in Applied Computational Electromagnetics Society*, pp. 983-990, Monterey, CA, March 1998.

[10] E. M. Tentzeris, R. L. Robertson, and J. F. Harvey, et al, "Stability and dispersion analysis of battle-lemarie-based MRTD schemes," *IEEE Trans. Microw. Theory Tech.*, vol. 47, no. 7, pp. 1004-1013, July. 1999.

[11] M. Fujii and W. J. R. Hoefer, "Dispersion of time-domain wavelet Galerkin method based on Daubechies compactly supported scaling

functions with three and four vanishing moments," *IEEE Microwave Guided Wave Lett.*, vol. 10, no. 7, pp. 1752-1760, July 2002.

[12] T. Dogaru and L. Carin, "Multiresolution time-domain using CDF biorthogonal wavelets," *IEEE Trans. Microw. Theory Tech.*, vol. 49, no. 5, pp. 902-3912, May 2001.

[13] X. Zhu, T. Dogaru, and L. Carin, "Three-dimensional biorthogonal multiresolution time-domain method and its application to scattering problems," *IEEE Trans. Microw. Theory Tech.*, vol. 51, no. 5, pp. 1085-1092, May 2003.

[14] H. I. Resnikoff and R. O. Wells Jr., *Wavelet Analysis*, Spring, New York, NY, 1998.

[15] A. Alighanbari and C. D. Sarris, "Dispersion properties and applications of the Coifman scaling function based S-MRTD," *IEEE Trans. Antennas Propagat.*, vol. 54, no. 8, pp. 2316-2325, Aug. 2006.

[16] Q. Cao and K. Tamma, "Multiresolution time domain for studies of planar stratified media," *19th Annual Review of Progress in Applied Computational Electromagnetics Society*, pp. 669-672, Monterey, CA, March 2003.

[17] Q. Cao and K. K. Tamma, "Multiresolution time domain based different wavelet basis studies of scattering of planar stratified medium and rectangular dielectric cylinder," *Appl. Comp. Electro. Society Journal*, vol. 20, no. 1, pp. 86-95, March 2005.

[18] M. Tentzeris and N. Bushyager, "Practical considerations in the MRTD modeling of microwave structures," *21st Annual Review of Progress in Applied Computational Electromagnetics Society*, Honolulu, Hi, 2005.

[19] C. Represa, C. Pereira, A. C. L. Cabeceira, I. Barba, and J. Represa, "PML absorbing boundary conditions for the multiresolution time-domain techniques based on the discrete wavelet transform," *Appl. Comp. Electro. Society (ACES) Journal*, vol. 20, no. 3, pp. 207-212, Nov. 2005.

[20] S. Gottlieb, C. -W. Shu, and E. Tadmor, "Strong stability-preserving high-order time discretization methods," *SIAM Rev.*, vol. 43, no. 1, pp. 89-112, 2001.

[21] M. –H. Chen, B. Cockburn, and F. Reitich, "High-order RKDG methods for computational electromagnetics," *Journal of Sci. Comput.*, vol. 22/23, no. 1-3, pp. 205-226, June 2005.

[22] Y. Liu, "Fourier analysis of numerical algorithms for the Maxwell's equation," *Journal of Comput. Phys.*, vol. 124, pp. 396-416, 1996.

[23] X. Chen and Q. Cao, "Analysis of characteristics of two-dimensional Runge-Kutta multiresolution time-domain scheme," *Progress In Electromagnetics Research M*, vol. 13, pp. 217-227, 2010.

[24] S. Zhao and G. W. Wei, "High-order FDTD methods via derivative matching for Maxwell's equations with material interfaces," *Journal Comput. Phys.*, vol. 200, pp. 60-103, Oct. 2004.

[25] G. Sun and C. W. Trueman, "Analysis and numerical experiments on the numerical dispersion of two-dimensional ADI-FDTD," *IEEE Antennas and Wireless Propagat. Lett.*, vol. 2, pp.78-81, 2003.

Study of Penetration Depth and Noise in Microwave Tomography Technique

Abas Sabouni[1] and Sima Noghanian[2]

[1] Department of Biomedical Engineering,
Ecole Polytechnique de Montreal, Montreal, Quebec, H3T1J4, Canada
abas.sabouni@polymtl.ca

[2] Department of Electrical Engineering, Collage of Engineering and Mines,
University of North Dakota, Grand Forks, North Dakota, 58203, USA
sima.noghanian@engr.und.edu

Abstract ─ The robustness of the microwave tomography method based on frequency dependent finite difference time domain numerical method and hybrid genetic algorithm for breast cancer imaging for different levels of noise are investigated in this paper. These results indicate the algorithm performs well in the case of data contaminated by various levels of additive white Gaussian noise (up to 15 % of signal strength). Noise levels above this value inhibit the efficacy of the method.

Index Terms ─ Breast cancer imaging, heterogeneous and dispersive breast tissue, inverse scattering problem, microwave tomography, and penetration depth for different breast types.

I. INTRODUCTION

Microwave tomography (MWT) is the process of creating an image based on dielectric properties' map from measured electric field qualities. The dielectric properties and measured field are related by a non-linear relationship that is modeled by Maxwell's equations. Inverse scattering problem, is the process to determine the physical quantities of the media from the knowledge of the electric field at a set of receiver points outside the scatterer, and knowledge of the source. Applications include non-destructive testing and medical imaging. In spite of the efforts and research in the field of inverse scattering problem, still many important analytical and computational challenges have remained untouched. Therefore, further efforts are necessary to allow their massive employment in real applications. From a computational point of view, the heterogeneous and dispersive media cause a high computational load. Most of the existing algorithms are very effective when the object under the test is simple. But for applications with complicated structures (such as biomedical imaging, which has a high degree of heterogeneity and high dielectric properties contrast), they may lead to non-real solutions. To deal with these complicated objects, we chose to make no simplification in the non-linear Maxwell's equations. Recently, the authors developed the numerical simulation method based on frequency dependent finite difference time domain ($(FD)^2TD$) and genetic algorithm (GA) for detecting breast cancer [1]. In this paper, the effectiveness of the proposed MWT approach is assessed by means of a numerical example (for breast cancer application) concerning a realistic cross-section of a phantom exposed to an electromagnetic illumination. In MWT imaging technique, the penetration depth plays an important role. Hence, we first analyze the penetration depth of the microwave signal in the breast tissue using anatomically realistic numerical breast phantoms. Then, the proposed microwave tomography technique is applied to a numerical breast phantom with an inhomogeneous scatterer profile, and the map of dielectric properties inside the breast phantom is reconstructed. The presence of noise in the synthetic data is also considered

Submitted On: Oct. 16, 2012
Accepted On: Mar. 17, 2013

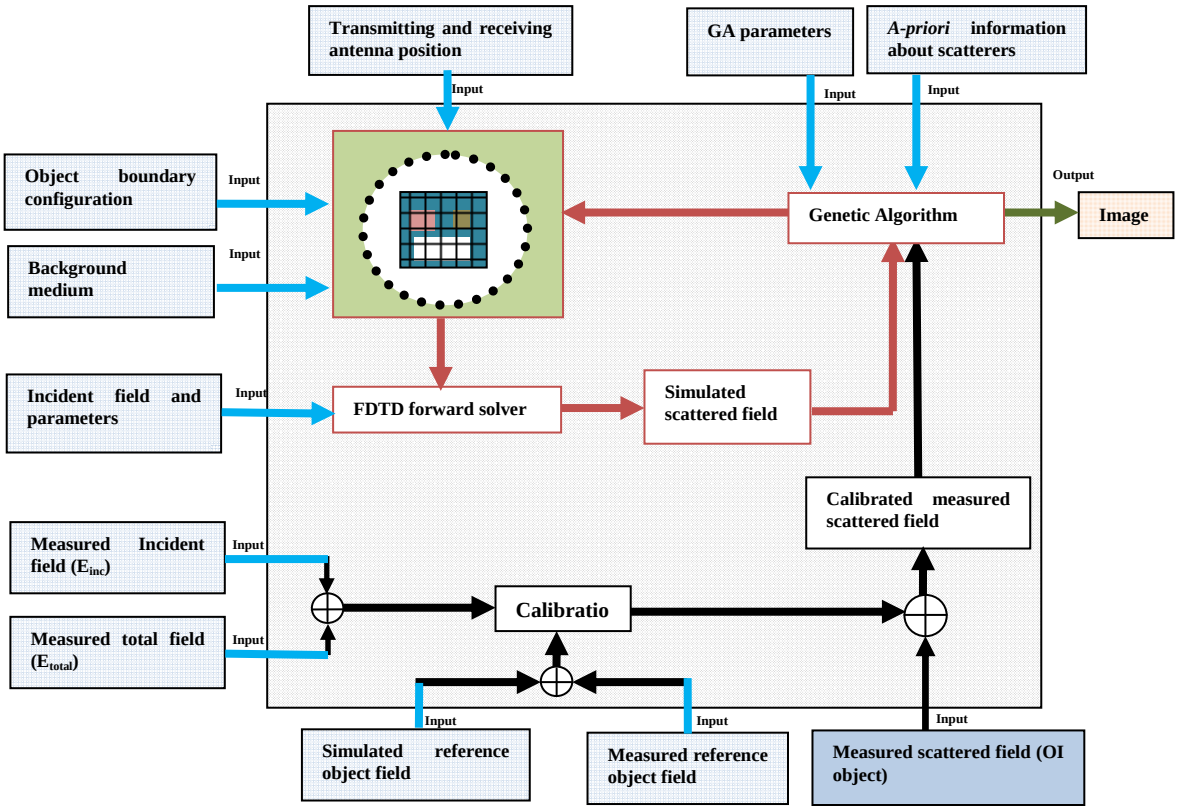

Fig. 1. Block diagram of the proposed MWT method.

and the dependence of the reconstruction accuracy on the signal-to-noise ratio (SNR) is investigated. The paper is organized as follows. In section II, the methodology for the proposed MWT system is explained. In section III we discuss MWT for breast cancer detection and penetration depth for different types of breast phantom is calculated. Section IV discusses the inversion results for the synthetic data and in section V we discuss the inversion results where noise is present.

II. METHODOLOGY

Figure 1 shows the block diagram of the proposed MWT method in [1]. The proposed MWT technique requires a priori information about object of interest (OI), imaging domain, background medium, and measured scattered field from an OI as well as a reference object. As can be seen in this figure, the quality of the images depends on the accuracy of a priori information, accuracy in measured fields, and forward and inverse algorithms. A priori information include information about scatterer, background medium, positions of the transmitter and receiver antennas, and scattered field of a known object for calibration purpose.

III. MICROWAVE IMAGING FOR BREAST CANCER DETECTION

In recent years, microwave imaging has attracted significant interest for biomedical applications in general and as an alternative or complementary method to X-ray mammography for breast imaging in particular. This method relies on the contrast between the electrical properties of tumor and those of normal tissue. Microwave breast imaging techniques can be divided into three main categories: passive [2], hybrid [3], and active methods [1]. In active imaging approaches, the patient lies in the prone position and the transmitter and receiver antennas are located around the breast. A transmitter antenna is fixed at the specific radius from the breast and transmits a signal; the scattered field is collected by receiver antennas around the breast at a specific radius while they are at the same plane of transmitter antenna. This imaging method uses energy at

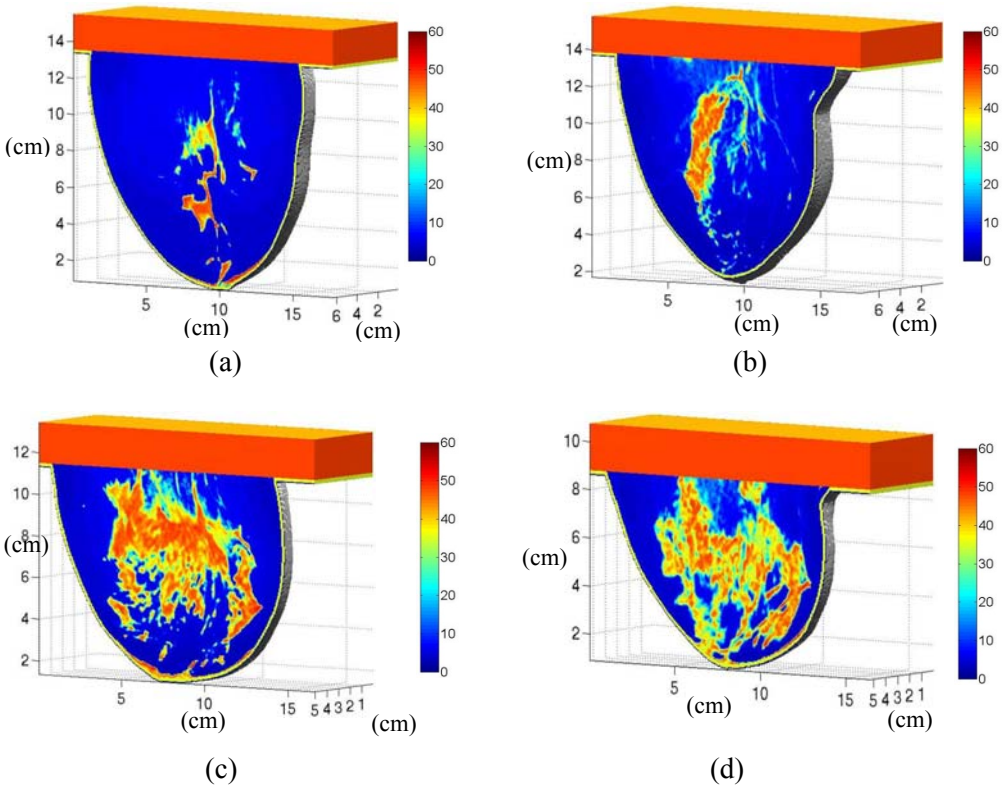

Fig. 2. 3D map of relative permittivity at 5 GHz for (a) mostly fatty, (b) scattered fibro-glandular, (c) heterogeneously dense, and (d) very dense breast type (generated from MRI data in [4]).

microwave frequency range to penetrate into the body and retrieve structural and functional information about the tissues via the scattered waves. Due to the difference between the dielectric properties of the normal and malignant tissues, a scattered electromagnetic field, corresponding to each incident field, will arise which is then measured outside the breast and used to find the shape, location, and dielectric properties of the normal and malignant tissue.

A. Numerical breast phantom

For simulating the breast, in this paper, we used a numerical breast phantom derived from magnetic resonance images (MRI). Figure 2 depicts maps of dielectric properties for the spatial distribution of media numbers for different breast types in terms of X-ray mammography descriptors: mostly fatty, scattered fibro-glandular, heterogeneously dense, and very dense. These were derived from a series of T1-weighted MRIs of the patient in a prone position, provided by the University of Wisconsin-Madison [4]. Figure 2 (a), (b), (c), and (d) show the corresponding dielectric map. Each phantom contains three variations of both fibro-glandular and a adipose tissues, as well as transitional tissues. Dimensions within the 3D region of the breast are described according to each axis. The *z*-axis signifies the depth, and the *x* and *y*-axes represent the span and breadth of the breast, respectively. In order to create the dielectric properties map from the MRI, the range of MRI pixel densities in the breast interior have been linearly mapped to the range of the percentage of water content and to tissue type, such as skin, muscle, fatty, fibro-glandular, and transitional, for each voxel. Figure 3 shows the cross-sectional view in the *x*-*y* plane of tissue types for different breast phantoms in terms of X-ray descriptors. The color bar in this figure indicates the different tissue types; the red color shows the fatty tissue, the orange color shows the transitional tissue, the yellow color shows the fibro-glandular tissue, and the dark blue represents the skin, while the medium blue color represents the immersion medium. Figure 4 shows the cross-sectional view in the *x*-*y* plane in terms of water content for four types of breast phantoms. The

color bar illustrates the water content over a pixel, ranging from zero to one. The fatty and fibro-glandular tissues were divided into three different groups. Therefore, in each group the water content varies independently within a range of values from zero to one.

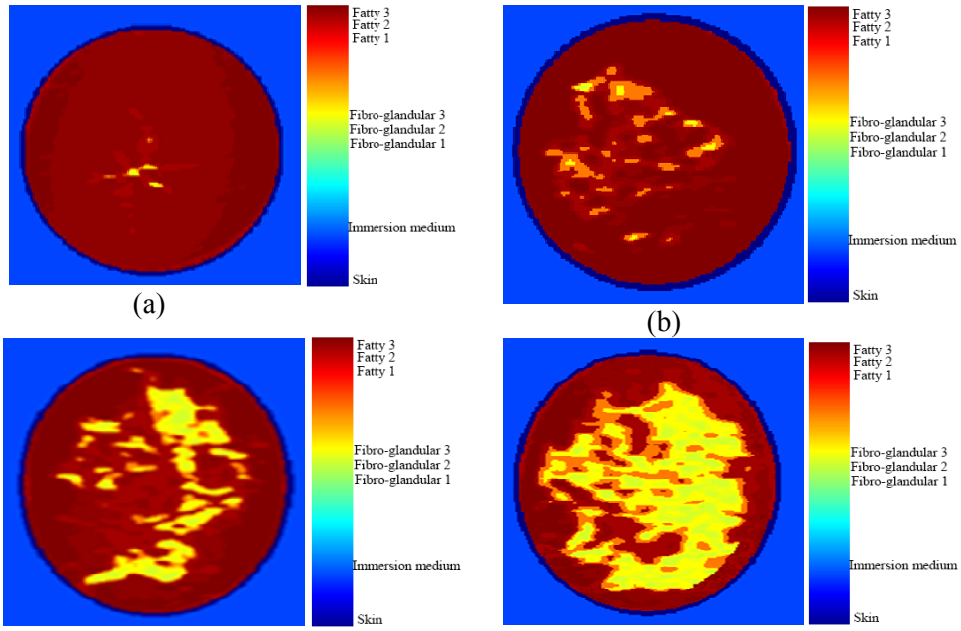

Fig. 3. 2D sectional views of the different breast phantoms in terms of media type (a) mostly fatty, (b) scattered fibro-glandular, (c) heterogeneously dense, and (d) very dense breast type.

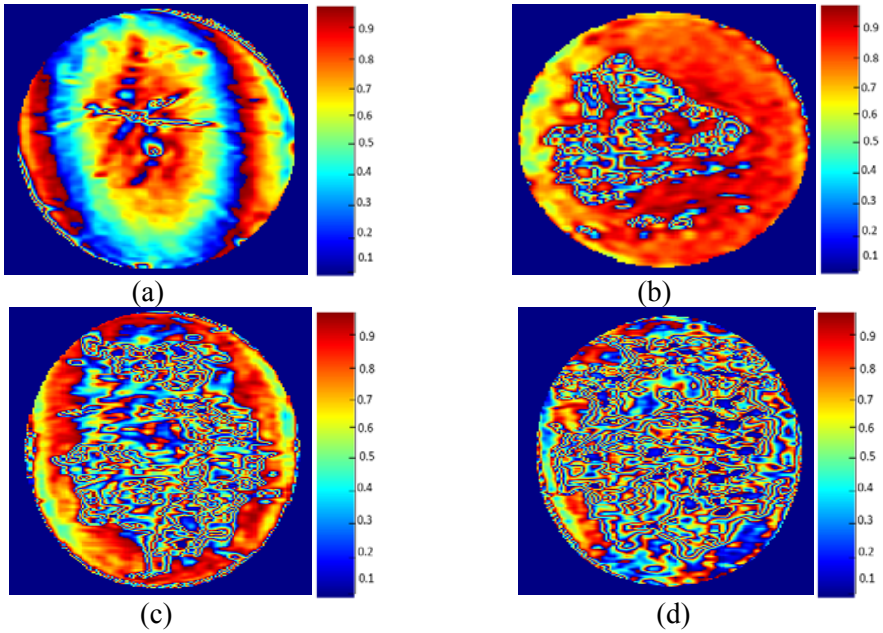

Fig. 4. 2D sectional views of the different breast phantoms in terms of water content (a) mostly fatty, (b) scattered fibro-glandular, (c) heterogeneously dense, and (d) very dense breast type.

We used these two pieces of information (type and water content), for each voxel and mapped them to appropriate Debye parameters [5]. In order to show the majority of fatty tissue in all types of

breast phantoms and how the amount of fibro-glandular tissue changes in these four types of breast tissue, we performed a data analysis. In an image of permittivity, each pixel of image has a value of permittivity ranging from 0 to 70. To calculate histograms of permittivity, the total number of pixel that fall into each value of permittivity, divided by the total number of pixels. Figure 5 shows the histogram of the permittivity for different numerical breast phantoms at 5 GHz.

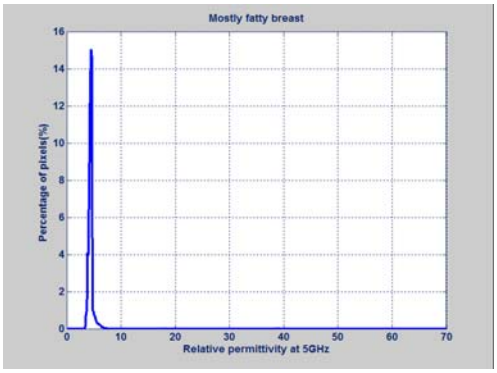

(a)

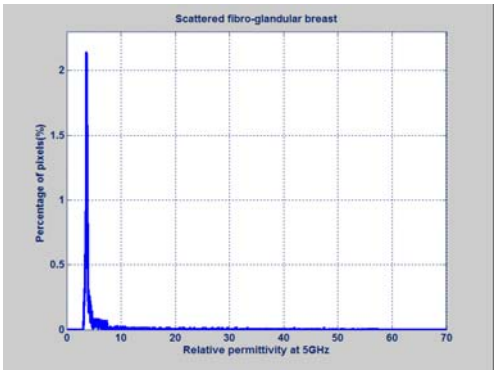

(b)

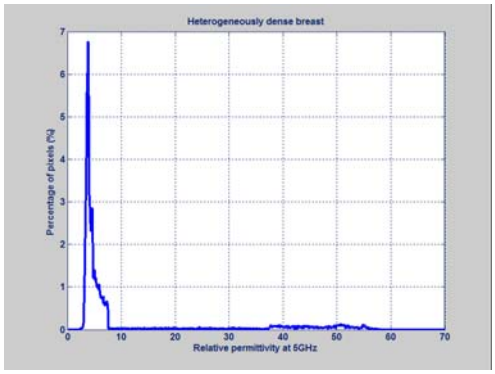

(c)

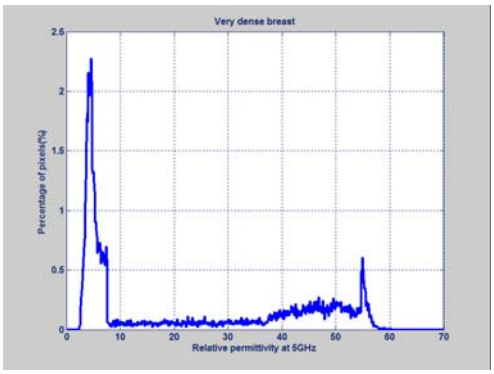

(d)

Fig. 5. The histogram of the permittivity for different numerical breast phantoms at 5 GHz (a) mostly fatty, (b) scattered fibro-glandular, (c) heterogeneously dense, and (d) very dense.

All the analysis is conducted at the cross-section 4 cm away from the nipple. Several observations can be drawn from these graphs. First, as we move from mostly fatty to the very dense breast phantom, the percentage of fatty tissue decreases, and the percentage of fibro-glandular tissue increases. Second, each breast phantom almost covers the entire range of dielectric constants from 0 to 70, and furthermore, the distribution of dielectric constants is not uniform.

B. Penetration depth

The principal limiting factor in penetration depth of the microwave is attenuation of the electromagnetic wave in the breast tissues. The attenuation predominantly results from the conversion of electromagnetic energy to thermal energy due to the high conductivities of the skin and breast tissue at high frequencies. Figure 6 illustrates that the conductivities of the skin, the fibro-glandular tissue, and the malignant tumor increase by increasing the frequency with a constant amount of water. In this section, we focus on the investigation of the penetration depth of the microwave pulse into the numerical breast phantom, and we compare the scattered fields for each case of Fig. 2. The penetration depth is the distance that the propagation wave will travel before the power density is decreased by a factor of *1/e*. The absorbed power density is given by,

$$\text{Absorb power density} = \frac{\sigma_{average}}{2}\left|E_{total}\right|^2 \quad (1)$$

where $\sigma_{average}$ is the average of conductivity for breast tissues and E_{total} is the total field. In order to calculate the penetration depth, we used 2D $(FD)^2TD$ that includes the water content [5, 6]. The $(FD)^2TD$ is an extended version of the conventional finite difference time domain (FDTD) that incorporates the Debye model into the difference equations and can handle dispersive materials more accurately [7]. The breast model is based on an MRI data taken from the breast phantom repository [4] as explained in section III-A. Each cell of the $(FD)^2TD$ contains its own tissue type and percentage of water content. For the study of the penetration depth, the breast is surrounded by free space. Figure 7 shows the depth of penetration as a function of frequency for different types of numerical breast phantoms.

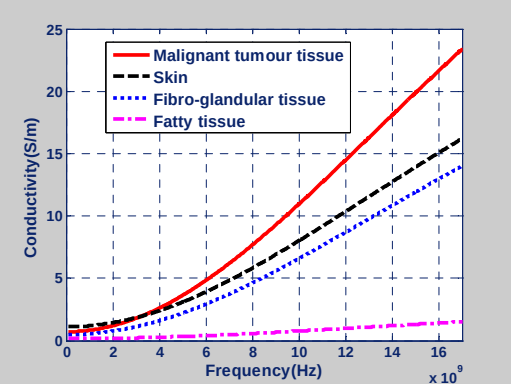

Fig. 6. Frequency variation of conductivity for different breast tissues with 50 percent water content based on Debye model.

As can be seen in this graph, the *1/e* depth of penetration is different for each case. This is due to different tissue compositions in different types of numerical breast phantoms. The penetration depth inside the dispersive lossy biological media decreases as the frequency increases. Therefore, employing higher frequencies to obtain better resolutions and improved imaging accuracy remains a challenge.

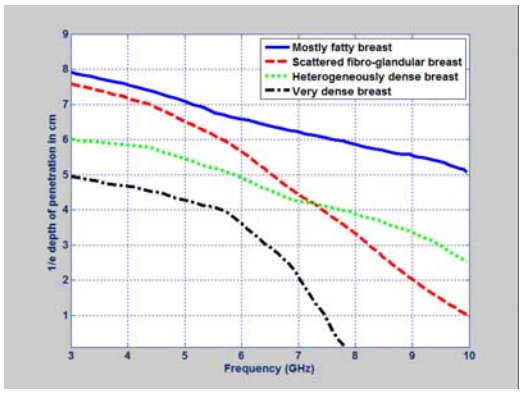

Fig. 7. The *1/e* penetration depth versus frequency for different breast phantoms.

IV. INVERSION RESULTS FOR BREAST CANCER DETECTION

In order to show the ability of the proposed method in terms of resolution, the breast phantom derived from MRI [4] data with a 7 mm resolution has been selected. Cross-sectional maps of the dielectric constant and effective conductivity distribution at 5 GHz for a "heterogeneously dense" breast phantom are shown in Fig. 8. The physical diameter of the breast phantom is approximately 8 cm. The phantom contains different tissue types ranging from the highest water content (fibro-glandular) tissue to lowest water content (fatty) tissue, and also a transitional region with various water content levels.

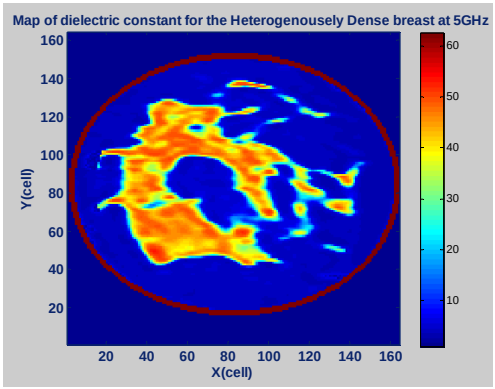

(a)

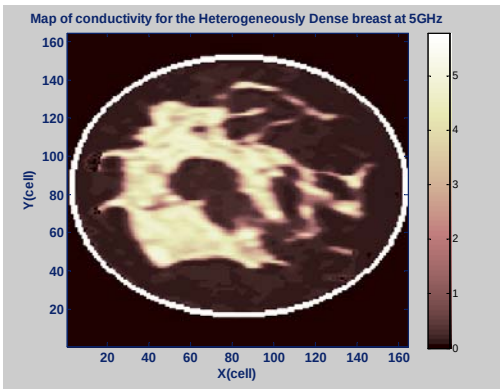

(b)

Fig. 8. Map of (a) permittivity and (b) conductivity of the heterogeneously dense breast phantom.

Figure 9 shows the map of the dielectric properties at 7 mm resolution of the numerical breast phantom shown in Fig. 8. A 7 mm square-shaped tumor was inserted inside the fibro-glandular tissue for the phantom used in the FDTD model. The tumor is placed at a x = 60 cm and y = 80 cm position. The breast is surrounded by the free space. In the examples considered herein, the following parameters have been used. 100 observation points are uniformly distributed around the investigation domain. A (Transverse Magnetic) TM_z Gaussian plane wave successively illuminates the breast and penetrates in the investigation domain, and the scattered fields are measured at the observation points around it. To enhance the accuracy of the image and reduce the ill-posedness of the inverse problem, the procedure is repeated for four different incident angles (0^o, 90^o, 180^o, and 270^o). In these examples the measurement data is replaced by hypothetical simulated data obtained by running a forward simulation using $(FD)^2TD$ with a 0.1 mm resolution. To prevent the inverse crime, a 0.5 mm resolution mesh has been used for the inverse solver. Equation 2 shows the fitness-function used in the GA optimization,

$$\text{Fitness} = 1 - \frac{1}{T}\sum_{i=1}^{T}\left\| \sum_{f=f_1}^{f_2}\sum_{\Phi=1}^{M} \frac{\left(E_{\Phi,i,f}^{measurement} - E_{\Phi,i,f}^{simulation}\right)^2}{\left(E_{\Phi,i,f}^{measurement}\right)^2} \right\|. \quad (2)$$

The $E_{\Phi,i,f}^{measurement}$ is the measured scattered electric field, $E_{\Phi,i,f}^{simulation}$ is the estimated scattered field obtained by performing a forward simulation, M is the number of observation points, T is the total number of illumination angles, and ϕ is an index to angle of the observation point from the axis of the incident wave. f refers to different sampling frequencies within f_1 and f_2.

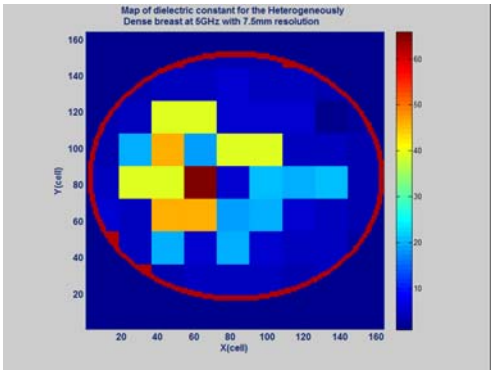

(a)

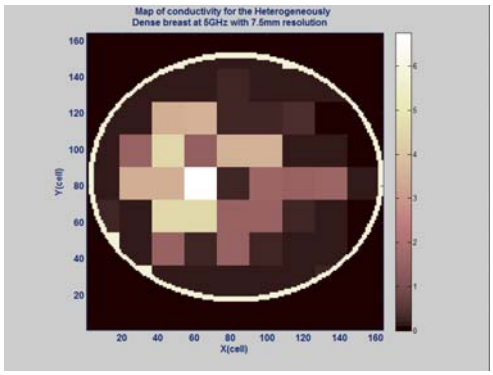

(b)

Fig. 9. Map of the (a) permittivity and (b) conductivity of the heterogeneously dense breast with 7 mm resolution.

Note that the data at each frequency are equally weighted in the inversion process. As a proof of concept, we have considered the noise-less scenario for the first example and in the second example the effect of the noise in inversion results is investigated.

A. Optimization procedure

In the GA program, the enclosed scattering region (inside the breast) is discretized into a number of small patches ($7\times7mm^2$). We assumed

that the location of the skin is known and can be found using skin detection technique [8]. Then the GA optimization starts from a homogeneous fatty tissue background and fills in some patches of possible materials inside the area and try to find a set of dielectric properties of the material for those patches that can generate the same scattered fields as the hypothetical simulated data.

The reconstruction algorithm consists of a combination of a binary and areal GA [9]. The GA optimization is divided into two steps. At the first step, the binary genetic algorithm (BGA) is employed in order to determine the type of the tissue for each patch. In the second step, by using real genetic algorithm (RGA) for the candidate solutions the search is performed for the right amount of water content. In the BGA, the look-up table consists of first order Debye parameters for four different tissue types: fibro-glandular, fatty, transitional, and malignant tissues with 50 percent water content given in Table 1 [10, 11].

Table 1: Look-up table of the Debye parameters for the BGA.

Medium	Fat	Transitional	Fibro-glandular	Malignant Tumour
ε_∞	4.33	22.46	52.020	76.170
ε_s	2.98	8.488	14.000	25.520
σ_s(S/m)	0.02	0.230	0.780	1.200
τ_0(ps)	13.0	13.00	13.00	13.00

For each patch, a two bit identifier can designate it as one of four types of tissue. In BGA the chromosome is expressed as a binary string. Therefore, the search space of the considered problem is mapped into a binary space. After reproducing an offspring, a decoder mapping is applied to the look up table to map them back to real space in order to compute their fitness-function values. The optimizing parameter here is the type of breast tissue for each patch of search space. The BGA program stops when the average quality of the population does not improve after a number of generations. The best individuals of the last generation of BGA are passed to the second step, which is RGA. For the RGA, the look-up table consists of first order Debye parameters from the upper to lower end of the range for four the same types of breast tissue with various water content levels (Table 2) [10, 11].

Table 2: Look-up table of the Debye parameters for the RGA.

Medium	Fat	Transitional	Fibro-glandular	Malignant Tumour
$\varepsilon_{\infty u}$	3.987	12.990	23.200	9.058
ε_{su}	7.535	37.190	69.250	60.360
σ_{su}(S/m)	0.080	0.397	1.306	0.899
$\varepsilon_{\infty l}$	2.309	3.987	12.990	23.200
ε_{sl}	2.401	7.535	37.190	69.250
σ_{sl}(S/m)	0.005	0.080	0.397	1.306
τ_0(ps)	13.00	13.00	13.00	13.00

RGA optimizes the percentage of water content. Including the percentage of water content into the Debye model has been discussed in reference [5]. The result of BGA is a map of the dielectric properties inside the breast phantom (assuming 50 % water content) and for the RGA is the water content of that tissue. It is worth mentioning that the GA programs are not guaranteed to converge to the optimal solution, but by using RGA and looking at the behavior of the best fitness values at different generations for each individual of those possible solutions obtained by BGA, one can choose a population that is adequate to the problem and thus increase the chance of success. Figure 10 shows the reconstructed image of permittivity and conductivity. Transects of the reconstructed permittivity and conductivity at 5 GHz in the horizontal direction at line y = 80 cell and x = 64 cell, compared with the actual distribution, are shown in Fig. 11.

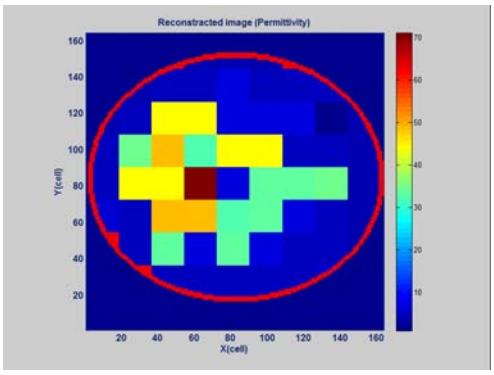

(a)

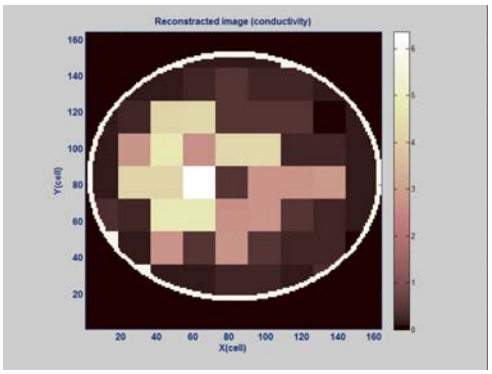

(b)

Fig. 10. Reconstructed image of (a) permittivity, and (b) conductivity for the breast phantom of Fig. 9.

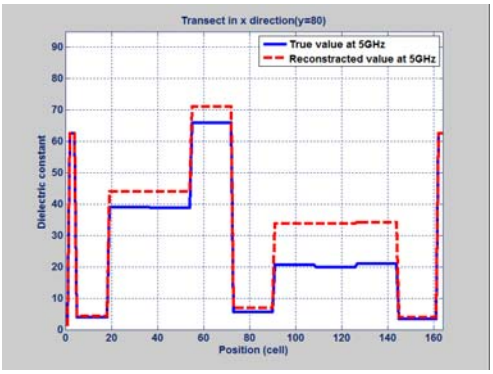

(a)

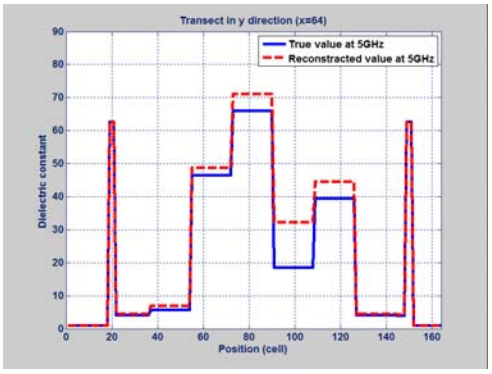

(b)

Fig. 11. Transects of the reconstructed permittivity image at (a) y = 80 cell horizontal direction and (b) x = 64 cell vertical direction profiles compared with the actual distribution.

One observation apparent in these images is the small degree of inaccuracy in the recovered permittivity and conductivity compared with the actual profile, since the percentage of water content, which affects dielectric properties, is not precisely known. However, the estimated percentage of water content is within the range for each tissue type to recognize the right tissue composition.

V. HGA/FDTD IN THE PRESENCE OF NOISE

Background noise is always present in any measurement and it must be taken into account. This is particularly important in biomedical applications, since for safety reasons, it is not possible to increase the energy of the incident field to overshadow the background noise. It is shown in this section that the proposed method is efficient and provides adequate accuracy even when the signal to noise ratio (SNR) is low. SNR is defined by [12]

$$\mathrm{S}NR = 10\log\left(\frac{P_s}{P_n}\right), \tag{3}$$

in which P_s is the total power of the scattered field and is proportional to

$$P_s = \frac{1}{2}\sum_{\mathrm{f}_1}^{\mathrm{f}_2}\left|\mathrm{E}_z\right|^2. \tag{4}$$

The symbol E_z is the scattered field at the different frequencies within f_1 - f_2 range, and P_n is the noise power. Figure 12 shows the tumor response for 1 cm tumor (Fig. 12 (a)) and 5 mm tumor (Fig. 12 (b)) while the data is contaminated with different levels of noise (SNR = 10, 20, 30, and 40 dB) for different types of breasts such as scattered fibro-glandular breast, heterogeneously dense breast, and very dense breast at 5 GHz. As can be seen in this figure the strength of tumor response for the scattered fibro-glandular breast is quite high compared to the heterogeneously dense breast and very dense breast. Because, the amount of the fibro-glandular tissue (which is a lossy material) in heterogeneously dense breast and very dense breast is significantly large. We artificially added some noise to the signal to mimic the existing noise in measurement setup. Figure 12 shows that for the scattered fibro-glandular breast by adding different level of noise the signal intensity is still well above the noise floor. However, for the very dense breast, due to small signal strength, it will

be difficult to distinguish between the signal and noise. We did not provide the results of mostly fatty breast here. Generally the tumor response for this type is stronger than all other breast.

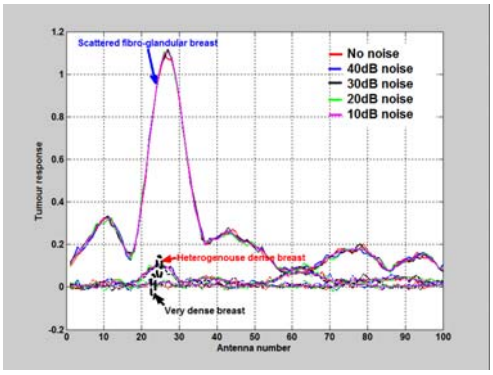

(a)

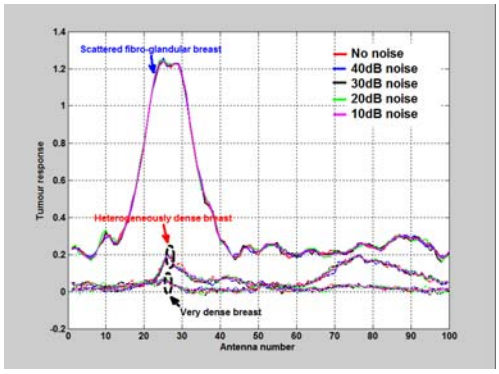

(b)

Fig. 12. Tumor response for diverse SNR and different breast types and tumor size with diameter (a) 1 cm and (b) 5 mm.

The 2 mm tumor response without noise for the heterogeneously dense breast and very dense breast are compared with the response of 1 cm and 5 mm tumors and are shown in Fig. 13. Table 3 also shows the maximum tumor response for the heterogeneously dense breast and very dense breast. As can be seen, the tumor response for the 2 mm tumor in heterogeneously dense breast is even higher than the response from 1 cm tumor in very dense breast.

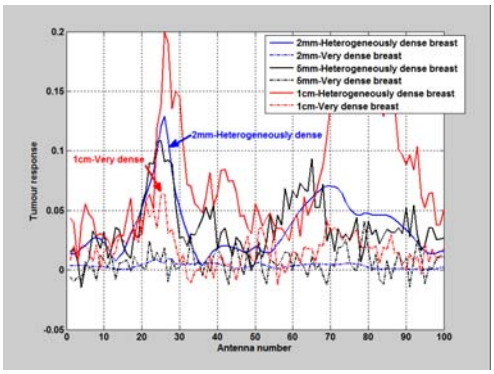

Fig. 13. Tumor response for 1 cm, 5 mm and, 2 mm diameter tumor sizes for the heterogeneously dense breast and very dense breast.

Table 3: Maximum tumor response.

Tumour size	1cm	5mm	2mm
Heterogeneously dense breast	0.199	0.108	0.128
Very dense breast	0.063	0.041	0.009

Therefore, detecting the small tumor becomes difficult as the amount of the fibro-glandular tissue increases in the breast. Therefore, the detectable tumor size depends on the breast type and SNR. Here, we investigated the performance of the proposed method at different SNR levels. Figure 14 shows the block diagram of the process of adding the noise to the measurement signal.

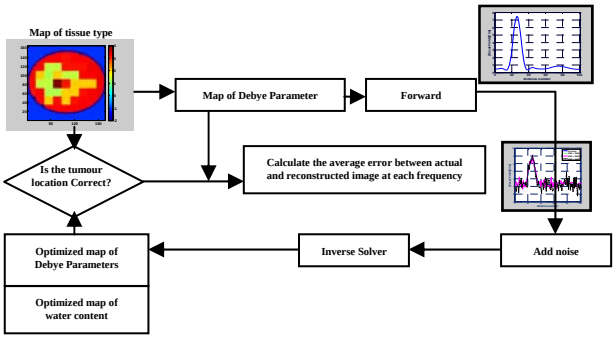

Fig. 14. Block diagram of adding noise in the proposed tomography method.

After recording the scattered fields at the observation points by using the $(FD)^2TD$ solver, an additive white Gaussian noise was added to

simulate the instrument noise, which can present in real measurements. The HGA optimization technique was then used to reconstruct the dielectric property map of the breast tissue inside the numerical breast phantom. Background noise generally considered as white noise, due to having an almost a constant power spectral density [12]. Figure 15 (a) shows the histogram of white noise. Figure 15 (b) shows the amplitude of white noise for each antenna at the observation point at 5 GHz. Figure 15 (c) presents the power spectral density of the white Gaussian noise for each antenna. The white noise was artificially added to all measurements of the scattered field at different frequencies in such a way that the power of noise was constant at all frequencies, but the power of the noise changed randomly with Gaussian distribution at each observation point.

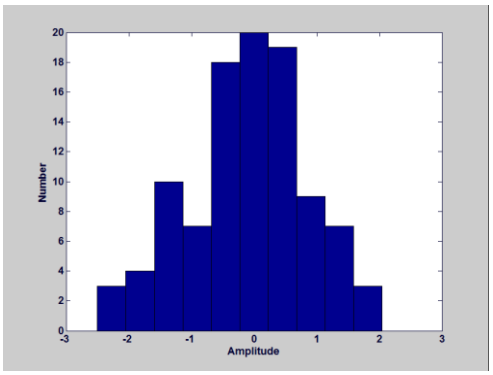

(a)

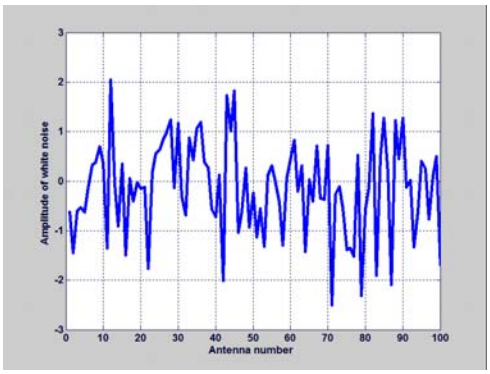

(b)

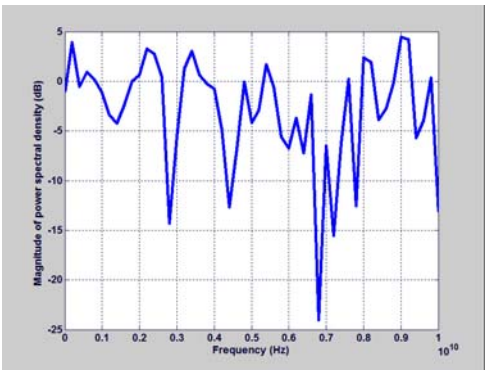

(c)

Fig. 15. (a) Histogram plot of the added white noise, (b) amplitude of white noise for each antenna at the observation point, and (c) power spectral density of the white Gaussian noise.

To illustrate the ability and robustness of the proposed HGA method, we added different levels of noise to the scattered field of the breast phantom of Fig. 9 by using the process shown in Fig. 14. Figures 16 (a) and (b) show the average error of the dielectric constant and conductivity versus SNR, respectively. These errors are averaged over the differences between the actual and the reconstructed permittivity and conductivity shown in equations (5) and (6), respectively,

$$\text{Average error in permittivity} = \sum_{f_1}^{f_2} \frac{\sum_i \sum_j \left| \varepsilon_{r(\text{reconstracted image})} - \varepsilon_{r(\text{real image})} \right|}{\text{number of cells}} \quad (5)$$

$$\text{Average error in conductivity} = \sum_{f_1}^{f_2} \frac{\sum_i \sum_j \left| \sigma_{(\text{reconstracted image})} - \sigma_{(\text{real image})} \right|}{\text{number of cells}}, \quad (6)$$

where f_1 and f_2 refer to different frequencies of reconstruction and i and j are the cell numbers in the x and y directions, respectively. These figures demonstrate that as the SNR decreases (noise level increases), the average error increases. It was observed that the proposed method still can find the tissue types of the heterogeneous structure even when the SNR is 23 dB, which is equivalent to 15 % background noise. When the background noise is greater than 15 %, the optimization program did not converge.

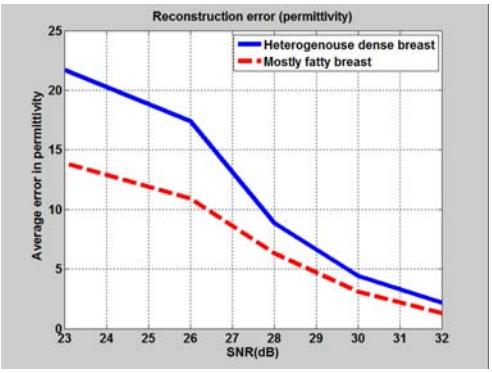

(a)

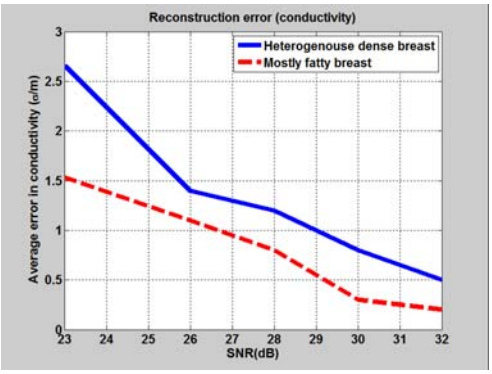

(b)

Fig. 16. The average error in (a) dielectric constant and (b) conductivity versus SNR.

It was also noticed that by increasing the noise level, the optimization time for convergence was significantly increased. The same procedure of adding noise was repeated for the mostly fatty breast. As indicated in Fig. 16, the average error of permittivity and conductivity are less, compared to heterogeneously dense breast with the same SNR.

VI. CONCLUSION

In this paper we studied the noise effects on $(FD)^2TD/GA$ algorithm for solving the inverse scattering problem for heterogeneous and dispersive objects. We presented an accurate simulation model for the breast cancer detection that considers the heterogeneity, dispersive characteristics, and the water content of the breast. Further, we calculated the penetration depth for different tissue compositions of breast phantoms categorized as: mostly fatty, scattered fibro-glandular, heterogeneously dense and very dense. We have presented the results of inversion and the effect of noise on the accuracy of proposed microwave tomography method. The simulation results illustrate that the proposed method is capable of detecting lesions in environments where they are surrounded by fibro-glandular tissue, which happens in most cases of breast cancer. We used 7 mm resolution for GA. Higher resolution images of the realistic phantom can be obtained by reducing the discretization unit size, which result in a longer run time. In this paper the breast cancer detection is chosen as a primary application to investigate the capabilities of the proposed technique due to the heterogeneous structure and dispersive characteristic of the breast. However, the proposed technique can be applied to many other applications.

ACKNOWLEDGMENT

The authors would like to acknowledge the financial support of Natural Sciences and Engineering Research Council of Canada, Cancer Care Manitoba, University of North Dakota, and North Dakota Experimental Program to Stimulate Competitive Research.

REFERENCES

[1] A. Sabouni, S. Noghanian, and S. Pistorius, "A global optimization technique for microwave imaging of the inhomogeneous and dispersive breast," *Canadian Journal of Electrical and Computer Engineering*, vol. 35, no.1, pp. 15-24, 2010.

[2] S. Iudicello and F. Bardati, "Functional imaging of compressed breast by microwave radiometry," *Applied Computational Electromagnetics Society (ACES) Journal*, vol. 24, no. 1, pp. 64-71, 2009.

[3] G. Zhu and M. Popovic, "Enhancing microwave breast tomography with microwave-induced thermo acoustic imaging," *Applied Computational Electromagnetics Society (ACES) Journal*, vol. 24, no. 6, pp. 618-627, 2009.

[4] E. Zastrow, S. K. Davis, M. Lazebnik, F. Kelcz, B. D. Van Veen, and S. C. Hagness, "Database of 3D grid-based numerical breast phantoms for use in computational electromagnetics simulations," *Instruction Manual*, University of Wisconsin-Madison.

[5] A. Sabouni, S. Noghanian, and S. Pistorius, "Water content and tissue composition effects on microwave tomography results," *in International Review of Progress in Applied Computational Electromagnetics (ACES)*, 2008.

[6] A. Sabouni, S. Noghanian, and S. Pistorius, "Frequency dispersion effects on FDTD model for breast tumor imaging application," *in IEEE Antennas and Propagation Society International Symposium*, pp. 1410-1413, 2006.

[7] M. Bui, S. Stuchly, and G. Costache, "Propagation of transients in dispersive dielectric media," *IEEE Transactions on Microwave Theory and Techniques*, vol. 39, no. 7, pp. 1165-1172, 1991.

[8] D. A. Woten and M. El-Shenawee, "Quantitative analysis of breast skin for tumor detection using electromagnetic waves," *Applied Computational Electromagnetics Society (ACES) Journal*, vol. 24, no. 5, pp. 458-463, 2009.

[9] A. Sabouni, A. Ashtari, S. Noghanian, G. Thomas, and S. Pistorius, "Hybrid binary-real GA for microwave breast tomography," *in Antennas and Propagation Society International Symposium*, pp. 1-4, July 2008.

[10] M. Lazebnik, L. McCartney, D. Popovic, B. Watkins, M. J. Lindstrom, J. Harter, S. Sewall, A. Magliocco, J. H. Booske, M. Okoniewski, and S. C. Hagness, "Large-scale study of the ultra-wideband microwave dielectric properties of normal breast tissue obtained from reduction surgeries," *Physics in Medicine and Biology*, vol. 52, pp. 2637-2656, 2007.

[11] M. Lazebnik, D. Popovic, L. McCartney, C. Watkins, M. Lindstrom, J. Harter, S. Sewall, T. Ogilvie, A. Magliocco, T. M.Breslin, W. Temple, D. Mew, J. H. Booske, M. Okoniewski, and S. C. Hagness, "A large-scale study of the ultra-wideband microwave dielectric properties of normal, benign, and malignant breast tissues obtained from cancer surgeries," *Physics in Medicine and Biology*, vol. 52, pp. 6093-6115, 2007.

[12] M. Moghaddam and W. Chew, "Study of some practical issues in inversion with the born iterative method using time-domain data," *IEEE Transactions on Antennas and Propagation,* vol. 41, no. 2, pp. 177-184, 1993.

Abas Sabouni received the M.Sc. degree in Electrical Engineering from K. N. Toosi University, Tehran, Iran, in 2005, and Ph.D. degree in Electrical Engineering, from the University of Manitoba, Winnipeg, MB, Canada, in 2011. Since 2010, he has been a Post-Doctoral Fellow in Biomedical Engineering Department at the Ecole Polytechnique de Montreal, and Research Associate at the Department of Electrical and Computer Engineering at the Concordia University from 2011. He was a Research and Development Engineer at PartoDadeh Inc., Tehran, Iran during 2001 through 2004. During 2005 and 2006, he was a Research Assistant in the Electromagnetic Group, University of Manitoba and a Research Associate at Cancer Care Manitoba. From 2009 to 2010, he was a Research Associate in the Department of Electrical Engineering, University of North Dakota, Grand Forks, North Dakota, USA. His research interests include inverse scattering problem, microwave imaging, UWB antenna design and modeling, and transcranial magnetic stimulation. Dr. Sabouni is the recipient of the IEEE AP-S Honorable Mention Student Paper Contest 2008. In 2013, he served as the Vice-President of IEEE Montreal section. Since 2010, he is the Chair of IEEE Montreal Antenna Propagation Chapter.

Sima Noghanian received the B.Sc. degree in Electrical Engineering from the Sharif University of Technology, Tehran, Iran, in 1992, and the M.Sc. and Ph.D. degrees, both in Electrical Engineering, from the University of Manitoba, Winnipeg, Canada, in 1996 and 2001, respectively. In 2001, she was at Yotta Yotta Corporation, Edmonton, Canada. She was an Assistant Professor in the Department of Electrical Engineering, Sharif University of Technology during 2002 and 2003. From 2003 to 2008, she was an Assistant Professor in the Department of Electrical and Computer Engineering, University of Manitoba. Since 2008, she has been an Assistant Professor in the Department of Electrical Engineering, University of North Dakota, Grand Forks. Her research interests include antenna design and modeling, wireless channel modeling, ultra-wideband antennas, and microwave imaging. Dr. Noghanian was IEEE Winnipeg Waves (joint Chapter of Antenna and Propagation/Microwave Theory and Techniques/Vehicular Technology societies) Chapter Chair during 2004 and 2005. She received a Postdoctoral Fellowship from Natural Sciences and Engineering Research Council of Canada at the University of Waterloo in 2002.

Near Field to Far Field Conversion for an Infinite Ground Micro-Strip Trace Using Genetic Algorithm

R. Rajabzadeh and G. Moradi

Department of Electrical Engineering, Amirkabir University of Technology, Tehran, Iran
r.rajabzadeh1803@gmail.com, ghmoradi@aut.ac.ir

Abstract – In this paper, an efficient combination of the near field to far field (NF-FF) transformation and the genetic algorithm (GA) is suggested for investigating of a microstrip trace on an infinite ground plane. Parameters of a set of ideal electric and magnetic dipoles are estimated by GA based on finite samples of near field data in the radiation region. Then, the far field pattern is determined, using the electromagnetic (EM) fields of equivalent ideal dipoles. The commercial software Ansoft High Frequency Structure Simulator (HFSS) is used for both, computing the near field data and validation of the proposed method. In addition, the influence of number of dipoles on the convergence rate is studied.

Index Terms – Genetic algorithm, microstrip, and near field to far field transformation.

I. INTRODUCTION

Open area test site (OATS) measurement is the most direct and universally accepted standard approach for measuring radiated emissions (RE) and radiation susceptibility (RS) of equipments. However, OATS is not always possible, due to space limitations. Therefore, number of measurement facilities and procedures have been developed to carry out such measurements in laboratories; e.g., microwave anechoic chamber, transverse electromagnetic cell (TEM cell), and reverberation chamber (RVC) [1]. These methods are costly and require complex processes such as calibration. The near field to far field (NF-FF) transformation is a low-cost and flexible alternative method for radiated emissions (RE) in electromagnetic interference (EMI) [2]. This method is often combined with an optimization strategy to properly estimate the FF. The large number of optimization parameters suggests application of stochastic optimization methods such as GA [3-9]. A comprehensive introduction to GA and its relation to traditional optimization methods can be found in [10].

In [11], the FF pattern of a printed circuit board (PCB) modem is determined based on the amplitude of the NF data, only. In 2007, Fan demonstrated the capability of GA in estimating the FF pattern by the NF-FF method [6]. He has also applied this combination to a grounded microstrip trace [3], using the uniqueness theorem.

In this paper, it is shown that the convergence rate can be increased by eliminating the need for applying the uniqueness theorem. Consequently, the CPU time is decreased while the accuracy is preserved in an acceptable level. To do this, radiation fields of the trace in NF radiation region are sampled. Then, employing only the magnitude data, parameters of ideal electric and magnetic dipoles are optimized by GA. Finally, the FF pattern is estimated based on analytic expressions of dipoles' EM fields.

II. SETTING UP THE OPTIMIZATION

A. Hybrid-coding

GA is used to optimally produce the parameters of N ideal dipoles for reconstructing the NF data at M observation points. Each individual includes N infinitesimal ideal dipole. The qth dipole, D_q, has the following parameters [2, 4, 7, 12, 13]:

- Dipole type: K_q, which is zero for magnetic and one for electric type, and thus, is a binary parameter.
- Dipole position: (x_q, y_q, z_q).

Submitted On: Nov. 7, 2012
Accepted On: Mar. 16, 2013

- Dipole complex moment: $m_q.e^{j\beta q}$, where m_q and β are real dipole moment and initial phase, respectively.
- Dipole direction: (θ_q, φ_q).

Therefore, each individual $S_K = \{D_q\}^N{}_{q=1}$, includes N dipoles, and each dipole D_q has a binary gen and seven real-coded gens, i.e.,

$$D_q = \{K_q,\ m_q,\ \beta_q, x_q, y_q, z_q, \theta_q, \varphi_q\}. \quad (1)$$

To simplify the software implementation and increase the convergence rate, the binary parameter can be eliminated by considering half of the dipoles to be magnetic and the rest being electric; leading to seven gens for each dipole. For more than two dipoles this simplifying assumption considerably decreases the computational cost.

As in [3], a 210 mm × 2.5 mm × 0.017 mm grounded microstrip is studied in this work, which is depicted in Fig. 1. The conductivity and relative permittivity of the substrate medium are σ = 0.0046 S/m and ε_r = 4.7, respectively. The structure is located above an infinite ground plane. Following [3] and for the purpose of comparison, the applied voltage to one end of the strip is 1.78 V, while the other end is terminated to a 22 pF capacitor.

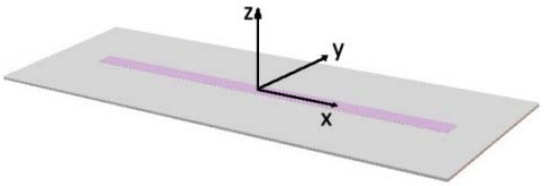

Fig. 1. Microstrip layout.

The variation ranges of gens are given by,

$$\begin{cases} -135\ mm \le x \le 135\ mm \\ -30\ mm \le y \le 30\ mm \\ 0\ mm \le z \le 5\ mm \\ 0 \le \theta_q \le \dfrac{\pi}{2} \\ 0 \le \varphi_q, \beta_q \le 2\pi \\ K_q = 0, 1 \end{cases} . \quad (2)$$

B. Fitness function

The fitness function of each individual, which is minimized by the GA is defined as,

$$T_m^{NF}(S_k) = \frac{20}{M}\sum_{m=1}^{M}\left|\log E_m^{NF} - \log f_{m,k}^{NF}\right|, \quad (3)$$

where $f_{m,k}^{NF}$ is the NF intensity of k^{th} individual at m^{th} observation point and E_m^{NF} is the magnitude of the corresponding NF. These field values can be calculated by analytical relations and proper coordinate transformations[14-15]. The unknown parameters are determined by running the optimization process until the averaged value of the fitness function over all points becomes less than 1.5 dB. It is worth mentioning that such a criteria is selected based on the most recognized electromagnetic compatibility (EMC) standards, e.g., CISPR 16 [16].

Since the fitness function does not include the phase information, it is not possible to make use of the uniqueness theorem. Therefore, there will be no unique dipole arrangements. Such a definition, also, leads to a smooth optimization space with less local minima compared to what introduced in [3]. Consequently, the convergence rate increased.

C. Estimating the FF pattern

Whenever unknown parameters of equivalent dipoles are determined, the FF pattern of the grounded microstrip can be simply estimated based on well-known analytical expressions [14]. The tolerance can be estimated by [3]

$$T^{FF}(S_k) = \frac{20}{M}\sum_{m=1}^{M}\left|\log E_m^{FF} - \log f_{m,k}^{FF}\right|, \quad (4)$$

in which E_m^{FF}'s are the FF simulated data, and $f_{m,k}^{FF}$'s are data predicted from FF pattern. In this study, simulated data are generated by Ansoft HFSS. T^{FF}'s are the tolerances between the simulated and predicted data. Lower values ofT^{FF} means better predictions.

III. CALCULATING EM FIELDS OF THE STRUCTURE

The EM fields of the structure can be computed by the infinite ground assumption and direct application of the image theorem [3]. This simplification is valid because the ground size is considerably greater than the microstrip transmission line. The parameters corresponding to the image of the q^{th} dipole is given in Table 1. As before, EM fields of ideal dipoles and their images are calculated based on an analytical expressions [14].

The input impedance of the structure is depicted in Fig. 2, which shows two pseudo-resonant frequencies in the range of 30 MHz to 1000 MHz. Ensuring proper matching condition, f_1 = 100

MHz, f_2 = 300 MHz, and f_3 = 700 MHz are selected as test frequencies.

Table 1: Parameters of diploes' images.

Main dipole	Image dipole	
K_q	1	0
$m_q e^{j\beta_q}$	$m_q e^{j\beta_q}$	$m_q e^{j\beta_q}$
(x_q, y_q, z_q)	$(x_q, y_q, -z_q)$	$(x_q, y_q, -z_q)$
θ_q	θ_q	$\pi - \theta_q$
φ_q	$\varphi_q + \pi$	φ_q

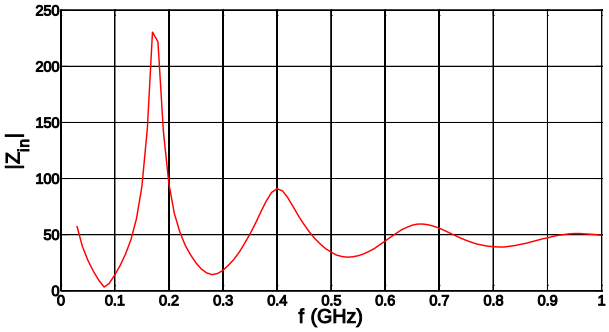

Fig. 2. Input impedance of the grounded microstrip.

The number of ideal dipoles is an important factor in estimating of the FF pattern and depends on the ratio of the largest antenna dimension (D) to the operating wavelength (λ) [3, 5]. In this study, D = 254 mm. Thus, at f_1, the condition of $D << \lambda$ is satisfied and the PCB can be properly approximated by an ideal dipole. In this case, N = 2 leads to acceptable result. However, at f_2 and f_3, the PCB has a moderate size, $\lambda/10 \leq D < \lambda$. In these cases, it is observed that N = 8 is a suitable choice. It should be noted that this method, is practical when $D < \lambda$. Furthermore, it is observed that the speed of the optimization process can be considerably increased by assuming equal number of electric and magnetic dipoles. For the problem at hand, this can be achieved by dividing PCB into four equal sections and considering two dipole, one electric and one magnetic, in each section.

IV. NF SAMPLING

For extracting amplitude and phase information of NF two planes are employed, which are positioned at $z_1 = \pm$ 200 mm and $z_2 = \pm$ 300 mm. These planes with their images are depicted in Fig. 3. It can be easily verified that at f_1, both of z_1 and z_2 are placed in the NF reactive range. At the second test frequency, z_1 and z_2 are located in reactive and radiation regions, respectively. Finally, at f_3, both planes are placed in the radiation NF. Based on [17], the dimension of each plane is selected to be 774 mm × 774 mm.

It should be noted that, the number of observation points depends on the number of dipoles and the number of dipoles depends on the electrical size of PCB. Thus, as mentioned earlier, when $D < \lambda/10$, it is sufficient to use two dipoles, which corresponds to 14 unknowns. When $\lambda/10 \leq D < \lambda$, employing eight diploes suffice, which leads to 56 unknowns. In addition, for properly handling of the optimization process, the number of observation points is selected to be more than twice the number of unknowns.

V. COMPARISON OF SIMULATED DATA WITH GA ESTIMATION

NF data on observation planes, computed by Ansoft HFSS, are used as reference values. These data are compared to NF data of the optimized equivalent dipoles. Figure 4 shows the NF data of the main source and those of the equivalent dipole at f_1. The NF and FF tolerances for this case at f_1 are 0.8 dB and 0.81 dB, respectively. It should be noted that in the most EMC standards, the limit for this tolerance is ±1.5 dB [16].

Figure 5 shows the radiation pattern of the original sources and the equivalent dipoles in 3 m range at f_1. At f_2, four dipoles are used. In this case, NF and FF tolerances are 0.45 dB and 1.04 dB, respectively. Reducing the number of dipoles from 8 to 4; halves the number of unknowns and consequently, multiplies the speed of the optimization process. Figures 6 and 7 show the FF radiation pattern of the original sources and the equivalent dipoles in 3 m range at f_2 and f_3, respectively. Table 2 presents T^{NF} and T^{FF} for test frequencies and parameters of equivalent dipoles are reported in Table 3.

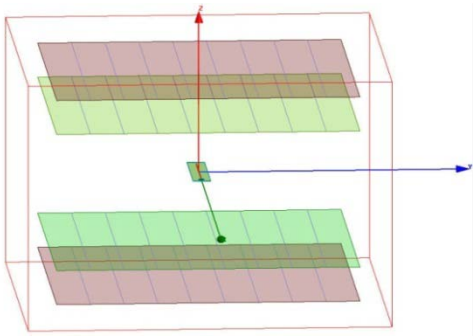

Fig. 3. HFSS simulation setup.

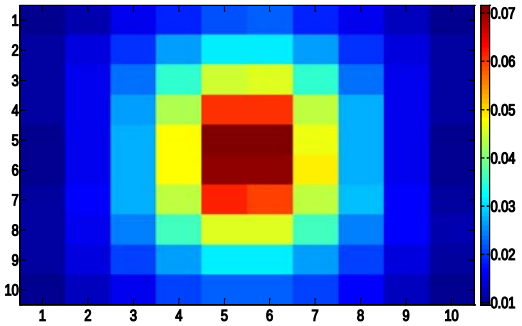

(a) Reference data at z_1.

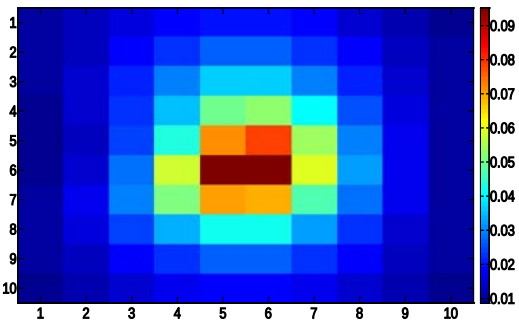

(b) GA data at z_1.

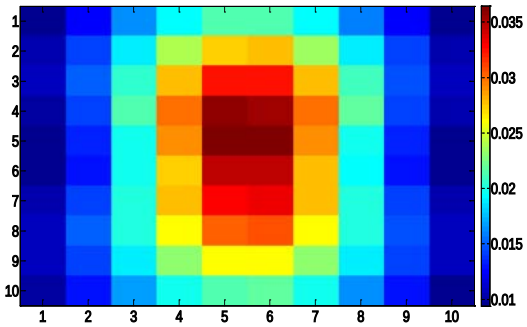

(c) Reference data at z_2.

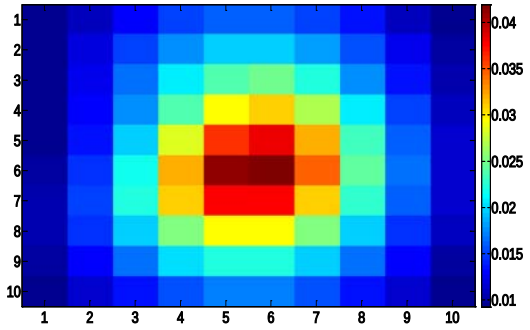

(d) GA data at z_2.

Fig. 4. Magnitude of the NF on the observation planes at f_1 with $N = 2$ and $T^{NF} = 0.8$ dB.

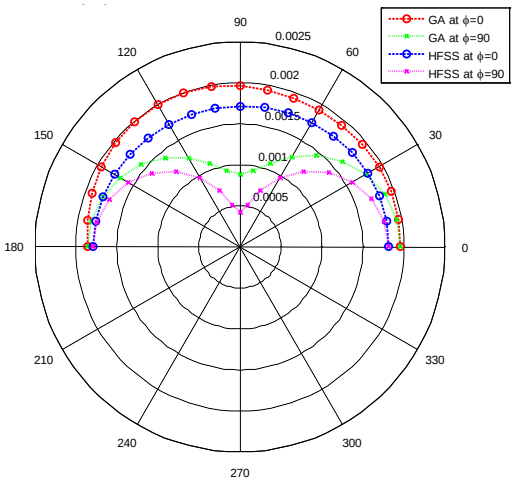

Fig. 5. FF radiation pattern at $f = 100$ MHz, $\varphi = 0^o$, 90^o with $N = 2$ and $T^{FF} = 0.81$ dB.

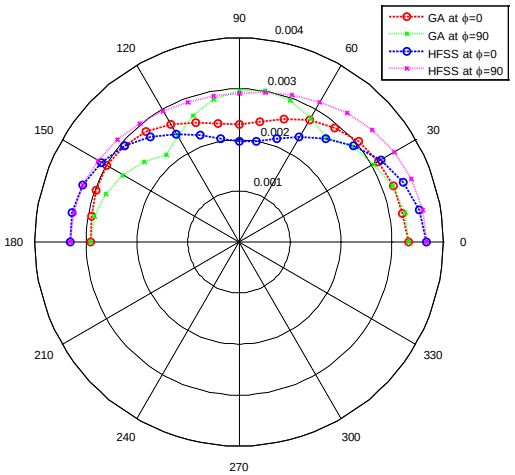

Fig. 6. FF radiation pattern at $f = 300$ MHz, $\varphi = 0^o$, 90^o with $N = 4$ and $T^{FF} = 1.04$ dB.

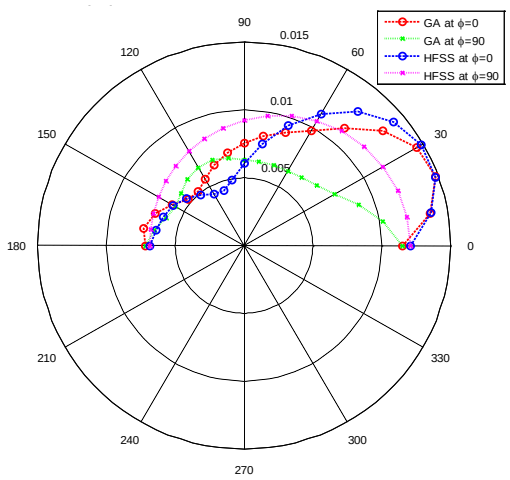

Fig. 7. FF radiation pattern at f =700 MHz, $\varphi = 0^o$, 90^o with $N = 8$ and T^{FF} =1 dB.

Table 2: NF and FF tolerances.

Frequency	N	T^{NF} (dB)	T^{FF} (dB)
f_1	2	0.79	0.81
f_2	4	0.45	1.04
f_3	8	0.45	1

Finally, Table 4 compares the results of the present work with those of [3], which properly validate the proposed method.

Table 3: Parameters of the ideal dipoles in GA model.

N	Frequency	K	m	β (rad)	x (m)	y (m)	z (m)	θ (rad)	φ (rad)
2	f_1	1	7.7×10^{-6}(m. A)	0.19	0.031	-0.02	0.004	0.014	1.96
		0	2.19×10^{-5}(m^2. A)	0.57	0.005	-0.002	0.0015	1.57	0.7
4	f_2	1	1×10^{-6}(m. A)	0.86	-0.134	-0.03	0.003	0.63	1.71
		0	3.1×10^{-7}(m^2. A)	0.9	-0.109	-0.012	0.004	1.64	1.47
		1	9.95×10^{-6}(m. A)	0.92	0.028	0.03	0.005	2.77	0.187
		0	5×10^{-6}(m^2. A)	0.42	0.05	-0.001	0.004	0.85	0.015
8	f_3	1	1.49×10^{-5}(m. A)	1.41	-0.11	0.018	0.0029	0.045	2.87
		0	5.4×10^{-7}(m^2. A)	0.68	-0.12	0.023	0.004	1.93	1.099
		1	1.2×10^{-5}(m. A)	1.74	-0.018	0.0005	0.0003	0.019	0.213
		0	1.17×10^{-6}(m^2. A)	0.629	-0.066	0.018	0.0014	0.466	0.199
		1	1.8×10^{-5}(m. A)	0.63	0.05	0.027	0.0028	1.6	0.04
		0	1.5×10^{-7}(m^2. A)	0.614	0.033	-0.03	0.0026	1.62	0.004
		1	1.3×10^{-5}(m. A)	1.22	0.092	0.002	0.005	0.031	0.005

Table 4: Comparison of the proposed method with [3].

f (MHz)	N	T^{NF} (dB)	T^{FF} (dB)
100	2	0.79	0.81
300	4	0.45	1.04
700	8	0.45	1
300	8	0.11	0.12
600	8	0.34	0.48
900	8	0.77	0.80

VI. INFLUENCE OF NUMBER OF DIPOLES ON CONVERGENCE RATE

The effect of number of dipoles, on CPU time and tolerance, is studied by considering the microstrip PCB at f_1. Figure 8 shows the required CPU time. Clearly, doubling of the N leads to considerable increase in the CPU time. Table 5 shows the influence of N on the simulation time and NF/FF tolerances. In all cases, number of generation is 400. Simulations are carried out on an Intel Core™2 Duo processor with CPU 2.8 GHz and 4 GB RAM.

Table 5: Influence of *N* on the convergence rate.

Frequency (MHz)	No. of dipoles	T^{NF} (dB)	T^{FF} (dB)	Number of points	Time to equivalent dipoles (min)	Number of generations	Initial population
100	2	0.79	0.81	66	7	400	62
100	4	0.39	1.39	66	25	400	102
100	6	0.43	1.23	100	55	400	102
100	8	0.41	1.3	100	70	400	102
100	10	0.41	1.5	200	180	400	132

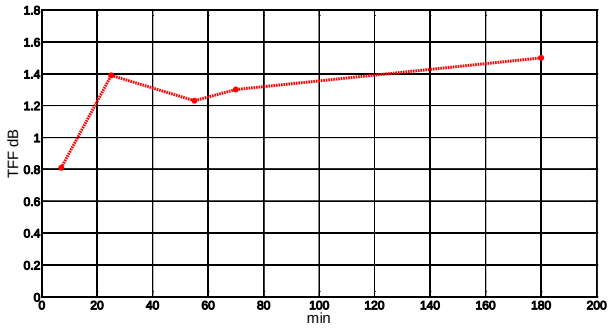

Fig. 8. Influence of *N* on the CPU time.

VII. CONCLUSION

A new combination of NF-FF transformation and GA is proposed for efficient FF pattern estimation of a grounded microstrip PCB. The method is independent of the uniqueness theorem and is just based on the magnitude information of the observation points, which has led to substantial decrease in the simulation time.

Acknowledgement

The authors would like to thank Amirkabir University of Technology and ITRC for supporting this work.

REFRENCES

[1] V. P. Kodali, *Engineering Electromagnetic Compatibility*, IEEE press, 2001.

[2] H. Fan and F. Schlagenhaufer, "Source identification and correlation between near field-far field tolerances when applying a genetic algorithm," *EMC Europe Int. Symp. EMC*, Hamburg, pp. 587-592, Sept. 2008.

[3] H. Fan, "Using radiating near field region to sample radiation of microstrip traces for far field prediction by genetic algorithms, "*IEEE Microwave And Wireless Components Letters*, vol. 19, no. 5, May 2009.

[4] H. Fan and F. Schlagenhaufer, "Near field far field transformation for loops based on genetic algorithm," *Proc. 4th Asia-Pacific Conf. Environ. Electromag*, Dalian, China, pp. 476-481, Aug. 2006.

[5] H. Fan and F. Schlagenhaufer, "Near field far field conversion based on genetic algorithm for predicting radiation from PCBs," Proc. *IEEE Int. Symp. Electromag. Compat.*, Honolulu, HI, pp. 1-6, July 2007.

[6] H. Fan and F. Schlagenhaufer, "Improvements of robustness of genetic algorithm for neafield -far field radiation conversion," *Proc. IEEE Int. Symp. Microw., Antenna, Propag. EMC Technol. Wireless Commun.*, Hangzhou, China, pp. 950-953, Aug. 2007.

[7] H. Fan and F. Schlagenhaufer, "Investigation of near field data sampling approaches for far field radiation prediction of PCBs by genetic algorithm," *Proc. 18th Int. Zurich Symp. Electromag. Compat.*, Munich, Germany, pp. 21-24, Sep. 2007.

[8] D. E. Goldberg, *Genetic Algorithms in Search, Optimization & Machine Learning. Reading*, MA: Addison-Wesley, 1989.

[9] Z. Michalewicz, *Genetic Algorithm Data Structures, Evolution Programs*, Berlin, Germany: Springer-Verlag, 1992.

[10] J. M. Johnson and Y. Rahmat-Samii, "Genetic algorithms in engineering electromagnetics," *IEEE Antennas and Propagation Magazine*, vol. 39, no. 4, August 1997.

[11] O. M. Bucci, G. D'Elia, G. Leone, and R. Pierri, "Far-field pattern determination from the near-field amplitude on two surfaces," *IEEE Transaction on Antennas and Propagation*, vol. 38, no. 1, Nov. 1990.

[12] H. Fan and F. Schlagenhaufer, "Source identification from near field measurements of loops using genetic algorithm," *5th Australian Symp. EMC*, Melbourne, pp. 35-42, Sept. 2006..

[13] H. Fan and F. Schlagenhaufer, "Number of infinitesimal dipoles in genetic algorithms for near field-far field conversion," *1st Asia-Pacific Symp. EMC*, Singapore, pp. 690-693 May 2008.

[14] C. A. Balanis, *Antenna Theory: Analysis and Design*, Hoboken, J. Wiley, 2005.

[15] Y. Rahmat-Samii, "Useful coordinate transformations for antenna applications," *IEEE Trans. Antennas And Propagation*, vol. 27, no. 4, July 1979.

[16] T. Williams, *EMC for Product designers*, Elsevier Ltd, 2007.

[17] H. Fan, "Correlation Between Near field and Far Field Radiated Emission of Printed Circuit Boards by Genetic Algorithms," *Ph.D. dissertation, Dept. Elect. Eng., Western Univ.*, Crawley, WA 6009, Australia, 2009.

Reza Rajabzadeh was born in Rasht, Guilan, Iran in 1985. He received his M.Sc. degree in Electrical Engineering from Tehran Polytechnic University, Tehran, Iran in 2012. His main research interests are numerical Electromagnetics, antennas, active microwave circuits and microwave measurements. Currently he is lecturer in Guilan University, Guilan, Rasht, Iran.

GholamrezaMoradi was born in Shahriar, Iran in 1966. He received his PhD degree in Electrical Engineering from Tehran Polytechnic University, Tehran, Iran in 2002. His main research interests are numerical Electromagnetics, antennas, active microwave circuits, mm-wave circuits and systems and microwave measurements. In 2003, he was selected as the exemplary researcher of Iranian Ministry of Road and Transportation. He has published several papers in the refereed journals and the local and international conferences. Also, he has co-authored six books entitled Communication Transmission Lines, Microwave Engineering, Engineering Mathematics, Engineering Probability and Statistics, Analysis of Signals and Systems, and Active Transmission Lines (in Persian). The latter was selected as the book of the year of Iran in 2008. He is currently an associate Professor with Electrical Engineering Department at Amirkabir University of Technology (Tehran Polytechnic), Tehran, Iran.

Through Wall Gap Detection Using Monostatic Radar

A. Elboushi[1], A. R. Sebak[1,2], and T. Denidni[3]

[1] Electrical and Computer Engineering Department,
Concordia University 1455 de Maisonneuve West, EV005.127, Montreal, Quebec H3G 1M8, Canada
ay_moh@encs.concordia.ca

[2] KACST Technology Innovation Center in RFTONICS, KSU, Riyadh 11421, Kingdom of Saudi Arabia

[3] INRS Place Bonaventure, 900 De la Gauchetière Ouest, Niveau C, Montréal, Quebec H5A 1C6, Canada
denidni@emt.inrs.ca

Abstract ─ In this paper, a new experimental system for through wall gap detection and concealed vacancies behind wall is introduced. The ultra wide band (UWB) system is based on the principles of time domain reflectometry (TDR) and ground-penetrating radar (GPR) for through wall imaging to detect hidden gaps and/or hiding persons behind walls. The system uses a very short pulse generated by the vector network analyzer (VNA) to illuminate the wall under investigation through an UWB antenna probe. The detection process is achieved using time domain measurements of the probe reflection coefficient S_{11}. Some numerical analyses have been carried out for verifying the principle of operation. The experimental results show a great ability not only for the gap detection between walls but also for estimation of the gap width with a very good accuracy (6.25 % in the worst case) for different types of walls.

Index Terms ─ GPR, monostatic radar, TDR, tunnels detection, time domain measurements, UWB antenna, and UWB pulse.

I. INTRODUCTION

Recently, many research efforts have been exerted for developing modern microwave imaging systems to work in home land security and other applications. UWB technology has been used for some time in ground penetrating radar (GPR) applications [1-3] and early breast cancer detection [4-6]. Recently, as a new trend, it is used in through wall imaging applications to help police to detect the existence of any hidden rooms or hidden people behind walls [7-9]. Many numerical analysis techniques have been employed for through wall imaging including geometrical optics (GO), ray tracing [10-11], and 2D method of moments (MoM) [12].

In this paper, a time domain reflectometry (TDR) UWB through wall gap detection system based on the operation principle of the UWB imaging system proposed by Chang et al [13] is presented. It is based on sending a short duration pulse that is synthesized by transmitting continuous wave (CW) signals at equidistant frequencies covering the entire UWB range from 3.1 GHz to 10.6 GHz. The signal is produced by a vector network analyzer (VNA) after proper calibration over the pre-stated frequency range. The time domain representation of the pulse can be obtained by performing inverse fast Fourier transform (IFFT) on both transmitted and received signals. The principle is used in [13] for building a complete UWB imaging system for breast cancer detection. Multiple numerical simulations have been carried out using a finite integration technique (FIT) simulator, CSTMWS [14], to address the possible multiple reflections due to the wall construction. These simulations are used to ensure the negligible effect of the higher order reflection on the gap detection accuracy.

The proposed UWB imaging system has an advantage over some of the available systems since it adopts the monostatic radar principle, i.e., it uses just one antenna for both transmission and reception. The UWB sensor is also another critical

Submitted On: Oct. 2, 2012
Accepted On: Mar. 17, 2013

design parameter regarding the cost, weight, and size. In the proposed system the heavy metallic UWB horn sensor is replaced by a low profile UWB microstrip antenna to maintain a high accuracy detection level.

II. THE PROPOSED THROUGH WALL GAP DETECTION SYSTEM

The proposed UWB imaging system for through wall gap detection is shown in Fig. 1. The system includes a fixed support to mount an UWB probe antenna. The probe antenna is connected to channel (1) of the VNA. An absorber is mounted vertically behind the antenna to prevent any undesired back reflections. The antenna is centered to face the first wall in the y-z plane, whereas the separation distance between the antenna and the first wall should be chosen carefully to ensure working in the far-field region of the antenna. Undesired reflections in UWB imaging systems considered as a great obstacle. To overcome this problem we focus on a prototype, which images the target using a synthesized pulse realized by sending continuous signals at equidistant frequencies over the required microwave band [13]. In order to check the imaging system capabilities for detecting hidden gaps behind walls, we made some practical tests using the setup shown in Fig. 1. The proper choice of the UWB antenna sensor is very critical issue for the system. In [15] three different UWB antenna prototypes were presented and maybe used as antenna probes covering the frequency band from 3 GHz to 10 GHz. The first prototype, shown in Fig. 2, consists of an elliptical aperture etched out from the ground plane of a PCB and a microstrip line with half circular shaped ring stub for excitation, which is chosen to work as an antenna probe in this system to satisfy the impedance bandwidth of the UWB range, as shown in Fig. 3, it relatively has a constant gain and stable radiation patterns over the UWB frequency range. The optimized antenna parameters in [15] are chosen according to multiple parametrical studies and optimizations carried out using CSTMWS. The final design antenna parameters are shown in Table 1.

Two different wall materials were studied. The first type with thickness equal 3 cm, length equals to 22 cm, and width equal to 30 cm is made of a reinforced papers with a lower attenuation coefficient (0.26 dB/cm) than the second one. The second material (5.5 cm thickness, 23 cm length, and 15 cm width) is made of sandy brick and has a very high attenuation coefficient (3.6 dB/cm). Figures 4 and 5 show different reflections from two walls separated by an air gap and from a solid wall, respectively. As shown in Fig. 3, we expect four reflection coefficients (Γ_1, ….., Γ_4) in case of having a gap between the two walls.

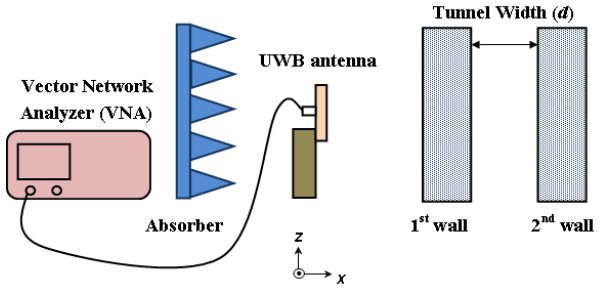

Fig. 1. The proposed UWB imaging system for through wall gap detection.

Table 1: Optimized dimensions for the UWB antenna (in mm) [15].

Parameter	Value
W	45
L	45
W_1	3
L_1	12.4
S	1.4
R_1	4.5
R_2	11
A	9.6
B	19

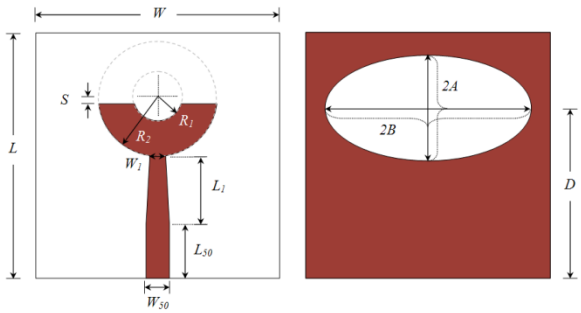

(a) (b)

Fig. 2. Geometry of the UWB antenna [15] (a) front view and (b) back view.

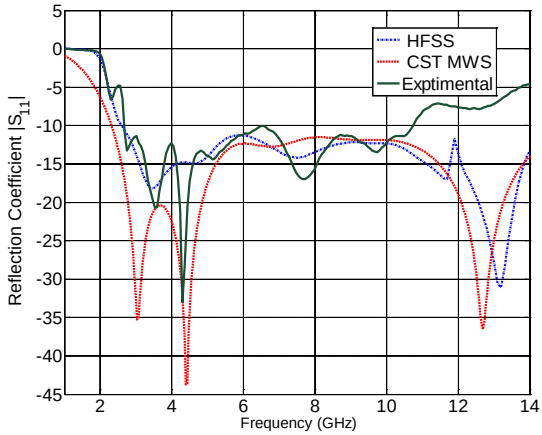

Fig. 3. Simulated and experimental return loss S_{11} of the UWB antenna [15].

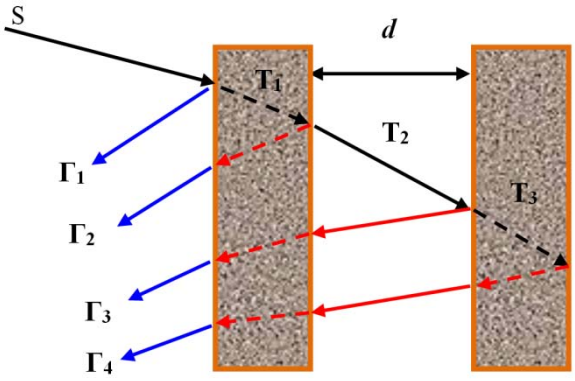

Fig. 4. Reflections from the 1st and the 2nd wall with a gap in between.

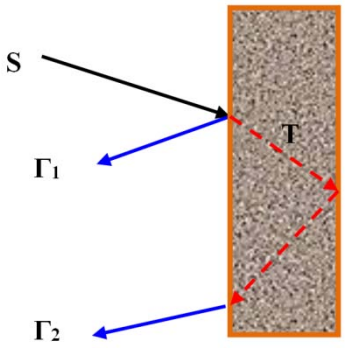

Fig. 5. Reflections from a solid wall without gaps.

The gap detection algorism begins by reading the reflection coefficient (S_{11}) from the VNA to obtain a frequency domain representation for the wall(s) reflections *G(f)*. Using inverse fast Fourier transform (IFFT) embedded code in the VNA, a time domain representation of the reflection can be obtained *g(t)*. In order to cancel the antenna, cables and connectors effect, the received reflections *g(t)* are subtracted from the antenna response in front of an absorber *a(t)*. The resulted signal *s(t)* contains only the reflection information from the wall(s) under study. By monitoring the peaks and their locations, the detection algorism will provide enough information to make a decision in regard to the structure with either a solid wall or two walls separated by a gap (*d*). The gap 'tunnel' width (*d*) separating the two walls can be evaluated using the separation time (*t*) between the second reflection $\boldsymbol{\Gamma_2}$ and the third reflection $\boldsymbol{\Gamma_3}$ from the following equation,

$$d = (t * c)/2 \qquad (1)$$

where *c* is the speed of light in free space. The flow chart of the gap detection algorism is shown in Fig. 6.

III. NUMERICAL INVESTIGATION OF THROUGH WALL GAP DETECTION USING CSTMWS

In order to verify the proposed system performance and study the possible sources of errors, especially from higher order reflections, some numerical simulations have been carried out using CSTMWS [14] simulator. Two different cases have been investigated to determine the expected time domain reflections. The first one is the single wall, while the second is two walls separated by an air gap (*d*). An UWB plane wave Gaussian pulse (3 GHz to 10 GHz), shown in Fig. 7, is used as a source of an incident wave, while the reflected back signals are monitored on the surface of the first wall. Two different scenarios for the internal construction of the walls under study are assumed. The first is for a lossless case with zero conductivity as an extreme case with no attenuation. While the other one assumes an actual sandy brick walls with finite conductivity (ε_r = 5.84 and the conductivity δ = 89 mS/m).

Figure 8 shows a comparison between the time domain reflection from the single wall and the reflections of the two walls separated by an air gap of 5 cm assuming the worst case of lossless walls with zero conductivity. It can be concluded that the first and second reflections for both cases are coincident with each other. However, the multiple

reflections (i.e., higher order reflections inside the single wall) are responsible for the lower amplitude reflections around 2.3 ns (solid red curve). The amplitudes of these reflections are much smaller compared with Γ_3. Figure 9 shows the reflections according to the second scenario of using sandy bricks walls. The effect of the higher order reflections decreased dramatically so that it cannot interfere with Γ_3. In the case of the two walls reflections, the air gap separation (d) is responsible for the time difference between Γ_2 and Γ_3. Some parametrical studies for different values of (d), shown in Fig. 10, illustrate that effect.

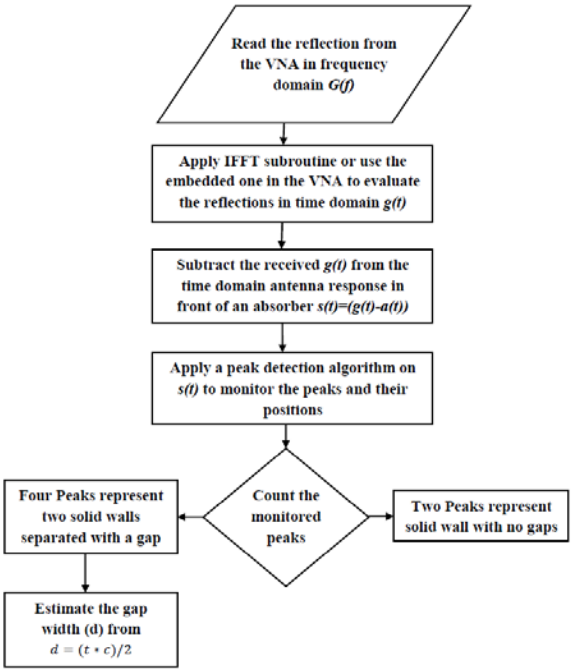

Fig. 6. Gap detection algorithm.

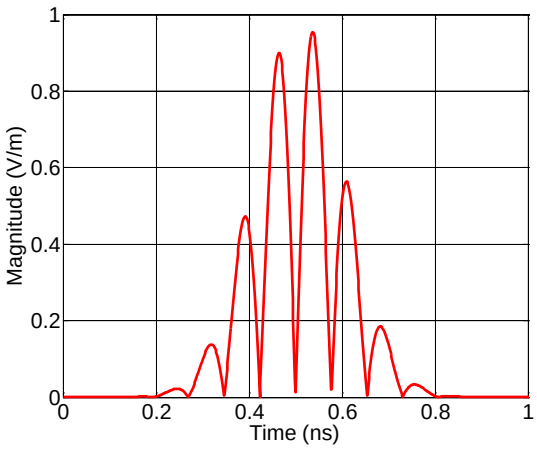

Fig. 7. UWB plane wave pulse used by CSTMWS.

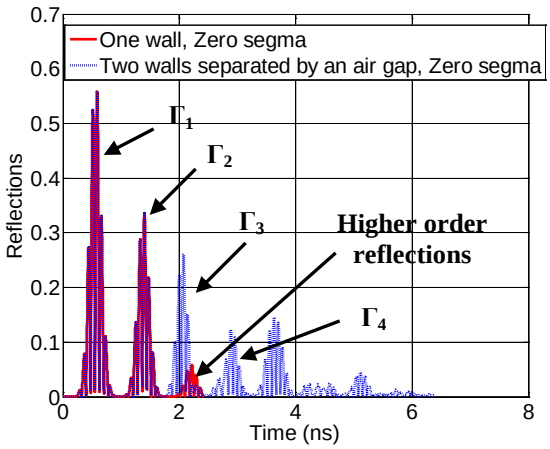

Fig. 8. Time domain reflection comparison using no attenuation walls.

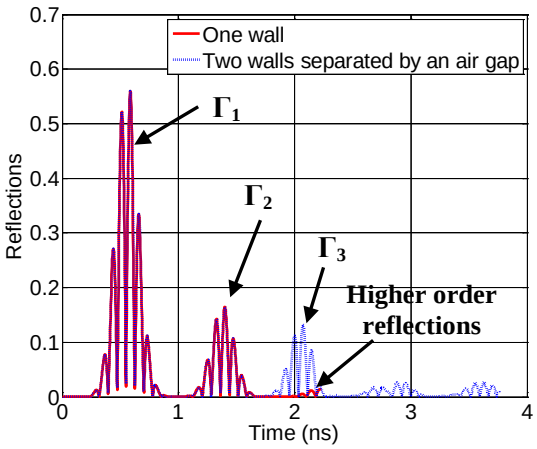

Fig. 9. Time domain reflection comparison using sandy bricks walls.

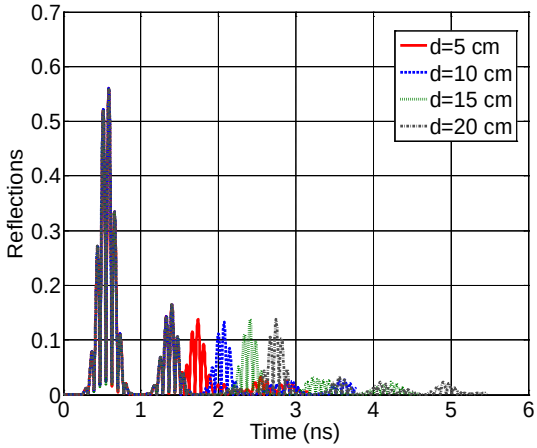

Fig. 10. Time domain reflections of two walls for different values of the air gap separation (d).

A. 1D Time domain results using one wall

After constructing the system shown in Fig. 1 and calibrating the VNA using standard calibration procedure in the frequency range of 3 GHz to 10 GHz, we measure the reflection coefficient in the frequency domain and then using the time domain conversion tool embedded in the VNA, we convert the response into time domain. Figure 11 shows the antenna response in front of an absorber and without any walls, where we can notice two large reflection peaks and some small reflections at a later time. The first peak accounts for the reflection from the interface between the microstrip feed line and the antenna, while the second peak results from reflection of the electromagnetic wave radiated by the antenna into free space. The minor reflections at later time can be accounted to multipath effects and scattering waves from the surrounding objects. Figure 12 shows a comparison between the time domain antenna response in front of an absorber and the esponse in front of a single low attenuation wall, 19 cm apart, where two huge peaks appeared as a result of the air/wall reflection (Γ_1) and wall/air reflection (Γ_2). Figure 13 (a) and 13 (b) shows a photo for the measurement setup.

B. 1D Time domain results using two walls of low attenuation coefficient with a gap between them

Figure 14 (a) to 14 (e) shows the multiple reflections due to two walls separated by a distance *d*. Table 2 shows a comparison between the actual gap dimensions and the calculated ones using equation (1). There is a good agreement between the actual and the calculated separation *d*, where the percentage error does not exceed 6.25 % for the considered cases. The error pattern here does not follow a certain pattern because of errors in antenna location adjustment, minor errors in the actual distance measurements and some errors due to multipath effect from the surrounding objects.

C. 1D Time domain results using two walls of high attenuation coefficient with a gap between them

The nature of the wall material has a great effect on the reflected back signals from the walls, for example, using a high attenuation walls (sandy bricks) will results in much lower reflection levels (Γ_2, Γ_3, Γ_4) after the first reflection. Time domain representation is shown in Fig. 15 for the reflections occur from a solid wall in front of the transreceiving antenna. The distance from the antenna probe to the first wall is reduced to 10 cm for reducing the round trip path loss. Two major peaks can be noticed; the first one is due to the air/wall reflection and the second is due to the wall/air reflection whose magnitude is very low (less than -60 dB) mainly due to the wave high attenuation inside the wall. Figure 16 illustrates the effect of 5.5 cm gap between the two walls, where just three reflections (Γ_1, Γ_2, Γ_3) can be detected while the forth one (Γ_4) cannot be detected because of the interference with the noise floor due to its small value. The calculated distance between the two walls is 5.25 cm, which is compared to the actual distance (5.5 cm) with a percentage error of 4.54 %.

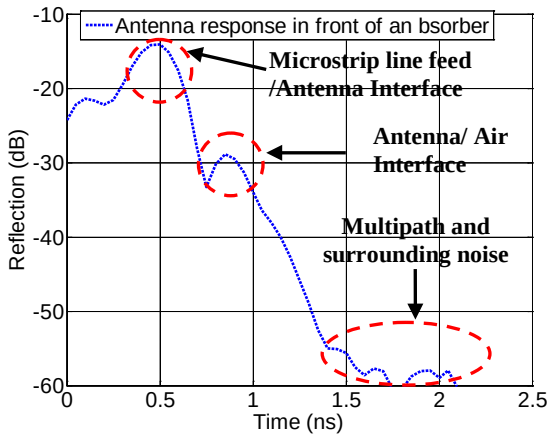

Fig. 11. Antenna response in front of an absorber.

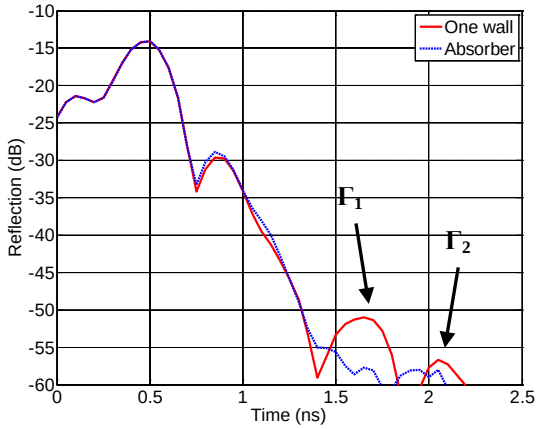

Fig. 12. Reflections from a solid low attenuation wall without gaps.

Table 2: Comparison between the actual and the calculated gap length between walls.

Actual Distance between two walls	Calculated Distance between two walls	Error %
7 cm	6.75 cm	3.5 %
8 cm	7.5 cm	6.25 %
10 cm	9.75 cm	2.5 %
12 cm	11.25 cm	6.25 %
15 cm	15 cm	0 %

(a)

(b)

Fig. 13. Practical measurement arrangements (a) solid sandy brick wall and (b) two walls separated by a distance *d*.

IV. CONCLUSION

In this work, an accurate and easy to built UWB through wall gap detection system based on TDR approach is presented. Some numerical and practical UWB imaging experiments have been carried out for gap detection between walls made of different materials using time domain measurements. The proposed system shows a remarkable performance in both gap detection and gap width determination with a very high precision with an error percentage not more than 6.25 % in the worst case.

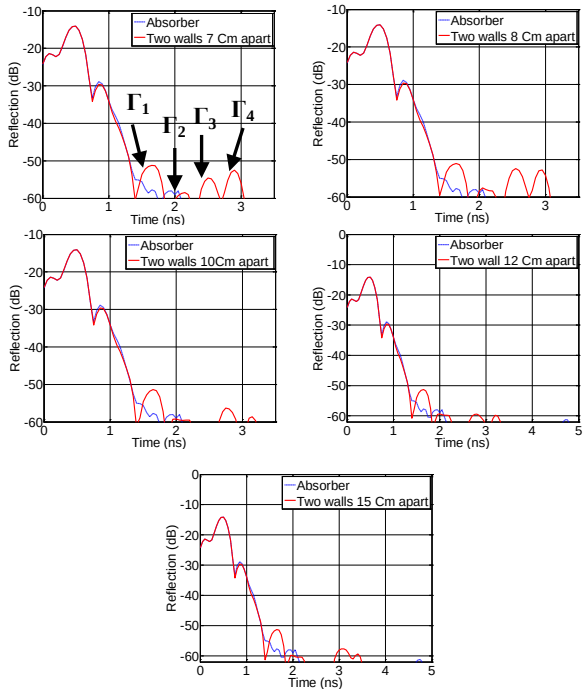

Fig. 14. Reflections from two low attenuation walls separated by an air gap (*d*).

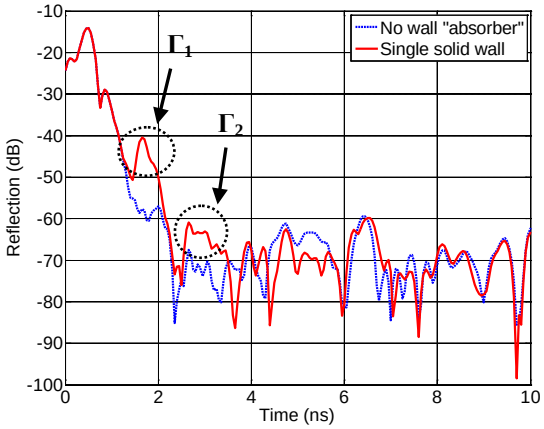

Fig. 15. Reflections from a solid single high attenuation wall without gaps.

ACKNOWLEDGMENT

This work is partly funded by the Canadian NSERC Discovery Program. And by a grant from King Abdulaziz City of Science and Technology (KACST)-Technology Innovation Center in RFTONICS at King Saud University.

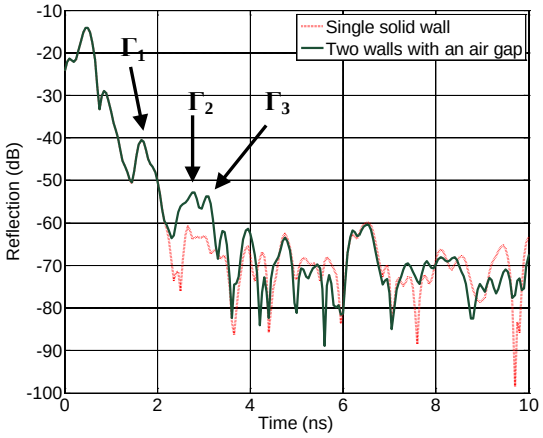

Fig. 16. Reflections from two high attenuation walls separated by an air gap of 5.5 cm.

REFERENCES

[1] A. B. Suksmono, E. Bharata, A. A. Lestari, A. G. Yarovoy, and L. P. Ligthart, "Compressive stepped-frequency continuous-wave ground-penetrating radar," *IEEE Geoscience and Remote Sensing Letters*, vol. 7, no. 4, pp. 665-669, Oct. 2010.

[2] C. -L. Huang, S. –P. Zhu, and M. Lu, "Miniature multimode deep ground penetrating radar," *13th International Conference on Ground Penetrating Radar (GPR)*, pp. 1-5, 21-25 June 2010.

[3] Y. Sun and J. Li, "Time-frequency analysis for plastic landmine detection via forward-looking ground penetrating radar," *IEE Proceedings on Radar, Sonar, and Navigation*, vol. 150, no. 4, pp. 253-261, Aug. 2003.

[4] Y. Zhou, "Microwave imaging based on wideband range profiles," *Progress In Electromagnetics Research Letters*, vol. 19, pp. 57-65, 2010.

[5] R. C. Conceição, M. O'Halloran, M. Glavin, and E. Jones, "Comparison of planar and circular antenna configurations for breast cancer detection using microwave imaging," *Progress In Electromagnetics Research*, vol. 99, pp. 1-20, 2009.

[6] S. A. AlShehri and S. Khatun, "UWB imaging for breast cancer detection using neural network," *Progress In Electromagnetics Research C*, vol. 7, pp. 79-93, 2009.

[7] F. Aryanfar and K. Sarabandi, "Through wall imaging at microwave frequencies using space-time focusing," *IEEE Antennas and Propagation Society International Symposium*, vol. 3, pp. 3063-3066, 20-25 June 2004.

[8] K. M. Yemelyanov, N. Engheta, A. Hoorfar, and J. A. McVay, "Adaptive polarization contrast techniques for through-wall microwave imaging applications," *IEEE Transactions on Geoscience and Remote Sensing*, vol. 47, no. 5, pp. 1362-1374, May 2009.

[9] V. M. Lubecke, O. Boric-Lubecke, A. Host-Madson, and A. E. Fathy, "Through-the-wall radar life detection and monitoring," *IEEE Microwave Symposium*, pp. 769-772, June 2007.

[10] C. Thajudeen, W. Zhang, and A. Hoorfar, "Efficient forward modeling of large scale buildings and through-the-wall radar imaging scenarios," *28th Annual Review of Progress in Applied Computational Electromagnetics (ACES)*, Columbus, Ohio, pp. 122-126, April 2012.

[11] A. Buonanno, M. D'Urso, G. Prisco, M. Ascione, and A. Farina, "A model-based signal processor to see inside buildings," *26th Annual Review of Progress in Applied Computational Electromagnetics (ACES)*, Tampere, Finland, pp. 846-851, April 2010.

[12] A. Buonanno, M. D'Urso, G. Prisco, M. Ascione, and A. Farina, "A model-based signal processor to see inside buildings," *26th Annual Review of Progress in Applied Computational Electromagnetics (ACES)*, Tampere, Finland, pp. 846-851, April 2010.

[13] K. W. Chang, M. E. Bialkowski, and S. Crozier, "Microwave imaging using a planar scanning system with step-frequency synthesized pulse," *Asia-Pacific Conference Proceedings on Microwave*, APMC, vol. 1, pp. 4, 4-7 Dec. 2005.

[14] CST Microwave Studio, ver. 2012, Framingham, MA, 2012.

[15] A. Elboushi, O. M. H. Ahmed, A. R. Sebak, and T. A. Denidni, "Study of ellpitical slot UWB antennas with a 5.0-6.0 GHz band-notch capability," *Progress In Electromagnetics Research C*, vol. 16, pp. 207-222, 2010.

Ayman Elboushi was born in Zagazig, Egypt, in 1978. He received the B.Sc. degree in Electrical Engineering from Zagazig University, Zagazig, Egypt, in 2000, and M.Sc. degree in Electrical Engineering from Ain Shams University, Cairo, Egypt, in 2007. From 2001 till 2008, he worked as a researcher assistant in Electronics Research Institute (ERI), Microstrip Dept., Cairo, Egypt. In 2008, he joined the Microwave group of Department of Electrical and Computer Engineering, Concordia University, as a researcher assistant and he is now working towards his Ph.D. degree.

Abdel-Razik Sebak received the B.Sc. degree in Electrical Engineering from Cairo University in 1976 and the M. Eng. and Ph. D. degrees from the University of Manitoba in 1982 and 1984, respectively. From 1984 to 1986, he was with the Canadian Marconi Company. From 1987 to 2002, he was a Professor of Electrical and Computer Engineering, University of Manitoba. He is currently a Professor of Electrical and Computer Engineering, Concordia University. His current research interests include phased array antennas, computational electromagnetics (EM), integrated antennas, EM theory, interaction of EM waves with new materials, and bio-EM. Dr. Sebak received the 2000 and 1992 University of Manitoba Merit Award for outstanding Teaching and Research, the 1994 Rh Award for Outstanding Contributions to Scholarship and Research in the Applied Sciences category, and the 1996 Faculty of Engineering Superior Academic Performance. He has served as Chair for the IEEE Canada Awards and Recognition Committee (2002–2004).

Tayeb A. Denidni received the B.Sc. degree in Electronics Engineering from the University of Setif, Setif, Algeria, in 1986, and the M.Sc. and Ph.D. degrees in Electrical Engineering from Laval University, Quebec, Canada, in 1990 and 1994, respectively. From 1994 to 2000, he was a Professor with the Engineering Department, Universite du Quebec, Rimouski, Quebec, Canada. Since August 2000, he has been a Professor with Institut National de la Recherche Scientifique (INRS), Universite du Quebec, Montreal, Canada. He is leading a large research group consisting of two research scientists, five Ph.D. students, and three M.Sc. students. Over the past 10 years, he has graduated numerous graduate students. His current research interests include planar microstrip filters, dielectric resonator antennas, EM-bandgap antennas, antenna arrays, and microwave and RF design for wireless applications. He has authored over 110 papers in refereed journals. He has also authored or coauthored over 150 conference papers.

High Selectivity Dual-Band Bandpass Filter with Flexible Passband Frequencies and Bandwidths

Yalin Ma[1,2], Wenquan Che[1], Wenjie Feng[1], and Jianxin Chen[3]

[1]Department of Communication Engineering, Nanjing University of Science and Technology, Nanjing 210094, China

[2]Faculty of Mathematics and Physics, Huaiyin Institute of Technology, Huai'an 223003, China

[3]School of Electronics and Information, Nantong University, Nantong 226019, China

yeeren_che @163.com

Abstract ─ A short-ended resonator with open stub loaded is presented in this paper. Resonance property is analyzed based on the transmission line theory. Analysis reveals that the odd/even-mode resonance frequency of the proposed resonator can be conveniently controlled. To realize two controllable bandwidths, two different coupling paths are introduced in the filter design. Furthermore, to improve the filter selectivity, the source-load coupling is adopted to create four transmission zeros (TZs) near the edges of the two passbands. Thus, a dual-band bandpass filter (BPF) with high selectivity can be achieved. One filter with two passband frequencies at 1.01 GHz and 2.4 GHz is designed and fabricated to provide an experimental verification on the design method.

Index Terms ─ Bandwidth, dual-band bandpass filter, passband frequency, and transmission zero.

I. INTRODUCTION

With the increasing demands for multi-band application in modern wireless system, it is popular for researches on the design of multi-band filters recently [1-9], especially dual-band filters [4-9]. In the past years, three design methods are introduced. The first one is to combine two sets of resonators with common input and output ports [3]. The passband frequencies can be independently controlled by using the proper configuration. However, the control of passband bandwidths is not discussed. The second one is to use stepped-impedance resonators (SIR) [5-7] and shorted-end resonators [8] to create two passbands. Although the passband frequencies can be tuned to the desire values, it is difficult to control the bandwidths. The last one is to use two coupling paths to realize the dual-band filters with controllable bandwidths, and the passband frequencies can be controlled by impedance ratio [9]. However, it is not convenient to realize the control of passband frequencies and bandwidth. To solve this problem, dual-band inverters are utilized to obtain the desired frequency and bandwidth at each passband [10].

In this paper, a short-ended resonator with open stub loaded for designing a dual-band filter with the flexible passband frequencies and bandwidths is proposed. The passband frequencies can be flexibly controlled by selecting the proper structure parameters of the open stubs and shorted ends. The bandwidths of the two passbands can be conveniently controlled by two coupling paths. By properly controlling the coupling coefficients of the coupling paths, the bandwidths can be controlled. As a result, both the passband frequencies and bandwidths can be easily adjusted. In addition, source-load coupling scheme (the third coupling path) is also introduced to create two TZs near the edges of each passband, resulting in high skirt selectivity.

Submitted On: Dec. 12, 2012
Accepted On: Feb. 6, 2013

II. ANALYSIS AND DESIGN OF PROPOSED BPF

Figure 1 shows the configuration of the proposed microstrip BPF, which is composed of two resonators and two feed lines. The resonator is constructed by a short-ended resonator with an open-circuited stub at the center. The resonators are folded to reduce the circuit area. As can be seen from Fig. 1, there are two coupling paths between the two resonators, i.e., *Path 1* and *Path 2*. *Path 1* indicates the coupling near the ends of the short-ended resonators, while *Path 2* is the coupling between the two open stubs. Furthermore, the source-load coupling between the two feed lines does exist, causing improvement of the selectivity, which is donated as *Path 3* in Fig. 1.

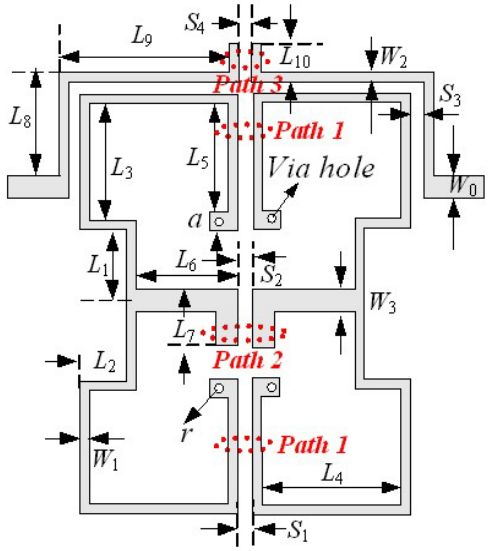

Fig. 1. Configuration of the proposed BPF.

A. Control of passband frequencies

Figure 2 (a) shows the structure of the proposed resonator, which is composed of short-circuited resonator at both ends and an open-circuited stub at the midpoint. If the odd-mode excitation is applied to Feed 1 and 2, there is a voltage null at the symmetric plane (*T*-*T*) of the resonator. Therefore, the equivalent circuit can be attained, as shown in Fig. 2 (b). The input admittance for the odd mode is given by,

$$Y_{ino} = -j\frac{Y}{\tan\theta_1} - j\frac{Y}{\tan\theta_2}. \quad (1)$$

Where $\theta_1 = \beta l_1$, $\theta_2 = \beta l_2$, β is the propagation constant of the fundamental frequency. Y donates the characteristic admittance of the transmission line with shorted ends. Thus, the resonance condition is that the imaginary part of Y_{ino} is equal to zero, the odd-mode fundamental resonance frequencies can be deduced as,

$$f_o = \frac{nc}{2(l_1+l_2)\sqrt{\varepsilon_e}}. \quad (2)$$

Where $l = 2\,(l_1 + l_2)$, n = 1, 2, 3 …, c is the speed of light in free space, and ε_e denotes the effective dielectric constant.

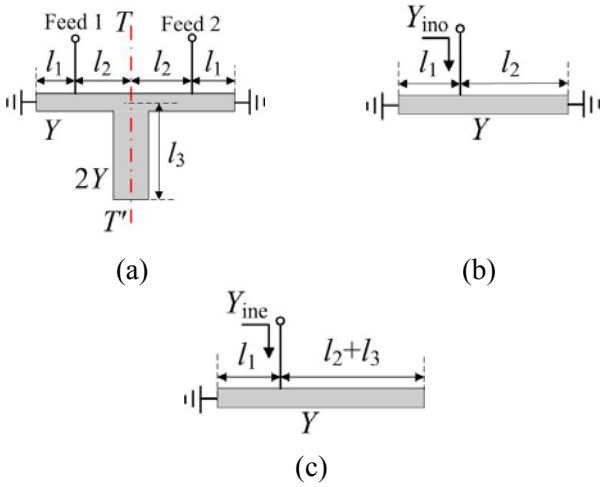

Fig. 2. (a) Structure of the proposed resonator, (b) equivalent circuit of the odd mode, and (c) equivalent circuit of the even mode.

If the even-mode excitation is applied to Feed 1 and 2 shown in Fig. 2 (a), there is no current flowing through the symmetric plane (*T*-*T*) of the transmission line. Therefore, the equivalent circuit can be attained by symmetrically bisecting the resonator, as shown in Fig. 2 (c). The input admittance for the even mode is expressed as

$$Y_{ine} = -j\frac{Y}{\tan\theta_1} + jY\frac{\tan\theta_2 + \tan\theta_3}{1-\tan\theta_2\tan\theta_3}, \quad (3)$$

where $\theta_3 = \beta l_3$. The resulted even-mode fundamental resonance frequencies can be attained as follow,

$$f_e = \frac{(2n-1)c}{2(l+2l_3)\sqrt{\varepsilon_e}}. \quad (4)$$

A full-wave EM eigenmode simulation is also used to study the resonance properties of the proposed resonator. The electric field pattern at the odd-mode resonance frequency is illustrated in Fig. 3 (a). It can be seen that the minimum fields are near the region of via hoes and stub. Furthermore, the field exhibits an anti-symmetric property along the symmetric line T-T'. As for the electric field pattern at the even-mode resonance frequency that is illustrated in Fig. 3 (b), the minimum fields are only near the region of via holes together with a symmetric property along the symmetric line T-T'.

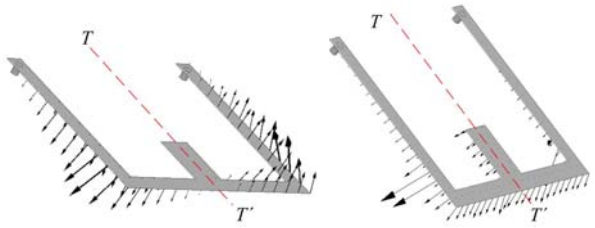

(a) (b)

Fig. 3. Simulated electric field patterns for the proposed resonator for (a) odd mode and (b) even mode.

It can be observed from equations (2) and (4) and Fig. 3 that the relation $f_o > 2f_e$ can be attained. Furthermore, the odd-mode resonance frequencies are determined by the length of the shorted ends and the even-mode resonance frequencies are determined by the lengths of the shorted ends and open stub, i.e., changing the even-mode resonance frequencies may not affect the odd-mode resonance frequencies. With this property, dual-band filters with the flexible passband frequencies can be designed. Using the configuration in Fig. 1, the passband frequencies can be conveniently controlled. For validation, full-wave simulation is carried out using HFSS. Other parameters of the filter in Fig. 1 are kept fixed and only the lengths of L_4 and L_7 are changed, respectively. The simulated responses of the passband frequencies versus the lengths of L_4 and L_7 are shown in Fig. 4 (a) and 4 (b), respectively. It can be seen that both passband frequencies are shifted down by changing the length of L_4. Moreover, the lower passband frequency (f_L) is shifted down by changing the length of L_7, while the upper one (f_H) is preserved. Besides, f_H is larger than twice of f_L.

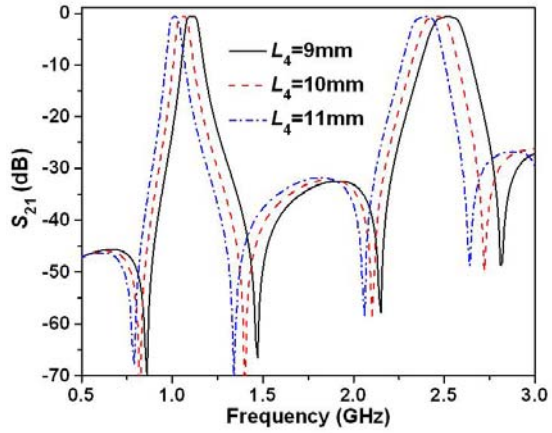

(a)

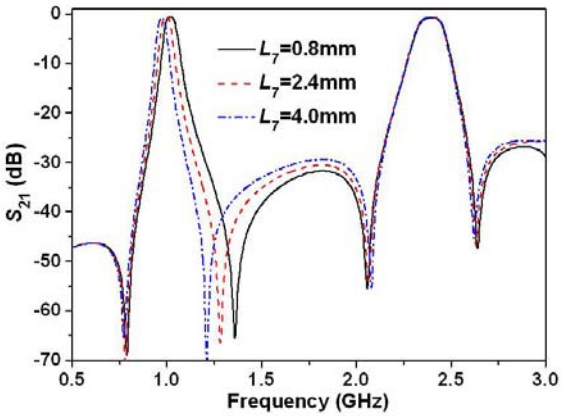

(b)

Fig. 4. Simulated responses of the passband frequencies versus length of (a) L_4 and (b) L_7.

B. Control of passband bandwidths

The coupling paths of the proposed filter are shown in Fig. 1. The coupling scheme for the two

bands is shown in Fig. 5. According to the above discussions, the lower passband is decided by the shorted ends and open stubs while the upper passband is only decided by the shorted ends. Thus, the two passband bandwidths are affected by the first two coupling paths and the upper passband bandwidth is only determined by the first coupling path. To determine the coupling bandwidths, two feed lines are weakly coupled to the two resonators, respectively. From the S_{21} plotted in Fig. 6, it is observed that the odd and even resonance modes are split into four transmission poles termed as f_{o1}, f_{o2}, f_{e1}, and f_{e2}. The coupling coefficients and absolute bandwidths (ABWs) for the two passbands are mainly determined by the coupling gaps and can be calculated as,

$$\begin{aligned} |k_L| &= \left|k_{path1L} + k_{path2L}\right| = \left|k_{eL} + k_{mL}\right| \\ &= x(S_1, S_2) = \left(f_{e2}^2 - f_{e1}^2\right) \Big/ \left(f_{e1}^2 + f_{e2}^2\right) \end{aligned} \tag{5}$$

$$\begin{aligned} |k_H| &= \left|k_{path1H}\right| = \left|k_{mH}\right| = x(S_1) \\ &= \left(f_{o2}^2 - f_{o1}^2\right) \Big/ \left(f_{o1}^2 + f_{o2}^2\right), \end{aligned} \tag{6}$$

$$\Delta_L = y(S_1, S_2) = f_{e2} - f_{e1}, \tag{7}$$

$$\Delta_H = y(S_1) = f_{o2} - f_{o1}. \tag{8}$$

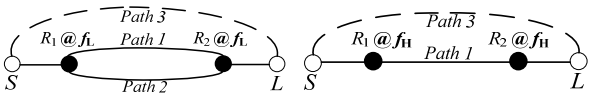

(a) (b)

Fig. 5. Coupling mechanism, (a) for the lower resonance frequency and (b) for the upper resonance frequency.

It can be seen from equations (6) and (8) that the coupling coefficients and ABWs of the upper passband ($|k_H|$ and Δ_H) are only affected by the gap of S_1 (*Path 1*), which can be confirmed from Figs. 7 and 8. It can be observed from equations (5) and (7) that $|k_L|$ and Δ_L are affected by the gaps of S_1 and S_2 (*Path 1* and *Path 2*). As discussed in [11], *Path 1* is the magnetic coupling and *Path 2* is the electric coupling, so $k_{path1L} = k_{mL} < 0$ and $k_{path2L} = k_{eL} > 0$ can be achieved. Furthermore, $|k_{path1L}|$ (= $|k_{mL}|$) is decreased with the increase of S_1 while k_{path2L} (= $k_{eL} > 0$) keeps unchanged. In addition, $|k_L|$ is decreased with the increase of S_1, as shown in Fig. 7 (a). According to equation (5), $|k_{path1L}| = |k_{mL}| > |k_{path2L}| = |k_{eL}|$ can be achieved. Thus, $|k_L|$ and Δ_L are increased with the increase of S_2, which can be seen from Figs. 7 (b) and 8 (b).

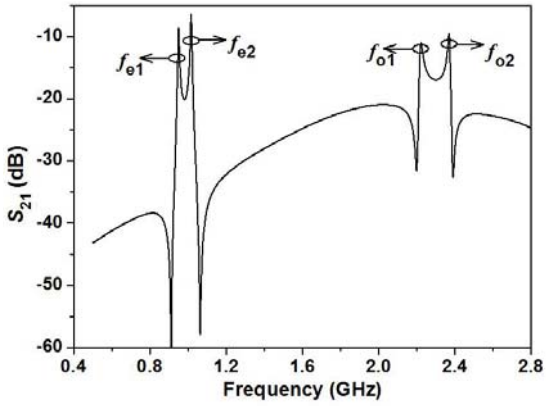

Fig. 6. Resonance frequency of the proposed BPF for S_3 = 1.0 mm.

Besides the coupling coefficients, the external quality factors (Q_es) also affects the bandwidths. In this design, Q_es for the two passbands may be determined by k' and L_8. Here k' (=(Z_E-Z_O) / (Z_E+Z_O)) is the coupling coefficient between the feeder and the resonator, and Z_E, Z_O are the even and odd characteristic impedances. The simulated Q_es for the two passbands against k' and L_8 are shown in Fig. 9. Here, Q_{e1} and Q_{e2} are the external quality factors for the lower and upper passbands, respectively. It can be observed that Q_es for the two passbands are increased with the increase of k' and slightly affected by L_8. Hence, Q_es for the two bandwidths can be tuned to the desired values by adjusting k' within a certain range. Therefore,

there are sufficient degrees of freedom to control the bandwidths at the two passbands.

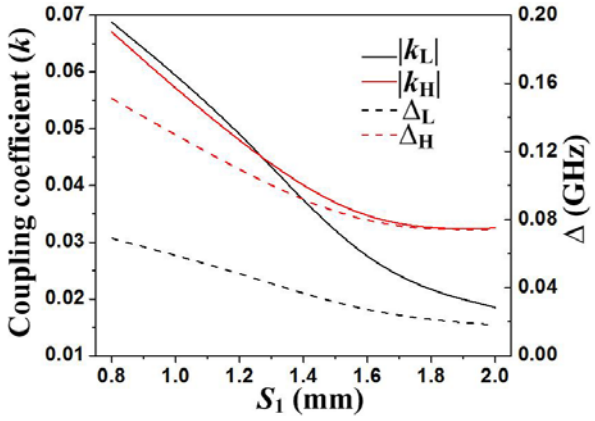

(a)

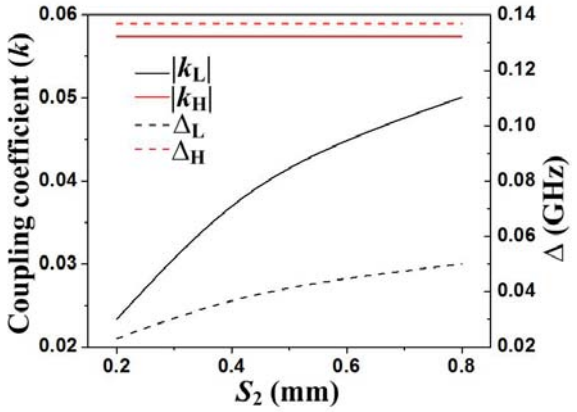

(b)

Fig. 7. k and Δ versus gap of (a) S_1 and (b) S_2.

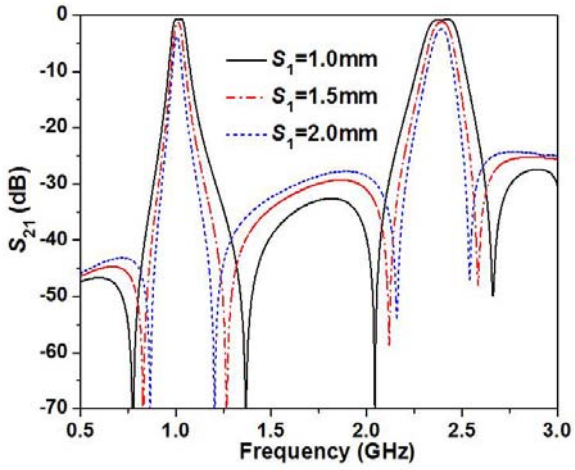

(a)

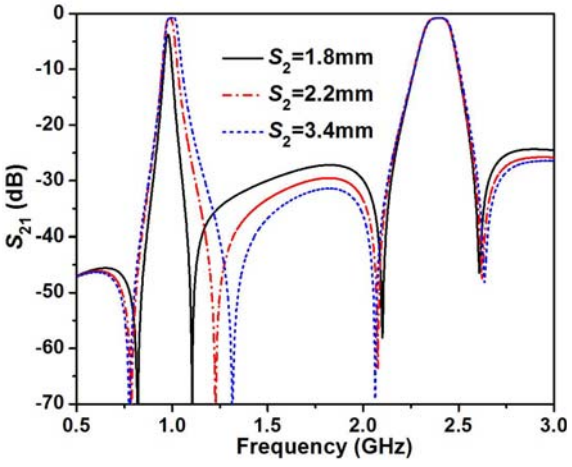

(b)

Fig. 8. Simulated responses of the passband bandwidths versus gap of (a) S_1 and (b) S_2.

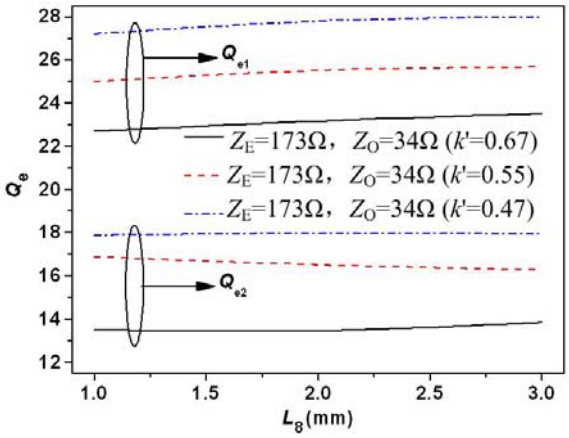

Fig. 9. Simulated Q_es for the passbands against k' and L_8.

C. Design methodology

To design the proposed filter, the first step is to obtain desirable passband frequencies. As stated above, the open stub will not affect f_H. Therefore, we first tune f_H to the desirable value by changing the length of the short-circuited line. After that, the open-stub length is adjusted to obtain desirable f_L without affecting f_H.

The second step is to obtain the required bandwidths at f_L and f_H. As stated previously, the coupling *Path 2* has no impact on the upper

passband. Hence, we first meet the requirement of $|k_H|$ and Δ_H by changing the dimensions of *Path 1* and then obtain desirable $|k_L|$ and Δ_L by altering the dimensions of *Path 2*. As for the Q_es, we can tune k' to control it. Finally, a fine tuning is performed to fulfill the requirements of both passbands.

III. MEASURED RESULTS AND DISCUSSIONS

To demonstrate our design, one prototype of the proposed dual-band BPF is implemented on a substrate with ε_r = 3.38 and h = 0.813 mm. The dimensions are determined as follows: W_0 = 1.9 mm, W_1 = 0.4 mm, W_2 = 0.4 mm, W_3 = 0.8 mm, S_1 = 1.1 mm, S_2 = 0.9 mm, S_3 = 0.15 mm, S_4 = 0.4 mm, L_1 = 5.7 mm, L_2 = 3.5 mm, L_3 = 10.1 mm, L_4 = 11.0 mm, L_5 = 9.2 mm, L_6 = 8.0 mm, L_7 = 1.2 mm, L_8 = 9.2 mm, L_9 = 12.3 mm, L_{10} = 1.1 mm, r = 0.3 mm, and a = 1.4 mm. Figure 10 shows the photograph and measured results of the proposed dual-band filter. The measured passband frequencies of the two passbands are 1.01 GHz and 2.4 GHz, and the measured minimum insertion loss (IL) of the two passbands are 0.9 dB and 1.0 dB, with the 3 dB fractional bandwidth (FBW) of 5.92 % and 5.86 %. Inside the passbands, the return loss is greater than 15.5 dB. Four TZs are created by the source-load coupling at 0.79 GHz, 1.34 GHz, 2.06 GHz, and 2.64 GHz near the edges of the two passbands, improving the selectivity of the filter. Furthermore, the rejection level between adjacent bands is better than -30 dB. Besides, a wide upper stopband with a good suppression of greater than 15 dB from 2.56 GHz to 4.8 GHz has been realized. Table 1 summarizes the comparisons of the proposed filter with previous reports. The proposed dual-band BPF has the advantages of compact size, wide upper stopband, high selectivity, and independent control of center frequencies and bandwidths.

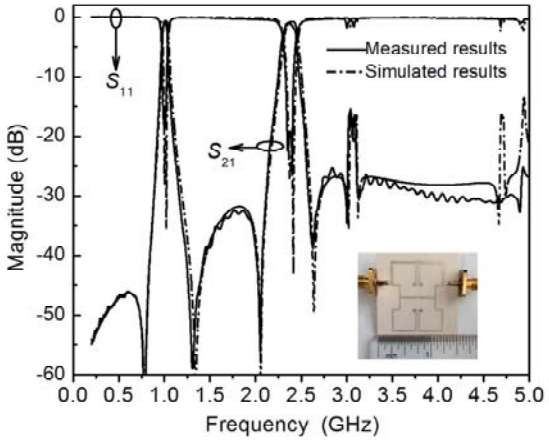

Fig. 10. Results and photograph of the proposed dual-band BPF.

Table 1: Comparisons of dual-band BPFs.

Ref.	Effective circuit size	TZs	IL (dB)	3-dB FBW (%)
[4]	$0.10\lambda_0\times0.25\lambda_0$	5	0.85/0.9	10/9.3
[5]	$0.21\lambda_0\times0.25\lambda_0$	1	1.8/2.9	7.0/4.0
[6]	$0.14\lambda_0\times0.14\lambda_0$	2	0.8/1.0	54/20
[7]	$0.25\lambda_0\times0.25\lambda_0$	6	1.58/1.54	2.0/3.3
[8]	$0.29\lambda_0\times0.37\lambda_0$	4	1.8/ 1.6	7.3/ 9.8
[9]	$0.22\lambda_0\times0.21\lambda_0$	2	1.46/1.16	5.5/4.5
Proposed filter	$0.14\lambda_0\times0.19\lambda_0$	6	0.9/1.0	5.9/5.8

λ_0 is the guided wavelength of the lower passband.

IV. CONCLUSION

This paper has proposed a resonator for the design of a dual-band BPF. The passband frequencies and bandwidths of the proposed filter can be conveniently controlled by adjusting the corresponding resonator structure parameters and the coupling coefficients properly. Four TZs near the edges of the passbands can be realized by source-load coupling. The filter has the advantages of flexible passband frequencies and bandwidths, compact size, high selectivity, and wide upper stopband. With all these properties, the proposed filter is applicable for dual-band wireless communication systems.

ACKNOWLEDGEMENT

This work was supported by the Natural Science Foundation of China (60971013), the 2009 Innovative Graduate Projects of Jiangsu Province and the Program for New Century Excellent Talents in University (NCET-11-0993).

REFERENCES

[1] S. Gao, S. Xiao, and J. L. Li, "Compact ultra-wideband (UWB) bandpass filter with dual notched bands," *Appl. Comp. Electro. Society Journal*, vol. 27, no. 10, pp. 795-800, Oct. 2012.

[2] C. Liu, Y. Li, and J. Zhang, "A novel UWB filter with WLAN and RFID stop-band rejection characteristic using tri-stage radial loaded stub resonators," *Appl. Comp. Electro. Society Journal*, vol. 27, no. 9, pp. 749-758, Sep. 2012.

[3] A. Eroglu and R. Smith, "Triple band bandpass filter design and implementation using SIRs," *26th Annual Review of Progress in Appl. Comp. Electro.*, Tampere, Finland, pp. 862-865, Apr. 2010.

[4] G. L. Dai, Y. X. Guo, and M. -Y. Xia, "Dual-band bandpass filter using parallel short-ended feed scheme," *IEEE Microw. Wireless Compon. Lett.*, vol. 20, no. 6, pp. 325–327, June 2010.

[5] S. Sun and L. Zhu, "Compact dual-band microstrip bandpass filter without external feeds," *IEEE Microw. Wireless Compon. Lett.*, vol. 15, no. 10, pp. 644-646, Oct. 2005.

[6] K. S. Chin and J. -H. Yeh, "Dual-wideband bandpass filter using short-circuited stepped-impedance resonators," *IEEE Microw. Wireless Compon. Lett.*, vol. 19, no. 3, pp. 155-157, Mar. 2009.

[7] C. W. Tang and P. H. Wu, "Design of a planar dual-band bandpass filter," *IEEE Microw. Wireless Compon. Lett.*, vol. 21, no. 7, pp. 362-364, July 2011.

[8] L. Gao and X. Y. Zhang, "Novel dual-band bandpass filters using stub-loaded short-ended resonators," *Microw. Opt. Tech. Lett.*, vol. 54, no. 12, pp. 2771-2774, Dec. 2012.

[9] X. Y. Zhang, C. H. Chan, Q. Xue, and B. J. Hu, "Dual-band bandpass filter with controllable bandwidths using two coupling paths," *IEEE Microw. Wireless Compon. Lett.*, vol. 20, no. 11, pp. 616-618, Nov. 2010.

[10] H. M. Lee and C. M. Tsai, "Dual-band filter design with flexible passband frequency and bandwidth selections," *IEEE Trans. Microwave Theory Tech.*, vol. 55, no.5, pp. 1002-1009, May 2007.

[11] J. S. Hong and M. J. Lancaster, *Microwave Filter for RF/Microwave Application*, New York: Wiley, 2001.

Yalin Ma received the M. Sc. degree from UESTC, Chengdu, China, in 2006. He is currently working toward the Ph.D. degree in Electromagnetic Field and Microwave Technology in NJUST. His research interest is the design of tunable circuits, differential network, etc.

Wenquan Che received the M.Sc. degree from NUST, Nanjing, China, in 1995, and the Ph.D. degree from the City University of Hong Kong (CITYU), Kowloon, Hong Kong, in 2003. She is currently a Professor with NUST, Nanjing, China. Her research interests include electromagnetic computation, planar/coplanar circuits and subsystems in RF/microwave frequency, microwave monolithic integrated circuits (MMICs) and medical application of microwave technology.

Wenjie Feng received the M.Sc. degree from NUST, Nanjing, China, in 2010, and is currently working toward the Ph.D. degree in Electromagnetic Field and Microwave Technology in NJUST. His research interests include ultra-wideband (UWB) circuits and technologies, etc.

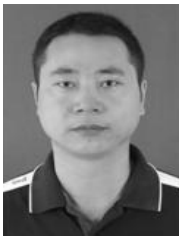

Jianxin Chen received the M.Sc. degree from UESTC, Chengdu, China, in 2004, and the Ph.D. degree from CITYU, Kowloon, Hong Kong, in 2008. He is currently a Professor with Nantong University, Jiangsu Province, China. His research interests include RF/microwave active and passive circuit designs.

A Compact Reconfigurable Antenna Using SIRs and Switches for Ultra Wideband and Multi-Band Wireless Communication Applications

Yingsong Li [1], Wenxing Li [1, 2], and Wenhua Yu [1, 2, 3]

[1] College of Information and Communications Engineering,
Harbin Engineering University, Harbin, Heilongjiang 150001, China
liyingsong82@gmail.com

[2] Institute of Electromagnetic and Wireless Engineering,
Harbin Engineering University, Harbin, Heilongjiang 150001, China
liwenxing@hrbeu.edu.cn

[3] COMU, Inc., State College, PA 16803
wenyu@2comu.com

Abstract ─ In this paper, a novel coplanar waveguide (CPW) fed ultra wideband (UWB) antenna with reconfigurable functions and notch band characteristics is proposed for wireless communication applications. The proposed UWB antenna has two stop bands that are achieved by using the stepped impedance stub (SIS) loaded stepped impedance resonators (SIRs). The reconfigurable functions are obtained by means of two ideal switches that are implemented on the proposed two SIRs. By controlling the status of the ideal switches ON/OFF, the proposed antenna can work in UWB operation band with both switches OFF and the antenna can be used as a dual notch band UWB antenna when the status of both switches is ON. The frequency domain characteristics are investigated, and the time domain characteristics, such as group delay, have been studied in details as well. The simulation and experiment results demonstrate that the proposed reconfigurable antenna can well meet the requirement for the UWB communication, notch band UWB, and multiband communication.

Index Terms ─ Multiband antenna, notch band antenna, reconfigurable antenna, time domain characteristic, and UWB antenna.

I. INTRODUCTION

With the rapid development of wireless communication, low power and high data rate communication systems have been becoming the key technologies in wireless communications. Especially, after the federal communications commission (FCC) has released the bandwidth ranging from 3.1 GHz to 10.6 GHz for indoor UWB communication applications in 2002 [1]. The UWB systems and radio frequency front-end based on ultra wideband technology operated in short distance has attracted more attention in both academic and industrial fields. Nevertheless, the ultra wideband antenna that is used as a transmitting and receiving component plays a critical role in the UWB systems. For the indoor communication applications, the UWB antenna should be small, low cost, and omni-directional for practical applications. In addition, the UWB antenna should also have a wide impedance bandwidth covering the entire bandwidth ranging from 3.1 GHz to 10.6 GHz. For the reasons above, a lot of printed UWB antennas have been developed to meet the requirements [2-8]. However, several narrow band communication systems, C-band at 4.4 GHz - 5 GHz for C-band satellite communication, HIPER-LAN/2 bands at 5.15 GHz - 5.35 GHz and 5.47 GHz - 5.725 GHz in Europe, and IEEE 802.11a/h/j/n bands at 4.9

Submitted On: Aug. 19, 2012
Accepted On: Apr. 2, 2013

GHz - 5.0 GHz, 5.035 GHz - 5.055 GHz, and 5.25 GHz - 5.725 GHz in Japan; 5.15 GHz - 5.35 GHz and 5.725 GHz - 5.825 GHz in US and X-band at 8.5 GHz - 9.5GHz for deep space communication, have been used for a long time [9]. For reducing or avoiding the potential interference between UWB systems and the narrow systems, the band-stop filters should be added at the end of the antenna or equipment. Thereby, both the cost and weight of the equipment will increase. Recently, printed UWB antennas with band notch functions have been proposed for reducing the potential interferences [10-24]. Though, these antennas can reduce the interference, most of the notch band antennas in the literatures have a complex structure, which would be difficult to redesign and the notch band is not tunable either. Furthermore, those notch band UWB antennas usually use various slots on either radiation patch or ground plane. These slots may result in the leaking of electromagnetic wave, which in turn, deteriorates the radiation patterns. To overcome the drawbacks, the most effective method is to insert open circuited stubs [17-18] into the UWB antenna, and integrate filters [24] in the fed line and active region. M. Ojaroudi et al. have also proposed a method by using tuning stubs to perturb matching impedance and create an open circuit to form a notch band at the undesired frequencies [25]. Some antennas using SRRs in the fed structures [19-20] are also utilized to improve the band limitation. However, those antennas are just used as UWB antennas or notch band UWB antennas. It is difficult to use the UWB antenna for two modes. Moreover, a lot of switchable antennas have been used for multimode communication applications [26-36]. In addition, most UWB antennas in the literatures are only investigated in the frequency characteristics. In this paper, a CPW feed wide slot UWB antenna with reconfigurable functions and notched band characteristics is presented and investigated numerically and experimentally. The proposed UWB antenna has two stop bands that are realized by using SIRs. Two ideal switches are used to control the mode of the proposed reconfigurable antenna. In this paper, the proposed reconfigurable UWB antenna consists of a dual-notch band UWB antenna and two ideal switches. The two notch band obtained using SIRs, which can be designed using SIRs theory. So, the notch can be designed flexibly and easily by means of the method proposed in [37]. Both, the frequency domain and time domain characteristics are investigated and discussed. The proposed antenna was designed, fabricated, and analyzed in details. The antenna parameters such as reflection coefficient, radiation pattern and group delay are discussed in this paper.

II. ANTENNA DESIGN

Figure 1 illustrates the geometry of the proposed UWB antenna with reconfigurable functions and dual notch band characteristics. The proposed reconfigurable UWB antennas are printed on a thin substrate plate with a relative permittivity of 2.65, a loss tangent of 0.002 and a thickness of h = 1.6 mm. The dimensions of the antenna structure are 32 mm in length, 24 mm in width, and 1.6 mm in height. The proposed UWB antenna consists of a circular slot on a rectangular PEC plate, a circular radiation patch inside the slot, two SIRs (upper and lower SIR), two ideal switches, and a 50 Ω CPW-fed structure. The black and blue parts indicate the PEC structure in Fig. 1. The 50 Ω CPW fed structure consists of the CPW transmission signal strip line with a signal strip width W7 = 3.6 mm, and a gap between the CPW ground plane and the transmission signal strip with width 0.2 mm. The 50 Ω CPW structure of the proposed UWB antenna is designed by using the formulas in [38]. The configuration of the proposed reconfigurable UWB antenna is shown in Fig. 1 (e). The detailed design procedure is illustrated in Figs. 1 (a) to 1 (f). First, a circular slot UWB antenna with a circular radiation patch has been proposed in Fig. 1 (a), which is referred as antenna1. In order to design a notch band UWB antenna, a SIR denoted as an upper SIR is etched on the circular radiation patch to reduce un-required signal from IEEE 802.11a and C-band. The upper SIR works at 5.5 GHz, and the proposed UWB antenna with an upper SIR is shown in Fig. 1 (b). Furthermore, a lower SIR is embedded inside the CPW excitation signal line to produce another notch band, which works in the X-band. The proposed UWB antenna with a lower SIR is shown in Fig. 1 (c). Figure 1 (d) is an UWB antenna with a dual notch band integrated with an upper and lower SIR. In order to make the proposed dual notch band UWB antenna for multiple modes, two ideal switches are employed

in this design, for example, the two ideal switches are cooperated into the two SIRs and denoted as switch 1 (SW1) and switch 2 (SW2). The reconfigurable UWB antenna is shown in Fig. 1 (e). Figure 1 (f) indicates the positions of the two ideal switches. In this design, SW1 and SW2 control the status of the proposed reconfigurable antenna. By adjusting the status of the proposed switches, the antenna can work as an UWB antenna or a dual notch UWB antenna/tri-band antenna. In this paper, the designed reconfigurable UWB antenna is denoted as antenna5 and shown in Fig. (e). The position of the ideal switches are shown in Fig. 1 (f). The proposed reconfigurable UWB antenna without the two ideal switches is a dual-notch band UWB antenna with two notch bands at 5.5 GHz and 9.2 GHz, respectively. This dual-notch band UWB antenna integrated with both SIRs is named antenna4 and is shown in Fig. 1 (d). Antenna4 with only upper SIR denoted as antenna2 has a notch band at 5.5 GHz. Antenna4 with only lower SIR denoted as antenna3 also has a notch band at 9.2 GHz. Antenna with neither lower SIR nor upper SIR is an UWB antenna and is denoted as antenna1.

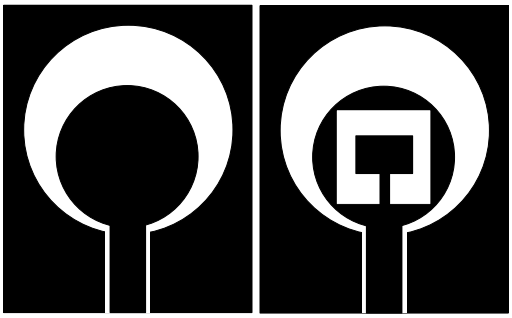

(a) (b)

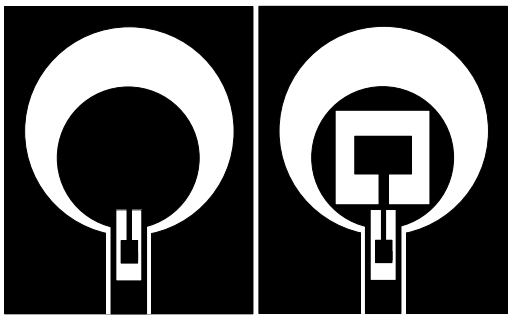

(c) (d)

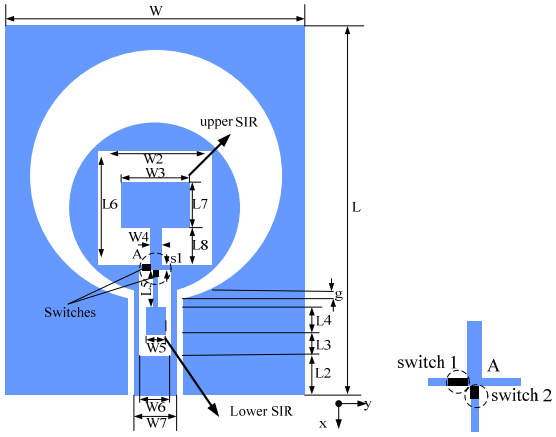

(e) (f)

Fig. 1. Design flowchart of the proposed reconfigurable antenna for the (a) proposed UWB antenna (antenna1), (b) UWB antenna with an upper SIR (antenna2), (c) UWB antenna with a lower SIR (antenna3), (d) UWB antenna with both the upper and lower SIR (antenna4), (e) reconfigurable antenna (antenna5), and (f) position of ideal switches.

III. RESULTS AND DISCUSSES

The proposed reconfigurable antenna is formed using the dual-notch band antenna4 and the two ideal switches. The center frequency of the notch band can be tunable by adjusting the dimensions of the two SIRs. In this section, we will discuss the simulation and measurement results for the proposed antenna structures. We begin with the notch band antenna.

A. Notch characteristics of proposed antennas

Figure 2 illustrates the notch characteristics of the proposed antennas. The results are obtained by using the finite element method (FEM) [39-41] and the finite difference time domain (FDTD) method [42-45]. Antenna4 without the two SIRs is an UWB antenna covering the entire UWB band ranging from 3.1 GHz to 10.6 GHz. This is also denoted as antenna1 in this paper. Antenna4 with only an upper SIR (antenna2) is an UWB antenna with a notch band near 5.5 GHz. This antenna can reduce the potential interference between the UWB systems and WLAN. Antenna4 with only a lower SIR is also an UWB antenna with a notch band at 9.2 GHz, which can suppress the un-required signal in the X-band. Antenna4 including

two SIRs is an UWB antenna with two stop bands. It is observed from Fig. 2 that the notch band near 5.5 GHz is generated by the upper SIR and the notch band near 9.2 GHz is given by the lower SIR. The impedance characteristics of antenna4 without SIRs, with one upper SIR and one lower SIR and two SIRs are obtained using the FEM method [32-34] and compared in Fig. 3. It is obvious from Fig. 3 that the real curves of the proposed antennas are around 50 Ω except the notch bands, which indicates the good impedance matching across the entire operating frequency band. It can be observed from Fig. 3 that the real parts of the impedance for the notch band antennas reach nearly zero at the lower notch band near 5.5 GHz and reach 100 Ω at the higher notch band near 8.7 GHz. The imaginary parts of the notched antennas also change sharply. The results illustrate that the inclusion of the SIRs causes the antennas non-responsive at the rejection bands.

B. Reconfigurable characteristics of proposed antenna

The proposed reconfigurable antenna with two ideal switches is shown in Fig. 1 (e). The reconfigurable antenna referred as antenna5 is based on antenna4 using two ideal switches, which are shown in Fig. 1 (f). The two ideal switches, switch 1 (SW1) and switch 2 (SW2), are metal bridges. In this paper, the ideal switch using the metallic copper strip is to approximate the switching devices [34]. During the simulation, the metal bridges with dimensions of 0.9 mm × 0.7 mm are used to approximate the SW1. SW2 is replaced by a microstrip line with a length of 0.8 mm and width 0.4 mm. The presence of the metal bridge represents that the switch status is ON; in contrast, the absence of the metal bridge represents that the switch status is OFF [29-30]. The simulated results for antenna5 are shown in Fig. 4. It can be observed from Fig. 4 that antenna5 with two switches OFF is an UWB antenna, which covers the entire UWB band with below -10 dB reflection. Antenna5 with SW1 OFF and SW2 ON is also an UWB antenna having a bandwidth of 7.8 GHz. Antenna5 with SW1 ON and SW2 OFF is a notch band UWB antenna or a dual band antenna. The notch band is near 5.5 GHz. Antenna5 with both switches ON is an UWB antenna with two rejection filter bands at 5.5 GHz and 9.2 GHz, respectively. This is also antenna4. Antenna5 with both switches ON can also be used as a tri-band antenna covering 2.8 GHz-5.0 GHz, 5.9 GHz-8.9 GHz, and 9.6 GHz-10.7 GHz. It is worth noticing that the proposed antenna without the two ideal switches is a dual band-notch UWB antenna and is denoted as antenna4 in this paper. The notch band of the proposed antenna is tuneable by adjusting the parameters of the SIRs.

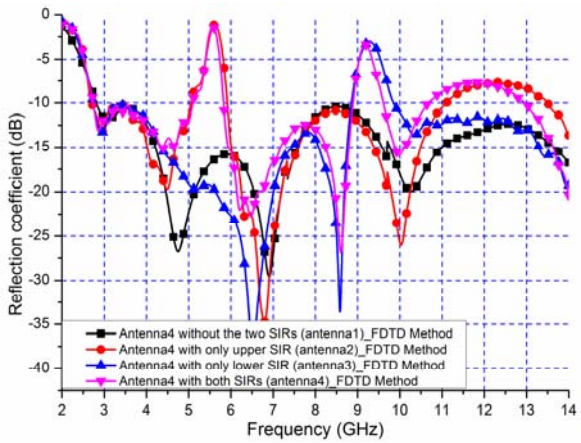

(a)

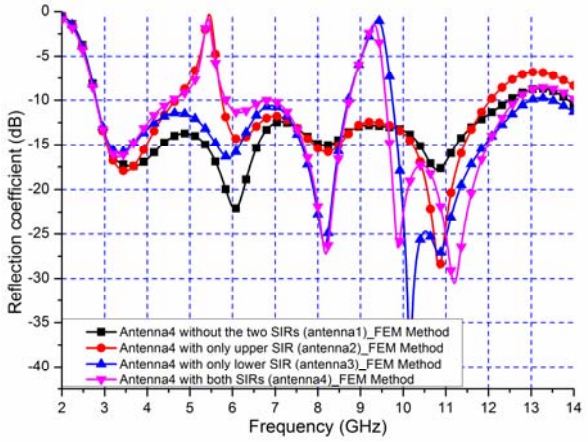

(b)

Fig. 2. Notch band characteristics of the proposed antennas (antenna4) using (a) the FDTD and (b) FEM methods.

The impedance versus frequency of the proposed antenna5 in the different status including, both switches OFF, with SW1 ON and SW2 OFF and with SW1 OFF and SW2 ON are plotted in Fig. 5 by using the FEM method. The antenna5 with both switches ON is also a dual notch band antenna, which is referred as antenna4. We can observe from Fig. 5 that the real part of the

impedance of antenna5 with switches OFF fluctuates around 50 Ω, which implies a good match over the UWB band. The reconfigurable antenna5 with SW1 ON and SW2 OFF is a notch band antenna and has a notch near 5.5 GHz. The real part of antenna5 with SW1 ON and SW2 OFF reaches zero near 5.5 GHz and the imaginary part of the impedance changes to 60 Ω. This results in no-responsive at 5.5 GHz. The reconfigurable antenna5 with SW1 OFF and SW2 ON is also an UWB antenna and the real part of the impedance is around 50 Ω, which coincides with the S-parameter results illustrated in Fig. 4.

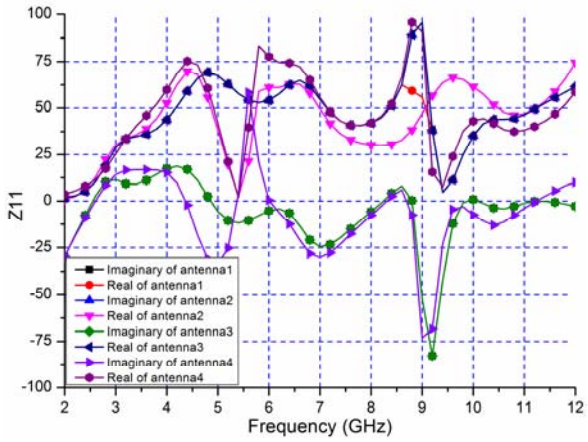

Fig. 3. Impedance characteristics of proposed notch band antennas.

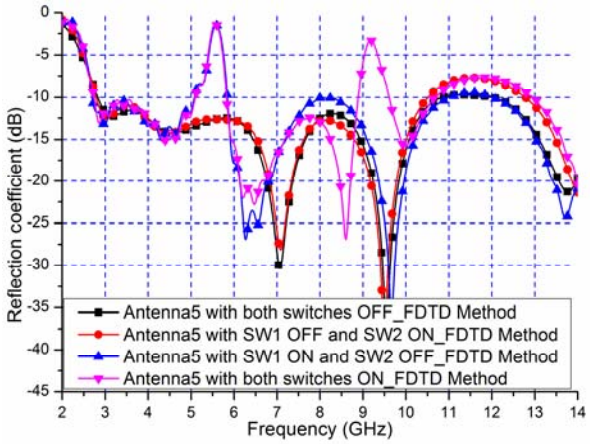

(a)

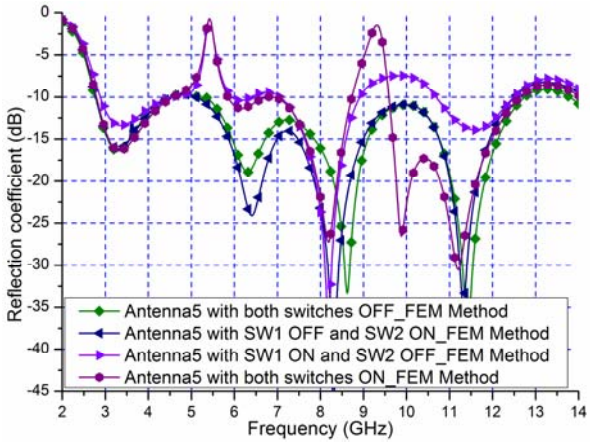

(b)

Fig. 4. Switchable characteristics of the proposed reconfigurable antenna (antenna5) using (a) FDTD and (b) FEM methods.

C. Measurement result analysis

To validate the simulation results above, the proposed antenna5 with both switch ON and OFF are optimized and the optimized parameters are as follows: W = 24 mm, L = 32 mm, D = 23.2 mm, D1 = 13 mm, W2 = L6 = 8 mm, L1 = 1.9 mm, L7 = 3 mm, W3 = 4 mm, L8 = 2 mm, W4 = 0.4 mm, W5 = 1.4 mm, W6 = 2.7 mm, L2 = 3 mm, L3 = 1.8 mm, L4 = 1.5 mm, L5 = 2.5 mm, W7 = 3.6 mm, and s1 = 0.7 mm. In order to verify the simulation results, two modes of the proposed reconfigurable antenna is fabricated and measured. The two fabricated antennas are just two states of the reconfigurable antenna. Here, we fabricate two antennas represented by two states. We believe that this approximation is acceptable and suitable to demonstrate the basic switching concept. In the practical application, the copper strip can be replaced by PINs and real RF switching circuits [34]. The optimized antennas, as shown in Fig. 6, are also fabricated and measured using HP8757D scalar network analyzer. The measurement results are illustrated in Fig. 7.

It can be seen from Fig. 7 that antenna5 with both switches ON is a dual notch band UWB antenna, and antenna5 with both switches OFF is an UWB antenna. The measurement results agree well with the simulated ones, which help to verify the accuracy of the simulation. The differences between the simulated and measured curves may be due to the errors of manufactured antennas.

Thereby, we can control the switches ON and OFF to let the proposed antenna work in an UWB mode, dual notch UWB mode/tri-band antenna mode, and a notch UWB/dual band antenna mode. The measured radiation patterns at 3.5 GHz, 7.0 GHz, and 10.0 GHz are shown in Fig. 8.

It is worthwhile to know from the radiation patterns that the radiation patterns of the reconfigurable antennas are omni-directional in the H-plane, which is also denoted as xz-plane and dipole-like in the E-plane, which is also denoted as yz-plane when both switches are turned ON or OFF, respectively. The E-plane radiation patterns of antenna5 with both switches ON have a little distortion, which is caused by the power leaking of two excited SIRs. In this paper, two SIRs etched on the radiation patch and the CPW-fed line will also leak electromagnetic wave, which deteriorates the radiation patterns a little. It is evident from the measurement and simulation results that the proposed reconfigurable antennas using the ideal switches well satisfy the requirement of the wideband communication applications. The peak gains of antenna5 with both switches ON and OFF are obtained by comparing with a double ridged horn antenna.

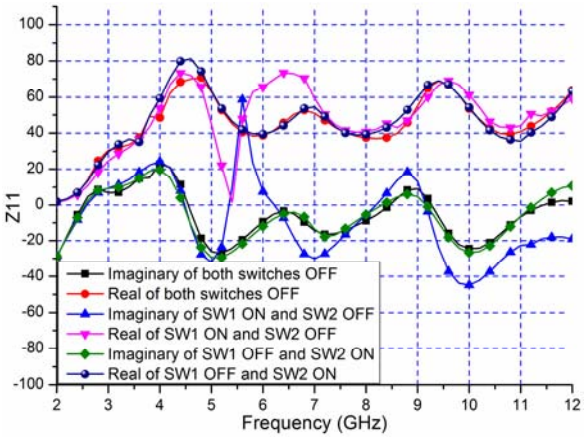

Fig. 5. Impedance characteristics of the proposed reconfigurable antennas.

The measured peak gains of the fabricated antennas are illustrated in Fig. 9. It is obvious from Fig. 9 that the stable gains of the fabricated antenna have been obtained throughout the operation band except the notched frequencies. As expected, antenna5 with both switches ON has two sharp gains, which decrease in the vicinity of 5.5 GHz and 9.2 GHz, namely, the gains drop deeply to –6.1 dBi and –4.6 dBi, respectively. The gain in this paper is little lower because of the two SIRs, which also leak energy. However, the antenna5 with both switches OFF has stable gains over the UWB band. The increased gains in the high frequency may be attributed to the deteriorated E-plane radiation patterns.

(a)

(b)

Fig. 6. Prototypes of the fabricated antennas (antenna5) used in the measurement when both switches are turned (a) ON and (b) OFF.

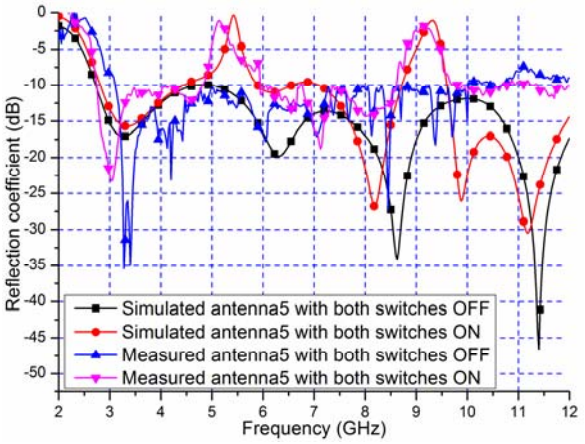

Fig. 7. Reflection coefficients of the fabricated antenna5 when switches are turned ON or OFF.

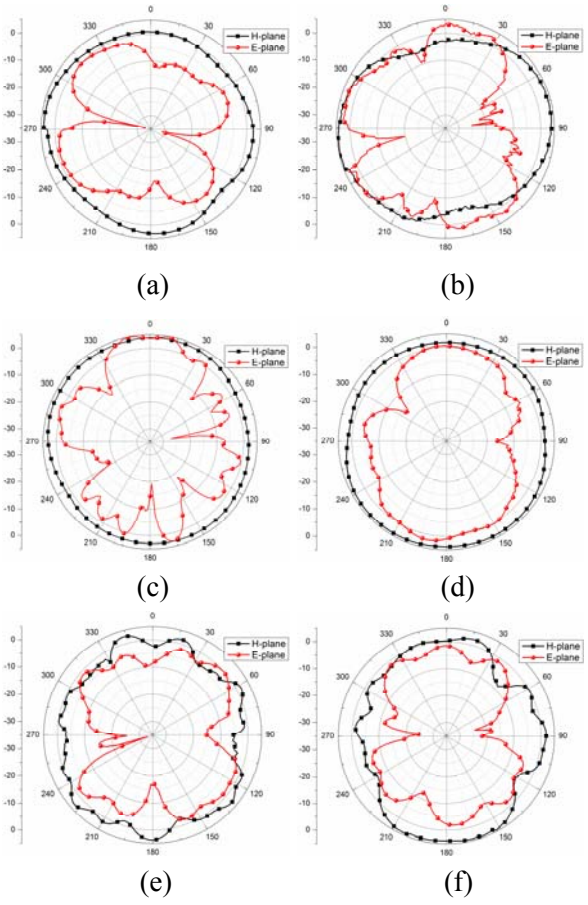

Fig. 8. Radiation patterns of antenna5 at different switch status and frequencies for (a) both switches ON at 3.5 GHz, (b) both switches ON at 7.0 GHz, (c) both switches ON at 10.0 GHz, (d) both switches OFF at 3.5 GHz, (e) both switches OFF at 7.0 GHz and (f) both switches OFF at 10.0 GHz.

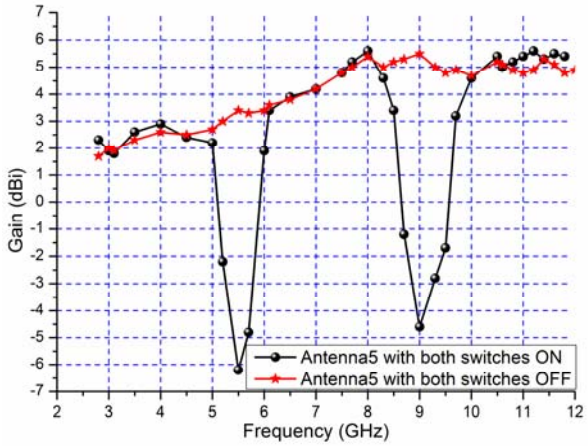

Fig. 9. Gains of the fabricated antennas when the status of the switches is ON or OFF, respectively.

D. Efficiency

The efficiency of the proposed reconfigurable antennas with both switches ON and OFF is obtained by using the FDTD method [37] and shown in Fig. 10. The antenna5 with both switches ON has an efficiency over 90 % during the UWB band except the two notch bands. In the notch band, the efficiency is reduced very quickly. The efficiency is 35 % in the lower notch band, which is near 5.5 GHz and the efficiency is 55 % in the higher notch band at 9 GHz. The antenna5 with both switches OFF has a stable efficiency in UWB band. In the operation band, the antenna5 with both switches OFF has a high efficiency, which is greater than 90 %.

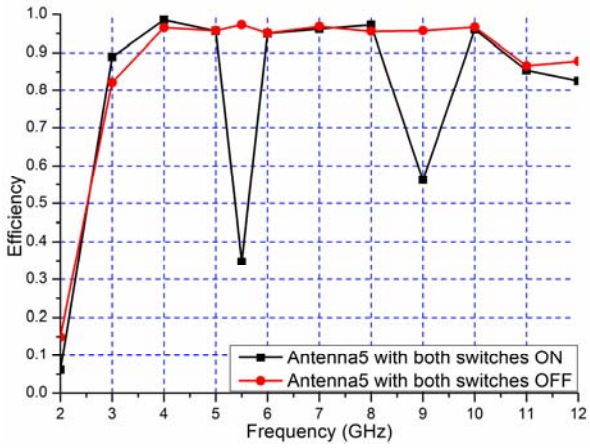

Fig. 10. Efficiency of the proposed antennas when the status of the switches is ON or OFF, respectively.

E. Group delay

As well-known fact, an UWB antenna should cover a wide band from 3.1 GHz to 10.6 GHz. Therefore, the analysis of the group delay is very important. An UWB antenna can be regarded as a filter by means of magnitude and phase responses [46]. When a signal goes through a filter, the signal will distort in both amplitude and phase. This distortion depends on the characteristics of the designed filter, which can determine the communication quality. By representing the transmitting and receiving antennas as a filter, the phase linearity and group delay at the operation band are very important for designing UWB antennas. The phase of the proposed notch band antennas and the reconfigurable antennas are shown in Fig. 11. It is interesting to notice that the inductance property abruptly changes to the capacitance property in the notch band of the proposed notch band antennas and the reconfigurable antenan5 with both switches ON, SW1 ON and SW2 OFF. The antenna1 and the reconfigurable antenna5 with both switches OFF, SW1 OFF and SW2 ON have a good linearity. The group delay is defined as the measurement of the signal transition time though a device. For the notched UWB antennas, the altered inductance properties result in a group delay of UWB antennas. We use the definition of the group delay [46] through the derivative of phase, which is expressed as,

$$\tau(\omega) = -\frac{\partial\varphi(\omega)}{\partial\omega}, \tag{1}$$

where $\varphi(\omega)$ and ω are the phase and angular frequencies, respectively. The group delay characteristic of the proposed notch band antennas and the reconfigurable antenna5 with switches ON and OFF are shown in Fig. 12. It is observed form Fig. 12 (a) that the group delay of antenna1 is less than 2 ns. The group delays of the notch band UWB antennas are less than 2 ns except the notch band. For the lower notch band near 5.5 GHz, the group delay is about 7 ns. For the higher notch band at 9 GHz, the group delay is about 6 ns. This also implies that the two notch band can reduce to void the potential interference from the narrow band, such as C-band and IEEE 802.11a.

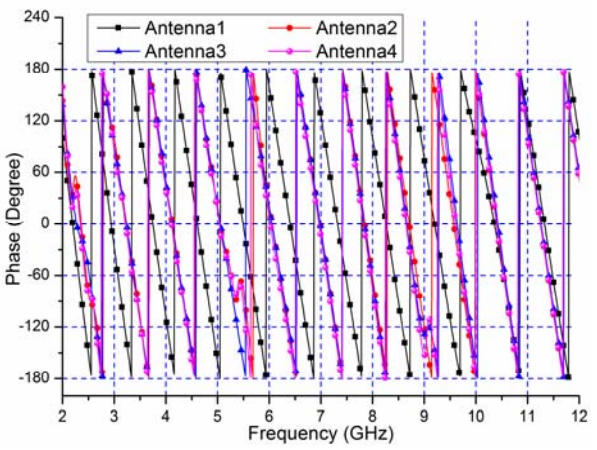

(a)

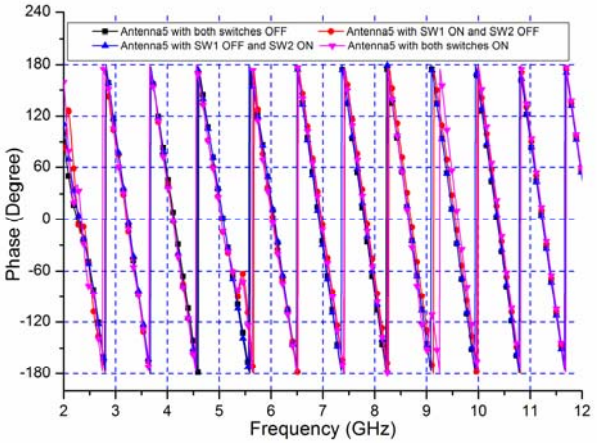

(b)

Fig. 11. Phase behaviour of the proposed antennas when the switches are in the different status for (a) the notch band UWB antennas and (b) the reconfigurable UWB antennas.

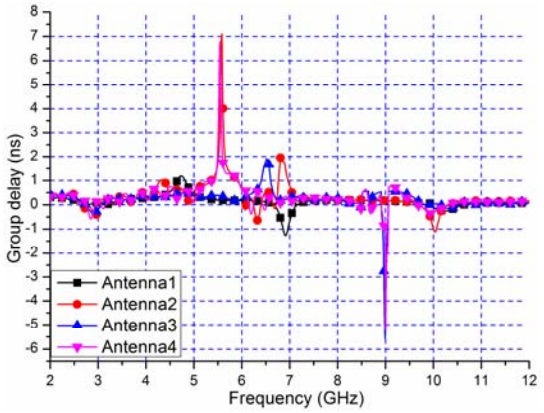

(a)

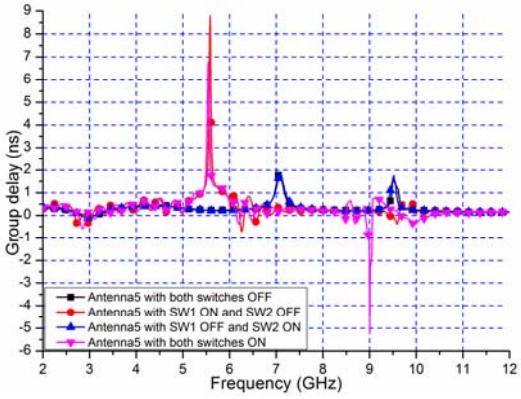

(b)

Fig. 12. Group delay characteristic of the proposed antennas when the switches are in the different status for (a) the notch band UWB antennas and (b) the reconfigurable UWB antennas.

For the reconfigurable antennas, the notched UWB antennas also have a high group delay at the notch band. The reconfigurable antenna5 with both switches OFF and antenna5 with SW1 OFF and SW2 ON are UWB antennas and the group delays are less than 2 ns over the operation band. For the UWB antenna1, the group is about 1 ns. The group of other antennas may be affected by the two SIRs in the UWB operation band. The group delay is caused by the SIRs, which change the inductance and capacitance of the antennas at the notch bands.

F. UWB system with two UWB antennas

To investigate the performance of the proposed antennas as a transmitter and a receiver in an UWB system [47], two identical antennas are mounted on the surface of the dielectric surface with 100 mm shift of their center points, and the antenna orientations are arranged in the four cases, as shown in Fig. 13. One of them works in the transmitting mode, and another one works in the receiving mode. The antenna in the transmitting mode is excited by using a modulated Gaussian pulse as shown in Fig. 14 (a). The received signal at the notch antennas and the reconfigurable antennas with different orientations are shown in Figs. 14 (b) and 14 (c).

It is observed from Fig. 14 that the received signals have been dispersed and distorted compared with the excitation pulse, which is caused by the free space attenuation [47-49]. The signal amplitudes of the received signals are also decreased due to the attenuation. The received signal of antenna5 with both switches ON deteriorates quickly than both switches are OFF. The distortion signal may be also attributed to the excited SIRs that result in the power leaking. This can also be assessed using fidelity and given as follows [47],

$$F = \max \left[\frac{\int_{-\infty}^{+\infty} s_t(t) s_r(t+\tau) d\tau}{\int_{-\infty}^{+\infty} |s_t(t)|^2 dt \int_{-\infty}^{+\infty} |s_r(t)|^2 dt} \right] \quad (2)$$

where $S_t(t)$ is the source pulse and $S_r(t)$ is a received signal in the far field zone. The fidelity (F) is the maximum correlation coefficient of the two signals by varying the time delay τ. In fact, the fidelity reflects the similarity between the transmitted and received signals. The group delay of antenna1, antenna5 with both switches OFF and antenna5 with both switches ON are also investigated herein and illustrated in Fig. 15.

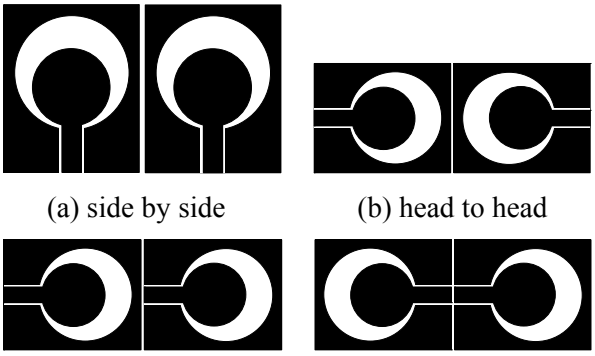

(a) side by side (b) head to head

(c) head to tail (d) tail to tail

Fig. 13. Relative positions of the two antennas for evaluating group delay.

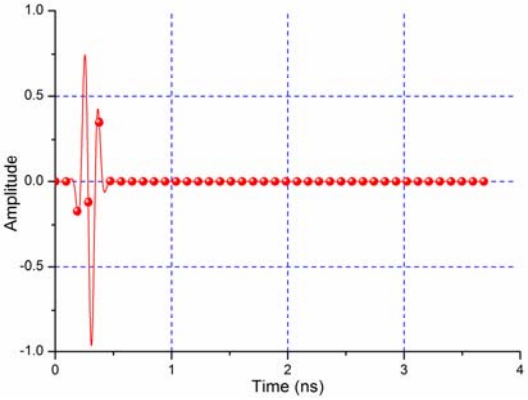

(a)

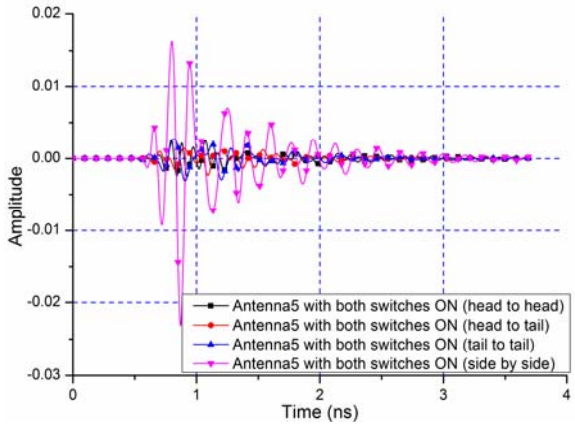

(b)

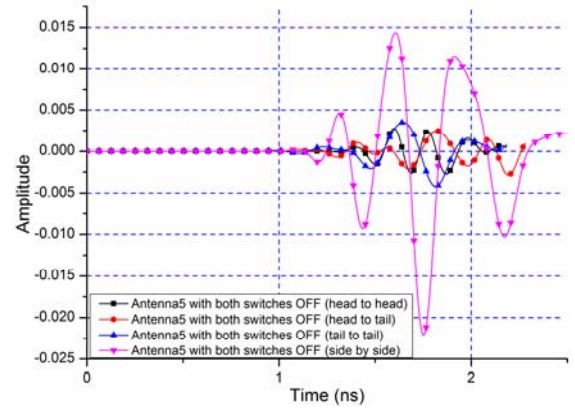

(c)

Fig. 14. Time domain characteristic of the proposed reconfigurable antennas for the different switch status: (a) excitation pulse used in the transmitting antenna, (b) Transmitted time domain signal measured at the antenna 5 with both switches ON, and (c) Transmitted time domain signal measured at the antenna5 both switches OFF.

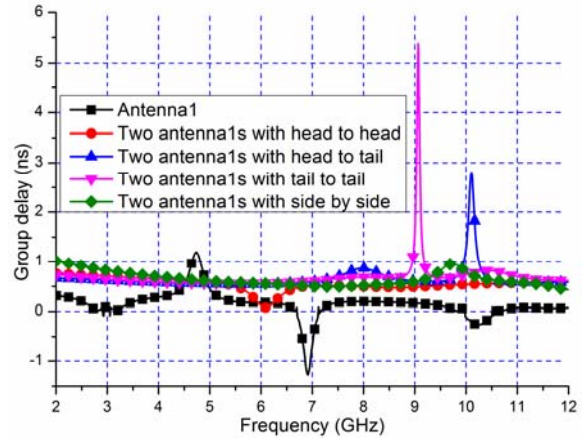

(a)

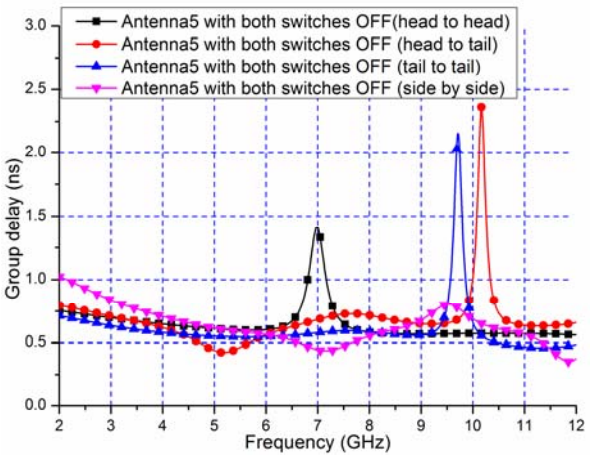

(b)

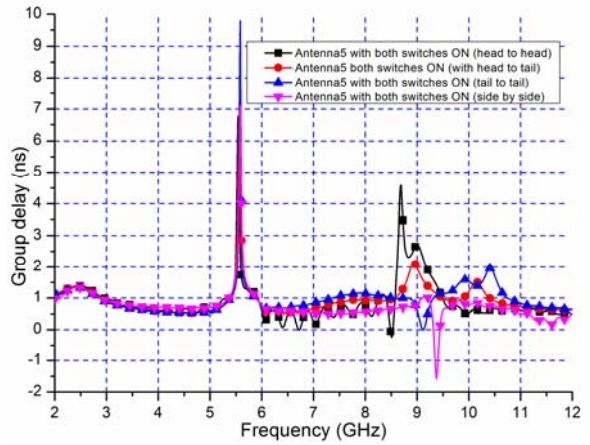

(c)

Fig. 15. Group delay characteristic of two antenna systems for the different relative locations for (a) antenna1, (b) antenna5 with both switches OFF, and (c) the antenna5 with both switches ON.

It can be seen from Fig. 15 (a) that antenna1 has a small group delay except the tail to tail case. When the antennas are placed in the tail to tail position, the signal has a longer path than other positions, which results in a larger group delay. For the proposed reconfigurable antennas, the antenna5 with both switches OFF has a small group delay, and however, the antenna5 with both switches ON has a large group delay at the notch bands. The group delays of antenna5 are similar to antenna1 expect in the notch bands.

IV. CONCLUSION

In this paper, a compact reconfigurable antenna for UWB and multi-band communication applications has been investigated numerically and experimentally. The reconfigurable functions are obtained using two ideal switches on SIRs. By switching ON and OFF status of the two switches, the proposed reconfigurable antenna can work in three modes, namely, UWB mode, notch band UWB mode/dual band antenna mode and dual notch band UWB mode/tri-band antenna mode. The switchable characteristic and notch functions are numerically investigated. The proposed switchable antenna with both switches ON and OFF are fabricated and measured. The impedance, group delay, and phase of the proposed antenna are also analyzed in this paper. We believe that PIN diodes or MEMS switches can be used to replace ideal switches to realize reconfigurable characteristics in the practical engineering. As a result, the proposed antenna can well meet the UWB communication requirement and effectively reduce the potential interference between UWB systems and existing narrow band systems.

ACKNOWLEDGMENT

This work was supported by a grant from the National Defense "973" Basic Research Development Program of China (No.6131380101). This paper is also supported by the National Nature Science Fund of China (No.60902014), Nature Science Fund of Heilongjiang (QC2009C66). This paper is also supported by the Fundamental Research Funds for the Central Universities (HEUCF1208). The authors are also thankful to Hebei VSTE Science and Technology Co., Ltd. for providing the measuring facility.

REFERENCES

[1] *Federal Communications Commission, First report and order, Revision of Part 15 of commission's rule regarding UWB transmission system FCC 02-48*, Washington, DC, April 22, 2002.

[2] S. H. Choi, J. K. Park, S. K. Kim, and J. Y. Park, "A new ultra-wideband antenna for UWB applications," *Microwave and Optical Technology Letters*, vol. 40, no. 5, pp. 399-401, 2004.

[3] R. Azim, M. T. Islam, and N. Misran, "Design of a planar UWB antenna with new band enhancement technique," *Appl. Comp. Electro. Society Journal*, vol. 26, no.10, pp. 856-862, 2011.

[4] M. Mighani, M. Akbari, and N. Felegari, "A novel SWB small rhombic microstrip antenna with parasitic rectangle into slot of the feed line," *Appl. Comp. Electro. Society Journal*, vol. 27, no. 1, pp. 74-79, 2012.

[5] T. G. Ma and S. K. Jeng, "A printed dipole antenna with tapered slot feed for ultrawide-band applications," *IEEE Trans. on Antennas and Propag.*, vol. 53, no. 11, pp. 3833-3836, 2005.

[6] D. S. Javan and O. H. Ghouchani, "Cross slot antenna with U-shaped tuning stub for ultra wideband applications," *Appl. Comp. Electro. Society Journal*, vol. 24, no. 4, pp. 427-432, 2009.

[7] K. Kiminami, A. Hirata, and T. Shiozawa, "Double sided printed bow-tie antenna for UWB communications," *Antennas and Wireless Propagation Letters*, vol. 3, pp. 152-153, 2004.

[8] R. Azim, M. T.Islam, and N. Misran, "Design of a planar UWB antenna with new band enhancement technique," *Appl. Comp. Electro. Society Journal*, vol. 26, no. 10, pp. 856-862, 2011.

[9] Y. S. Li, X. D. Yang, Q. Yang, and C. Y. Liu, "Compact coplanar waveguide fed ultra wideband antenna with a notch band characteristic," *AEU - Int. Journal of Electro. and Comm.*, vol. 65, no. 11, pp. 961-966, 2011.

[10] J. William and R. Nakkeeran, "A new UWB slot antenna with rejection of WiMax and WLAN band," *Appl. Comp. Electro. Society Journal*, vol. 25, no. 9, pp. 787-793, 2010.

[11] X. L. Bao and M. J. Ammann, "Investigation on UWB printed monopole antenna with rectangular slitted groundplane," *Microwave and Optical Technology Letters*, vol. 49, no. 7, pp. 1585-1587, 2007.

[12] Y. Zhao, L. Zhong, J. S. Hong, and G. M. Zhang, "A monopole antenna with SIR ground for harmonic suppression and bandwidth enhancement," *Appl. Comp. Electro. Society Journal*, vol. 26, no. 8, pp. 705-708, 2011.

[13] K. H. Kim, Y. J. Cho, S. H. Hwang, and S. O. Park, "Band-notched UWB planar monopole antenna with two parasitic patches," *Electronics Letters*, vol. 41, no. 14, pp. 1783-785, 2005.

[14] K. Chung, T. Yun, and J. Choi, "Wideband CPW-fed monopole antenna with parasitic elements and slots," *Electronics letters*, vol. 40, no. 17, pp.1038-1040, 2004.

[15] N. Choi, C. Jung, J. Byun, F. J. Harackiewicz, M. J. Park, Y. S. Chung, T. Kim, and B. Lee, "Compact UWB antenna with I-shaped band notch parasitic element for Laptop applications," *Antennas and Wireless Propagation Letters*, vol. 8, pp. 580-582, 2009.

[16] R. Zaker, C. Ghobadi, and J. Nourinia, "Novel modified UWB planar monopole antenna with variable frequency band notch function," *Antennas*

and Wireless Propagation Letters, vol. 7, pp. 112-114, 2008.

[17] K. S. Ryu and A. A. Kishk, "UWB antenna with single or dual band-notches for lower WLAN band and upper WLAN band," *IEEE Trans. on Antennas and Propag.*, vol. 57, no. 12, pp. 3942-3950, 2009.

[18] Y. S. Li, X. D. Yang, C. Y. Liu, and T. Jiang, "Miniaturization cantor set fractal ultra wideband antenna with a notch band characteristic," *Microwave and Optical Technology Letters*, vol. 54, no. 5, pp. 1227-1230, 2012.

[19] J. Kim, C. S. Cho, and J. W. Lee, "5.2 GHz notched ultra wideband antenna using slot-type SRR," *Electronics Letters*, vol. 42, no. 6, pp. 315-316, 2006.

[20] Y. Zhang, W. Hong, C. Yu, Z. Q. Kuai, Y. D. Don, and J. Y. Zhou, "Planar ultra wideband antennas with multiple notched bands based on etched slots on the patch and/or split ring resonators on the feed line," *IEEE Trans. on Antennas and Propag.*, vol. 56, no. 9, pp. 3063-3068, 2008.

[21] J. C. Ding, Z. L. Lin, Z. N. Ying, and S. L. He, "A compact ultra-wideband slot antenna with multiple notch frequency bands," *Microwave and Optical Technology Letter*, vol. 49, no. 12, pp. 3056-3060, 2007.

[22] S. Sadat, S. D. S. Javan, and M. Houshmand, "Design of a microstrip square-ring slot antenna filled by an H-shape slot for UWB applications," *IEEE AP-S International Symposium on Antennas and Propagation*, pp. 705-708, 2007.

[23] M. N. Jahromi and N. Komjani-Barchloui, "Analysis of the behavior of Sierpinski carpet monopole antenna," *Appl. Comp. Electro. Society Journal*, vol. 24, no. 1, pp. 32-36, 2009.

[24] A. Djaiz, M. Nedil, M. A. habib, and T. A. Denidni, "Design of a new UWB integrated antenna filter with a rejected WLAN band at 5.8GHz," *Microwave and optical Technology Letters*, vol. 53, pp. 1298-1302, 2011.

[25] M. Ojaroudi, G. Ghanbari, N. Ojaroudi, and C. Ghobadi, "Small square monopole antenna for UWB applications with variable frequency band-notch function," *IEEE Antenna and Wireless Propagation Letters*, vol. 8, pp. 1061-1064, 2009.

[26] C. Y. D. Sim, W. T. Chung, and C. H. Lee, "Planar UWB antenna with 5 GHz band rejection switching function at ground plane," *Progress In Electromagnetics Research*, vol. 106, pp. 321-333, 2010.

[27] S. Nikolaou, N. D. Kingsley, G. E. Ponchak, J. Papapolymerou, and M. M. Tentzeris, "UWB elliptical monopoles with a reconfigurable band notch using MEMS switches actuated without bias lines," *IEEE Trans. on Antennas and Propag.*, vol. 57, no. 8, pp. 2242-2251, 2009.

[28] R. Bakshi and S. K. sharma, "A wideband U-slot loaded modified E-shape microstrip patch antenna and frequency agile behavior by employing different height ground plane and ribbon type switches," *Appl. Comp. Electro. Society Journal*, vol. 26, no. 7, pp. 539-550, 2011.

[29] G. Zhang, J. S. Hong, B. Z. Wang, and G. Song, "Switched band-notched UWB/ WLAN monopole antenna," *Appl. Comp. Electro. Society Journal*, vol. 27, no. 3, pp. 256-260, 2012.

[30] G. Zhang, J. S. Hong, B. Z. Wang, and G. Song, "Switched band-notched UWB/ WLAN monopole antenna," *Appl. Comp. Electro. Society Journal*, vol. 27, no. 3, pp. 256-260, 2012.

[31] B. Li, J. Hong, and B. Z. Wang, "Switched band-notched UWB/dual-band WLAN slot antenna with inverted S-shaped slots," *IEEE Antennas and Wireless Propagation Letters*, vol. 11, pp. 572-575, 2012.

[32] Y. Li, W. Li, and R. Mittra, "A cognitive radio antenna integrated with narrow/ ultra-wideband antenna and switches," *IEICE Electronics Express*, vol. 9, no. 15, pp. 1273-1283, 2012.

[33] M. R. Hamid, P. S. Hall, P. Gardner, and F. Ghanem, "Switched WLAN-wideband tapered slot antenna," *Electronics Letters*, vol. 46, no. 1, pp. 23-24, 2010.

[34] M. R. Hamid, P. Gardner, P. S. Hall, and F. Ghanem, "Reconfigurable Vivaldi antenna," *Microwave and Optical Technology Letters*, vol. 52, pp. 785-787, 2010.

[35] J. R. Kelly, P. S. Hall, and P. Gardner, "Ultra-wideband antenna with ON/OFF band notch control," *Microwave and optical Technology Letters*, vol. 52, pp. 2743-2746, 2010.

[36] S. A. Hosseini, J. R. D. Luis, and F. D. Flaviis, "A new dual-band antenna controlled by reconfigurable notch filters," *IEEE AP-S International Symposium on Antennas and Propagation*, pp. 705-708, 2007.

[37] M. Makimoto and S. Yamashita, *Microwave Resonators and Filters for Wireless Communication: Theory, Design and Application*, Springer, 2001.

[38] R. Garg, P. Bhartia, I. Bahl, and A. Ittipiboon, *Microstrip Antenna Design Hand Book*, 1st ed. Artech House, pp. 794-795, 2001.

[39] J. M. Fernández, V. D. L. Rubia, J. M. Gil, and J. Zapata, "Frequency notched UWB planar monopole antenna optimization using a finite element method based approach," *IEEE Trans. on Antennas and Propag.*, vol. 56, no. 9, pp.2884-2893, 2008.

[40] G. Fotyga, K. Nyka, and M. Mrozowski, "Efficient model order reduction for FEM analysis of waveguide structures and resonators," *Progress In*

Electromagnetics Research, vol. 127, pp. 277-295, 2012.

[41] Y. Li, W. Li, and W. Yu, "A switchable UWB slot antenna using SIS-HSIR and SIS-SIR for multi-mode wireless communications applications," *Appl. Comp. Electro. Society Journal*, vol. 27, no. 4, pp. 340-351, 2012.

[42] K. H. Lee, C. C. Chen, F. L. Teixeira, and R. Lee, "Modeling and investigation of a geometrically complex UWB GPR antenna using FDTD," *IEEE Trans. on Antennas and Propag.*, vol. 52, no. 8, pp. 1983-1991, 2004.

[43] D. Manteuffel and J. Kunisch, "Efficient characterization of UWB antennas using the FDTD method," *IEEE Antennas and Propagation Society International Symposium*, 2004.

[44] W. Yu, X. Yang, Y. Liu, R. Mittra, D. C. Chang, C. H. Liao, M. Akira, W. Li, and L. Zhao, "New development of parallel conformal FDTD method in computational electromagnetics engineering," *IEEE Antennas and Propagation Magazine*, vol. 53, no. 3, pp. 14-41, 2011.

[45] R. W. Brocato, *FDTD Simulation Tools for UWB Antenna Analysis*, Sandia Report, SAND 2004 - 6577, Sandia National Laboratories.

[46] K. Y. Yazdandoost and R. Kohno, "Design and analysis of an antenna for ultra-wideband system," *14th IST Mobile and Wireless Communications Summit*, 2005.

[47] L. Akhoondzadeh-Asl, M. Fardis, A. Abolghasemi, and G. Dadashzadeh, "Frequency and time domain characteristic of a novel notch frequency UWB antenna," *Progress In Electromagnetics Research*, vol. 80, pp. 337-348, 2008.

[48] D. H. Kwon, "Effect of antenna gain and group delay variations on pulse-preserving capabilities of ultra-wideband antennas," *IEEE Trans. on Antennas and Propag.*, vol. 54, no. 8, pp. 2208-2215, 2009.

[49] Z. N. Chen, "Novel Bi-arm rolled monopole for UWB applications," *IEEE Trans. on Antennas and Propag.*, vol. 53, no. 2, pp. 672-677, 2005.

Yingsong LI received his B.Sc. degree in Electrical and Information Engineering in 2006, and M.Sc. degree in Electromagnetic Field and Microwave Technology from Harbin Engineering University, 2006 and 2011, respectively. Now he is a Ph.D. Candidate in Harbin Engineering University, China. He is a student member of Chinese Institute of Electronics (CIA), IEEE, IEICE and The Applied Computational Electromagnetics Society (ACES). He serves as reviewers for the journals IEEE Antennas and Wireless Propagation Letters, IET Electronics Letters, International Journal of Electronics, Progress In Electromagnetics Research Series, Journal of Electromagnetic Waves and Applications, COMPEL: The International Journal for Computation and Mathematics in Electrical and Electronic Engineering and Applied Computational Electromagnetics Society Journal. His recent research interests are mainly in microwave theory, small antenna technologies and computational electromagnetic.

Wenxing LI received the B.Sc. and M.Sc. degrees from Harbin Engineering University, Harbin, Heilongjiang, China, in 1982, 1985, respectively. He is currently a full professor of College of Information and Communication Engineering, Harbin Engineering University, China. He is also the head of Research Centre of EM Engineering & RF Technology. He visited the Department of Electrical Engineering, The Pennsylvania State University, USA from June to August 2010. And he visited Oriental Institute of Technology, Taiwan from August to October, 2010. He is also the organizer of the 30th Progress in Electromagnetics Research Symposium (PIERS), IEEE International Workshop on Electromagnetics (iWEM) , TPC of 2012 Asia-Pacific Symposium on Electromagnetic Compatibility (APEMC 2012) and 2012 Global Symposium on Millimeter Waves (GSMM 2012). His recent research interests are mainly in computational electromagnetic, microwave engineering, modern antenna design and microwave and millimeter wave circuits.

Wenhua Yu joined the Department of Electrical Engineering of the Pennsylvania State University, and has been a group leader of electromagnetic communication lab since 1996. He received his PhD in Electrical Engineering from the Southwest Jiaotong University in 1994. He worked at Beijing Institute of Technology as a Postdoctoral Research Associate from February 1995 to August 1996. He has published one book on CFDTD software and two FDTD books: Conformal Finite-Difference Time-Domain Maxwell's Equations Solver: Software and User's Guide (Artech House, 2003), Parallel Finite-Difference Time-Domain (CUC Press of China, 2005, in Chinese), and Parallel Finite-Difference Time-Domain Method (Artech House, 2006). He has

published over 100 technical papers and four book chapters. He developed created the Computer and Communication Unlimited company (Http://www.2comu.com), and serves as its President. He is a Senior Member of the IEEE. He was included in Who' Who in America, Who' Who in Science and Engineering, and Who's Who in Education. He is also a visiting professor and PhD advisor of the Communication University of China. Dr. Yu's research interests include computational electromagnetic, numerical techniques, parallel computational techniques, and the theory and design of parallel computing systems.

Bandwidth Enhancement of Compact Planar Microstrip Antenna

H. Shirzad [1], B. Virdee [2], Ch. Ghobadi [3], M. Shokri [3], T. Sedghi [3], S. Asiaban [3], and J. Pourahmadazar [1]

[1] Young Researchers and Elite Club, Urmia Branch, Islamic Azad University, Urmia, Iran
Hamedeshirzad@gmail.com

[2] Faculty of Life Sciences and Computing, Center for Communications Technology,
London Metropolitan University, London, UK

[3] Department of Electrical & Electronic Engineering, Urmia branch, Islamic Azad University, Urmia, Iran

Abstract – A novel monopole antenna is presented for ultra-wideband (UWB) applications. Enhancement in the antenna's bandwidth was obtained by using a new radiating patch structure that includes a q-shaped slots in the ground plane. UWB performance is achieved without increasing the overall size of the antenna's structure. The antenna operates between 2.4 GHz – 13.9 GHz for $S_{11} \leq$ -10 dB. The antenna radiates omni-directionally over its operating band. The antenna occupies an area of about 25 × 25 mm^2 when fabricated on FR4 substrate with thickness of 1 mm and relative permittivity of $\varepsilon_r = 4.4$.

Index Terms – Microstrip antenna, monopole antenna, and ultra-wide band antenna.

I. INTRODUCTION

Nowadays there is a great demand for antennas that are capable of operating over an ultra-wideband frequency range. Over the past few years many broadband monopole antennas have been proposed consisting of various geometries [1-21]. This type of antenna is the most widely used in the architecture of mobile communications systems as it provides the desired radiation patterns and can be easily integrated within mobile handsets. Wide band technology is becoming increasingly attractive in wireless communication as it allows greater system capacity and data exchange. Since the U.S Federal Communication Commission (FCC) has specified 3.1 GHz – 10.6 GHz frequency band for ultra-wideband usage, the UWB technology has become the preferred candidate for future short range and high rate indoor data communication systems.

Research on printed planar antennas is growing because this type of antenna implementation offers desirable characteristic like ease in fabrication, low cost, and integration [7-10]. Due to these features the planar antenna is considered the best choice for the use in UWB systems. However, one serious disadvantage of patch antennas is their narrow bandwidth. Therefore researchers are investigating the utilization of different methods and techniques for designing wideband patch antennas. Various techniques have been used in order to increase the bandwidth of the monopole antenna, for instance, fractal structures [7-9], embedding a dielectric slot in the radiating patch or in the ground surface [9], employing several radiating elements to form an array antenna [10-11], employing capacitive coupling between the radiating element and the ground plane [12], addition of slots in the radiating element [13-14], using a tapered feed line [15], notching the ground plane and/or the patch [16-17], modifying the shape of the radiating element and adding a shorting pin [18], and modifying the top side of the ground plane [19-20].

In this paper, an UWB antenna is described as compact in size and exhibits good radiation characteristics. It is shown that by increasing the number of dielectric slots and by finely tuning the dimensions of slots, additional resonance

Submitted On: May 27, 2012
Accepted On: Mar. 18, 2013

responses can be generated to realize enhanced impedance matching. The performance of the UWB antenna was simulated and optimized using HFSS ver. 11.1 [21].

II. ANTENNA STRUCTURE

The geometry and dimensions of the proposed monopole antenna are shown in Fig. 1. The antenna is created from a hollowed rectangular patch structure that forms a loop, and within this is embedded another loop structure. The antenna's ground plane is defected to enhance its impedance bandwidth. The actual size of the antenna is 25 × 25 × 1 mm^3, which was constructed on an inexpensive FR4 substrate with relative permittivity of 4.4 and loss of tangent of 0.024. The antenna is fed through a microstrip line of width Wf = 1.875 mm corresponding to a 50 Ω characteristic impedance. The optimized dimensions (in mm) of the antenna, which were obtained through parametric study using HFSS, are: W1 = 1, L1 = 1.5 ,W5 = 1.5, W4 = 1, L4 = 2.2, Lp = 11.4, Wp = 9, W2 = 1.6, W3 = 1, L2 = 2, L3 = 3.5, L5 = 0.4, L6 = 1, W7 = 1.5, and W8 = 0.5, while the ground plane parameters are: Lg = 5.5, W6 = 2.5, W9 = 2.5, and feed-line parameters are: Wf = 1.875 and Lf = 6.6. The antenna is made using two steps: firstly, the ground plane is essentially a rectangle containing two q-shaped slots, which are rotated by ± 90° and located at the two sides of the ground plane, as shown in Fig. 1.

The q-shape slots increase the surface currents on the ground plane. This phenomenon occurs because the slots perturb the current distribution over the ground plane structure. Ground plane parameters were fine tuned to optimize the antenna's impedance bandwidth. The second step involves the creation of the patch, which is essentially a rectangular loop that envelopes an inner ring that is connected to the outer rectangular loop at the top and bottom, as shown in Fig. 1.The dimensions of the outer rectangular loop are: Lp = 11.4 mm and Wp = 9 mm. The inner ring resembles a rectangle with the top half being narrower than the bottom half. Inside the inner ring is an inverted T-shaped stub. The resulting antenna structure enables omni-directional radiation and enhanced impedance bandwidth. In addition, the structure provides an effective impedance match and return-loss characteristics with linear phase variation for transmission and reception of narrow pulses used UWB systems [7-9].

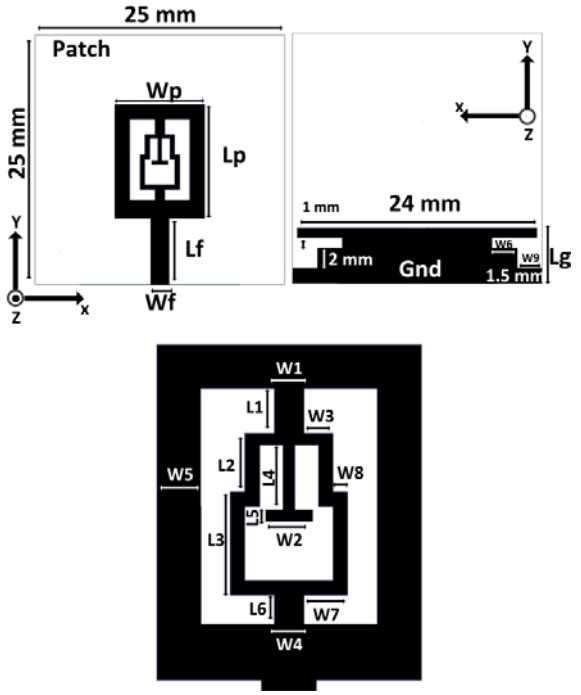

Fig. 1. Structure of the proposed monopole antenna with optimized dimensions.

III. SIMULATION AND MEASUERMENT RESULTS

The proposed antenna was designed using Ansoft HFSS [21]. The optimized design was then realized on printed circuit board. The proposed antenna was fabricated on a common FR4 substrate. Figure 2 shows a photograph of the antenna. The width (Wf) and length (Lf) of the microstrip feed-line are 1.875 mm and 6.6 mm, respectively. The impedance bandwidth of the antenna was measured using Agilent 8722ES vector network analyzer. It is observed from Fig. 3, that the impedance bandwidth is tightly related to W6. The bandwidth decreases when the length of W6 is varied from its optimum value (W6 = 2.5 mm) in either direction. Moreover, as depicted in Fig. 4, the bandwidth is also affected by parameter W5. By increasing W5, the frequency of the upper band edge decreases. Parametric study also showed the operating frequency band of the antenna is affected by the space between the patch and ground plane (Lf). Other parameters such as L3 and W7, have negligible influence on the

return-loss (S11) of the antenna. The proposed antenna structure is shown to fulfill the requirements for UWB systems.

The effect of the inner and outer ring parameters on the prototype antenna's response are shown in Fig. 5. It shows five absorption resonances within the antenna's bandwidth at different frequencies. There is good agreement between the measured and simulated results. The antenna's gain between 2 GHz to 11 GHz is plotted in Fig. 6. The antenna's gain figure varies between 1 dBi and 4 dBi over the UWB bandwidth, and the variation is approximately linear. The far field radiation characteristics were also studied. Figure 7 show the co-polarization and cross-polarization radiation patterns in the E- and H-planes at three different spot frequencies 3 GHz, 6 GHz, and 10 GHz. The H-plane pattern is omni-directional over the entire UWB operating band. This antenna performs similarly to conventional printed monopole antennas with the advantage of being significantly smaller in size and possessing enhanced bandwidth.

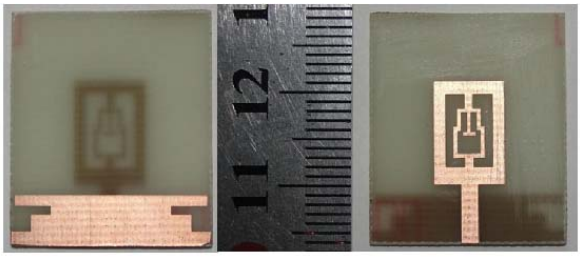

Fig. 2. Photograph of the printed monopole antenna.

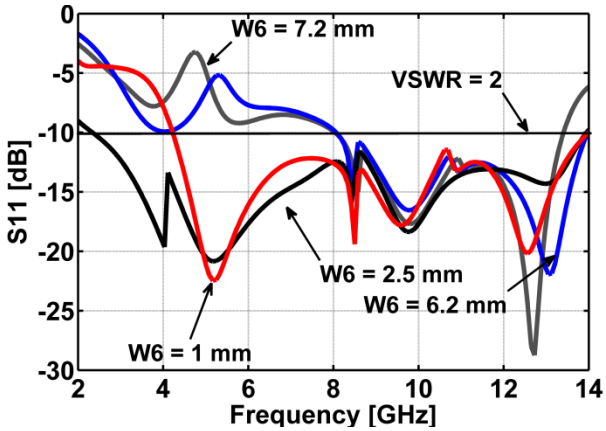

Fig. 3. Simulated return-loss (S11) frequency response as a function of parameter W6.

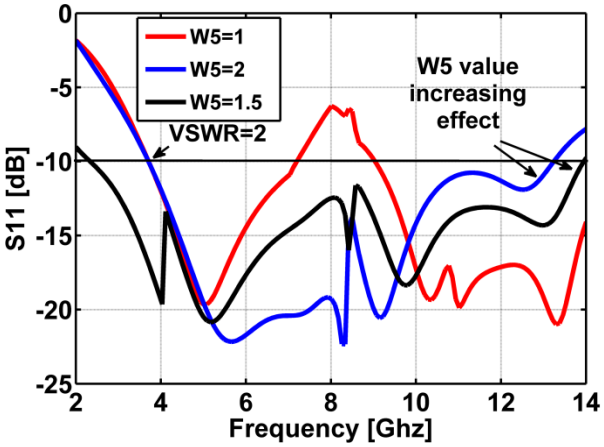

Fig. 4. Return-loss (S11) frequency response as a function of parameter W5 (in mm).

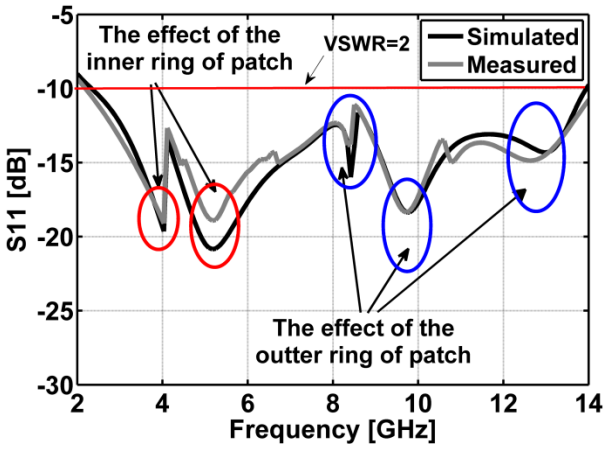

Fig. 5. Measured and simulated return-loss of the antenna using optimized values with embedded slots (inner and outer rings).

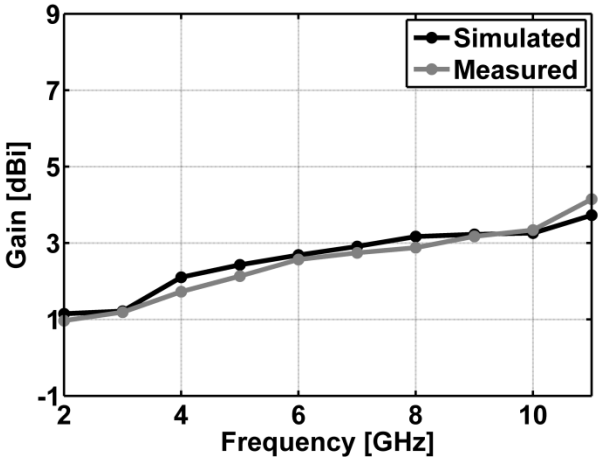

Fig. 6. Measured and simulated antenna gain response of the prototype antenna.

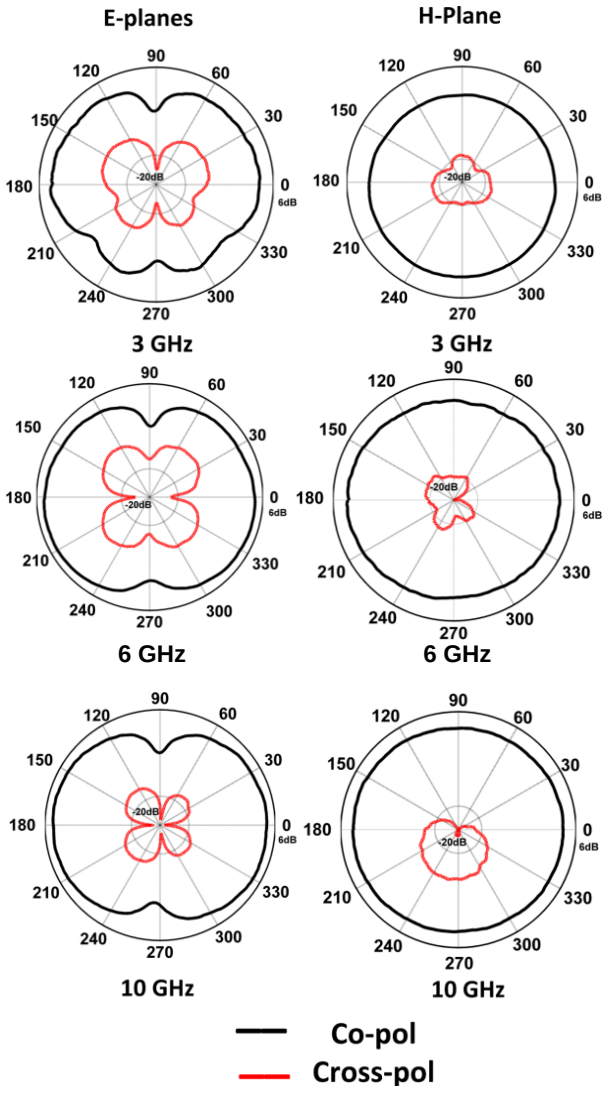

Fig. 7. Measured E- and H-plane patterns at spot frequencies of 3 GHz, 6 GHz, and 10 GHz.

IV. CONCLUSION

A compact and novel monopole antenna was proposed and fabricated for ultra-wideband applications. The antenna's bandwidth performance was enhanced by embedding slots inside the antenna's ground-plane structure. Impedance matching was optimized over the ultra-wideband frequency range by optimizing the current density distribution over the antenna's ground structure. The antenna operated over a frequency range 2.4 GHz to 13.9 GHz, which complies with the UWB specification. The antenna was fed through a microstrip-line. The simulation and measurement results are in good agreement. These results confirm the proposed antenna as a good candidate for UWB wireless technology.

REFERENCES

[1] M. Mighani, M. Akbari, and N. Felegari, "A novel SWB small rhombic microstrip antenna with parasitic rectangle into slot of the feed line," *Appl. Comp. Electro. Society (ACES) Journal*, vol. 27, no. 1, pp. 74-79, January 2012.

[2] M. Mighani, M. Akbari, and N. Felegari, "A CPW dual band notched UWB antenna," *Appl. Comp. Electro. Society (ACES) Journa*l, vol. 27, no. 4, pp. 352-359, April 2012.

[3] R. Azim, M. T. Islam, and N. Misran, "Design of a planar UWB antenna with new band enhancement technique," *Appl. Comp. Electro. Society (ACES) Journal*, vol. 26, no. 10, pp. 856-862, Oct. 2011.

[4] J. William and R. Nakkeeran, "A new UWB slot antenna with rejection of WiMax and WLAN bands," *Appl. Comp. Electro. Society (ACES) Journal*, vol. 25, no. 9, pp. 787-793, Sep. 2010.

[5] D. S. Javan and O. H. Ghouchani, "Cross slot antenna with U-shaped tuning stub for ultra wideband applications," *Appl. Comp. Electro. Society (ACES) Journal*, vol. 24, no. 4, pp. 427-432, August 2009.

[6] M. N. -Jahromi and N. K. -Barchloui, "Analysis of the behavior of Sierpinski carpet monopole antenna," *Appl. Comp. Electro. Society (ACES) Journal*, vol. 24, no. 1, pp. 32-36, Feb. 2009.

[7] M. Naser-Moghaddasi, R. A. Sadeghzadeh, M. Fakheri, T. Aribi, T. Sedghi, and B. S. Virdee, "Miniature hook-shaped multiband antenna for mobile applications," *IEEE Antennas and Wireless Propagation Letters*, vol. 11, 2012.

[8] J. Pourahmadazar, Ch. Ghobadi, J. Nourinia, and H. Shirzad, "Multiband ring fractal monopole antenna for mobile devices," *IEEE Ant. Wireless. Propage. Lett.*, vol. 9, pp. 863-866, 2010.

[9] J. Pourahmadazar, Ch. Ghobadi, and J. Nourinia, "Novel modified pythagorean tree fractal monopole antennas for UWB applications," *IEEE Ant. Wireless. Propage. Lett.*, vol. 10, pp. 484-487, 2011.

[10] M. Naser-Moghadasi, R. A. Sadeghzadeh, T. Aribi, T. Sedghi, and B. S. Virdee, "UWB monopole microstrip antenna using fractal tree unit-cells," *Microwave and Optical Technology Letters*, vol. 50, pp. 936-939, Oct. 2012.

[11] R. Zaker and A. Abdipour, "A very compact ultra wideband printed omni directional monopole antenna," *IEEE Ant. Wireless. Propag. Lett.*, vol. 9, 2010.

[12] C. A. Balanis, *Antenna Theory Analysis and Design*, John Wiley & Sons, New York, 1997.
[13] M. K. Rahim and P. Gardner, "The design of nine element quasi microstrip log periodic antenna," *RF and Microwave Conference*, Malaysia, pp. 132-135, Oct. 2004.
[14] H. Rmili and J. M. Floc'h, "Design and analysis of wideband double-sided printed spiral dipole antenna with capacitive coupling," *Microwave and Optical Technology Letters*, vol. 50, no. 5, pp. 1312-1317, May 2008.
[15] A. K. Shackelford, K. F. Lee, and K. M. Luk, "Design of small size wide-bandwidth microstrip patch antennas," *IEEE Antennas and Propagation Magazine*, vol. 45, no. 1, pp. 75-83, Feb. 2003.
[16] J. Y. Chiou, J. Y. Sze, and K. L. Wong, "A broad-band CPW fed strip loaded square slot antenna," *IEEE Transactions on Antennas and Propagation*, vol. 51, no. 4, pp. 719-721, April 2003.
[17] R. S. Kshetrimayum and R. Pillalamarri, "Novel UWB printed monopole antenna with triangular tapered feed lines," *IEICE Electronics Express*, vol. 5, no. 8, pp. 242- 247, April 2008.
[18] S. Tourette, N. Fortino, and G. Kossiavas, "Compact UWB printed antennas for low frequency applications matched to different transmission lines," *Microwave and Optical Technology Letters*, vol. 49, no. 6, pp. 1282-1287, June 2007.
[19] X. Zhang, W. Wu, Z. H. Yan, J. B. Jiang, and Y. Song, "Design of CPW-fed monopole UWB antenna with a novel notched ground," *Microwave and Optical Technology Letters*, vol. 51, no. 1, pp. 88-91, Jan. 2009.
[20] M. N. Shakib, M. T. Islam, and N. Misran, "Stacked patch antenna with folded patch feed for ultra-wideband application," *IET Microwave Antennas Propagation*, vol. 4, no. 10, pp. 1456-1461, Oct. 2010.
[21] R. Azim, M. T. Islam, and N. Misran, "Design of a planar UWB antenna with new band enhancement technique" *Appl. Comp. Electro. Society (ACES) Journal*, vol. 26, no. 10, pp. 856-862, Oct. 2011.
[22] Ansoft High Frequency Structures Simulation (HFSS), ver. 11.1 Ansoft Corporations 2008.

HamedShirzad was born in 1985 in Iran. He received the B.Sc. and M.Sc. degrees in Electrical Engineering from the IAU, and Urmia University in 2008, and 2012, respectively.

BalVirdee is a Professor of Microwave Communications Technology in the Faculty of Life Sciences and Computing at London Metropolitan University where he Heads the Center for Communications Technology and is the Director of London Metropolitan Microwaves.

Changiz Ghobadi was born on 21 of April, 1954 in Iran. He received the B.Sc. and M.Sc. degrees in Electrical Engineering from the Isfahan University of Technology (IUT), Isfahan, Iran, and the Ph.D. degree from University of Bath, United Kingdom, in 1985, 1987, and 1998, respectively. In 2008, he received Iran Telecommunication Research Center (ITRC) grant to establish Northwest Antenna and Microwave Research Laboratory(NAMRL) in Urmia University.

MajidShokri was born in1980 in Iran. He received the B.Sc. and M.Sc. degrees from the IAU, and Urmia University in 2006, and 2012, respectively, all in Electrical Engineering.

Tohid Sedghi received the B.Sc. and M.Sc. degrees from the IAU, and Urmia University in 2008, and 2011, respectively, all in Electrical Engineering. He is working as a PhD student in Science and Research Branch, IAU.

SomayehAsiaban was born in 1984 in Iran. She received the B.Sc. degrees from the Urmia branch, IAU in Electrical Engineering, 2008.

Javad Pourahmadazar was born in 1985 in Iran. He received the B.Sc. and M.Sc. degrees in Electrical Engineering in 2008, and 2011, respectively. He is now working as a Research assistant in Northwest Antenna and Microwave Research Laboratory in Urmia University.

Compact Printed Band-Notched UWB Antenna With 90 Degree Rotation Angle CSRR

Di Jiang, Yuehang Xu, Ruimin Xu, and Weigan Lin

Fundamental Science on EHF LaboratoryUniversity of Electronic Science and Technology of China
Chengdu, China
merryjiangdi@163.com, yhxu@uestc.edu.cn, rmxu@uestc.edu.cn, wglin@uestc.edu.cn

Abstract ― A novel band-notched ultra-wideband monopole antenna is presented. The proposed antenna consists of a swallow shape radiating patch, two novel 90 degree rotation angle complementary splitring resonator (CSRR) structures for generating band-notched function instead of changing the patchor feeding shapes, and a trapezoidal ground plane that provides a wide usable bandwidth of more than 143 % (2 GHz – 11.2 GHz). With two novel 90 degree rotation angle complementary SRR structures, band-stop frequency performance is realized, and some key characteristics such as band-notched frequency and bandwidth can be controlled easily. The designed antenna has a small size of 25 × 27.9 mm^2, showing the band-rejection performance in the frequency band of 3.9 GHz / 5.9GHz. The antenna demonstrates omni-directional and stable radiation patterns across all the relevant bands. Moreover, a prototype of the proposed antenna is fabricated, and the measured results are shown to be in good agreement with the simulated results.

Index Terms ― Complementary split ring resonator (CSRR), multiband, notch bands, and ultra-wideband (UWB).

I. INTRODUCTION

Wideband antennas with band-notched characteristics will play an important role in future wideband communication systems. In 2002 the FCC designated the area of the frequency spectrum, which can be occupied by unlicensed ultra-wideband (UWB) communication systems. Unfortunately, this overlaps various narrow band communication systems such as C-band (3.7 GHz – 4.2 GHz) satellite communication systems and WLAN. The front-end receiver for an UWB system incorporates a high gain LNA, which could be saturated by interference from a narrow band system in the vicinity [1]. One of the more attractive solutions to this problem is to integrate a band notch filter performance into a wideband omni-directional antenna [2].

In this paper, we present a compact printed antenna with novel 90 degree rotation angle complementary split ring resonator (CSRR) structures, which has an UWB operating bandwidth with a tunable dual-notched frequency at 3.9 GHz and 5.9GHz is presented. Band-notched operation is achieved by novel 90 degree rotation angle CSRR slots on swallow shape radiated patch [3]. The CSRR has been implemented in designing left-hand material, the 90 degree rotation angle CSRR is promising for UWB antennas to ensure multiple notched bands [4]. Both dual-band-notched characteristics and compact size are achieved in our design. The antenna has promising features, including good impedance matching performance over the whole operating frequency band, stable radiation patterns, and flexible frequency notched function [5].

II. ANTENNA DESIGN

Compared with microstrip, coplanar waveguides (CPW) have several advantages, including low loss, high integration, low dispersion, weak coupling, and compact size.

Submitted On: Nov. 1, 2012
Accepted On: Mar. 23, 2013

Moreover, it enjoys low complexity since the CPW-fed is coplanar with the ground. In addition, it can be integrated with other components straight forwardly. Therefore, it is considered as a milestone in the development of the monolithic microwave integrated circuit. These characteristics enable the CPW to be used in the application of high frequency microwave integrated circuits. Especially, when applied in the antenna feeding, it broadens the bandwidth of the antenna obviously. Therefore, the CPW-fed is widely used in the printed antenna. Antenna feeding based on CPW, in fact, is a kind of electromagnetic coupling. The electromagnetic coupling can be easily controlled by the distance between CPW-fed and the radiating patch since they are in the same layer. If the radiating patch has gradient shape, wide bandwidth can be achieved.

To fabricate swallow-shaped antenna mentioned in this paper, a half ellipse is cut from a rectangle radiating patch firstly and then moved into the bottom side of the radiating patch. This new shape with a gradient structure has the same area as the rectangle one. In addition, the ground of the antenna has a chamber-like shape so that ground also has a gradient structure. Since both the radiating patch and the ground have a gradient structure, the antenna can ensure a smooth transition from one mode to another. In this case, the antenna will have a good impedance matching within a broad bandwidth.

The performance of this antenna depends on the distance between the ground and the CPW-fed as well as the shape of the ground. As illustrated in Fig. 1, the distance between the CPW-fed and the ground (S_1) will influence the voltage standing wave ratio (VSWR), resulting in the drift of band-notched at the high frequency.

As shown in Fig. 2, the width of the ground (W_1) has a relatively small effect on the band-notched at the low frequency. However, its impact on the high frequency is very obvious. As shown in Fig. 3, the VSWR of the proposed antenna have little change with the height of the ground layer (H).

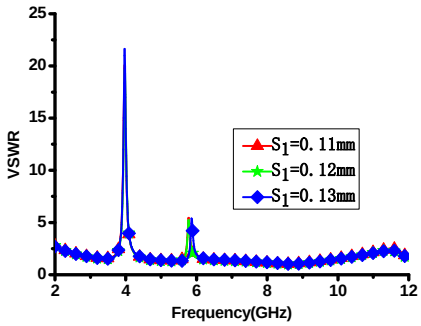

Fig. 1. S-parameters of different width of gap (S_1).

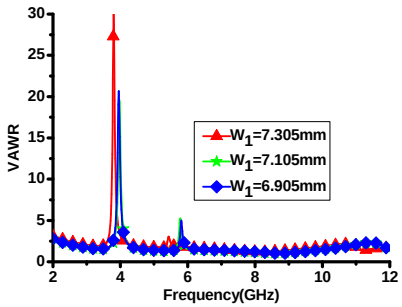

Fig. 2. S-parameters of different width of ground (W_1).

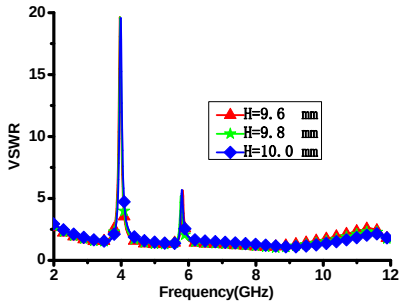

Fig. 3. S-parameters of different height of ground (H).

According to earlier research, the band-notched can realized by the complementary splitring resonator (CSRR) structures in the radiating patch. If the length of the CSRR is roughly the same as the half wavelength of the corresponding central band-notched frequency, the currency is restricted around the CSRR, resulting antenna cannot radiate. This is due to

band-notched. In order to achieve two notched bands, two complementary split ring resonators, which are perpendicular to each other, are introduced into the radiating patch in the antenna. This can be expressed by,

$$L = \frac{C}{2 f_{notch} \sqrt{\varepsilon_r}} \quad (1)$$

C represents the light speed, f central frequency of the band-notched, ε_r effectively dielectric constant.

The size of inner-square (R_1, R_2) should be adjusted to determine the dual-band-notched frequency of the antenna. If other parameters are fixed, the dual-band-notched frequency will increase with the decrease of R_1 and R_2. Moreover, if R_1 and R_2 are fixed, the resonance frequency could be also enhanced by increasing slit width of squares (g). For the convenience of optimization, the width of squares (d_1, d_2) and distance between squares are set to be the same as (g). After that, the distance (C_1,C_2) between these two CSRRs should be also optimized. These optimization works were managed by using commercial 3-D electromagnetic software HFSS.

The geometry of the proposed novel 90 degree rotation angle CSRR slot UWB antenna with band-notched function is depicted in Fig. 4. The antenna is located on the *xz* - plane and the normal direction is parallel to the *y*-axis [6, 7]. The radiating ring is fed via the 50 Ω coplanar waveguide (CPW) feed-line of width 2.55 mm, as illustrated in Fig. 5. The proposed antenna was fabricated on a dielectric substrate RT5880 with a relative permittivity (ε_r) of 2.2 and thickness of 0.508 mm. A novel 90 degree rotation angle complementary SRR slot are used and fabricated on the swallow shape radiation patch. To achieve good impedance matching for the ultra-wideband operation, the swallow radiator is feed by coplanar waveguide (CPW) transmission line with trapezoidal ground-plane, which is terminated with a sub miniature A (SMA) connector for the measurement purpose [8-15]. Since the antenna and the feeding are fabricated on the same side of the plane, only one layer of the substrate with single-sided metallization is used, and the manufacturing of antenna is very easy and extremely low cost. Good performance of multiple band-notched characteristic is simply accomplished by embedding 90 degree rotation angle complementary split ring resonators to the swallow shape radiation patch. The novel 90 degree rotation angle complementary SRR can show distinct double band gaps due to the weaker mutual coupling between the inner and outer rings even the two band gaps are adjacent. Thus, 90 degree rotation angle complementary SRR is selected to obtain adjacent dual notched-bands for C-band (3.7 GHz – 4.2 GHz) satellite communication systems and upper WLAN [16-21]. Figure 5 shows the photograph of the dual band-notched UWB antenna. It is noted that the inner and outer openings are just 90 degrees.

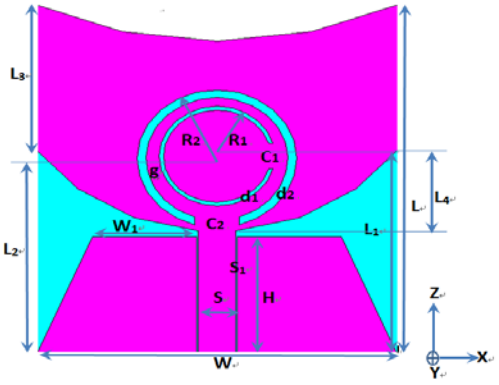

Fig. 4. Geometry of the antenna, with dimensions R_1 = 3.65 mm, R_2 = 4.85 mm, C_1 = 2 mm, C_2 = 3 mm, d_1 = 0.3 mm, d_2 = 0.6 mm, S = 2.55 mm, S_1 = 0.12 mm, H = 9.8 mm, W = 25 mm, W_1 = 7.105 mm, L = 27.9 mm, L_1 = 16.5 mm, L_2 = 16 mm, L_3 = 11.34 mm, and L_4 = 6.61 mm.

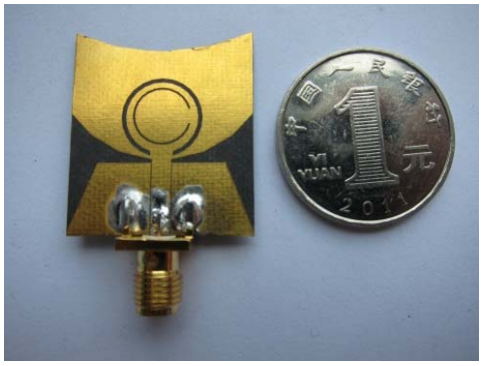

(a)

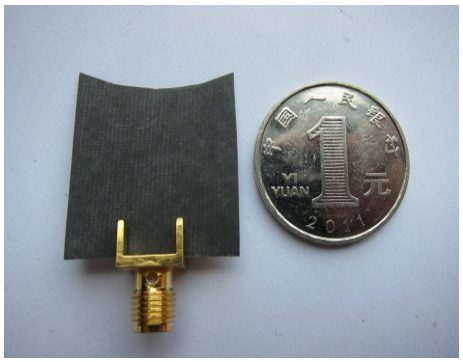

(b)

Fig. 5. Photograph of the proposed antenna; (a) top view and (b) bottom view.

Figure 6 shows the current distributions at dual center notched bands. The dimensions of two 90 degree rotation angle complementary SRRs are corresponding to the dual notched bands. When the antenna is working at the center of lower notched band near 3.9 GHz, the outer complementary SRR behaves as a separator as shown in Fig. 6 (a), which almost has no relation to the other band-notched. Similarly, from Fig. 6 (b), the upper notched band near 5.9 GHz is ensured by the inner complementary SRR.

III. RESULTS AND DISCUSSION

The VSWR performance of the fabricated prototype was measured with an Agilent 85052C vector network analyzer. Figure 7 shows the simulated and measured VSWRs for the proposed antenna. By introducing the novel 90 degree rotation angle complementary SRR, band-notched function is obtained. The designed antenna has an impedance bandwidth of 2 GHz – 11.2 GHz for VSWR less than 2, except the frequency-notched-band of 3.68 GHz – 4.20 GHz and 5.72 GHz – 6.12 GHz, respectively. Obviously, this measured frequency range covers commercial UWB band (3.1 GHz – 10.6 GHz) and rejects the frequency band of C-band satellite communication systems and IEEE802.11a to overcome the electromagnetic interference (EMI) problems among UWB [22-25]. As shown in Fig. 7, it is also observed the measured notched-band width is slightly wider than the simulated result. This may have been caused by the use of an SMA connector and fabrication error.

The measured far-field radiation patterns of the proposed antenna in the H-plane (*xy*-plane) and E-plane (*yz*-plane) at frequencies 4.75 GHz and 7.5 GHz are plotted in Fig. 8, respectively. Like the behavior of conventional wide slot antennas, the proposed antenna has relatively omni-directional *xy*-plane radiation patterns with non circularity of about 5–8 dB over the operating frequency band [26-28]. The radiation patterns in the *yz*-plane (E-plane) are monopole alike. All the obtained radiation patterns accord with those of the conventional printed UWB monopole antennas. The proposed antenna has proved to be capable of providing favorable spatial-independent band-notched characteristics.

The gain patterns (total realized gain) of the antenna are measured in an anechoic chamber. A fiber-optic link connected to the antenna under test has been used in order to measure the radiation pattern of our proposed compact antenna. This technique aims at limiting alterations of measurement coaxial cable on omni-directional radiation antennas. Figure 9 reveals that the antenna gain ranges from 1.9 dBi to 7 dBi within the 2 GHz – 12 GHz frequency band. Of course, this is except for the notched band decreases significantly to about -8 dBi and -1.5 dBi. This confirms that the proposed antenna provides a high level of rejection to signal frequencies within the notched band. Figure 10 shows the measured radiation efficiency of the antenna. The proposed antenna features an efficiency between 50 % and 70 % over the whole UWB frequency and lower than 5 % in the notch band. The features of about 60 % average radiation efficiency is good enough to satisfy an acceptable variation for practical power transmission.

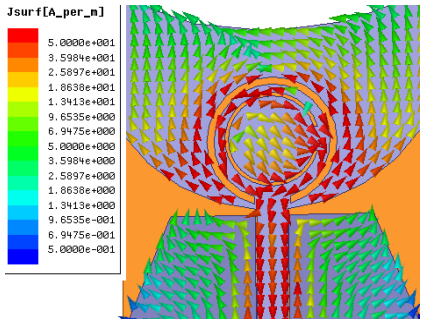

(a)

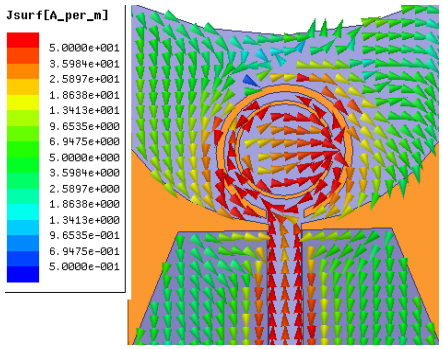

(b)

Fig. 6. The current distribution at (a) 3.9 GHz and (b) 5.9 GHz.

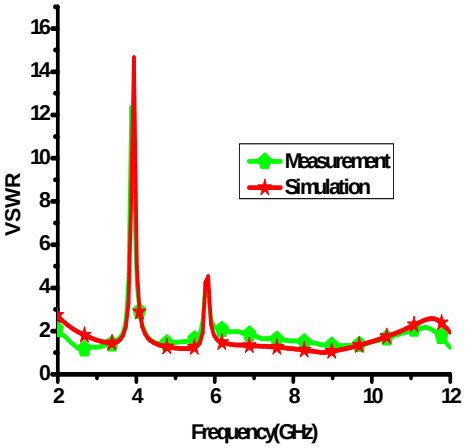

Fig. 7. Comparison of the simulated and measured VSWR of the proposed antenna.

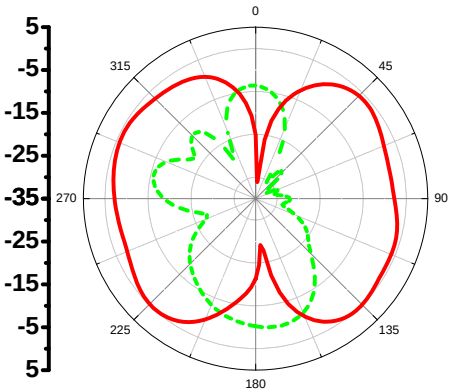

f = 4.75GHz

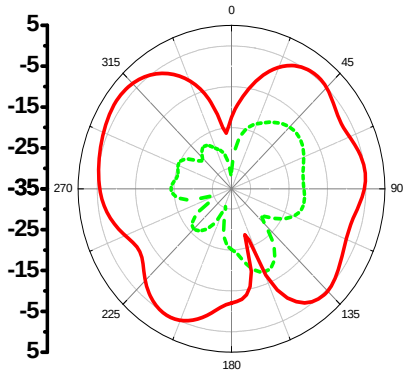

f = 7.5GHz

(a)

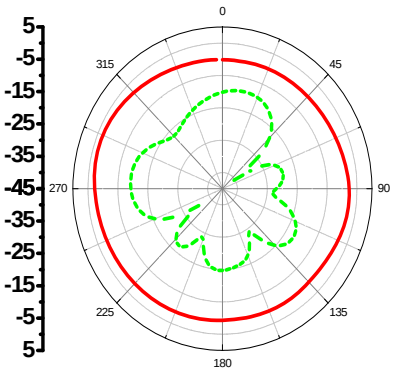

f = 4.75 GHz

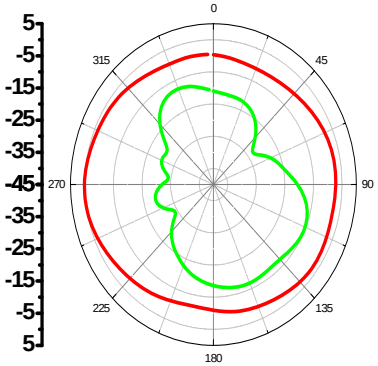

f = 7.5 GHz

(b)

Co-polar: Cross-polar:

Fig. 8. Measured radiation patterns at (a) *yz* -plane and (b) *xy*-plane.

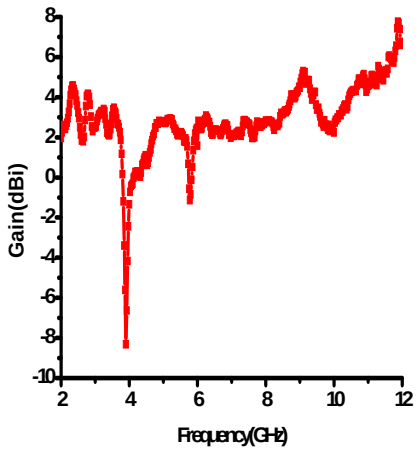

Fig. 9. Measured gain of the proposed antenna.

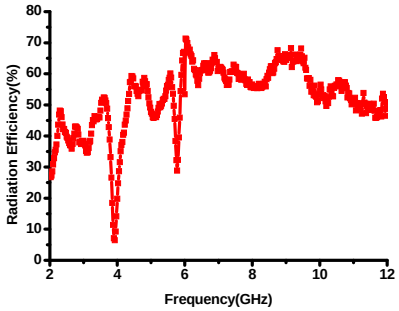

Fig.10. Measured radiation efficiency of the proposed antenna.

IV. CONCLUSION

A very compact CPW-fed UWB printed monopole antenna with dual band-notched characteristics was proposed, fabricated, and discussed. The two designed notched bands were realized by etching 90 degree rotation angle complementary SRRs slots in the radiating patch. The effects of the width and position of the slot in the radiating patch were analyzed to find the optimized configuration of the slot to get a good level of band rejection even at high frequencies. Surface current distributions were used to show the effect of these slots in getting the notched bands. The fabricated antenna showed good agreement between measured and simulated results within a wide bandwidth from 2 GHz to 11.2 GHz and two intended notched bands in asmall size.

ACKNOWLEDGMENT

This work is supported by National Natural Science Foundation of China (Grant No.61106115 and 60971037) and the Fundamental Research Funds for the Central Universities (ZYGX2011J018).

REFERENCES

[1] S. Cheng, P. Hallbjorner, and A. Rydberg, "Printed slot planar inverted cone antenna for ultra-wideband applications," *IEEE Antennas and Wireless Propag. lett.*, vol. 7, pp. 18-21, 2008.

[2] A. Foudazi, H. R. Hassani, and S. M. Alinezhad, "Small UWB planar monopole antenna with added GPS/GSM/WLAN bands," *IEEE Trans. on Antennas and Propagation*, vol. 60, no. 6, pp. 2987-2992, June 2012.

[3] Y. Sung, "UWB monopole antenna with two notched bands based on the folded stepped impedance resonator," *IEEE Antennas and Wireless Propag. lett.*, vol. 11, pp. 500-502, 2012.

[4] M. Mighani, M. Akbari, and N. Felegari, "A novel SWB small rhombic microstrip antenna with parasitic rectangle into slot of the feed line,"" *Appl. Comp. Electro. Society (ACES) Journal*, vol. 27, no. 1, pp. 74-79, Jan. 2012.

[5] D. S. Javan and O. H. Ghouchani, "Cross slot antenna with U-shaped tuning stub for ultra wideband applications,"" *Appl. Comp. Electro. Society (ACES) Journal*, vol. 24, no. 4, pp. 427-432, August 2009.

[6] C. -Y. Huang, S. -A. Huang, and C. -F. Yang, "Band-notched ultra-wideband circular slot antenna with inverted C-shaped parasitic strip," *Electron. lett.*, vol. 45, no. 25, Dec. 2009.

[7] M. Mighani, M. Akbari, and N. Felegari, "A CPW dual band notched UWB antenna,"" *Appl. Comp. Electro. Society (ACES) Journal*, vol. 27, no. 4, pp. 352-359, April 2012.

[8] L. -H. Ye and Q. -X. Chu, "Improved band-notched UWB slot antenna," *Electron. lett.*, vol. 44, no. 15, July 2008.

[9] N. Farrokh-Heshmat, J. Nourinia, and C. Ghobadi, "Band notchd ultra-wideband printed open-slot antenna using variable on-ground slits," *Electron. lett.*, vol. 45, no. 21, Oct. 2008.

[10] W. J. Lui, C. -H. Cheng, and H. B. Zhu, "Improved frequency notched ultra-wideband slot antenna using square ring resonator," *IEEE*

Trans. on Antennas and Propagation, vol. 55, no. 9, pp. 2445-2450, Sep. 2007.

[11] T. Li, H. Zhai, G. Li, L. Li, and C. Liang, "Compact UWB band-notched antenna design using inter digital capacitance loading loop resonator," *IEEE Antennas And Wireless Propag. lett.*, vol. 11, pp.724-727, 2008.

[12] R. Azim, M. T. Islam, and N. Misran, "Design of a planar UWB antenna with new band enhancement technique," *Appl. Comp. Electro. Society (ACES) Journal*, vol. 26, no. 10, pp. 856-862, Oct. 2011.

[13] C. -T. Chuang, T. -J. Lin, and S. -J. Chung, "A band-notched UWB monopole antenna with high notch-band-edge selectivity," *IEEE Trans. on Antennas and Propagation*, vol. 60, no. 10, pp. 4492-4499, Oct. 2012.

[14] L. - H. Ye and Q. - X. Chu, "3.5/5.5 GHz dual band-notch ultra-wideband slot antenna with compact size," *Electron. lett.*, vol. 45, no. 25, March 2010.

[15] B. S. Yildirim, B. A. Cetiner, G. Roqueta, and L. Jofre, "Integrated bluetooth and UWB antenna," *IEEE Antennas and Wireless Propag. lett.*, vol. 8, pp. 149-152, 2009.

[16] D. Jiang, Y. Xu, R. Xu, and W. Lin, "Compact dual-band-notched UWB planar monopole antenna with modified CSRR," *Electron. Lett.*, vol. 48, no. 20, pp. 1250-1252, Sep. 2012.

[17] J. William and R. Nakkeeran, "A new UWB slot antenna with rejection of WiMax and WLAN bands," *Appl. Comp. Electro. Society (ACES) Journal*, vol. 25, no. 9, pp. 787-793, Sep. 2010.

[18] C. -M. Wu, Y. -L. Chen, and W. -C. Liu, "A compact ultra wideband slotted patch antenna for Wireless USB dongle application," *IEEE Antennas and Wireless Propag. lett.*, vol. 11, pp. 596-599, 2012.

[19] I. -J. Yoon, H. Kim, and Y. J. Yoon, "UWB RF receiver front-end withband-notch characteristic of 5 GHz WLAN," *Proc. IEEE Int. Antennas and Propagation Symp. Digest*, pp. 1303-1306, July 2006.

[20] W. Jiang and W. Che, "A novel UWB antenna with dual notched bands for WiMAX and WLAN applications," *IEEE Antennas And Wireless Propag. lett*., vol. 11, pp. 293-5296, 2012.

[21] J. Kim, C. S. Cho, and J. W. Lee, "5.2 GHz notched ultra-wideband antenna using slot-type SRR," *Electron. Lett.*, vol. 42, no. 6, pp. 315-316, 2006.

[22] K. -H. Kim and S. -O. Park, "Analysis of the small band-rejected antennawith the parasitic strip for UWB," *IEEE Trans. Antennas Propag.*, vol. 54, no. 6, pp. 1688-1692, 2006.

[23] C. -C. Lin, P. Jin, and R. W. Ziolkowski, "Single, dual and tri-band-notched ultra wideband (UWB) antennas using capacitively loaded loop (CLL) resonators," *IEEE Trans. on Antennas and Propagation*, vol. 60, no. 1, pp. 102-109, Jan. 2012.

[24] R. Fallahi, A. -A. Kalteh, and M. G. Roozbahani, "A novel UWB elliptical slot antenna with band-notched characteristics," *Prog. Electromag. Res.*, PIER 82, pp. 127-136, 2008.

[25] M. N. -Jahromi and N. K. -Barchloui, "Analysis of the behavior of Sierpinski carpet monopole antenna," *Appl. Comp. Electro. Society (ACES) Journal*, vol. 24, no. 1, pp. 32-36, Feb. 2009.

[26] M. N. -Moghadasi, G. R. DadashZadeh, A. -A. Kalteh, and B. S. Virdee, "Design of a novel band-notched slot patch antenna for UWB communication systems," *Microw. Opt. Technol. Lett.*, vol. 52, no. 7, pp. 1599-1603, 2010.

[27] C. J. Panagamuwa, A. Chauraya, J. C. Vardaxoglou, "Frequency and beam reconfigurable antenna using photo conducting switches," *IEEE Trans. Antennas Propag.*, vol. 54, no. 2, pp. 449-454, 2006.

[28] S. Nikolaou, N. D. Kingsley, G. E. Ponchak, J. Papapolymerou, and M. M. Tentzeris, "UWB elliptical monopoles with a reconfigurableband notch using MEMS switches actuated without bias lines," *IEEE Trans. Antennas Propag.*, vol. 57, no. 8, pp. 2242-2251, 2009.

Di jiang received the B.Sc. degree in Communication Engineering from the GuiLin University of Electronic Technology (GLIET), China, in 2004, and is currently pursuingthe Ph.D. degree in Electromagnetic Field and Microwave Technology at the University of Electronic Science and Technology of China(UESTC), Chengdu, China. His research interest includes miniature antenna, RF circuit, and metamaterial design and its application.

Yuehang Xu received the B. Sc, M.Sc., and Ph.D. Degrees in 2004, 2007, and 2010, respectively in electromagnetic field and microwave technology from the University of Electronic Science and Technology of China(UESTC). He was a visiting scholar in Columbia University working on graphene RF devices during Sep. 2009 to Sep. 2010. He has been a lecture in UESTC since 2010. His research interests include wide band-gap semiconductor material and graphene based RF devices.

Ruimin Xu received the Ph.D. Degree in Electrical Engineering from the University of Electronic Science and Technology of China (UESTC), Chengdu, China. At present as a university of electronic science and technology extremely high frequency complex system, deputy director of the national defense key discipline laboratory. The main research fields including microwave millimeter-wave circuits and systems, microwave monolithic integrated circuit.

Ganwei Lin born at Guang Dongtaishan county. The Father of Microwaves in China, Chinese communist party members, Chinese academy of sciences, University of Electronic Science and Technology of China, professor, doctoral supervisor. China electronics association, member of IEEE microwave theory and technology to Beijing branch chairman.

Substrate Integrated Waveguide-Fed Tapered Slot Antenna With Smooth Performance Characteristics Over an Ultra-Wide Bandwidth

Lisa S. Locke [1, 2], Jens Bornemann [1], and Stéphane Claude [2]

[1] Department of Electrical Engineering
University of Victoria, Victoria, BC V8W 3P6, Canada
lsl@uvic.ca, j.bornemann@ieee.org

[2] Herzberg Institute of Astrophysics, Victoria, BC, V9E 2E7, Canada
Stéphane.Claude@nrc-cnrc.gc.ca

Abstract ─ We present an ultra-wide extended K-band (18 GHz – 30 GHz) planar linear tapered slot antenna (LTSA) design. From a parametric study involving eight designs, the best compromise LTSA is selected in terms of flattest gain and beam width and most symmetric beam width. The design is antipodal with alumina ($\varepsilon_r = 10$) substrate and fed with substrate integrated waveguide (SIW). Regular corrugations improve cross-polarization, input return loss, and gain. Numerical simulations use finite element analysis and time domain finite integration technique field solvers. The resulting design has half power beam widths (HPBW) of only ± 3.2° and ± 2.5° variation in frequency in the E- and H-planes, respectively. Cross-polarization levels at boresight are 35.7 dB at 18 GHz and 17.4 dB at 30 GHz, return loss is better than -11.7 dB and gain is 9.23 dB with ± 0.40 dB variation with frequency. Alternatively, for imaging systems requiring efficient illumination of a reflector or focusing elements, a second resulting design shows near-perfect beam symmetry with $HPBW_E/HPBW_H = 0.91$. These two LTSAs are good candidates for dual-polarization focal plane array feed applications in astronomy imaging.

Index Terms ─ Antipodal tapered slot antenna, beam width, gain, polarization, substrate integrated waveguide, and ultra-wideband.

I. INTRODUCTION

Microwave and millimeter wave astronomy telescopes with mature low noise single pixel receivers are being upgraded with focal plane arrays for faster survey speeds at lower manufacturing costs. This step in instrumentation requires a low-profile, compact, and easily-fabricated antenna element to incorporate into a dual-polarized array, which has been accomplished for general phased arrays [1] and more recently for radio astronomy in the L Band (1 GHz - 2 GHz) [2, 3]. Looking ahead to higher frequencies, it is required to determine a suitable antenna element and array architecture to allow for a two dimensional densely packed array, having a feeding structure with appropriate impedance match, with the capability to work at millimeter wavelengths and active component integration. A planar imaging array in the ultra-wide extended K-band (18 GHz – 30 GHz) will demonstrate suitable antenna architecture and feeding type for use in conjunction with reflectors for an astronomy millimeter wave focal plane array.

An ideal antenna element for this application is the tapered slot antenna (TSA) because it is highly directive and compact. Gibson's TSA antenna [4], termed "Vivaldi" is a planar end fire antenna with an exponential taper. The electromagnetic wave propagates along the increasingly separated metalized tapers until the distance between the edges is large enough to allow wave separation from the antenna structure and thus radiation occurs. An early comprehensive study [5] of the TSA element illustrates the beam width and the impedance effects of various dielectric substrates and taper shapes. A follow-up investigation of the arrays of the TSA elements [6] introduces the important concept of effective dielectric thickness, t_{eff}, and the recommended range of t_{eff} to ensure the

Submitted On: Aug. 2, 2012
Accepted On: Mar. 16, 2013

main beam integrity. Due to its planar nature and narrow width, the TSA elements can be placed with minimal transverse spacing without adversely affecting the performance.

Due to its popularity and ease of planar circuit integration, there are other variations beside the linear TSA and the Vivaldi antenna, which include the continuous width slot antenna (CWSA), bunny-ear or balanced antipodal Vivaldi antenna (BAVA) [7], and the Fermi antenna [8]. Moreover, number of different feed structures for TSAs are presented. For the antipodal TSA, a microstrip feed is an easy and obvious choice. In the millimeter wave range, however, microstrip technology is increasingly lossy and, therefore, such designs do not lend themselves to be scaled to 100 GHz applications. Thus, they are usually used in the lower Gigahertz frequency range [9, 10]. A uniplanar TSA can be fed by a coplanar waveguide (CPW) circuit. However, such a feed is narrowband and requires a number of tuning slots [11], whose sizes and configurations are not well suited for in line feeding techniques at millimeter wave frequencies. The wire model of the TSA presented in [12] is interesting, especially including the use of reflector elements, but this technique, in a millimeter wave printed circuit version, will experience the same high losses as the microstrip technology.

Therefore, our proposed feed structure is a substrate integrated waveguide (SIW) [13], an innovative planar transmission line paradigm that allows for waveguide like transmission and offers a compromise between bulky expensive waveguide and lossy planar microstrip. The SIW performs as a planar waveguide, with substrate metalized on both top and bottom surfaces and is flanked by two parallel arrays of circular via holes, which allows for a contained propagating wave. Short SIW transitions to microstrip [14] or coplanar waveguide [15] are provided for integration with MMICs. The combination of planar antipodal LTSA elements and SIW feeding structure is ideally suited for array imaging systems due to its compact nature, high gain, and excellent beam symmetry and frequency scalability above 100 GHz.

The antipodal LTSA with SIW feed, as shown in Fig. 1, has flared metallic faces on opposite sides of the alumina substrate matching the two conductor SIW feed perfectly. In the SIW, the electric field is oriented perpendicular to the substrate as shown in the bottom view of Fig. 1. This is similar to the fundamental mode in an all-dielectric waveguide. As the top and bottom metallization begin to flare, the electric field, due to the changing boundary conditions, is slowly rotated to be parallel with the substrate in the antenna aperture. Note that this transition is extremely wideband and covers the entire fundamental mode range of the feeding substrate integrated waveguide.

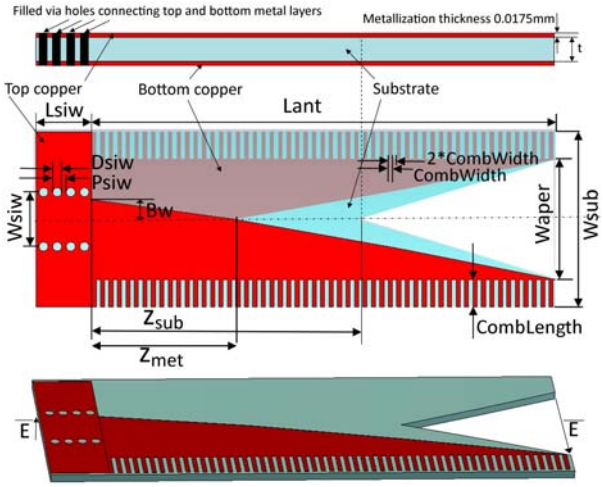

Fig. 1. Antipodal LTSA with SIW feed with a cross sectional view showing top copper metal layer, substrate, bottom copper metal layer, and metal filled via holes that electrically connect top and bottom layers. A Plan view is presented with slightly transparent substrate, and a perspective view. The antenna is sensitive to the horizontal E-fields across the aperture; the antipodal flares rotate the E-vector to a vertical E-field at the SIW feed.

Antipodal LTSAs have poor cross-polarization performance [16] due to the non-zero transverse distance between the metal faces allowing the small unwanted perpendicular (cross-polar) component to the co-polar field. To remedy this, comb-like corrugations are cut out of the metalized layers along the antenna's outside length to improve the main beam shape and reduce sidelobe levels [17].

In this paper, we propose additional benefits of corrugations, which includes improved cross-polarization, reduced VSWR ,and increased on-axis gain. We demonstrate over the extended K-band frequency range of 18 GHz - 30 GHz a constant beam width, constant gain TSA utilizing side corrugations that significantly improve the cross-polarization performance and the input return loss.

II. DESIGN

The antipodal TSA with SIW feed input is shown in Fig. 1. The alumina substrate has copper top and bottom faces and a triangular cut at the aperture end to reduce the discontinuity between the substrate and the free space, thus improving the input return loss. Along the outside edges of the antenna regular comb-like corrugations are cut into the metallized top and bottom layers.

The substrate, 0.381 mm alumina ceramic (Al_2O_3), has excellent thermal conductivity; 31 W/mK at 20°C for active component heat dissipation and a high mechanical strength. The high relative permittivity $\varepsilon_r = 10$ is needed to reduce the total width of the SIW feed by sqrt(ε_r). Since a focal plane array is intended, the distance between each antenna should be $W_{sub} \leq \lambda_0/2$ to avoid grating lobes [6]. The integrated antipodal antenna and feed structure is displayed in Fig. 1 and the dimensions are listed in Table 1.

Table 1: LTSA and feed parameters.

W_{siw}	Via hole center-to-center spacing in y-direction	3.6 mm
D_{siw}	Via hole diameter	0.6 mm
P_{siw}	Via hole center-to-center spacing in z-direction	0.9 mm
L_{siw}	Length of SIW feeding section	3.7 mm
Bw	Distance from center to start of metalized flare	1.3 mm
Comb-width	Corrugation width in z-direction	0.28 mm
t	Thickness of substrate	0.381 mm
ε_r	Relative permittivity of ceramic alumina (Al_2O_3)	10
W_{siweff}	Equivalent waveguide width	3.138mm

Yngvesson in [6] provides a general formula for the effective substrate thickness, $t_{eff} = t$*sqrt(ε_r – 1) and the optimum range is normalized to free space wavelength λ_0 for main lobe integrity and low sidelobes,

$$0.005 < t_{eff} / \lambda_0 < 0.03. \quad (1)$$

Despite being above this range, at t_{eff} / λ_0 = 0.049, 0.082 for 18 GHz and 30 GHz, respectively, the main beam and sidelobes are acceptable. For future arrays at higher frequencies, the inequality will be more difficult to satisfy and will largely determine the type of dielectric required. Figure 2 plots the upper and lower bounds of equation (1) as a function of frequency for two dielectrics, Rogers RT/Duroid 5880 and alumina, ε_r = 2.94 and 10, respectively.

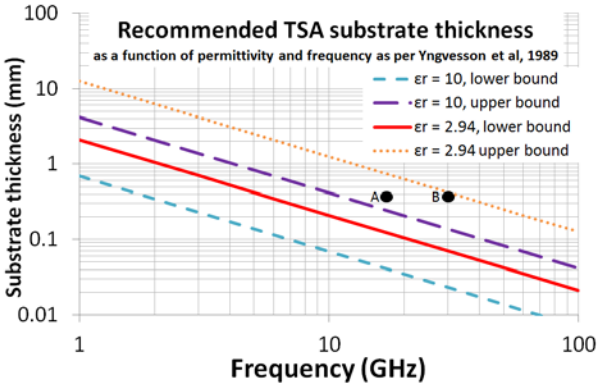

Fig. 2. Upper and lower bounds to Yngvesson's recommended range for a substrate thickness t_{eff} of ε_r = 10 (alumina) and 2.94 (Rogers RT/Duroid 6002). Points are marked for 18 GHz (A) and 30 GHz (B) for a 0.381 mm alumina substrate.

A. SIW parameters

Using standard waveguide equations [18], the cut-off frequency of the SIW circuit with ε_r = 10 and W_{siw} = 3.6 mm can be analyzed by computing W_{siweff} = 3.138 mm, the width of an equivalent waveguide section with the same ε_r. For a cut-off frequency of 15.1 GHz in alumina, the equivalent TE_{10} waveguide has a width a = 3.141 mm. This allows for single-mode operation up to 30.2 GHz.

B. Taper

The taper is basically linear, with opening rate R = 0.05 and shape determined by $z = c_1 e^{Ry} + c_2$ where c_1 and c_2 are the coordinates of the first and last points of the exponential.

C. Simulation setup

The coordinate system is oriented so that the substrate is in the y-z plane with x being the transverse direction (height), z is the propagation direction. As per convention, φ is measured from x in the x-y plane and θ is measured from z. Because the electric field vector is perpendicular to the metal faces, it is oriented in the x direction in the SIW

region and in the y-direction at the aperture as the tapers transition to free space (c.f. Fig. 1, bottom). Thus the E-plane is y-z at φ = 90° and the H-plane is x-z at φ = 0°. Table 2 outlines eight designs varying substrate width W_{sub}, aperture width W_{aper}, total length L_{ant}, metal crossover point z_{met}, and substrate cut length z_{sub}, defined in Fig. 1 and depicted in Fig. 3.

Table 2: Antenna dimensions in mm for designs 1 through 8 as defined in Fig. 1. λ_0 = 12.5 mm, the free space wavelength at mid-band, i.e., 24 GHz. λ_{er} = 4.0 mm, the wavelength in alumina dielectric.

	W_{sub}	W_{aper} (λ_0)	L_{ant} (λ_{er})	z_{met}	z_{sub}
1	10.2	5.8 (.46)	89.7 (22.7)	27.6	51.2
2	11.2	6.8 (.54)	89.7 (22.7)	27.6	51.2
3	12.4	8.0 (.64)	89.7 (22.7)	27.6	51.2
4	11.6	8.0 (.64)	89.7 (22.7)	27.6	51.2
5	11.6	8.0 (.64)	62.8 (15.9)	19.3	35.9
6	11.6	8.0 (.64)	44.0 (11.1)	13.5	25.1
7	11.6	8.0 (.64)	30.8 (7.8)	9.5	17.6
8	11.6	8.0 (.64)	21.5 (5.4)	6.6	12.3

Designs 1 to 4 vary based on the aperture opening W_{aper} and the antenna width W_{sub} (c.f. Fig. 1) while keeping the antenna length L_{ant} constant at 89.7 mm. Designs 5 to 8 vary based on the L_{ant} from 89.7 mm to 21.5 mm, with the widths W_{aper} = 8 mm and W_{sub} = 11.6 mm held constant. Design 1 was modeled after Dousset [19]. In all designs, the goal is to achieve constant gain, constant beam width, and symmetric beams, along with keeping the input return loss and the cross-polarization as good as possible.

Ansoft HFSS finite-element solver (FEM) and CST microwave studio time domain finite integration technique solver (FIT) are used to calculate the S-parameters, far-field gain, HPBW, and cross-polar levels. The spherical coordinate system with Ludwig 3 polarization definition is used [20]. Comparing field solvers results in similar input return loss characteristics are shown in Fig. 4.

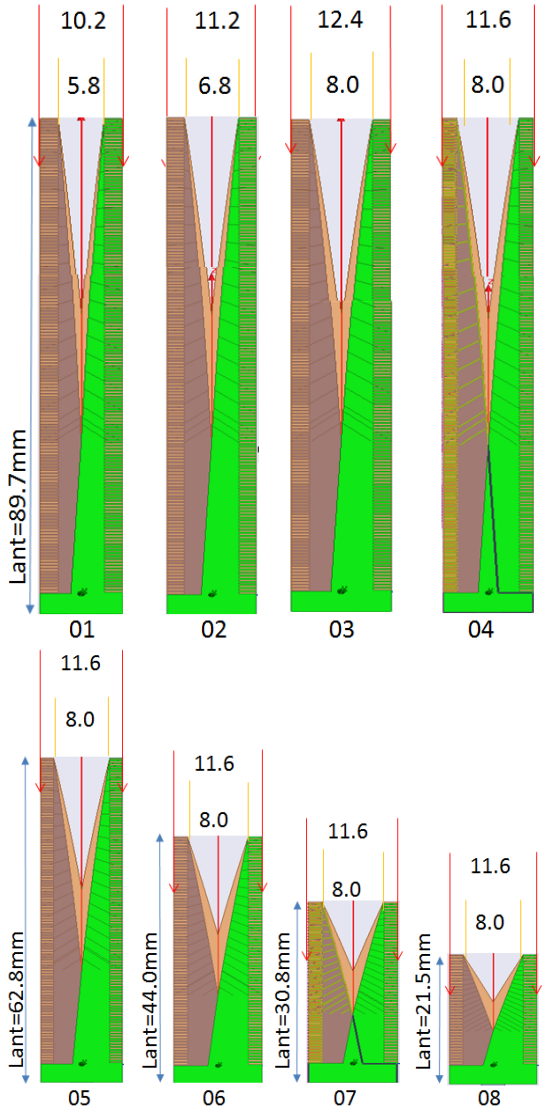

Fig. 3. LTSA dimensions for designs 1 through 8. W_{sub}: the antenna width is the upper number (mm). W_{aper}: the opening aperture width is the lower number (mm).

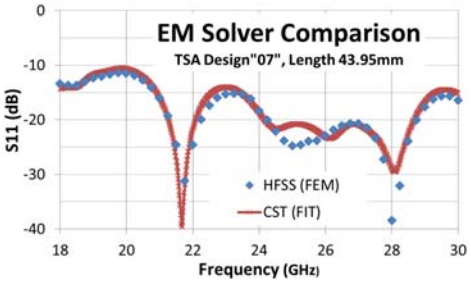

Fig. 4. Field solver comparison for design 7.

III. RESULTS

A. Input return loss

The input return loss is measured at the waveguide port, and the results incorporate both the feed and the antenna element. As seen in Fig. 5, the input return loss values for designs 1 to 4 are very similar, trending from -12 dB to -25 dB at the band edges.

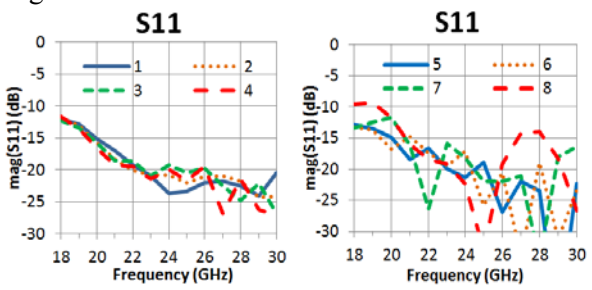

(a) (b)

Fig. 5. Input return loss versus frequency, designs (a) 1 to 4 and (b) 5 to 8.

For the shorter length designs 5 to 8, the return loss stays below -15 dB from 21 GHz to 30 GHz except for the shortest; design 8 rises to -14 dB at the upper edge of the band. Over 18 GHz to 30 GHz, designs 1 to 5 have input return loss values better than -15 dB for 20 GHz to 30 GHz.

B. Gain

The first design goal is a flat co-polar gain response throughout the 18 GHz to 30 GHz band. Figure 6 shows designs 1 to 4 having gains varying at least 3 dB with a positive gain slope. Varying the width produces minimal change to the gain response. However, the shorter lengths in designs 6 to 8 show an increased gain at low frequencies and remarkably flat gain curves. The least variation with frequency is achieved by design 7 with only 0.8 dB (9 % of mean value, 9.23 dB) followed closely by design 8 with 1.1 dB (12 % of mean value 9.00 dB) variation. Decreasing the length beyond that of design 8 reduces the gain significantly, which is not recommended.

C. Beam width

The second goal is a constant beam width in E- and H-planes versus frequency. Gazit in [21] indicates that the radiation mechanism, aperture or travelling wave, is dependent on the opening aperture width, W_{aper}. When $W_{aper} > 2\lambda$, the antenna operates as a travelling wave antenna. For $W_{aper} < 2\lambda$ the antenna operates as an aperture antenna and the E- and H-plane beam widths decrease with frequency. All designs from 1 to 8 are within the aperture antenna region and, as expected, the half-power beam widths generally decrease with frequency.

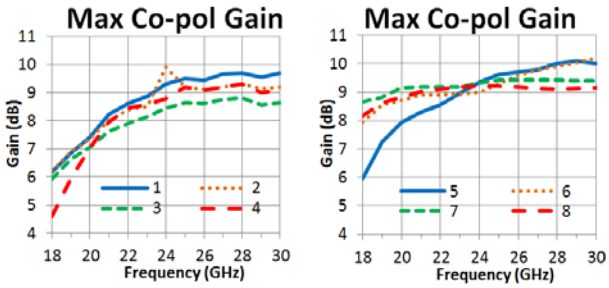

(a) (b)

Fig. 6. Co-polar gain versus frequency for designs (a) 1 to 4 and (b) 5 to 8 at θ = 0°. Flattest gain is design 7 with 0.8 dB variation across the band.

For each design, the E-plane (φ = 90°, θ = 0°) HPBW is shown in Fig. 7 and H-plane (φ = 0°, θ = 0°) HPBW is shown in Fig. 8. The flattest beam width versus frequency is achieved by design 7. The average HPBW over frequency and percent variation is: E-plane 49° ± 3.2°, 13 %, and H-plane 69° ± 2.5°, 7 %. However, the most symmetric is design 1: E-plane 41.3° ± 7.5° and H-plane 45.1° ± 10.6°. E- to H-plane HPBW ratios as a function of design number are shown in Fig. 9. A ratio of 1.0 represents a perfectly symmetric beam with equal E- and H- beam widths. Design 1 has the most symmetric beam at $HPBW_E/HPBW_H = 0.91$ and the least symmetric beam is for design 8 at 0.65.

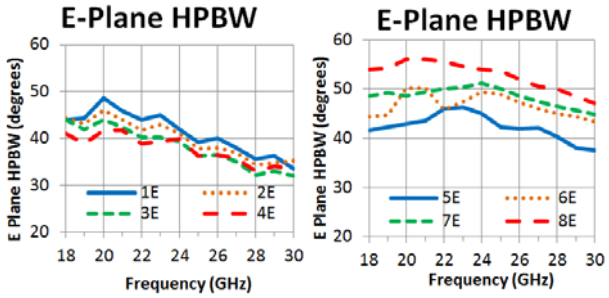

(a) (b)

Fig. 7. E-plane HPBW for designs (a) 1 to 4 and (b) 5 to 8.

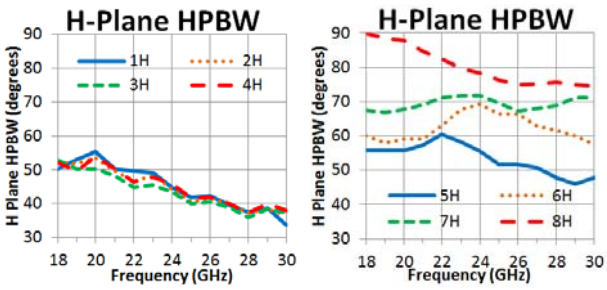

(a) (b)

Fig. 8. H-plane HPBW for designs (a) 1 to 4 and (b) 5 to 8.

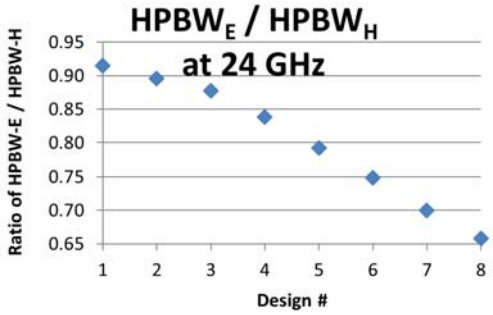

Fig. 9. A measure of the beam symmetry for the E- to H-plane HPBW ratio.

D. Effect of corrugations

The metal top and bottom faces have corrugated cuts placed axially along the outside length of the antenna. The mid-band far field gain patterns versus θ for the three principle planes E (φ = 90°), D (φ = 45°) and H (φ = 0°), with and without corrugations are shown in Fig. 10 for design 1 and Fig. 11 for design 7; summarized results are in Table 3.

As with Sato's Fermi antenna with corrugations [22], a parallel mode is seen in the current phase distribution along the taper and on the outer edges of the antenna. This mode is reduced when using corrugations, leading to improved input return loss and cross-polarization levels.

Although the corrugation effects on radiation patterns are only shown for designs 1 and 7, in every design the presence of corrugations increases the bore sight gain, improved cross-polarization response and reduced S11 are shown in Fig. 12. The combination of the increased on-axis gain and the reduced D-plane cross-polarization values off-axis significantly widens the useable beam width, which are free of cross-polarization, up to scan angles of ± 30°. Comparing the performances of designs 1 to 8, it is concluded that design 7 provides the best compromise towards an ultra-wideband, flat beam width, flat gain, and low return loss performance. However, it should be noted that design 1 presents an alternative solution with the most symmetric beam, ideal for imaging systems requiring efficient illumination of a reflector or lens. Cross-polarization levels of 28.2 dB at 18 GHz, 14.7 dB at 30 GHz and a maximum return loss of -12.0 dB are on par with design 7. The small positive gain slope (6.2 dB to 9.7 dB) of this antenna design can be cancelled out in the receiver chain.

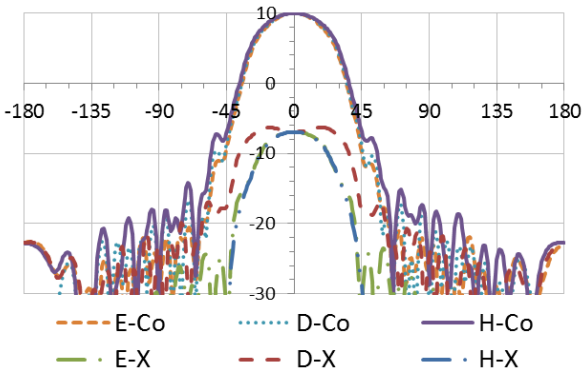

(a)

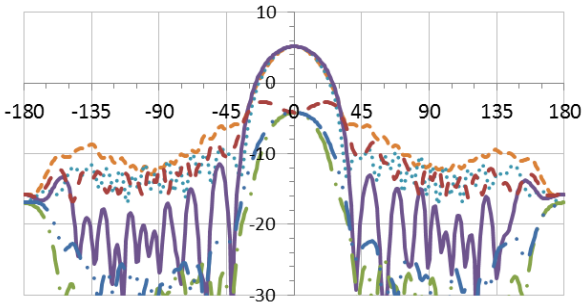

(b)

Fig. 10. Far field gain patterns versus θ in degrees, 24 GHz, design, for (a) with corrugations and (b) without corrugations; showing both co- (Co) and cross- (X) polarizations.

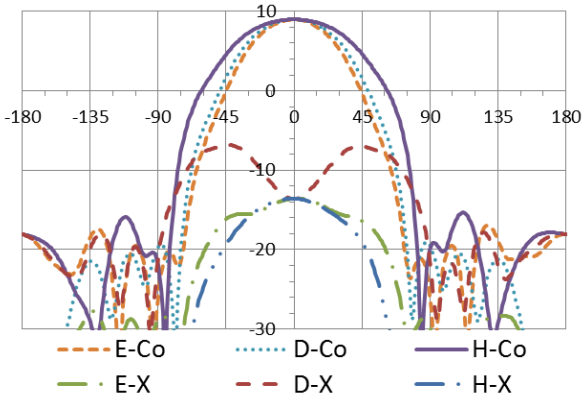

(a)

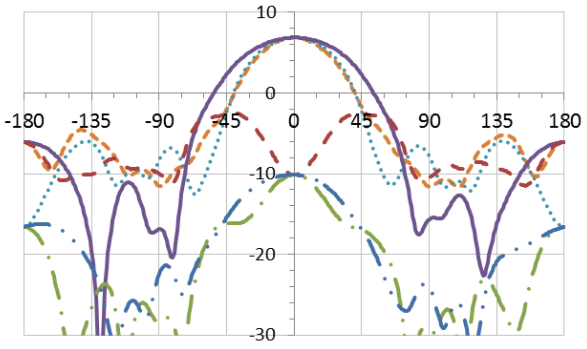

(b)

Fig. 11. Far field gain patterns versus θ in degrees, 24 GHz, design 7, for (a) with corrugations and (b) without corrugations; showing both co- (Co) and cross- (X) polarizations.

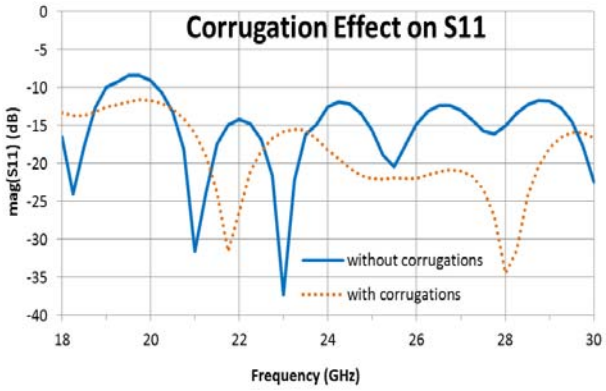

Fig. 12. Corrugation effect on the input return loss versus frequency in GHz for design 7. All designs show similar improvement with corrugations.

Table 3: Radiation pattern data from Figs. 10 and 11, with and without corrugations. The cross-polarization free beam width in the D-plane: Co-pol–X-pol ≥ 10°.

	Design 1		Design 7	
Corrugations?	**Yes**	**No**	**Yes**	**No**
Cross-pol (dB) at boresight	19.6	13.5	33.4	16.7
Peak Gain (dB)	1.0	0.3	6.7	9.2
HPBW E-plane	43°	33°	51°	51°
HPBW H-plane	42°	33°	57°	54°
HPBW D-plane	45°	36°	71°	66°
HPBW symmetry $HPBW_E/HPBW_H$	0.92	0.91	0.71	0.70
Cross-pol free Beam width	<1°	60°	40°	72°

IV. CONCLUSION

A planar antipodal TSA element for use in the ultra-wide extended K Band, 18 GHz - 30 GHz with SIW input feed network is selected from a parametric study. The design uses ceramic alumina substrate and takes advantage of regular corrugations along the outside axial length of the antenna. Simulation results of design 7 show a 12 % gain variation, 13 % and 7 % HPBW variations in the E- and H-planes, respectively, over the band. Cross-polarization levels at the bore sight vary from 35.7 dB at 18 GHz to 17.4 dB at 30 GHz, and the return loss stays below -11.7 dB. Alternatively, design 1 has excellent beam symmetry ($HPBW_E/HPBW_H$ = 0.91) and cross-polarization (19.6 dB at 24 GHz) and would be ideal for efficiently illuminating a focusing element such as a reflector or lens. Thus both LTSA designs 1 and 7 presented show excellent performance for ultra-wideband dual-polarization focal plane array feed applications.

ACKNOWLEDGMENT

The authors would like to acknowledge support of this work from the National Science and Engineering Research Council of Canada.

REFERENCES

[1] H. Holter, T. -H. Chio, and D. Schaubert, "Experimental results of 144-element dual-polarized endfire tapered-slot phased arrays," *IEEE Trans. Antennas Propagat.*, vol. 48, pp. 1707-1718, 2000.

[2] W. A. van Cappellen and L. Bakker, "APERTIF: phased array feeds for the Westerbork synthesis radio telescope," *IEEE Int. Symp. Phased Array Systems Tech.*, pp. 640-647, Waltham, MA, Oct. 2010.

[3] B. Veidt, G. Hovey, T. Burgess, R. Smegal, R. Messing, A. Willis, A. Gray, and P. Dewdney, "Demonstration of a dual-polarized phased-array feed," *IEEE Trans. Antennas Propagat.,* vol. 59, pp. 2047-2057, 2011.

[4] P. Gibson, "The Vivaldi aerial," *Proc. 9th European Microwave Conf.*, pp. 101-105, Brighton, UK, June 1979.

[5] K. Yngvesson, D. Schaubert, T. Korzeniowski, E. Kollberg, T. Thungren, and J. Johansson, "Endfire tapered slot antennas on dielectric substrates," *IEEE Trans. Antennas Propagat.*, vol. 33, pp. 1392-1400, 1985.

[6] K. S. Yngvesson, T. L. Korzeniowski, Y. -S. Kim, E. Kollberg, and J. F. Johansson, "The tapered slot antenna - A new integrated element for millimeter wave applications," *IEEE Trans. on Microwave Theory Tech.*, vol. 37, pp. 365-374, Feb. 1989.

[7] M. W. Elsallal and J. C. Mather, "An ultra-thin, decade (10:10) bandwidth, modular "BAVA" array with low cross-polarization," *IEEE AP-S Int. Symp. Dig.*, pp. 1980-1983, Spokane, WA, July 2011.

[8] S. Sugawara, Y. Maita, K. Adachi, K. Mori, and K. Mizuno, "A mm-wave tapered slot antenna with improved radiation pattern," *IEEE MTT-S Int. Microwave Symp. Dig.*, pp. 959-962, Denver, CO, June 1997.

[9] C. -M. Hsu, L. Murphy, T. -L. Chin, and E. Arvas, "Vivaldi antenna for GPR," *Proc. ACES Conf.*, pp. 490-494, Monterey, CA, Mar. 2009.

[10] T. Namas and M. Hasanovic, "Ultrawideband antipodal Vivaldi antenna for road surface scanner based on inverse scattering," *Proc. ACES Conf.*, pp. 882-887, Monterey, CA, Apr. 2012.

[11] Z. -L. Zhou, L. Li, J. -S. Hong, and B. -Z. Wang, "A novel harmonic suppression antenna with both compact size and wide bandwidth," *ACES Journal*, vol. 27, pp. 435-440, May 2012.

[12] W. O'Keefe Coburn and A. I. Zaghloul, "Wire realization of a tapered slot antenna with reconfigurable elements," *Proc. ACES Conf.*, pp. 324-329, Monterey, CA, Mar. 2011.

[13] D. Deslandes and K. Wu, "Integrated microstrip and rectangular waveguide in planar form," *IEEE Microwave Wireless Comp. Lett.*, vol. 11, pp. 68-70, Feb. 2001.

[14] D. Deslandes, "Design equations for tapered microstrip-to-substrate integrated waveguide transitions," *IEEE MTT-S Int. Microwave Symp. Dig.*, pp. 707-707, Anaheim, CA, 2010.

[15] F. Taringou and J. Bornemann, "New substrate-integrated to coplanar waveguide transition," *Proc. 41st European Microwave Conf.*, pp. 428-431, Manchester, UK, 2011.

[16] N. Fourikis, N. Lioutas, and N. Shuley, "Parametric study of the co- and cross-polarisation characteristics of tapered planar and anitpodal slotline antennas," *IEE Proc. Microw. Antennas Propag.*, vol. 140, pp. 17-22, Feb. 1993.

[17] S. Sugawara, Y. Maita, K. Adachi, K. Mori, and K. Mizuno, "Characteristics of a mm-wave tapered slot antenna with corrugated edges," *IEEE MTT-S Int. Microwave Symp. Dig.*, pp. 533-536, Baltimore, MD, June 1998.

[18] L. Yan, W. Hong, G. Hua, J. Chen, K. Wu, and T. Cui, "Simulation and experiment on SIW slot array antennas," *IEEE Microwave Wireless Comp. Lett.,* vol. 14, pp. 446-448, Sep. 2004.

[19] D. Dousset, *Développement de Composants SIW dans la Bande 3 d'ALMA (84-116 GHz) et Conception d'une Jonction Orthomode (OMT) dans la Bande 1 d'ALMA (31-45 GHz) en Technologie Guide d'onde*, Ph.D. dissertation, École Polytechnique de Montréal, Montreal, Canada, Aug. 2010.

[20] A. Ludwig, "The definition of cross-polarisation," *IEEE Trans. Antennas Propag.*, vol. 21, pp. 116-119, 1973.

[21] E. Gazit, "Improved design of the Vivaldi antenna," *IEE Proc. Microw. Antennas Propag.*, vol. 135, pp. 89-92, Apr. 1988.

[22] H. Sato, K. Sawaya, N. Arai, Y. Wagatsuma, and K. Mizuno, "Broadband FDTD analysis of Fermi antenna with narrow width substrate," *IEEE AP-S Int. Symp. Dig.*, pp. 261-264, Columbus, OH, June 2003.

Lisa Shannon Locke was born in the Northwest Territories, Canada. She received the B.Sc. degree in Electrical Engineering from the University of Alberta, Edmonton, AB, Canada in 1997 and a M.Sc. degree in Electrical Engineering in 2001 from the University of Cape Town, South Africa. She worked as a student engineer for the California Institute of Technology on a K-band water vapor radiometer at the millimeter array at Owens Valley Radio Observatory in 1996. She continued work on water vapor radiometers at the National Radio

Astronomy Observatory, Green Bank, WV on a 86-GHz tipping radiometer and the prime-focus L-band receiver for the Green Bank Telescope. For five years she was with the receiver group at the National Astronomy and Ionosphere Center's Arecibo Observatory in Puerto Rico. In 2005 she joined the National Radio Astronomy Observatory, Socorro, NM where she was involved with the upgrade of cryogenic receiver front-ends for the expanded very large array (EVLA).

Currently she is working on a PhD degree in electrical engineering at the University of Victoria, BC, Canada and the Hertzberg Institute of Astrophysics, Victoria, BC in the field of focal plane array antennas.

Jens Bornemann received the Dipl.-Ing. and the Dr.-Ing. degrees, both in Electrical Engineering, from the University of Bremen, Germany, in 1980 and 1984, respectively. From 1984 to 1985, he was a consulting engineer. In 1985, he joined the University of Bremen, Germany, as an Assistant Professor. Since April 1988, he has been with the Department of Electrical and Computer Engineering, University of Victoria, Victoria, B.C., Canada, where he became a Professor in 1992. From 1992 to 1995, he was a Fellow of the British Columbia Advanced Systems Institute. In 1996, he was a Visiting Scientist at Spar Aerospace Limited (now MDA Space), Ste-Anne-de-Bellevue, Québec, Canada, and a Visiting Professor at the Microwave Department, University of Ulm, Germany. From 1997 to 2002, he was a co-director of the Center for Advanced Materials and Related Technology (CAMTEC), University of Victoria. From 1999 to 2002, he served as an Associate Editor of the *IEEE Transactions on Microwave Theory and Techniques* in the area of Microwave Modeling and CAD. In 2003, he was a Visiting Professor at the Laboratory for Electromagnetic Fields and Microwave Electronics, ETH Zurich, Switzerland. He has coauthored *Waveguide Components for Antenna Feed Systems. Theory and Design* (Artech House, 1993) and has authored/coauthored more than 250 technical papers. His research activities include RF/wireless/microwave/ millimeter-wave components and systems design, and field-theory-based modeling of integrated circuits, feed networks and antennas.

Dr. Bornemann is a Registered Professional Engineer in the Province of British Columbia, Canada. He is a Fellow IEEE, a Fellow of the Canadian Academy of Engineering and served on the Technical Program Committee of the *IEEE MTT-S International Microwave Symposium* and the Editorial Boards of the *International Journal of Numerical Modeling* and the *International Journal of Electronics and Communication (AEÜ)*.

Stéphane Claude received the Engineering degree in material sciences from the Ecole Nationale Supérieure d'Ingénieurs de Caen, France, 1990 and the PhD degree in Physics from London University, Queen Mary and Westfield College, London, UK, 1996. From 1990 to 1996, he was a research associate at the Rutherford Appleton Laboratory, U.K., where he developed techniques for the fabrication of Superconducting-Insulator-Superconducting (SIS) mixer chips, for low noise sub-millimeter receivers in Radio-Astronomy. Part of his PhD work was to commission a 500 GHz receiver at the James Clerk Maxwell Telescope (JCMT), Hawaii. In 1996 he joined the Herzberg Institute of Astrophysics, B.C., Victoria, Canada where he continued development on low noise receivers for astronomy, including a 200 GHz receiver for the JCMT and a sideband separating mixer design. From 2000 to 2002 he joined the Institut de Radioastronomie Millimétrique (IRAM), Grenoble, France, where he worked on the design of a 275-370 GHz receiver (Band 7) for the Atacama Large Millimetre Array (ALMA). Since 2002, he has been leading the millimeter instrumentation team at the Herzberg Institute of Astrophysics, Victoria, B.C. He was project engineer for the 84-116 GHz receiver (Band 3) developed for the ALMA. He is also adjunct professor at the University of Victoria, Victoria, B.C., Canada. His research interests include millimeter-wave low noise receivers and phased array feeds for radio astronomy.

Broadband Variable Radial Waveguide Power Combiner Using Multi-Section Impedance Matching Technique

Gang Xu, Xue-Song Yang, Jia-Lin Li, and Zhi-Ming Tian

School of Physical Electronics
University of Electronic Science and Technology of China, Chengdu, 610054, China
xsyang@uestc.edu.cn

Abstract ― An L-band spatial variable radial waveguide power combiner with broad bandwidth and high power capacity is proposed. By adopting several techniques simultaneously, including multi-section impedance matching probes, grounded disc, and axial slots, the performance of the power combiner is improved. The parameters of the combiner are calculated, simulated and tested. It has a measured operation bandwidth ranging from 1.2 GHz to 2 GHz with VSWRs less than 1.4 at all ports. The extra insertion losses between the input ports and output port are less than 0.3 dB and the isolation between the input ports is better than 15 dB. The power capacity can reach 600 W and the combining efficiency achieves 90 %. The results from calculation, simulation, and measurement reasonably agree with each other.

Index Terms ― Broadband power combiner, microwave components, multi-section impedance matching, spatial power combiner, and variable radial waveguide.

I. INTRODUCTION

The power combiner/divider has been used extensively in wireless communications and Radar systems [1-4]. Recently, a lot of attention has been paid to the power combiner/divider with high efficiency, high power capacity and broadband characteristics. However, some traditional power combiner/divider, such as Wilkinson power divider, Lange coupler, and branch line coupler are limited by their low combining efficiency [1], while the rectangular waveguide circuits [3-5] are restricted by the difficulty of achieving wide bandwidth due to the cut-off frequency. Besides, quasi-optical cavity [6] and oversized coaxial waveguide power combiner/divider suffer from large insertion loss, although they can achieve wide bandwidth [7, 8]. Compared with the aforementioned ones, radial waveguide combiner/divider has advantages of easy fabrication, wide bandwidth, and high combining efficiency [9-11]. However, there still exist some shortcomings, such as excess insertion losses and poor isolation performance between ports.

In this paper, a three-way spatial power combiner is proposed based on the variable radial waveguide. The developed combiner exhibits good insertion losses between input and output ports, as well as enhanced port-to-port isolation between input ports. Besides, good return losses are given at all ports. In order to improve the port-to-port isolation between input ports, three axial slots are etched on the cavity sidewall. Furthermore, a grounded disc on the wall of the cavity is used to improve the port-to-port isolation performance, as well as the impedance matching. Besides, multi-section matching technology is adopted to improve the impedance matching of the combiner [12]. The paper is organized as follows, section II introduces the design of the power combiner. Section III gives the calculation, simulation, and measurement results. Conclusion is provided in section IV.

II. DESIGN OF THE POWER COMBINER

The proposed three-way spatial power combiner is shown in Fig. 1. The combiner

Submitted On: July 24, 2012
Accepted On: Mar. 18, 2013

consists of a radial waveguide with three peripheral coaxial probes, used as input ports, and one center coaxial probe, used as output port. Each coaxial probe has a cylindrical shape, including three stepped matching sections. The multi-section impedance transformer probe is advantageous to improve the impedance matching of each port [13]. A grounded disc with diameter d_t, located on the wall of the waveguide at the center of the peripheral probes side, is introduced to improve the port-to-port isolation, as well as improve the impedance matching [12]. Furthermore, three axial slots etched on the cylinder sidewall of the radial waveguide, are used to improve the isolation performance between the input ports [14]. According to the perturbation theory, the grounded disc opposite to the output probe weakens the coherent electric field on the output probe, while the axial slots on the sidewall weaken the coherent electric field on the input probes. Consequently, the isolation performance is improved by adopting these two structures substantially. The interaction between probes (including coupling and interference) can be analyzed based on the generalized balance theory [15, 16].

The three peripheral probes are identical and radially distributed at one side of the radial waveguide. Consequently, one of the input coaxial probes can be taken for analysis because of the structural symmetry. The longitudinal section including the output port and one input port is shown in Fig. 1 (b). The probes are fixed in the cavity with the use of poly-tetra-fluorethylene (PTFE). The three matching sections of the output probe are named Matching Sections -1, -2, and -3, and those of the input probe are named Matching Sections -4, -5, and -6, respectively. The lengths and diameters of Matching Sections -1 to -6 are l_1 to l_6 and d_1 to d_6, respectively, as shown in Fig. 1 (b). In order to design the combiner, the distance R_g between the axes of the input and output probes, as shown in Fig. 1 (b), should be calculated. This can be done based on the theory of parallel coupled transmission lines. After that, the output probe and one input probe are analyzed as a two-port network. By this way, the equivalent impedance of each probe can be calculated. According to the multi-section impedance matching theory, the structural parameters of the input and output probes can be obtained, as formulated below.

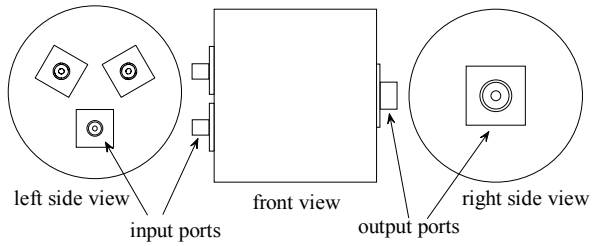

(a) Outside view.

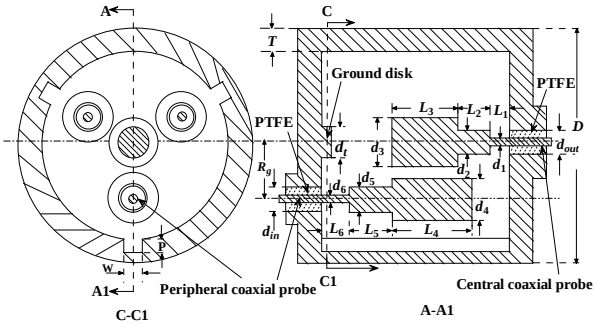

(b) Cross-section view and longitudinal-section view.

Fig. 1. Structure of the three-way variable radial-waveguide power combiner.

For the sake of analysis, each matching section of the probe can be viewed as a virtual coaxial line (inner diameter of d_i and outer diameter of D_i). The inner diameter of the virtual coaxial line is actually the diameter of the matching section. Due to the interaction between the input and output probes, the outer conductor diameter D_i is an equivalent value or calculated value, which is given by the following expressions [10]

$$\begin{cases} D_i = k_i(B-2T) & (i=1,2) \\ D_i = 2R_g & (i=3,4), \\ D_i = k_i(B-2T-2R_g) & (i=5,6) \end{cases} \quad (1)$$

where B is the diameter of the cavity, T is the thickness of the cavity wall, R_g is the distance between input and output probes, and k_i is the weighting factor, which is given as

$$k_i = \frac{B-2T-d_i}{2R_g} \quad (i=1,2,5,6). \quad (2)$$

The equivalent impedance of each matching section of each probe can be expressed as,

$$Z_i = R_i + jX_i \quad (i=1,2,...,6) \quad (3)$$

where R_i and X_i are the real and imaginary parts of the equivalent impedance, respectively.

The real part of the equivalent impedance of the probe is actually the characteristic impedance of the coaxial line, which can be obtained by

$$R_i = \frac{60}{\sqrt{\varepsilon_0}} \frac{d_i}{D_i} \quad (i = 1, 2, \cdots, 6), \tag{4}$$

where d_i is the inner conductor diameter, and ε_0 is the vacuum dielectric constant.

According to the parallel lines coupling theory, the mutual coupling between input and output probes can be taken as mutual impedance, and is further equivalent to the imaginary part of the input impedance of the probe. Since Matching Sectoin-1 is more independent, the imaginary part of its input impedance can be calculated as [10]

$$X_1 = \frac{\mu_0 l_1}{8\pi}, \tag{5}$$

where μ_0 is the vacuum permeability.

Since the spacing between Matching Sections-2, -3, and Section-4 are small, there exists strong coupling between them and then electrical coupling plays a major role. The imaginary part of the input impedance is given as [10]

$$X_i = 2\pi\varepsilon_0 \left(\frac{1}{\ln\frac{D_i}{d_3}} - \frac{1}{\ln\frac{D_i}{d_4}}\right) P_i \quad (i = 2, 3, 4), \tag{6}$$

where P_i is the length of the common part of two parallel sections.

The radii of Matching Sections-5 and -6 are much smaller than the distance between two input probes. As a result, the magnetic coupling plays a major role and the imaginary part of the input impedance can be calculated as [10]

$$X_i = \frac{\mu_0 d_i^4 \pi}{32\left[\left(\frac{D_i}{2}\right)^2 + \left(\frac{d_i}{2}\right)^2\right]^{3/2}} \quad (i = 5, 6). \tag{7}$$

According to the multi-section impedance matching theory [17], the reflection coefficient of each matching section can be expressed as,

$$\Gamma_{si} = \frac{Z_i - Z_{i-1}}{Z_i + Z_{i-1}} \quad (i = 2, 3) \tag{8}$$

$$\Gamma_{si} = \frac{Z_i - Z_{i+1}}{Z_i + Z_{i+1}} \quad (i = 4, 5), \tag{9}$$

$$\Gamma_{si} = \frac{Z_i - Z_0}{Z_i + Z_0} \quad (i = 1, 6), \tag{10}$$

where Z_i is the equivalent impedance of Matching Section-i and Z_0 is 50 ohm.

In order to describe the combiner more clearly, the output port is named Port-1, and the three input ports are named Ports-2, -3, and -4, respectively. The reflection coefficient of the port can be calculated by,

$$\Gamma_{p1} = \Gamma_{s1} + (1-\Gamma_{s1})\Gamma_{s2} + \left[1-\left(1-\Gamma_{s1}\right)\Gamma_{s2}\right]\Gamma_{s3} \tag{11}$$

$$\Gamma_{pj} = \Gamma_{s6} + (1-\Gamma_{s6})\Gamma_{s5} + \left[1-\left(1-\Gamma_{s6}\right)\Gamma_{s5}\right]\Gamma_{s4} \quad (j=2, 3, 4), \tag{12}$$

where Γ_{si} is the reflection coefficient of the Matching Sections-i (i=1,2,…,6), and Γ_{pj} is the total reflection coefficient of port j (j = 1, 2, 3 and 4), when the reflection coefficient of each Matching Section is independent.

Then, the VSWR and input impedance of each port can be calculated by,

$$VSWR_j = \frac{1+\left|\Gamma_{pj}\right|}{1-\left|\Gamma_{pj}\right|} \quad (j=1, 2, 3, 4). \tag{13}$$

Consequently, with the given VSWR, the dimensions of the probes can be calculated conversely.

III. PERFORMANCE OF THE COMBINER

A. Impedance matching, insertion loss, and isolation

A combiner is designed and fabricated with the structural parameters listed in Table 1. The performance of the combiner is simulated by using Ansoft's HFSS. The fabricated combiner, as shown in Fig. 2, is measured with the use of an HP vector network analyzer HP8753C. The simulated and measured parameters are shown in Fig. 3.

Basically, performances of the three input ports are the same, thus only one input port VSWR is given. As shown in Fig. 3 (a), the simulated VSWRs of both Port-1 and Port-2 are less than 1.22 ($|S_{11}|$ = -20 dB) within the bandwidth from 1.2 GHz to 2 GHz, while the measured ones are less than 1.4 ($|S_{11}|$ = -15.5 dB), indicating good impedance matching at both input and output ports. The phase imbalance of the three input ports is better than 1 degree, which is shown in Fig. 3 (b), where the phase of S_{41} is taken as a reference.

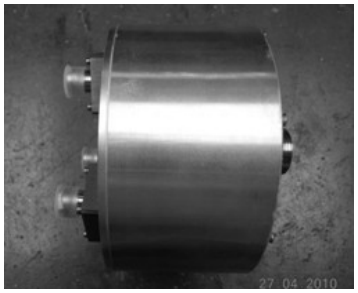

Fig. 2. Fabricated combiner.

Table 1: Dimensions of the power combiner (unit: mm).

l_1	l_2	l_3	l_4	l_5	l_6
26	13	6	25	14	10
d_1	d_2	d_3	d_4	d_5	d_6
8	16	36	24	8	4
B	T	d_{in}	d_{out}	R_q	d_t
150	7.5	9.2	18	46	12

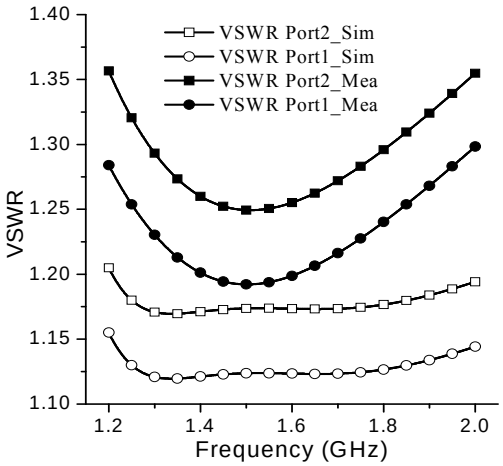

(a) VSWR.

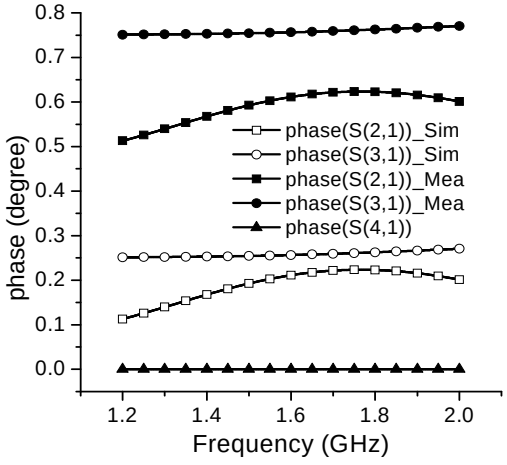

(b) Phase.

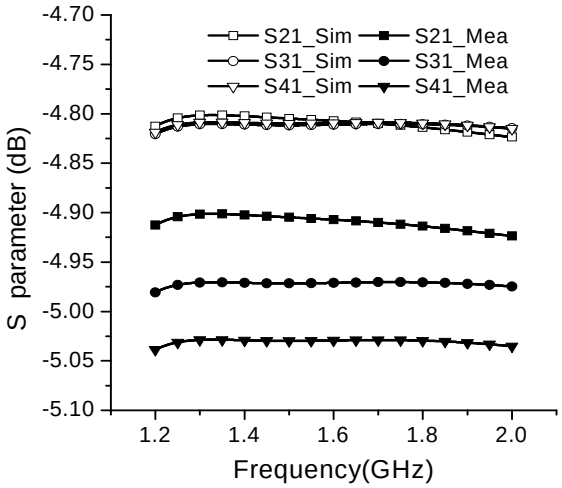

(c) S-parameters between the input ports and output port.

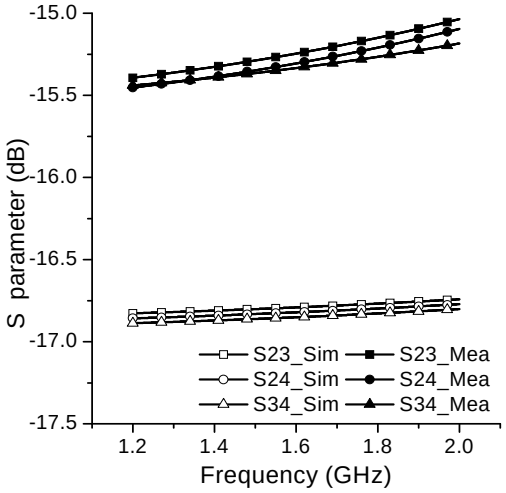

(d) S-parameters between the input ports.

Fig. 3. Simulated and measured results.

Figure 3 (c) presents the power dividing performance of the three ways. The simulation results show that the insertion loss of each way is very close to the theoretical value of 4.78 dB (10log(1/3) = -4.78), while the test curves range between 4.9 dB and 5.05 dB, revealing a maximum in-band additional insertion losses being less than 0.3 dB. Figure 3 (d) shows both the simulated and the measured isolation between any two input ports. The values are better than 15 dB, which meet the design requirements.

From Figure 3, it is clear that the three-way power combiner show a good equalization of power division among three input ports while

maintaining relatively low return loss at each port over a wide bandwidth.

Based on the structural parameters of the combiner, the S-parameters can be calculated, as listed in Table 2. It can be found that the calculated results are consistent with the simulated and measured ones.

Table 2: Calculated S-parameters.

VSWR		S_{21} (dB)	S_{31} (dB)	S_{41} (dB)	S_{23} (dB)	S_{24} (dB)
input port	output port					
1.2	1.25	- 4.8	- 4.8	- 4.9	- 15	- 15

B. Efficiency and power capacity

Since the power capacity of the combiner is determined by the heat breakdown voltage of PTFE [18], according to the theorem of energy storage capacitor, the total capacity of the combiner is calculated by

$$W_e = \frac{3 \times \varepsilon_r \times D^2}{2}, \tag{14}$$

where ε_r is the dielectric constant of PTFE and D is the electric displacement vector. The calculated power capacity W_e is higher than 600 Watt according to the simulation.

The combining efficiency can be calculated by,

$$\eta = \frac{P_{out}}{P_{in}} \tag{15}$$

where P_{out} and P_{in} are the output power and input power, respectively. The measured output and input powers are 540 Watt and 600 Watt, respectively. Consequently, the combining efficiency of this combiner reaches 90 %.

IV. CONCLUSION

In this article, an L-band broadband power combiner has been designed based on variable radial waveguide spatial power combining technology. The developed combiner exhibits good insertion losses between the input and output ports, as well as enhanced port-to-port isolation between input ports. Three axial slots on the cavity sidewall and a grounded disc on the wall of cavity have improved the port-to-port isolation between input ports. Moreover, good VSWR has been obtained with the use of multi-section impedance matching. The tested operating bandwidth ranges from 1.2 GHz to 2 GHz with VSWRs less than 1.4 at all ports. The extra insertion losses between the input and output ports are less than 0.3 dB and the isolation between the input ports is better than 15 dB. The power capacity has reached 600 W and the combining efficiency has achieved 90 %. Results from experiments have validated the design expectation with good agreement.

ACKNOWLEDGMENT

This work was supported by the Natural Science Foundation of China (61271027, 61271025).

REFERENCES

[1] M. Belaid, R. Martinez, and K. Wu, "A mode transformer using fin-line array for spatial power -combiner applications," *IEEE Transactions on Microwave Theory and Techniques*, vol. 52, no. 4, pp. 1191-1198, 2004.

[2] D. I. L. de Villiers, P. W. Van der Walt, and P. Meyer, "Design of a ten-way conical transmission line power combiner," *IEEE Transactions on Microwave Theory and Techniques*, vol. 55, no. 2, Part 1, pp. 302-308, 2007.

[3] J. P. Becker and A. M. Oudghiri, "A planar probe double ladder waveguide power divider," *IEEE Microwave and Wireless Components Letters*, vol. 15, no. 3, pp. 168-170, 2005.

[4] P. Jia, L. -Y. Chen, A. Alexanian, and R. A. York, "Broad-band high-power amplifier using spatial power- combining technique," *IEEE Transactions on Microwave Theory and Techniques*, vol. 51, no. 12, pp. 2469-2475, 2003.

[5] S. C. Ortiz, J. Hubert, L. Mirth, E. Schlecht, and A. Mortazawi, "A high-power Ka-band quasi-optical amplifier array," *IEEE Transactions on Microwave Theory and Techniques*, vol. 50, no. 2, pp. 487-494, 2002.

[6] M. P. Delisio and R. A. York, "Quasi-optical and spatial power combining," *IEEE Transactions on Microwave Theory and Techniques*, vol. 50, no. 3, pp. 929-936, 2002.

[7] P. Jia, L. -Y. Chen, A. Alexanian, and R. A. York, "Multioctave spatial power combining in oversized coaxial waveguide," *IEEE Transactions on Microwave Theory and Techniques*, vol. 50, no. 5, pp. 1355-1360, 2002.

[8] K. Song, Y. Fan, and X. Zhou, "Broadband millimeter-wave passive spatial combiner based on coaxial waveguide," *IET Microwaves, Antennas and Propagation*, vol. 3, no. 4, pp.

607-613, 2009.

[9] K. Song, Y. Fan, and Z. He, "Broadband radial waveguide spatial combiner," *IEEE Microwave and Wireless Components Letters*, vol. 18, no. 2, pp. 73-75, 2008.

[10] D. M. Pozar, *Microwave Engineering*, John Wiley & Sons, 3rd Edition, pp. 244-250, 2005.

[11] Y. -P. Hong, D. F. Kimball, P. M. Asbeck, J. -G. Yook, and L. E. Larson, "Single-ended and differential radial power combiners implemented with a compact broadband probe," *IEEE Transactions on Microwave Theory and Techniques*, vol. 58, no. 6, pp. 1565-1568, 2010.

[12] M. E. Bialkowski, "Analysis of a coaxial-to-waveguide adaptor including a discended probe and a tuning post," *IEEE Transactions on Microwave Theory and Techniques*, vol. 43, no. 2, pp. 344-349, 1995.

[13] R. E. Collin, *Fundamentals of Microwave Engineering*, Wiley-IEEE Press, 2nd Edition, pp. 64-179, 2000.

[14] Y. -P. Hong, D. F. Kimball, P. M. Asbeck, J. -G. Yook, and L. E. Larson, "Switch-controlled multi-octave bandwidth radial power divider/combiner," *IEEE Microwave Symposium Digest (MTT)*, pp. 932-935, 2010.

[15] C. M. Montiel, "Sonnet EM simulation of printed Baluns using PCB data extraction," *27th Annual Review of Progress in Applied Computational Electromagnetics*, Williamsburg, Virginia, pp. 357 -362, March 27-31, 2011.

[16] C. M. Montiel, "Folded Marchand Balun Design and Validation Using Sonnet," *28th Annual Review of Progress in Applied Computational Electromagnetics*, Columbus, Ohio, pp. 680-685, April 10-14, 2012.

[17] G. L. Matthaei, L. Young, and E. M. T. Jones, *Microwave Filter Impedance-Matching Networks and Coupling Structures*, McGraw-Hill book Co., Inc., New York, pp. 126-128, 1985.

[18] H. R Zeller, "Breakdown and pre-breakdown phenomena in solid dielectrics," *IEEE Transactions on Electrical Insulation*, vol. 22, no. 2, pp. 115-122, 1987.

Gang Xu received the M.Sc. degree from UESTC, Chengdu, China. He was with the UESTC and now is with the CETC. His current interest is microwave circuits.

Xue-Song Yang received the Ph.D. degree in Radio Physics from UESTC, Chengdu, China. She joined the UESTC in 2002, where she is currently an Associate Professor. She has been a research fellow at the City University of Hong Kong, a Visiting Scholar at the University of Southern California. Her current research interests include reconfigurable antennas, UWB antennas and wireless channel modeling.

Jia-Lin Li received the M.Sc. degree from UESTC, Chengdu, China, in 2004, and the Ph.D. degree from the City University of Hong Kong, Hong Kong, in 2009, both in Electronic Engineering. Since Sept. 2009, he has been with the Institute of Applied Physics, School of Physical Electronics, UESTC, where he is currently a Professor. His research interests include the high performance active / passive microwave / millimeter-wave antennas, circuits and systems realized on PCB, multilayer PCB, LTCC, etc.

Zhi-Ming Tian received the B.Sc. degree in Physics form Tangshan Normal University, Tangshan, China, in 2009, and the Master degree from UESTC, Chengdu, China in 2012. His current research interests include wireless channel modeling and antennas design.

2013 INSTITUTIONAL MEMBERS

DTIC-OCP LIBRARY
8725 John J. Kingman Rd, Ste 0944
Fort Belvoir, VA 22060-6218

AUSTRALIAN DEFENCE LIBRARY
Northcott Drive
Canberra, A.C.T. 2600 Australia

BEIJING BOOK CO, INC
701 E Linden Avenue
Linden, NJ 07036-2495

DARTMOUTH COLLEGE
6025 Baker/Berry Library
Hanover, NH 03755-3560

DSTO EDINBURGH
AU/33851-AP, PO Box 830470
Birmingham, AL 35283

SIMEON J. EARL – BAE SYSTEMS
W432A, Warton Aerodome
Preston, Lancs., UK PR4 1AX

ENERGY KEN LIBRARY
PO Box 300613
Jamaica, NY, 11430

ENGINEERING INFORMATION, INC
PO Box 543
Amsterdam, Netherlands 1000 Am

ETSE TELECOMUNICACION
Biblioteca, Campus Lagoas
Vigo, 36200 Spain

GA INSTITUTE OF TECHNOLOGY
EBS-Lib Mail code 0900
74 Cherry Street
Atlanta, GA 30332

TIMOTHY HOLZHEIMER
Raytheon
PO Box 1044
Rockwall, TX 75087

HRL LABS, RESEARCH LIBRARY
3011 Malibu Canyon
Malibu, CA 90265

IEE INSPEC
Michael Faraday House
6 Hills Way
Stevenage, Herts UK SG1 2AY

INSTITUTE FOR SCIENTIFIC INFO.
Publication Processing Dept.
3501 Market St.Philadelphia, PA
19104-3302

LIBRARY – DRDC OTTAWA
3701 Carling Avenue
Ottawa, Ontario, Canada K1A OZ4

LIBRARY of CONGRESS
Reg. Of Copyrights
Washington DC, 20559

LINDA HALL LIBRARY
5109 Cherry Street
Kansas City, MO 64110-2498

MISSOURI S&T
400 W 14th Street
Rolla, MO 56409

MIT LINCOLN LABORATORY
244 Wood Street
Lexington, MA 02420

NATIONAL CHI NAN UNIVERSITY
Lily Journal & Book Co, Ltd
20920 Glenbrook Drive
Walnut, CA 91789-3809

JOHN NORGARD
UCCS
20340 Pine Shadow Drive
Colorado Springs, CO 80908

OSAMA MOHAMMED
Florida International University
10555 W Flagler Street
Miami, FL 33174

NAVAL POSTGRADUATE SCHOOL
Attn:J. Rozdal/411 Dyer Rd./ Rm 111
Monterey, CA 93943-5101

NDL KAGAKU
C/0 KWE-ACCESS
PO Box 300613 (JFK A/P)
Jamaica, NY 11430-0613

OVIEDO LIBRARY
PO BOX 830679
Birmingham, AL 35283

DAVID PAULSEN
E3Compliance
1523 North Joe Wilson Road
Cedr Hill, TX 75104-1437

PENN STATE UNIVERSITY
126 Paterno Library
University Park, PA 16802-1808

DAVID J. PINION
1122 E Pike Street #1217
SEATTLE, WA 98122

KATHERINE SIAKAVARA
Gymnasiou 8
Thessaloniki, Greece 55236

SWETS INFORMATION SERVICES
160 Ninth Avenue, Suite A
Runnemede, NJ 08078

YUTAKA TANGE
Maizuru Natl College of Technology
Maizuru, Kyoto, Japan 625-8511

TIB & UNIV. BIB. HANNOVER
Welfengarten 1B
Hannover, Germany 30167

UEKAE
PO Box 830470
Birmingham, AL 35283

UNIV OF CENTRAL FLORIDA
4000 Central Florida Boulevard
Orlando, FL 32816-8005

UNIVERSITY OF COLORADO
1720 Pleasant Street, 184 UCB
Boulder, CO 80309-0184

UNIVERSITY OF KANSAS – WATSON
1425 Jayhawk Blvd 210S
Lawrence, KS 66045-7594

UNIVERSITY OF MISSISSIPPI
JD Williams Library
University, MS 38677-1848

UNIVERSITY LIBRARY/HKUST
Clear Water Bay Road
Kowloon, Honk Kong

CHUAN CHENG WANG
8F, No. 31, Lane 546
MingCheng 2nd Road, Zuoying Dist
Kaoshiung City, Taiwan 813

THOMAS WEILAND
TU Darmstadt
Schlossgartenstrasse 8
Darmstadt, Hessen, Germany 64289

STEVEN WEISS
US Army Research Lab
2800 Powder Mill Road
Adelphi, MD 20783

YOSHIHIDE YAMADA
NATIONAL DEFENSE ACADEMY
1-10-20 Hashirimizu
Yokosuka, Kanagawa,
Japan 239-8686

APPLIED COMPUTATIONAL ELECTROMAGNETICS SOCIETY JOURNAL
http://aces.ee.olemiss.edu

INFORMATION FOR AUTHORS

PUBLICATION CRITERIA

Each paper is required to manifest some relation to applied computational electromagnetics. **Papers may address general issues in applied computational electromagnetics, or they may focus on specific applications, techniques, codes, or computational issues.** While the following list is not exhaustive, each paper will generally relate to at least one of these areas:

1. **Code validation.** This is done using internal checks or experimental, analytical or other computational data. Measured data of potential utility to code validation efforts will also be considered for publication.

2. **Code performance analysis.** This usually involves identification of numerical accuracy or other limitations, solution convergence, numerical and physical modeling error, and parameter tradeoffs. However, it is also permissible to address issues such as ease-of-use, set-up time, run time, special outputs, or other special features.

3. **Computational studies of basic physics.** This involves using a code, algorithm, or computational technique to simulate reality in such a way that better, or new physical insight or understanding, is achieved.

4. **New computational techniques** or new applications for existing computational techniques or codes.

5. **"Tricks of the trade"** in selecting and applying codes and techniques.

6. **New codes, algorithms, code enhancement, and code fixes.** This category is self-explanatory, but includes significant changes to existing codes, such as applicability extensions, algorithm optimization, problem correction, limitation removal, or other performance improvement. **Note: Code (or algorithm) capability descriptions are not acceptable, unless they contain sufficient technical material to justify consideration.**

7. **Code input/output issues.** This normally involves innovations in input (such as input geometry standardization, automatic mesh generation, or computer-aided design) or in output (whether it be tabular, graphical, statistical, Fourier-transformed, or otherwise signal-processed). Material dealing with input/output database management, output interpretation, or other input/output issues will also be considered for publication.

8. **Computer hardware issues.** This is the category for analysis of hardware capabilities and limitations of various types of electromagnetics computational requirements. Vector and parallel computational techniques and implementation are of particular interest.

Applications of interest include, but are not limited to, antennas (and their electromagnetic environments), networks, static fields, radar cross section, inverse scattering, shielding, radiation hazards, biological effects, biomedical applications, electromagnetic pulse (EMP), electromagnetic interference (EMI), electromagnetic compatibility (EMC), power transmission, charge transport, dielectric, magnetic and nonlinear materials, microwave components, MEMS, RFID, and MMIC technologies, remote sensing and geometrical and physical optics, radar and communications systems, sensors, fiber optics, plasmas, particle accelerators, generators and motors, electromagnetic wave propagation, non-destructive evaluation, eddy currents, and inverse scattering.

Techniques of interest include but not limited to frequency-domain and time-domain techniques, integral equation and differential equation techniques, diffraction theories, physical and geometrical optics, method of moments, finite differences and finite element techniques, transmission line method, modal expansions, perturbation methods, and hybrid methods.

Where possible and appropriate, authors are required to provide statements of quantitative accuracy for measured and/or computed data. This issue is discussed in "Accuracy & Publication: Requiring, quantitative accuracy statements to accompany data," by E. K. Miller, *ACES Newsletter*, Vol. 9, No. 3, pp. 23-29, 1994, ISBN 1056-9170.

SUBMITTAL PROCEDURE

All submissions should be uploaded to ACES server through ACES web site (http://aces.ee.olemiss.edu) by using the upload button, journal section. Only pdf files are accepted for submission. The file size should not be larger than 5MB, otherwise permission from the Editor-in-Chief should be obtained first. Automated acknowledgment of the electronic submission, after the upload process is successfully completed, will be sent to the corresponding author only. It is the responsibility of the corresponding author to keep the remaining authors, if applicable, informed. Email submission is not accepted and will not be processed.

EDITORIAL REVIEW

In order to ensure an appropriate level of quality control, papers are peer reviewed. They are reviewed both for technical correctness and for adherence to the listed guidelines regarding information content and format.

PAPER FORMAT

Only camera-ready electronic files are accepted for publication. The term **"camera-ready" means that the material is neat, legible, reproducible, and in accordance with the final version format listed below.**

The following requirements are in effect for the final version of an ACES Journal paper:

1. The paper title should not be placed on a separate page.

The title, author(s), abstract, and (space permitting) beginning of the paper itself should all be on the first page. The title, author(s), and author affiliations should be centered (center-justified) on the first page. The title should be of font size 16 and bolded, the author names should be of font size 12 and bolded, and the author affiliation should be of font size 12 (regular font, neither italic nor bolded).

2. An abstract is required. The abstract should be a brief summary of the work described in the paper. It should state the computer codes, computational techniques, and applications discussed in the paper (as applicable) and should otherwise be usable by technical abstracting and indexing services. The word "Abstract" has to be placed at the left margin of the paper, and should be bolded and italic. It also should be followed by a hyphen (—) with the main text of the abstract starting on the same line.

3. All section titles have to be centered and all the title letters should be written in caps. The section titles need to be numbered using roman numbering (I. II. ….)

4. Either British English or American English spellings may be used, provided that each word is spelled consistently throughout the paper.

5. Internal consistency of references format should be maintained. As a guideline for authors, we recommend that references be given using numerical numbering in the body of the paper (with numerical listing of all references at the end of the paper). The first letter of the authors' first name should be listed followed by a period, which in turn, followed by the authors' complete last name. Use a coma (,) to separate between the authors' names. Titles of papers or articles should be in quotation marks (" "), followed by the title of journal, which should be in italic font. The journal volume (vol.), issue number (no.), page numbering (pp.), month and year of publication should come after the journal title in the sequence listed here.

6. Internal consistency shall also be maintained for other elements of style, such as equation numbering. Equation numbers should be placed in parentheses at the right column margin. All symbols in any equation have to be defined before the equation appears or right immediately following the equation.

7. The use of SI units is strongly encouraged. English units may be used as secondary units (in parentheses).

8. Figures and tables should be formatted appropriately (centered within the column, side-by-side, etc.) on the page such that the presented data appears close to and after it is being referenced in the text. When including figures and tables, all care should be taken so that they will appear appropriately when printed in black and white. For better visibility of paper on computer screen, it is good to make color figures with different line styles for figures with multiple curves. Colors should also be tested to insure their ability to be distinguished after black and white printing. Avoid the use of large symbols with curves in a figure. It is always better to use different line styles such as solid, dotted, dashed, etc.

9. A figure caption should be located directly beneath the corresponding figure, and should be fully justified.

10. The intent and meaning of all text must be clear. For authors who are not masters of the English language, the ACES Editorial Staff will provide assistance with grammar (subject to clarity of intent and meaning). However, this may delay the scheduled publication date.

11. Unused space should be minimized. Sections and subsections should not normally begin on a new page.

ACES reserves the right to edit any uploaded material, however, this is not generally done. It is the author(s) responsibility to provide acceptable camera-ready files in pdf and MSWord formats. Incompatible or incomplete files will not be processed for publication, and authors will be requested to re-upload a revised acceptable version.

COPYRIGHTS AND RELEASES

Each primary author must execute the online copyright form and obtain a release from his/her organization vesting the copyright with ACES. Both the author(s) and affiliated organization(s) are allowed to use the copyrighted material freely for their own private purposes.

Permission is granted to quote short passages and reproduce figures and tables from and ACES Journal issue provided the source is cited. Copies of ACES Journal articles may be made in accordance with usage permitted by Sections 107 or 108 of the U.S. Copyright Law. This consent does not extend to other kinds of copying, such as for general distribution, for advertising or promotional purposes, for creating new collective works, or for resale. The reproduction of multiple copies and the use of articles or extracts for commercial purposes require the consent of the author and specific permission from ACES. Institutional members are allowed to copy any ACES Journal issue for their internal distribution only.

PUBLICATION CHARGES

All authors are allowed for 8 printed pages per paper without charge. Mandatory page charges of $75 a page apply to all pages in excess of 8 printed pages. Authors are entitled to one, free of charge, copy of the printed journal issue in which their paper was published. Additional reprints are available for $ 50. Requests for additional re-prints should be submitted to the managing editor or ACES Secretary.

Corresponding author is required to complete the online form for the over page charge payment right after the initial acceptance of the paper is conveyed to the corresponding author by email.

ACES Journal is abstracted in INSPEC, in Engineering Index, DTIC, Science Citation Index Expanded, the Research Alert, and to Current Contents/Engineering, Computing & Technology.